UNIVERSITY OF SOUTHAMPTON

FACULTY OF ENGINEERING AND THE ENVIRONMENT

Institute of Sound and Vibration Research

ROAD AND SOIL DYNAMIC CHARACTERIZATION FROM SURFACE MEASUREMENTS

By

Michele Iodice

Thesis for the degree of Doctor of Philosophy

February 2017

UNIVERSITY OF SOUTHAMPTON

ABSTRACT

FACULTY OF ENGINEERING AND THE ENVIRONMENT

INSTITUTE OF SOUND AND VIBRATION RESEARCH

Thesis for the degree of Doctor of Philosophy

ROAD AND SOIL DYNAMIC CHARACTERIZATION FROM SURFACE MEASUREMENTS

Michele Iodice

The increased demand for non-destructive evaluation of the shear wave profiling, condition monitoring and performance assessment of soils and roads in a dynamic state has made seismic methods the most desirable and effective non-destructive techniques. Surface wave methods have gained popularity over the last decades since they monitor the propagation of the surface wave with non-invasive transducers working from the surface. Nonetheless, their use is restricted by resolution problems and their ability to assess the actual dispersive behaviour of Rayleigh wave. Non-destructive, *in-situ* methods for characterizing existing infrastructures require the ability to detect structural damage and features such as cracking and discontinuities. The proper assessment of the location and of the extension of such discontinuities is crucial for the determination of the level of deterioration of an infrastructure and for planning the maintenance interventions. Damage in a pavement structure is usually initiated in the asphalt layers, making the Rayleigh wave ideally suited for the detection of shallow surface defects. Nonetheless, the practical application of crack detection methods in asphalt is hampered due to the heterogeneous and dispersive nature of the material tested.

This thesis describes new signal processing methods and the novel application of existing methods to tackle the problems that hinder the non-destructive surface wave methods.

The spectral convolution method proposed in this thesis, based on the simultaneous exploitation of the vertical and the horizontal components of a seismic event, improved the resolution and the overall accuracy of the spectral image in the frequency-wavenumber (*f-k*) domain. Hence, it led to more accurate seismic inversion by reducing the amount of uncertainty coming from a seismic survey. This research investigated the use of this new proposed method in soils and asphalts for the

measurement of surface wave dispersion through conceptual analysis and numerical investigation alongside experimental investigation on soil and asphalt.

The application of spectral wave methods and the transformation of the wavefield into the frequency-wavenumber domain allowed the identification of the position and the extension of vertical defects. The joint use of the Multichannel Analysis of Surface Waves and the Multiple Impact of Surface Waves methods in numerical and experimental investigations presented in this thesis proved to be effective for crack detection and sizing. Moreover, the space-normalised seismogram helped in the interpretation of *f-k* spectra for cracks detection.

Here, the wave decomposition method for crack interrogation consisted of a signal processing algorithm capable of computing the direct and reflected waves' amplitudes and phase angles from the signals of a deployment of sensors. It solved linear systems with a number of measurements much bigger than the number of unknowns. It tackled the measurement errors naturally present in experimental data by finding a least square approximate solution with the help of the pseudo-inverse matrix for overdetermined systems. The results coming from numerical simulations and experimental investigations showed the effectiveness of the wave decomposition method for the assessment of the location and of the depth of surface-breaking cracks in the half-space and in layered systems. Contrary to other techniques, it was able to cope with the heterogeneities and the dispersive nature of layered system, thus making possible to detect and assess the depth of surface-breaking cracks in roads.

Table of Contents

Declaration of Authorship

I, Michele Iodice, declare that this thesis entitled "ROAD AND SOIL DYNAMIC CHARACTERIZATION FROM SURFACE MEASUREMENTS" and the work presented in it are my own and have been generated by me as the result of my own original research.

I confirm that:

1. This work was done wholly or mainly while in candidature for a research degree at this University;
2. Where any part of this thesis has previously been submitted for a degree or any other qualification at this University or any other institution, this has been clearly stated;
3. Where I have consulted the published work of others, this is always clearly attributed;
4. Where I have quoted from the work of others, the source is always given. With the exception of such quotations, this thesis is entirely my own work;
5. I have acknowledged all main sources of help;
6. Where the thesis is based on work done by myself jointly with others, I have made clear exactly what was done by others and what I have contributed myself;
7. Parts of this work have been published as:

Iodice, M., Rustighi, E. and Muggleton, J., *"Comparison of Soil Excitation Methods for Surface Wave Speed Measurements", International Conference on Noise and Vibration Engineering*, Leuven, Belgium, 2014.

Iodice, M., Rustighi, E. and Muggleton, J., *"A Multi-Component Approach to the Seismic Characterization of Real Multi-Layered Media", NDT-CE 2015 International Symposium Non-Destructive Testing in Civil Engineering,* Berlin, Germany, 2015.

Iodice, M., et al., *"Joint Use of Seismic and Electromagnetic Methods in Geophysical Surveys", NDT-CE 2015 International Symposium Non-Destructive Testing in Civil Engineering,* Berlin, Germany, 2015.

Iodice, M., Rustighi, E. and Muggleton, J., *"The Detection of Vertical Cracks in Asphalt Using Seismic Surface Wave Methods", Journal of Physics Conference Series,* 2016.

Signed: ……

Date: ……

Acknowledgements

This work would have not been possible without the invaluable support and guidance of a number of people. I am deeply grateful for the help, the wisdom and the patience of my supervisors, Emiliano Rustighi and Jen Muggleton. Their constant supervision and inspiration has been undoubtedly an essential ingredient for the accomplishment of this project.

I would like to express my sincere gratitude to the members of my internal review panels, David Thompson and Phil Joseph, for their helpful comments during my doctorate.

I would also like to thank the people working at the mechanical and electric workshops within the Institute of Sound and Vibration Research. They promptly satisfied any request and made a significant contribution to this thesis.

I had also the pleasure to collaborate with academics and researcher from other renowned universities within the Assessing the Underworld programme. My gratitude goes to the many that stimulated and inspired my research along the way. A special mention goes to Giulio Curioni.

Finally yet importantly, I would like to give special thanks to the people of the Dynamics Group and of the Signal Processing and Control Group, always keen on talking, exchanging ideas, giving, and receiving valuable hints.

For all the aforementioned reasons the Institute of Sound and Vibration Research has been an inspiring and vibrant environment for the development of my doctorate.

Abbreviations and Definitions

CBR	California Bearing Ratio
DCP	Dynamic Cone Penetrometer
DoF	degrees of freedom
DPI	DCP penetration index
EU	engineering units
FEM	Finite Element Method
f-k	frequency-wavenumber
FRF	Frequency Response Function
FWD	Falling Weight Deflectometer
GWC	Gravimetric Water Content
H/V	Ellipticity
HVSR	Horizontal to Vertical Spectral Ratio
IE	Impact Echo
MASW	Multichannel Analysis of Surface Waves
MISW	Multiple Impact of Surface Waves
PDE	partial differential equations
P-wave	primary or compressional wave
ReMi	Refraction Microtremor
R-wave	Rayleigh or surface wave
SASW	Spectral Analysis of Surface Waves
SCPT	Seismic Cone Penetration Test
SH-wave	shear horizontal wave
SV-wave	shear vertical wave
S-wave	secondary or shear wave
TDR	Time Domain Reflectometry
UBW	Ultrasonic Body Wave
USW	Ultrasonic Surface Wave
VWC	Volumetric Water Content

List of Symbols

a	width of the finite vibrating line
b	arm of the moment
c_c	compression index
c_m	wave speed in the medium
c_ω	phase velocity
c_{xy}	coherence function between $x(t)$ and $y(t)$
d	layer's thickness
d_i	mode integer index
d_r	damping of the geophone
e	void ratio
f	frequency
f_{max}	maximum desired frequency
f_{res}	resonant frequency
f_s	sampling frequency
Δf	resolution in frequency domain
h	depth of the surface-breaking crack
i	imaginary unit
k	wavenumber
k^*	complex wavenumber
Δk	resolution in wavenumber domain
$l_{\max}$	maximum mesh size at the surface of the model
m	moving mass of the geophone
n	number of points in time
$p(x,t)$	spectral convolution space-time representation
Δp	offset between reflection phenomena in the MISW simulation
$\mathbf{p}$	external "load vector"
r	distance from the source
r^+, r^-	amplitudes of positive and negative going waves
$\mathbf{r}$	amplitude vector
s	source
t	time

$t(f)$	time delay between two signals
Δt	temporal sampling interval
$\Delta t_{\max}$	maximum temporal sampling interval
$\mathbf{u}$	displacements vector
$u(x,t)$	vertical space-time domain representation
u_x	displacements in *x*-direction
u_y	displacements in *y*-direction
u_z	displacements in *z*-direction
$\dot{u}_x, \dot{u}_y, \dot{u}_z$	velocities
$w(x,t)$	horizontal space-time representation
x	space
$x(t)$	time history of the signal
x_a	absolute displacement of the frame
x_0	distance from a reference point
x_1	offset between source and the first receiver
$\mathbf{x}^*$	approximate solution vector
$y(t)$	time history of the signal
$z(x,t)$	product of the vertical (or horizontal) component of the displacement by itself
$\mathbf{z}_j$	state vector of the j-th layer
A, B	amplitudes of a wave
A_0	initial wave amplitude
$A(x,\omega)$	amplitude spectrum
$\mathbf{A, B, G, M}$	stiffness matrices
$\mathbf{A_w}$	constant terms matrix
C	coefficient of surface breaking crack
$\mathbf{C}$	damping matrix
D	sensors spacing/spatial sampling interval
E	Young's Modulus
$\mathbf{E}$	expected value
E_n	peak strain energy
ΔE_n	energy loss per cycle
G	shear Modulus
G_{max}	maximum shear Modulus
$\mathbf{H}$	vector potential
$\mathbf{H}_j$	transfer matrix of the j-th layer

I	inductance of the geophone
$J_v(kx)$	Bessel function of the first kind of order v
$\mathbf{K}$	stiffness matrix of the layer
L_f	length of the signal
L_s	length of the sensor line
L_1	length of $U(x,\omega)$
L_2	length of $W(x,\omega)$
M	mismatch between observed and the predicted spectra
M_s	mass of the solid
M_w	mass of the water
N	number of sensors
N_f	frequency bandwidth
N_L	total number of layers in the analytical model
$P(k,\omega)$	spectral convolution frequency-wavenumber domain representation
$P(k,\omega)_{obs}$	observed spectral convolution frequency-wavenumber domain representation
R	receiver or geophone
Re_1	internal resistance of geophone
Re_2	electrical resistance
S	degree of saturation
S_u	undrained shear strength of clays
$S_x(f)$	linear spectrum of $x(t)$
$S_y(f)$	linear spectrum of $y(t)$
$S_{xx}(f)$	auto-spectrum of $x(t)$
$S_{xy}(f)$	cross-power spectrum between $x(t)$ and $y(t)$
$S_{yy}(f)$	auto-spectrum of $y(t)$
$\mathbf{S}$	stiffness matrix
T	duration of the simulation
T_2	transducer constant
$\mathbf{T}$	mass matrix
$U(x,\omega)$	vertical space-frequency domain representation
$U(x,\omega)_{pred}$	predicted vertical space-frequency domain representation
$U(k,\omega)$	vertical frequency-wavenumber domain representation
$U(k,\omega)_{an}$	analytical vertical frequency-wavenumber domain representation
$U(k,\omega)_{pred}$	predicted vertical frequency-wavenumber domain representation
V	total volume of the soil

V_s	volume of the solid state
V_v	volume of voids
V_w	volume of the water
V_{ph}	apparent phase velocity
V_{out}	output of the geophone
V_P	compressional wave velocity
V_R	Rayleigh wave velocity
V_S	shear wave velocity
$V_{s,A}$, $V_{p,A}$	shear wave velocity and body wave velocity in medium A
$V_{s,B}$, $V_{p,B}$	shear wave velocity and body wave velocity in medium B
$W(x,\omega)$	horizontal space-frequency domain representation
$W(k,\omega)$	horizontal frequency-wavenumber domain representation
α,β	incident angles of compressional and shear waves
α_1,β_1	reflected angles of compressional and shear waves
α_2,β_2	refracted angles of compressional and shear waves
α_c	critical incident angle
α_d	mass-proportional damping coefficient
β_d	stiffness-proportional damping coefficient
γ	shear strain
ε	normal strain
λ,μ	Lame constants
λ_R	Rayleigh wavelength
λ_S	minimum shear wavelength
$\lambda_{\max}$	maximum desired wavelength
$\lambda_{\min}$	minimum desired wavelength
ν	Poisson's ratio
ξ	damping ratio
η	quality factor
ρ	total density of the medium
ρ_d	bulk or dry density
ρ_w	water density
σ	normal stress
σ_{SP}	ratio between shear and compressional wave velocities

τ	tangential stress
ϕ	porosity
$\phi(f)$	phase difference between two signals
$\boldsymbol{\varphi}$	vector of eigenvectors
χ	constant
ω	angular frequency
ω_n	natural resonant frequency of the geophone
Φ	scalar potential
Υ	ellipticity
∇	Nabla operator
∇^2	gradient of the nabla operator
$\bullet$	scalar product
$\times$	vector product

Chapter 1: Introduction and Literature Review

1.1 Background

The problem addressed in this thesis is that of dynamic characterization of soils and pavement systems. The biggest challenge that industry has accepted in recent years is the non-invasive characterization of complex system, i.e. the ability to describe characters and qualities of complex systems, avoiding any excavation or disruption to the service, but relying on the aid of sensors working from the surface.

Shear and Young's moduli are crucial parameters in civil engineering. Shear Modulus is used for the assessment of seismic hazards and for stability of slopes; Young's Modulus is a key performance parameter used in the civil and environmental industry. Elastic moduli, body wave speeds and bulk density are linked together through the wave equation of motion. The evaluation of these mechanical parameters in a dynamic state is advantageous in most of the cases, especially in the case of road construction, where a static parameter is usually not representative of the strain and stress rates that the material will undergo during its service life.

The exploitation of seismic waves for civil engineering purposes has seen recently an increase in popularity compared with traditional methods. The advantages of non-destructive seismic methods are their effectiveness, reliability and accessibility. Moreover, they allow the assessment of other relevant information about the state of an infrastructure, such as the location and the depth of damages and cracking, or the detection of buried infrastructures and voids. Seismic methods have proven to be successful in determining the potential level of deterioration in the road overall and the infrastructure beneath it.

Nonetheless, surface wave methods suffer from ambiguity due to their ability in assessing an unequivocal dispersion curve. Often experimental results are misinterpreted and the inversion problem does not have a unique solution.

Geotechnical parameters are likewise important in civil engineering, especially for design and construction purposes. They are generally assessed with laboratory tests, which are not representative of the state of stress of soil since the specimen is disturbed, or with cumbersome, expensive and inaccurate *in-situ* tests. The indirect relationships between some of the key geotechnical parameters and the shear velocity could fill some gaps in the field of ground investigation.

Generally, there is a lack of non-invasive, fast and accurate *in-situ* testing methods for the assessment of the dynamic modulus and thicknesses of the layers of ground and pavement systems, making

difficult to perform regular maintenance inspections. The assessment of construction material properties is a crucial aspect in every phase of the life of an infrastructure. The request of monitoring the properties of materials also during and after construction is justified by the value of the infrastructure itself, which is now considered by the community as a good to defend rather than a construction to abandon to its own fate.

In this Chapter, the overall problem of soil and roads dynamic characterization is faced taking into account its vastness and complexity, by introducing physical principles and highlighting the drawbacks of seismic methods. The research motivations and aims are also reported to introduce the forthcoming studies on waves' propagation on ground and asphalt.

1.2 Constitutive Behaviour of Soil

The soil is generally a non-linear, elasto-plastic and anisotropic material which is composed of solid particles and inter-particle voids called pores. The pores could be partially or completely filled with water. Thus, soils are systems where the three states of matter are present at the same time: gas, liquid and solid. For all of these reasons, models for soil behaviour are extremely complex [1].

However, the response of soils to dynamic, low-strain loadings is controlled by their associated mechanical properties, such as shear modulus G and Young's modulus E. By knowing the velocity of seismic waves in a medium, both moduli can be calculated. For this purpose, several seismic *in-situ* tests can be used to determine the shear velocity in a dynamic state, which will be briefly reviewed in this Chapter. All the seismic methods share the same principle: the material is undergoing very small level of strain, so that the constitutive behaviour is assumed to be linear. Therefore, soil is generally modelled as an elastic medium, which could be horizontally layered. Each layer is assumed isotropic and homogeneous. In actual fact, the layers are not perfectly horizontal but there is a camber in the road structure. This generally causes uncertainties difficult to estimate and compensate for.

The behaviour of soil under cyclic loading is described by its hysteresis loop, which is the plot of load versus displacements or, in other terms, the stress-strain path [1, 2]. The area enclosed by the hysteresis loop is a measure of the energy dissipated during each cycle. The dissipation of energy can manifest itself in different ways: heat, friction between solid particles in the skeleton, relative motion between the solid skeleton and the fluid, plastic deformations [1]. The shape of the hysteresis loop is a good indicator of two mechanical parameters, the maximum shear secant modulus $G_{\max}$, represented by the slope of the tangent to the hysteresis curve at zero strain, and the damping ratio ξ. Although the stress-strain curve is generally non-linear, for small levels of strain (lower than 10^{-3}) the behaviour of soils is assumed to be linear [3].

1.3 Pavement Structure and Measurement of the Dynamic Modulus

Paved roads provide a smooth and regular surface for vehicles to move along easily and safely. The structure of the paved road consists of a multi-layered system of bitumen-bound and unbound materials disposed on top of each other. Since vehicles concentrate their weight in a very small area (the contact area between the tyres and the surface), the surface of paved roads should be able to resist under cycling loads and in the meanwhile carry and distribute the stresses to the underlying layers. The layers are usually stiffer in the shallow surface, where the stress is bigger, being less stiff with depth. Hence, stiffer asphalt-based layers are at the top of the road system and withstand the highest stresses. Asphalt is a composite material made from a composition of natural aggregates of different sizes and bitumen. A typical flexible road structure comprises the following layers (see Figure 1.1):

- surface course made of asphalt: it ensures the good and regular rolling surface for tires and it is exposed to the natural environment;
- binder course, made of asphalt;
- base course, usually made of asphalt with bigger aggregate sizes;
- foundation layer, made of mixed concrete or aggregates;
- sub-base layer, made of improved soil.

The road structure sits on top of natural subgrade soil with adequate mechanical properties.

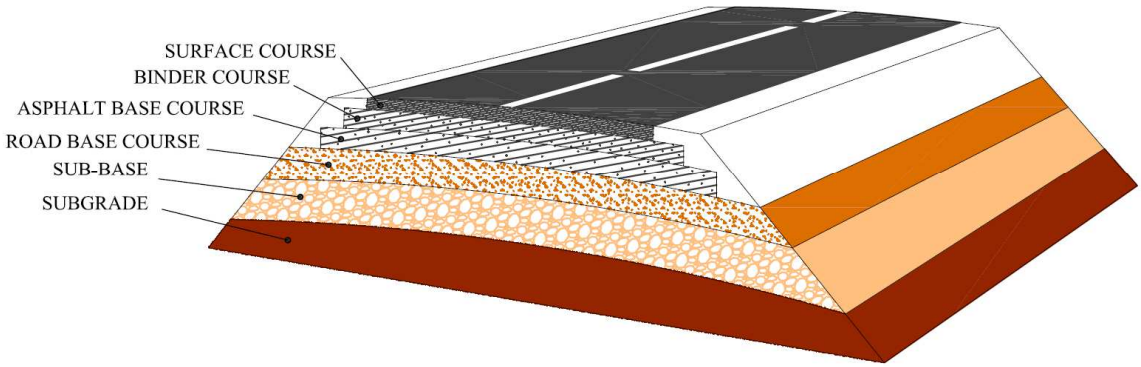

Figure 1.1: Road pavement system.

The most common *in-situ* method for the assessment of the dynamic modulus of a road's layers is the Falling Weight Deflectometer (FWD). The apparatus consists of a system of springs and masses dropped from a predetermined height in order to produce and infer the wanted state of stress on the road system. Displacements caused by the impact load are measured by means of geophones at different distances from the source. A numerical inversion minimizes the differences between the magnitudes of the displacements of experimental and numerical data, determining the actual stiffness profile. The method is based on the contradictory use of a static solution to process a dynamic event. In addition, FWD works at large strain load levels, thus estimating the non-linear response of the road for the assessment of an elastic parameter. FWD needs the number and thicknesses of layers to be known in advance prior to the numerical inversion. This *a-priori* information is usually collected with the aid of ground penetrating radars or by drilling cores.

1.4 Methods for the *in-situ* Measurement of the Velocity of Seismic Waves in Soils

As will be illustrated in the forthcoming chapter, there are two fundamental kinds of seismic waves: those propagating inside a medium (body waves) and those travelling along the surface of it (surface waves). Compressional waves, sometimes referred to as P-waves, and shear waves, sometimes referred to as S-waves, are body waves, while the Rayleigh wave, sometimes referred to as the R-wave, is one kind of surface wave.

Different *in-situ* seismic techniques have been developed with the aim of evaluating the P-wave and S-wave velocities of soils. These physical quantities are linked to the mechanical properties of soils, mainly the shear modulus G and elastic stiffness modulus E, through constitutive relationships.

In-situ seismic wave techniques are based on the generation of stress waves, by ground excitation, and on the measurement of the associated wavefield over a wide range of wavelengths, at specified distances from the excitation point. A first general classification among different type of seismic wave methods can be done with respect to the type of wave to be measured: the choice depends on the nature of material to be tested, on the depth of the survey, on the type of excitation, on the technology to be adopted. Some of them measure the body wave velocity; some are based on the measurement of the surface wave velocity.

In-situ tests have some advantages compared to laboratory tests. The latter require sampling, which causes the mechanical disturbance of the soil structure, and it may change the stress distribution because of the effects of the surrounding volume of ground [1, 3]. *In-situ* tests may require boreholes to be dug, but they do not need sampling and consequently the main volume of tested ground remains undisturbed, at its *in-situ* stress, density and level of saturation. In addition, field results are usually

representative of a large volume of ground. All the discontinuities and the changes in the mechanical properties among depth, as well as the effects of fissures and fracturing influence the measurement and the result is an averaging of soil parameters. This leads to measure an equivalent overall soil response to dynamic excitations.

Since such methods estimate the stiffness at very low level of strain (i.e. less than 10^{-3}) [3], they provide the upper bound for stiffness, i.e. the maximum value of the modulus that occurs at strains values close to zero [4]. The stiffness at operational strain level ($10^{-1} \div 10^{-2}$) is usually lower, about 25% in the case of soft clays, and even 50% lower for stiff clays and rocks [3, 5].

The wave source can be passive or active [6, 7]. Passive sources do not generate energy artificially, but exploit the ground motion induced by background noise and microtremors, so they are not adjustable to fit case by case. They also usually do not provide high-frequency energy; hence they are utilised for deep depth investigations. Active sources are typically classified as transient or continuous. Transient sources are excitations that last for a short finite period of time and they are usually impulsive, such as sledgehammers, mallets, falling masses and explosives [8-10]. Typical continuous sources are hydraulic or pneumatic vibrators and electromechanical shakers. The signal is usually a sine sweep or a white noise [4, 7].

The seismic *in-situ* methods can be divided into two main groups, destructive and non-destructive methods. Those which need boreholes to be dug belong to the first group, while methods which do not need any excavation, but are undertaken entirely from the surface, belong to the second group. To the first group belong methods like the cross-hole, down-hole and up-hole testing, which consist of one or more boreholes where receivers and sources are deployed. These methods usually use impulsive sources like falling weights or sledgehammers [1, 2, 11, 12]. More complex, costly and cumbersome equipment like the seismic cone penetration test (SCPT) and the suspension logging, are also destructive methods since need boreholes to be dug to determine the speed of body waves at various depth [1, 2, 11]. To the second group belong methods like the seismic refraction and reflection, and the Spectral Analysis of Surface Waves (SASW), which has evolved in the Multichannel Analysis of Surface Waves (MASW) and in the Multiple Impact of Surface Waves (MISW). They all use active sources and the deployment of an array of two or more sensors [1, 2, 6, 9, 13]. Seismic refraction and reflection techniques are based on the refraction and reflection of body wave energy at the interfaces between subsurface layers of different velocity. They cannot cope with the presence of a velocity inversion or of thin layers [1, 11]. SASW, MASW and MISW allow the measurement of the variation in soil stiffness with depth exploiting the dispersive behaviour of surface waves. MISW uses a reduced number of sensors, but multiple source location, with respect to MASW. Refraction Microtremor (ReMi) and Horizontal to Vertical Spectral Ratio (HVSR) are

non-destructive tests which use passive sources like microtremors and background noise [7, 11, 14]. Non-destructive surface wave methods will be described in more details in the forthcoming sections.

Non-destructive seismic methods are mainly based on the measurement of Rayleigh, or surface, waves, which propagate along the shallow surface. The amplitude of Rayleigh waves decreases exponentially with depth with most of the energy being contained within the depth of one wavelength. Surface wave methods exploit the dispersive behaviour of Rayleigh waves in vertically heterogeneous media, i.e. different frequency components travel at different speed and depths.

Imaging techniques are usually adopted to extract relevant information from the seismic survey. Typically, the frequency-wavenumber (*f-k*) transformation is applied to the seismic record, yielding to a spectral image of the dispersion. Then, peaks of energy are usually extracted from the spectral image to obtain the dispersion curve of the site. Often the traditional signal processing techniques fail in the identification or in the separation of different modes of propagation due to lack of resolution, leading to a misinterpretation of the seismic data [15-18]. In normally dispersive media, the fundamental mode is dominant throughout the frequency range of interest, although higher modes exist to some extent. In layered system with velocity inversion or with a strong impedance contrast, the energy spreads onto several higher order modes [19, 20]. Sometimes, a higher mode or multiple modes dominate in some frequency range. Sometimes different modes with close velocity of propagation are merged under the same energy peaks due to a lack of resolution or to the location of sensors, becoming undistinguishable [20]. The resolution is a key factor in separating the different modal contributions: often a peak in the *f-k* domain is not associated with a single mode, but is rather a superposition of several different modes. This can then lead to erroneous interpretation of the results [17, 21].

As it will be shown in the forthcoming chapters, the R-wave has two components of motion resulting in an elliptical motion with retrograde rotation. The vertical component of displacement is normal to the direction of propagation; the horizontal component is parallel to the direction of propagation. In the common practice, only the vertical component of displacements is acquired and processed during a seismic survey. Although in a perfectly isotropic system the vertical and horizontal components of displacement would carry the same information, the dispersion curves obtained from the horizontal and the vertical components or Rayleigh waves are in general different, especially when multiple modes have dominant effects at the same time [20, 22]. Hence, favouring one direction with respect to the other and/or the lack of resolution in the *f-k* domain could lead to misinterpretation of seismic survey and to ambiguous and erroneous results [22, 23].

The main difficulty of the common approaches remains the identification of the mode number and of the actual univocal dispersion curve [24].

The shear wave velocity profile is usually obtained through a numerical inversion of the experimental dispersion curve (i.e. the phase velocity-frequency curve), trying to match the experimental dispersion curve with that coming from an analytical or a numerical model. Inversion is usually accomplished fixing the density of soil and varying the mechanical properties and the thicknesses of each layer in the numerical simulations until an acceptable mismatch between the two dispersion curves is reached. Finer signal processing methods and numerical inversion techniques are needed in order to reduce the intrinsic uncertainty of seismic measurement. Inversion is the most delicate step for every seismic survey and it is affected by a significant amount of uncertainty. It may lead to erroneous interpretation of field data and it is a source of uncertainty, since the problem has not a unique solution [25]. Further details will be discussed in Section 4.3.

In an attempt to minimize the ambiguity and to reduce the problems related to the non-uniqueness of the dispersion curve, sometimes analyses are performed jointly inverting the horizontal and the vertical spectra, or exploiting the spectral ratio between the horizontal and the vertical components of the background microtremor field (HVSR) [14, 20, 22].

Many efforts have been put during the past few decades in searching for good correlations between seismic wave velocities and geotechnical parameters of soils and rocks, i.e. their mechanical properties. Many empirical correlations have been proposed between P-wave velocity and dry density of rocks, with satisfactory correlation coefficients [26]. Kulkarni and co-workers found good relationships between geotechnical parameters and S-wave velocity of clays from coastal regions. In particular, it has been shown that the shear wave velocity in soils can be employed for estimating void ratio, bulk density, shear strength and gravimetric water content, with a certain degree of confidence. This investigation was based on the assessment of the shear velocity and geotechnical properties by means of laboratory tests on disturbed specimens [27]. Research by other authors [28] led to similar empirical relationship between shear strength and natural water content of soils, depending on their natural physical composition. Parks [29] jointly used electromagnetic and seismic reflection method to evaluate the groundwater table in soil deposits, i.e. to identify the shallow water surface. An overview of the most important geotechnical parameters is presented in Appendix A.

In this thesis, a new imaging technique jointly exploiting the horizontal and vertical components of displacement of a seismic event is proposed. This original contribution has the double aim of increasing the resolution and of reducing the ambiguity of dispersion curves.

Moreover, the thesis contains the results of a combined application of a seismic and an electromagnetic method at two field test sites. This work was accomplished in parallel with the University of Birmingham and the relevant results are displayed in Appendix F. This preliminary study aims at understanding the potential of surface wave and electromagnetic methods for the

assessment of some geotechnical properties of soils and attempt to clarify the usefulness of a joint use of the two technologies.

The forthcoming sections describe the common non-invasive surface wave methods utilised as seismic measurements.

1.4.1 Spectral Analysis of Surface Waves (SASW)

Spectral Analysis of Surface Waves (SASW) is a non-destructive seismic method used to determine the dynamic shear modulus and thicknesses of shallow soil layers. It is also a valid technique for the determination of the damping ratios [1]. The SASW method has the advantages of being non-invasive, easy and quick to be executed. The method does not require boreholes, since the measurements are taken entirely from the ground surface [2].

The SASW testing relies on the measurement of the wavefield of Rayleigh waves. The R-wave propagates along the shallow surface and decays exponentially with depth. Surface wave methods are based on the dispersion characteristics of Rayleigh waves in layered media. In an ideal, homogeneous, elastic half-space, the R-wave velocity is independent of frequency. However, the R-wave becomes dispersive if the properties of material vary with depth (as is generally the case for soil) and each different frequency component of surface wave travels with different propagation velocity and at different depth (section 2.2). The raw data of the SASW testing is a dispersion curve, i.e. the plot of different frequencies versus the associated phase velocities.

The concept of apparent phase velocity has been introduced to denote a velocity which does not necessarily correspond to the velocity of one mode of propagation, but is rather an average value among different modes [15].

According to empirical and analytical observations, it is assumed that the “centre of gravity” of the vertical displacement of R-wave occurs at a depth equal to one third of its wavelength λ_R [30]. At a depth approximately equal to one wavelength, the amplitude of a Rayleigh wave is negligible, hence the displacements are small. It is clear that the final measurement is an average measure of the properties within a depth of one wavelength. Thus, higher frequencies travel at shallow depths and typically lower velocities, while lower frequencies travel at greater depths and typically higher velocities.

Several different sources have been used for the SASW method among the years, both transient and continuous: sledgehammers, explosives, falling masses, mallets, hydraulic or pneumatic vibrators and electro-mechanical shakers are only a few. It is not unusual to use multiple sources on the same test site, providing that the desired range of frequencies is excited with adequate energy [1].

An early version of SASW consists of applying a steady-state harmonic excitation with frequency f on the surface and then moving one vertical transducer until the distance between successive peaks of the wave is reached. The distance between the source and the transducer is assumed to equal the wavelength, and hence the wave speed is computed. By changing the value of the frequency excitation, and by finding the relative wavelength, the experimental dispersion curve can be determined. This approach is quite time consuming and inefficient [1, 2, 9].

A more efficient field set-up for the SASW testing consists of a source capable of exciting a wide range of frequencies, two or more receivers placed on the ground surface, spaced a distance D apart, and a data acquisition device (Figure 1.2).

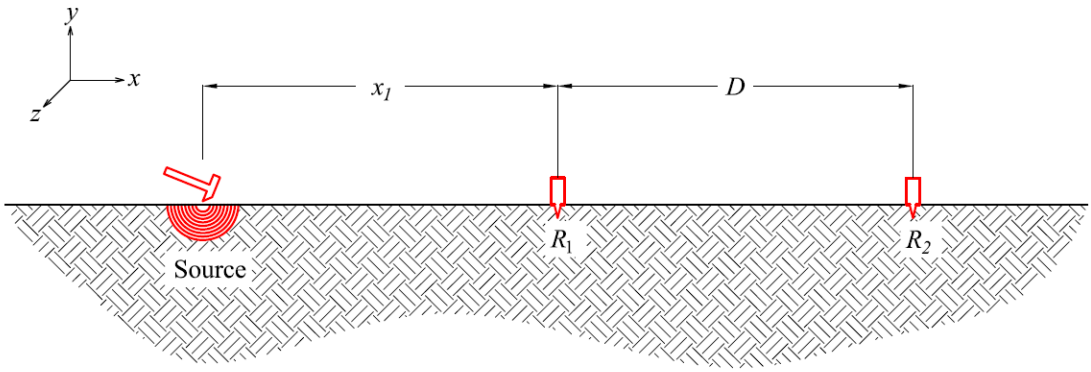

Figure 1.2: Typical SASW configuration, where x_1 is the source offset, R refers to a geophone and D is the receiver spacing.

The vertical motion induced by the passage of the Rayleigh wave is recorded at different distances from the source. The data is processed in the frequency domain computing the cross-power spectrum between two signals at two different positions. Knowing the phase difference between two signals, the travel time and hence the phase velocity of each frequency component can be obtained, leading to the construction of the so-called dispersion curve for the tested medium. Repeating the same procedure for each possible receiver distance adds a contribution to the dispersion curve. It has to be noticed that the Rayleigh phase velocity obtained with this method is the average characteristic of the entire volume of material investigated between the receivers [2].

Typically, the test method comprises the following phases [5, 25]:

- Generation of predominantly Rayleigh wave type, by means of vertical transient or continuous sources;

- Measurement of the soil response at different position away from the source, by means of two or more sensors placed in line with the source;
- Signal data processing and generation of a Rayleigh wave dispersion curve in the phase velocity-frequency domain;
- Inversion of the dispersion curve, to obtain the actual shear velocity profile with depth.

The traditional signal processing method used with the SASW to recover the phase velocity is based on the computation of the cross-power spectrum between the wave's signals at two different locations. It relies on the assumption that the entire signal is composed only by one wave type. It is unable to discern different waves, modes of propagation and osculation points of the R-wave (i.e. when the energy switches from one mode to the higher orders), but it is rather an average measure of all the phenomena occurring in the surveyed medium.

In reality, a variety of seismic waves are generated simultaneously at the time of impact: on top of the direct Rayleigh wave and body waves (both P-wave and S-wave), refracted and reflected body waves and scattered Rayleigh waves can show up depending on the vertical and lateral heterogeneity of the surveyed system. More than one mode of propagation of Rayleigh wave can appear at the same frequency, complicating the processing of data. The dispersion measurement obtained with the SASW data is highly affected by the presence of multiple waves and generally overestimates the R-wave velocity. Hence, the need of a signal processing method that can cope with the presence of multiple waves is essential [6, 7, 31].

For this reason, SASW is a reliable method for normally dispersive layered system, when the fundamental mode is dominant over other waves and modes for the entire frequency spectrum, but has proven not to be reliable for dispersion measurement of irregular profiles, when a low-stiffness layer is sandwiched between two layers of higher stiffness or when there is a big velocity contrast between layers. In the aforementioned cases, the fundamental Rayleigh mode is no longer the dominant wave, resulting in a false interpretation of the dispersion curve. The strong influence of higher order Rayleigh modes on the propagation wavefield and the inability of traditional signal processing techniques to distinguish different modes of propagation concur on the uncertainty in case of irregular soil profiles [19, 32]. A deeper insight of the cross-power spectral method used in conjunction with the SASW method is given in section 3.2.

In addition, the SASW method is not suitable for deep survey, due to the Rayleigh wave attenuation properties: typically, it is possible to investigate soil deposits up to a depth of 10-15 metres. This depth is related to the usual length of the array, which is up to a few tens of metres.

Moreover, there is lack of standardisation, in terms of type of source to be used, coupling between source and the ground, experimental set-up to be adopted, receiver spacing and difficulties in performing real-time quality check of experimental data [6, 31, 33].

1.4.2 Multichannel Analysis of Surface Waves (MASW)

Multichannel Analysis of Surface Waves (MASW) tries to overcome a few weaknesses of the SASW test. The set-up configuration consists of a source of seismic energy and multiple receivers (typically 24, but also up to 48 or more) placed on the ground surface with an equal spacing along a survey line (Figure 1.3) [7, 13]. The source offset x_1 and the spacing between receivers D are chosen according to the wavelength and hence the depth of investigation. As a rule of thumb, the depth of the survey is equal to the length of the survey. All the receivers record the vertical ground vibration response simultaneously. MASW typically uses a continuous source like a vibroseis or an impulsive source like a sledgehammer [6].

The data analysis and processing is usually somewhat different from the one processed in the SASW testing. In MASW the experimental data can be analyzed in the time domain in a seismogram format (where each trace is offset vertically to represent the spatial separation of each measurement point) or transformed from the time domain into different domains, typically through the frequency-wavenumber (*f-k*) transformation, the slowness-frequency or the swept-frequency transformation [34]. Theoretically, the *f-k* transformation allows the identification of different wave-types and higher order Rayleigh modes [15, 35], which significantly affect the determination of the actual dispersion curve [6]. A deeper insight of the frequency-wavenumber transformation is given in section 3.3. The MASW is a pattern recognition method enabling the identification of different types of seismic waves [6].

When the MASW is used to determine the shear wave profile, the soil is assumed to behave as a isotropic horizontally-layered model with no lateral variation in elastic properties [33]. The disadvantages of a long deployment have been observed by many researchers: horizontal heterogeneities can lead to perturbations on the estimation of the phase velocity [7, 36].

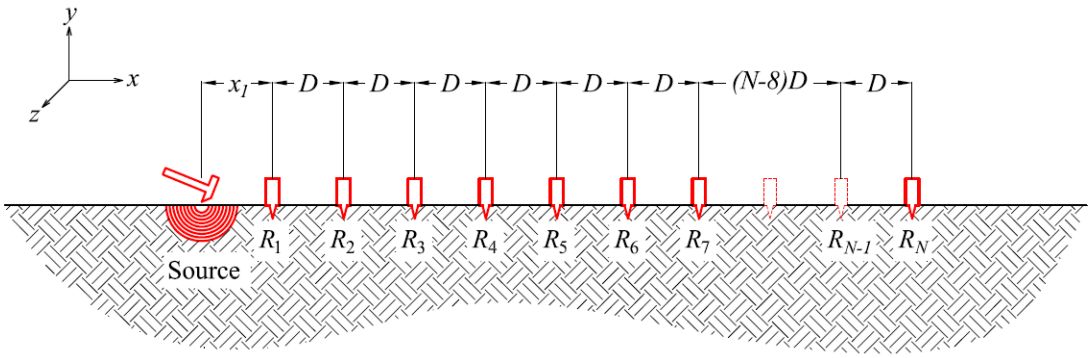

Figure 1.3: Typical MASW configuration in the case of an isotropic medium with absence of discontinuity, where x_1 is the source offset, R refers to a geophone, D is the receiver spacing and N is the number of receivers.

1.4.3 Multiple Impact Surface Waves (MISW)

Multiple Impact Surface Waves (MISW) is an alternative to the common MASW technique to obtain a multichannel record: sometimes a true multichannel survey can be cumbersome, requiring many bulky receivers deployed simultaneously in a small area. MISW consists in the employment of a limited number of sensors (possibly only one) and in the generation of seismic waves by means of several hammer impacts (Figure 1.4) [13, 37]. The source is consecutively moved by the same distance along the survey line: eventually, a simulated multichannel record is constructed by compiling the subsequent seismic traces. The signals can be correctly compiled into a multichannel record, as shown in the figure, only if the data acquisition is triggered with respect to the hammer impact.

MISW gives identical results to that obtained through a true multichannel survey if the following conditions are met:

- No significant lateral change in the thickness of each layer;
- No significant inconsistency in triggering.
- Homogeneity of the ground over the survey area.

MISW, as MASW, theoretically allows a reliable separation of different modes of propagation through conventional signal processing methods.

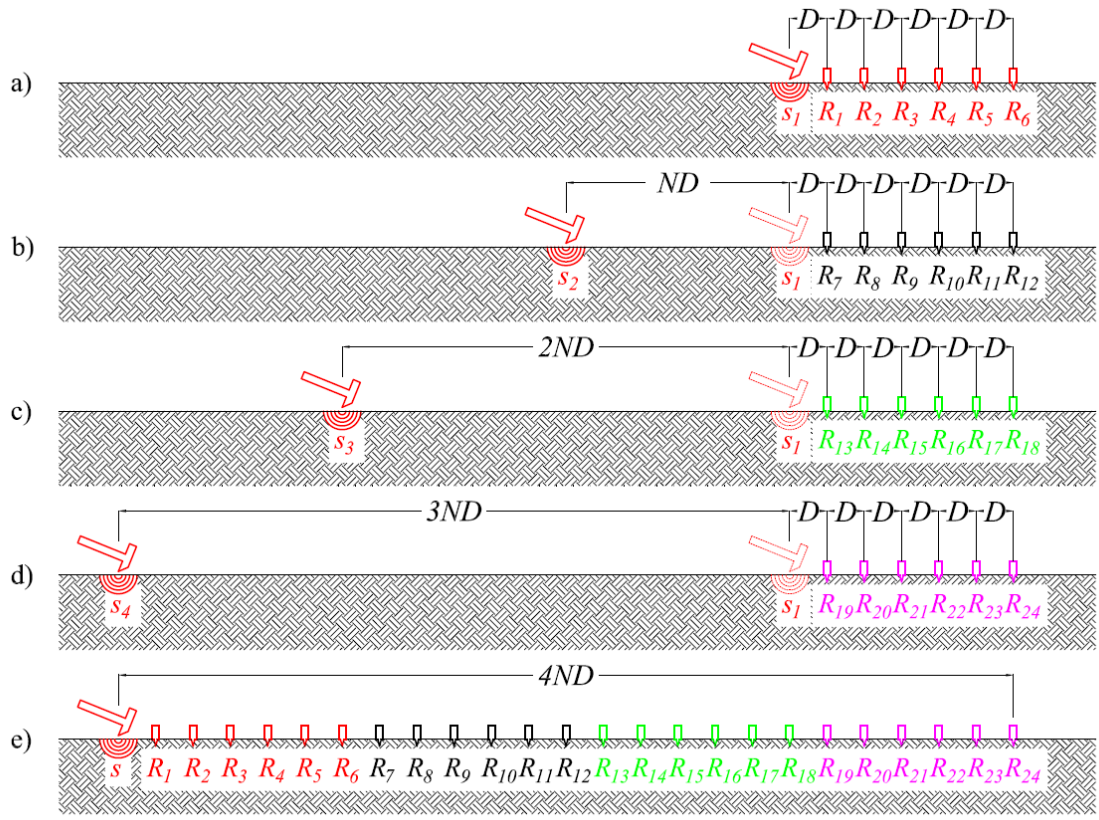

Figure 1.4: Typical MISW configuration in the case of an isotropic medium with absence of discontinuity, where *R* refers to a geophone, *s* refers to a source, *D* is the receiver spacing and *N* is the number of receivers. From the original configuration (a), the source is consecutively moved three times along the survey line (b,c,d), leading to the equivalent multichannel configuration (e).

1.4.4 Refraction Microtremor (ReMi) Testing

A limitation for seismic methods based on the SASW testing is the maximum depth of investigation, which is usually up to a few tens of metres. Refraction Microtremor (ReMi) testing uses a one dimensional array of sensors and a combination of active and passive sources, such as microtremors caused by natural phenomena (wind, ocean waves) or anthropic activities, to tackle this limitation [7, 11]. Typically, the length of the array of sensors is up to a few hundred metres. The ambient noise is processed in the same way of MASW data and jointly inverted with the spectrum obtained through active sources. Energy associated with passive source has typically very low frequencies, and thus exploiting this particular type of source it is possible to investigate great depths (up to a 100 metres) [7].

1.4.5 Horizontal to Vertical Spectral Ratio (HVSR)

Horizontal to vertical Spectral Ratio (HVSR) is a seismic method firstly developed by Nakamura [14], and sometimes recalled with his name, for seismic deep exploration of ground and rocks using vertical and horizontal components induced by microtremors. It consists on the measurement of the displacements caused by the ambient noise in three directions with a single 3D sensor placed on the surface, and on the computation of the ratio between the Fourier amplitude of the horizontal and vertical components of microtremors. Some authors exclude the effect of Love waves and treat the HVSR as simply representative of the R-wave ellipticity, i.e. the spectral ratio of the horizontal to the vertical components of displacement [22]. The ratio assumes the form of a transfer function and it is potentially able to identify resonance effects of the subsoil. The original purpose of the HVSR was to eliminate the presence of surface waves from seismic measurements of microtremors [38]. Nevertheless, peaks in the transfer function are mostly related to the ellipticity of the Rayleigh waves [23] and to the so-called "shear wave resonance" of the top layer [39], as described in Section 2.8. The experimental transfer function is usually inverted with the aid of numerical models in order to extract the ground profile. Inversion shares the same weaknesses of the surface wave methods, bearing in mind that is more difficult to get *a-priori* information of big depths and that this method is suitable for low frequencies, usually up to 20 Hz. The method is rather sometimes utilized to constrain the dispersion problem jointly using HVSR and MASW together and jointly inverting their spectra [40].

1.5 Methods for the *in-situ* Measurement of the Velocity of Seismic Waves in Asphalts

Although the first studies among acoustic dispersion on roads were carried out in the 1960s [41], a huge amount of work was accomplished in the 1980s with the aim of getting a stiffness profile of the road system from the inversion of dispersion curves obtained experimentally. When surface wave methods were firstly used on asphalts, the dispersion of surface waves in roads was based on a fundamental normal-mode approach, which belonged to the soil testing [42, 43]. Since the assumption of a single R-wave mode of propagation is violated in road pavements, complications due to higher order modes arose [16], leading to erroneous results and interpretation of dispersion curves of roads. The inability of the traditional signal processing techniques based on the cross-power spectrum to distinguish different wave propagating modes made the attempts to measure stiffness of road layers unsuccessful.

In recent times MASW has been employed for profiling of road pavement systems due to its advantages in dispersion measurement of profiles with velocity inversion [44, 45]. The possibility to

analyse seismic data in different domains and hence the ability to discern different wave-types and different Rayleigh-modes of propagation make MASW the most used seismic technique for road dispersion evaluation.

Although the suitability of MASW testing for road layers is undoubted, the method shares the same shortcomings existing in the case of soil. Additional problems arise when testing roads:

- Generation of high frequency energy, in order to have a high resolution and evaluate the properties of thin layers (up to 20 kHz).
- Coupling between sensors and shallow surface is often tricky and complicated to achieve.
- Finer inversion techniques to be used to take into account thin layers, and more *a-priori* information required.

MISW is also exploited for roads seismic surveys [13, 46] in isotropic media with absence of discontinuities. Since the coupling between asphalt surface and sensors can be difficult to achieve, it becomes quite advantageous in case of road surveys, since it needs a reduced number of sensors. A comparison among different types of coupling between the sensors and the road surface is accomplished within this thesis.

The experimental dispersion curve measured during conventional MASW tests on roads is often a combination of several modes of propagation. In fact, in a layered media with irregular seismic velocity structure as a road pavement system, many energetic propagation modes occur and they make the interpretation of data more complicated. In normally dispersive soils the fundamental mode is dominant (i.e. carries more energy). Conversely, for irregular profiles (i.e. roads) or when the velocity does not increase with depth, the fundamental mode is no longer dominant and the dispersion analysis should be able to discern different modes and osculation points, i.e. when the energy switches from one mode to the higher orders. Inversion process should also take into account higher order propagation modes [25]. This is usually achieved by means of algorithms that can account for mode superposition effects [15]. The ambiguity of the uniqueness of the solution can be reduced by considering more Rayleigh wave modes [21, 41].

Ultrasonic Body Waves (UBW) and Ultrasonic Surface Waves (USW) are seismic methods derived from the SASW and MASW testing. These two ultrasonic techniques utilize the ultrasonic body and surface waves for measuring the Young's and Shear moduli of the upper layer of a road system. They consist of a two-receiver system and an impact source (generally a hammer). The principle of the two techniques is based on the generation of stress waves and on checking their propagation, up to frequencies of 40 kHz [47]. The main assumption relying on these methods is that the uppermost road layer is uniform, i.e. the velocity is constant throughout its thickness [47, 48]. Since they are restricted to the first upper layer, they are not considered within this thesis.

1.6 Seismic Methods for Crack Detection

Non-destructive, *in-situ* methods for characterizing existing infrastructures require the ability to detect structural damage and features such as cracking and discontinuities.

Surface wave propagation has been exploited by many [49-51] to monitor asphalt deterioration. It has been well established that a drop of about 30% of the initial (i.e. at the beginning of the infrastructure's service life) value of the stiffness modulus of asphalt is a signal of incipient failure, or in other words the beginning of the phenomenon of fractures. Seismic methods for asphalt condition monitoring have shown good repeatability and the ability to cope with the inhomogeneity and anisotropy of the road pavement modulus. Although it seems possible to measure the residual life of an infrastructure with non-destructive seismic methods before cracking begins to appear, there are significant challenges still to be addressed. For example, a reference value of the stiffness for every different asphalt mixture is required; the influences of temperature and self-repairing mechanisms ongoing in an asphalt road during its life are yet to be understood, etc.

Damage in a road structure is usually initiated in the asphalt layers, making the R-wave ideally suited for the detection of shallow surface defects. The proper assessment of the location and of the extension of such discontinuities is crucial for the determination of the level of deterioration of an infrastructure and for decisions regarding maintenance, strengthening and rebuilding of existing infrastructures. In fact, a surface-breaking crack in concrete and asphalt is a symptom of incipient failure of the structures [52]. The vertical crack has a resonance type feature, which occurs periodically at certain frequencies and has found to be associated with the depths of the cracks [53-55]. Moreover the edges of surface defects like cracks act like a source that excites surface waves which propagate along the crack surface [54, 56]. The finite depth of the crack blocks shorter-wavelengths, allowing only the longer wavelengths to proceed and hence it acts as a low-pass filter. In general, cracks are likely to generate reflections and to change both the time history and the frequency content (the spectral response) of a seismic signal at surface [57].

Detection of vertical cracking is normally based on the study of the scattering caused by the boundaries of the crack, even though reflections from cavity surfaces have weak energy and limited frequency range, making this process difficult to implement [57]. Particularly, the resonant effects of the scattering waves [54] or leaky Rayleigh waves [55] in the ultrasonic range of frequencies (up to 150 MHz) are exploited to extract the information about the depth and the length of a surface crack, with ambiguous results. Wave transmission and attenuation measurements and the spectral ratio of the transmitted wave on the incident wave are also exploited by various authors for detection and sizing of surface discontinuities [52, 58, 59]. Spectral methods are also sometimes used for crack

detection [60]. Time-of-flight of the transmitted Rayleigh wave has also been explored by many authors as a tool for crack interrogation [55, 56].

Numerical approaches to surface-breaking discontinuity detection show that the dispersion curve, and hence the wavefield, changes if the signal travels across a vertical discontinuity, which can be a crack or a slot [60]. Hence some authors suggested the use of an array of sensors to jointly compute auto-spectra for the location of the cracking, and the frequency-wavenumber spectral image for the assessment of the crack depth in a homogeneous Plexiglas sheet [58]. Although autospectral density plots showed to be sensitive to the crack location, the assessment of depth showed to be inaccurate. Other numerical studies suggest a time-frequency analysis of the response for anomaly detection in layered media based on the wavelet transform [57]. Time differences between energy peaks and the range of frequencies of different energy levels in the time-frequency spectral image could lead to the estimation of the approximate location and size of defects.

The biggest challenge of the surface wave methods for asphalt crack interrogation is their application to real cases. Time-of flight methods have shown not to be effective when realistic structures are tested [52]. The practical measurement of reflection and transmission coefficient for crack detection on asphalt and concrete has been restricted due to the heterogeneous nature of the materials tested, incoherent signals, geometrical attenuation and receivers coupling disruptive effects [52]. Particularly, the dispersive nature of the material tested inevitably makes these methods dependent on the velocity of the material at different depths.

Impact Echo (IE) is often jointly used in conjunction with UBW and USW to evaluate the thickness of the top paving layer [47, 61]. It consists of a single receiver and of a seismic source placed as close as possible to it: the source is usually a small metallic sphere dropped from a certain height. The resonant frequency of the P-wave is determined through the linear spectrum of the signal and hence is the thickness of the upper layer. IE has been also successfully employed for delamination detection, i.e. horizontal cracking, in concrete slabs, and it is based on the fundamental assumption of horizontality of the layers and absence of S-waves if the receiver is very close to the vertical source of excitation.

In this thesis a signal processing algorithm for the detection and the assessment of vertical surface breaking cracks in asphalt layers is developed. Its efficiency is investigated with the aid of numerical and experimental investigations. The new method tries to overcome the difficulties and limitations in computing the reflection and the transmission coefficients that current methods share. Particularly, it copes with the dispersive and heterogeneous nature of materials, as is the case of roads.

1.7 Inversion Problem

The procedure for the determination of the actual R-wave velocity of propagation at different depths is known as inversion. It is the most delicate step in geophysical surveys based on the measurement of surface waves.

A simple, crude and preliminary way to convert a field dispersion curve into a Rayleigh velocity-depth curve is to consider that the effective depth of investigation is equal to one third of the wavelength [30, 62]. This inversion process seems to be applicable for the shallow layers of generally uniform soil sites, where changes in the stiffness profile can be neglected or are regular with depth, or as a very preliminary real-time check [42].

The inversion process consists of estimating an initial shear wave profile from a numerical model, comparing the experimental and numerical dispersion curve, and adjusting the shear velocity profile until the difference between the experimental and numerical dispersion curve is below a certain threshold, or when the global minimum has found. The minimization between the experimental and numerical dispersion curve is achieved by using optimization algorithms (the most used are the least square optimization and the genetic algorithms). There are two approaches for the calculation of the numerical dispersion curve: the use of the numerical finite element model method, and the use of the transfer matrix method, later developed in the more robust dynamic stiffness matrix method [7, 63], as explained in section 2.5. Since the analytical models used for the inversion are not linear, the inverse problem is non-linear itself.

The classical approach to inversion of seismic data is to pick a dispersion curve following the amplitude maxima of the frequency-wavenumber spectral image. The main problems arise in the first step, when the dispersion curve has to be chosen [16]. The extraction of a dispersion curve, being a subjective task, can lead to erroneous results and misjudging of seismic spectra. Alternatively, the analysis may be performed in a more pragmatic way using the full-waveform inversion approach, in which the subjective extraction of a dispersion curve is unnecessary.

Usually the inversion process is performed assuming a reasonable value for density and Poisson's ratio of each layer, and varying the values of thickness, shear modulus and number of layers of the analytical model [17]. Generally, the number of layers to describe the shear velocity profile is assumed to be less than ten [7].

The inversion is an ambiguous, ill posed problem since the solution is not unique, i.e. more than just one profile can describe the measured dispersion curve with a tolerable mismatch. This may be due to the presence of higher order modes with non-negligible energy, lack of resolution of the spectrum, subjective extractions of dispersion curves based on wrong maxima of the *f-k* spectrum. In shallow

seismic surveys of irregular profiles, higher order modes of propagation contribute to the final dispersion measurement, and if the resolution of the spectrum is not high enough or when the noise is too big, different modes smear out in the spectrum and it becomes impossible to distinguish them. In such cases, it is possible to fit these higher order modes with a fundamental normal mode, hence leading to an erroneous profile. Attenuation emphasizes higher order modes and their role should be considered in the inversion process [22].

In case of complex profiles, with low stiffness layers sandwiched between stiffer layers, the utilization of higher order modes in the inversion process is theoretically beneficial, since it adds more information and may help in constraining the results [7]. It is generally recognized that failing to properly consider higher order modes in the inversion process can lead to erroneous results [36].

Vertical (normal) and horizontal (parallel) components of motion carry the same dispersive information if the material under investigation is assumed to be perfectly isotropic [64]. In reality, the soil being anisotropic, they often show a different distribution of energy among different modes: often one component only shows evidence of one mode (the fundamental or some higher order mode), while the other is a mixture of fundamental and higher order modes. Depending on which component is considered, the risk of misinterpret seismic data is very high [22]. In an attempt to minimize the ambiguity and to face the non-uniqueness of the solution, joint analysis are sporadically performed inverting the spectra obtained with the horizontal and vertical traces, or exploiting the spectral ratio between the horizontal and vertical components of the microtremor (HSVR). Ambiguity is also usually tackled by adding *a-priori* information, i.e. the results coming from additional geological and geotechnical tests (Ground Penetrating Radar, boreholes, Dynamic Cone Penetrometer, electromagnetic ground conductivity tests), which can be helpful in constraining the inversion problem.

The Dynamic Cone Penetrometer (DCP) is an instrument for rapid *in-situ* measurement of the strength of unbound road pavement layers and soils and for the thickness and location of underlying soil layers. It consists of a rod with a pointed cone at one edge, which is driven into the soil by dropping an 8-kg weight through a height of 575 mm. By measuring the penetration of the rod after each hammer drop, the strength of the underlying soil is then determined. This value, known as the DCP penetration index (DPI), is recorded in mm/blow and it is usually plot versus depth. The DPI can be correlated to other soil strength parameters, such as the California Bearing Ratio (CBR) [65].

In this thesis, the DCP has been utilized in various site investigations to have *a-priori* information, to constrain the inversion problem.

1.8 Aims & Objectives

The aim of this research project is the development of new techniques and the novel application of existing ones, for the *in-situ*, non-destructive characterization of ground and road pavements, exploiting surface waves. Based on the literature review presented herein and in Chapter 3, the following objectives will be pursued in this thesis:

- Develop a new imaging technique to obtain Rayleigh wave dispersion curves with increased resolution and reduced ambiguity;
- Study and compare different types of couplings between asphalt and surface measurement transducers;
- Apply existing surface wave techniques for the detection and the assessment of the depth of vertical surface-breaking cracks in asphalts;
- Develop and apply a new technique for the detection and the assessment of the depth of vertical surface-breaking cracks in asphalts;
- Study and compare different ground excitation methods, source orientations and couplings of the source to the ground;
- Study the potential correlation between shear velocity and some geotechnical parameters of soil, i.e. parameters that are able to describe its features and qualities;
- Assess the suitability of electromagnetic techniques to complement surface wave techniques for ground investigation;

The approach adopted in fulfilling the aforementioned objectives is described in the next paragraph.

1.9 Overview and Approach

This thesis consists of eight chapters. Chapter 2 introduces the theory of elastic wave propagation in half-space and in multi-layered media, illustrating the analytical solution of the free and of the forced vibration problem. Chapter 3 reviews the common signal processing methods of seismic data. Moreover, it outlines the features and properties of a numerical model assembled with the Finite Element Method (FEM) to simulate the propagation of elastic waves in multi-layered systems of arbitrary geometry and features. Chapter 4 introduces two new signal processing methods, respectively for the imaging of the dispersion of R-waves and for the detection and assessment of surface-breaking cracks. This chapter also illustrates simple numerical case studies. Chapter 5 displays the application of the traditional and proposed methods for R-wave dispersion measurement

on various experimental investigations in soils and asphalts. Numerical inversions of seismic spectra help in the interpretation of results. Chapter 5 also illustrates the comparison between different sources of waves and among different couplings between seismic sensors and the medium surface. Chapter 6 focusses on the application of surface wave methods for the detection of vertical anomalies. The interpretation of the results is supported by numerical simulations with the FEM model. Chapter 7 describes the application on real data of traditional surface wave methods for detection of surface-breaking cracks in asphalt. It also shows the result of the application of the new proposed signal processing method for the detection and the assessment of vertical discontinuities in asphalt. Finally, Chapter 8 draws conclusions.

1.10 Original Contributions

1. **Proposal of the spectral convolution method to improve the estimation of actual experimental dispersion measurement.** Each frequency component of the vertical motion of R-wave is 90 degrees out-of-phase with the corresponding frequency components of the horizontal motion. The spectral convolution method exploits this peculiar feature of the R-wave to obtain a spectral image with better resolution and accuracy than traditional methods. The new method tackles the resolution issues that hinder the imaging of R-wave in soils and asphalts. The method has proven advantageous for dispersion measurement in normally dispersive media as well as in not normally dispersive media, such as roads. It has also found to improve the accuracy of dispersion curves at the lower frequencies.

2. **Novel application of two existing surface wave methods for detection of vertical discontinuities in asphalt.** Vertical discontinuities act like a filter, allowing the passage of certain wavelengths and reflecting others, thus changing both the time history and the frequency content of the seismic signal at the surface. Spectral images of the wavefield, in the presence of anomalies, in both the frequency-wavenumber and in the time-space domains allow for the detection and, to some extent, the assessment of the depth of vertical discontinuities in shallow asphalt layers. In this thesis, a strategy for the detection and the assessment of surface-breaking cracks in asphalt, synergistically using two existing seismic spectral methods, is proposed.

3. **Application of the wave decomposition method for interrogation of vertical discontinuities in asphalt.** A new signal processing technique for the measurement of the amplitude and phase of the direct and reflected R-wave in roads is proposed. It decomposes the signal in its direct and reflected components. The method uses multiple receivers and hence it finds an approximate solution with a least square optimization. The resonant peak frequencies of the reflection coefficient and the cut-off frequencies of the transmission

coefficient are used for assessing the depth of the crack; the phase of the reflection coefficient to get the information about the location of the crack. The method has proven to be successful for assessment of cracks both numerically and experimentally, despite the heterogeneous and dispersive nature of roads.

4. **Influence of the coupling between transducers and asphalt on seismic measurement.** A comparison among a variety of different coupling between seismic sensors and the medium surface is accomplished with the aim of finding the optimal way for seismic measurements in asphalt.

5. **Comparison of soil excitation methods for surface wave dispersion measurements.** A comparison among different seismic sources, source orientations and source-to-ground couplings is performed within this thesis. It has the aim of investigating the influence of each of the aforementioned variable with respect to the assessment of the phase velocity.

Moreover, a study on the correlation between shear wave velocity and electromagnetic parameters in soils is performed. This work was accomplished in parallel with this research project, in collaboration with the University of Birmingham. The results are shown in Appendix F in the form of a conference paper. The fundamental aim of this parallel joint effort was to find relevant correlations between some of the electromagnetic parameters and the shear velocity of soils. In particular, one aim was to try to indirectly measure the volumetric water content of soils with the seismic methods.

Chapter 2: Theory of Elastic Wave Propagation

This chapter presents the basic elasticity equations for an infinite and semi-infinite elastic space. It is shown that two types of wave can propagate in an infinite elastic medium: dilatational and distortional, with each being characterized by a specific velocity. The reciprocal interaction between shear and body waves caused by the introduction of a free surface in the system allows the formation of Rayleigh waves. Properties of Rayleigh waves will be briefly shown and discussed, alongside the wave attenuation phenomenon. In addition, an analytical solution for the wave propagation in layered media is explained and presented, constituting a reliable and powerful tool for seismic data inversion and interpretation.

The basic theories of elastic wave propagation are well established and documented [66, 67] , so for the purposes of this work a rigorous overview is omitted.

2.1 Wave Propagation in an Infinite Elastic Medium

The most general, analytical description of body waves is considering the propagation within an infinite elastic medium, which is considered to be unbounded in all dimensions, linearly elastic, homogenous and isotropic.

The governing equations describing an infinite elastic medium in terms of displacements are the Navier's stress equation of motion:

$$(\lambda+\mu)\nabla(\nabla\bullet\mathbf{u})+\mu\nabla^2\mathbf{u}=\rho\frac{\partial^2\mathbf{u}}{\partial t^2}, \tag{2.1}$$

where λ and μ are the Lame constants:

$$\lambda=\frac{\nu\cdot E}{(1+\nu)\cdot(1-2\cdot\nu)}, \tag{2.2}$$

$$\mu=\frac{E}{2\cdot(1+\nu)}, \tag{2.3}$$

E is the Young's modulus of the medium, ν is the Poisson's ratio of the medium, ρ is the density of the medium, ($\bullet$) is the scalar product, ∇ is the nabla operator, defined in Cartesian coordinates as:

$$\nabla = \left(\frac{\partial}{\partial x}, \frac{\partial}{\partial y}, \frac{\partial}{\partial z} \right), \tag{2.4}$$

$\mathbf{u}$ is the deformation displacements vector in Cartesian coordinates defined as $\mathbf{u}(x, y, z) = u_x + u_y + u_z$, and ∇^2 is the Laplacian, defined as the gradient of the nabla operator.

Performing the vector operation of divergence to both sides of the governing displacement equation gives:

$$\nabla^2 \Phi = \frac{1}{V_P} \cdot \frac{\partial^2 \Phi}{\partial t^2}, \tag{2.5}$$

where

$$V_P = \sqrt{\frac{\lambda + 2\mu}{\rho}}, \tag{2.6}$$

and

$$\Phi = \nabla \bullet \mathbf{u}, \tag{2.7}$$

Physically, the divergence of the displacements corresponds to a change in volume, which propagates with a direction of motion that is coincident with the direction of propagation and a non-dispersive velocity V_P. This characteristic velocity is referred to as the propagation velocity of compressional waves.

Operating the curl of the governing equation and knowing that the curl of the gradient of a scalar is zero gives:

$$\nabla^2 \mathbf{H} = \frac{1}{V_S} \cdot \frac{\partial^2 \mathbf{H}}{\partial t^2}, \tag{2.8}$$

where

$$V_S = \sqrt{\frac{\mu}{\rho}}, \tag{2.9}$$

and

$$\mathbf{H} = \nabla \times \mathbf{u}, \tag{2.10}$$

where $(\times)$ is the vector product.

Since the curl operator describes the circulation of a vector field along a closed loop, rotational wave propagates with a direction of motion that is perpendicular to the direction of propagation and a non-dispersive velocity V_S. This characteristic velocity is referred to as the propagation velocity of shear waves. Due to its features, shear wave can be polarised with respect to two different directions, meaning that the particle motion can be perpendicular to the directions of polarisation and to the direction of propagation.

The ratio of shear and compressional wave velocity, defined as σ_{SP}, only depends on the Poisson's ratio, as follows:

$$\sigma_{SP} = \frac{V_S}{V_P} = \sqrt{\frac{\mu}{\lambda + 2\mu}} = \sqrt{\frac{1 - 2 \cdot \nu}{2 \cdot (1 - \nu)}}, \tag{2.11}$$

Shear wave (or S-wave) does not propagate through fluids, since they cannot transmit shearing forces. Thus, shear wave velocity is a property belonging totally to the solid skeleton of soil. The compressional wave (or P-wave) can instead travel through fluids and its velocity varies with the degree of saturation of the porous medium [62].

2.2 Wave Propagation in a Semi-Infinite Elastic Medium

To include other relevant types of propagating wave, a free surface is introduced. For convenience, the free surface is assumed to lie in the *x-z* plane, also called the "horizontal" plane, in contrast with the *x-y* plane, also called the "vertical" plane, with *y* positive in the downward direction. The particle motion due to the dilatational effects lies in the vertical plane, while the particle motion due to shear effects may have components in the vertical and horizontal plane. In fact, each shear wave can be decomposed in its two components, a SV-wave that polarizes in a plane perpendicular to the plane of the interface, and a SH-wave that polarizes in a plane parallel to the interface. The general situation is displayed in Figure 2.1. Finally, since every point along the vertical plane is ongoing the same displacement (plane strain), the motion is invariant with respect to the *z* direction if the wave is in the vertical plane. The governing equations for the investigation are:

$$u_x = \frac{\partial \Phi}{\partial x} + \frac{\partial H_z}{\partial y},\ u_y = \frac{\partial \Phi}{\partial y} - \frac{\partial H_z}{\partial x}, u_z = -\frac{\partial H_x}{\partial y} + \frac{\partial H_y}{\partial x} = 0 \tag{2.12}$$

where Φ and H are potential functions related to the dilatation and to the rotation of the medium.

The motion of the medium can thus be viewed as superposition of compressional and rotational motions. Substituting the potential form of displacement into the equation of motion of the system gives:

$$\rho \frac{\partial}{\partial y}\left(\frac{\partial^2 \Phi}{\partial t^2}\right) - \rho \frac{\partial}{\partial x}\left(\frac{\partial^2 H_z}{\partial t^2}\right) = (\lambda + \mu)\frac{\partial}{\partial y}\left(\nabla^2 \Phi\right) - \mu \frac{\partial}{\partial x}\left(\nabla^2 H_z\right), \tag{2.13}$$

For the *y*-direction, and

$$\rho \frac{\partial}{\partial x}\left(\frac{\partial^2 \Phi}{\partial t^2}\right) + \rho \frac{\partial}{\partial y}\left(\frac{\partial^2 H_z}{\partial t^2}\right) = (\lambda + \mu)\frac{\partial}{\partial x}\left(\nabla^2 \Phi\right) + \mu \frac{\partial}{\partial y}\left(\nabla^2 H_z\right), \tag{2.14}$$

For the *x*-direction.

Two wave equations are obtained, one for each potential:

$$\nabla^2 \Phi = \frac{1}{V_P} \cdot \frac{\partial^2 \Phi}{\partial t^2},\ \nabla^2 H = \frac{1}{V_S} \cdot \frac{\partial^2 H}{\partial t^2}, \tag{2.15}$$

They have velocities corresponding to the compressional and shear wave velocities. The two equations can be solved by applying the boundary conditions at the free surface:

$$\tau_{zx} = \tau_{zz} = \tau_{zy} = 0, \tag{2.16}$$

where τ_{ij} is a stress, with the first subscript denoting the plane on which the stress acts, the second subscript denoting the direction in which it acts. The implementation and the resolution of the potential equations, given the boundary conditions, are omitted in this work for sake of brevity. Eventually, applying two boundary conditions leads to the following equation:

$$\left(2 - \frac{V_R^2}{V_S^2}\right)^2 = 4\sqrt{\left(1 - \frac{V_R^2}{V_P^2}\right)}\sqrt{\left(1 - \frac{V_R^2}{V_S^2}\right)}, \tag{2.17}$$

where V_R is a characteristic velocity referred to as the propagation velocity of Rayleigh waves. From equation (2.17) is evident that the Rayleigh wave (or R-wave) velocity is a function of compressional and shear wave velocity. Ratio between Rayleigh, compressional and shear wave velocities varies with the Poisson's ratio: in general, compressional wave is the fastest, while shear wave in only slightly faster than the Rayleigh wave, which is the slowest seismic wave.

Miller and Pursey [68] and Graff [66] proposed analytical results for the displacements vector on the free surface of the infinite half-space in the case of "an infinitely long strip of finite width vibrating in a direction normal to the surface of the medium". The results are, for ν=0.33:

$$u_x(x,0) \approx 0.198 \cdot \frac{a}{\mu} \mathrm{e}^{(-2.145\mathrm{i}kx)} \cdot \mathrm{e}^{(-k\xi x)} \tag{2.18}$$

$$u_y(x,0) \approx 0.311 \cdot \frac{\mathrm{i}a}{\mu} \mathrm{e}^{(-2.145\mathrm{i}kx)} \cdot \mathrm{e}^{(-k\xi x)} \tag{2.19}$$

where u_x is the displacement in the horizontal direction, u_y is the displacement in the vertical direction, a is the width of the finite vibrating line, x is the desired position in the *x*-direction, $k = \omega / V_P$ is the wavenumber of the body wave, $\omega = 2\pi f$ is the angular frequency, f is the frequency of excitation, ξ is the damping ratio.

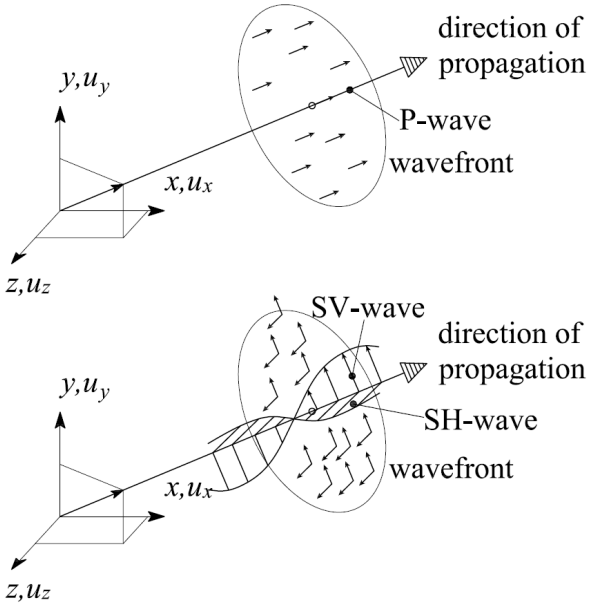

Figure 2.1: Displacements associated with body waves. Top: P-wave. Bottom: S-wave. The figure is modified from [67].

Each frequency component of the vertical motion is $\pi/2$ out-of-phase with the corresponding frequency components of the horizontal motion, as designated by the imaginary component. Vertical displacements are always positive and peak near the surface, while horizontal displacements decrease progressively with depth, becoming negative and resulting in an elliptical motion with retrograde rotation. Anyway, at a depth approximately equal to one and a half the wavelength, the vertical displacements (i.e. the amplitude) of a Rayleigh wave is about 10% of the amplitude at the surface, hence negligible. It is assumed from literature that the centre of gravity of the vertical displacement occurs at a depth equal to one third of the wavelength [30].

In an ideal, homogeneous, elastic half-space, where the material properties do not change with depth, Rayleigh wave velocity is independent of frequency. However, if the properties of material vary with depth (it is generally the case of soil), each different frequency component of surface wave travels with different propagation velocity, different wavelength λ_R , then travelling at different depth. This property of Rayleigh waves is called dispersion.

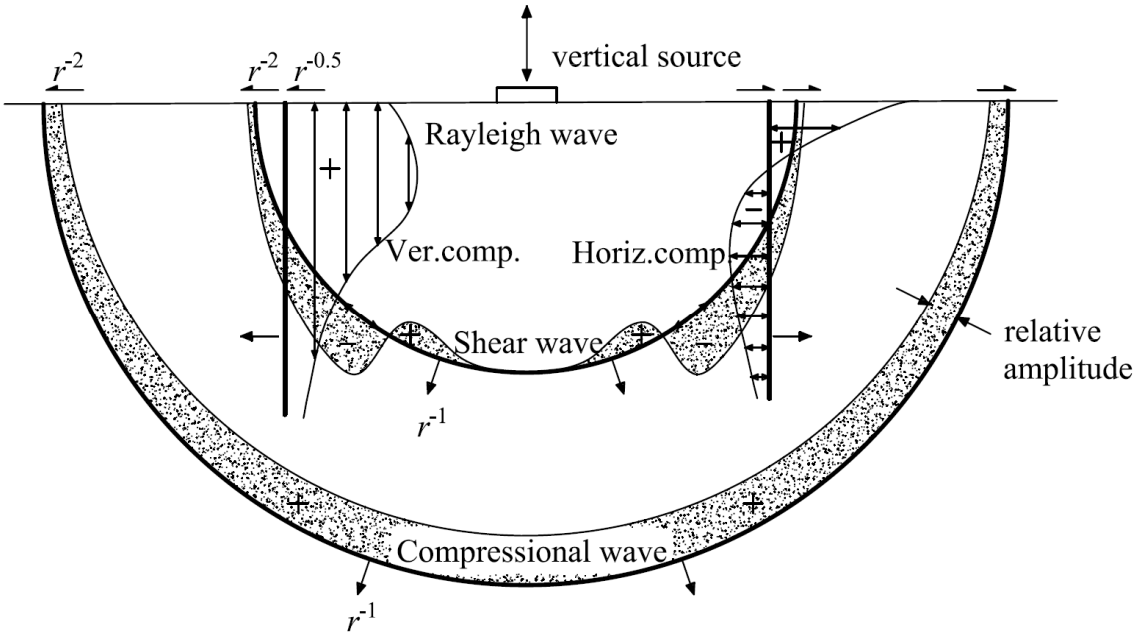

Figure 2.2: Distribution of displacement and energy in compressional, shear and surface waves from a harmonic, normal load on a half-space for $\nu = 0.33$ [66]. The thick black lines denote the position of the wavefronts, in accordance to the relative wave speeds. The relative amplitude of the vertical and the horizontal components of Rayleigh wave are depicted respectively on the left and on the right of the source as a function of depth. The geometrical attenuation of waves is expressed as a function of the distance from the source r and it will be introduced in the next section.

When an harmonic point load is applied to the surface (i.e. when the width of the finite vibrating line a tends to zero), approximately 67 percent of the energy imparted on a system is converted into

Rayleigh wave energy, while 26 percent of the input energy propagates away in the form of shear waves and only 7 percent in the form of compressional wave [69]. Figure 2.2 shows the propagation of seismic waves in a semi-infinite media from a harmonic normal load and the aspect ratio for compressional, shear and Rayleigh wave. The spacing among wavefronts is in accordance with their velocities.

2.3 Introduction to Wave Attenuation

Different phenomena are responsible for the decay of seismic wave's amplitude with distance within a homogeneous or heterogeneous media. In general, two mechanisms can be observed: geometrical spreading and intrinsic attenuation [70]. By analysing the propagation of surface waves, it can be noticed that different frequencies have not just different phase velocities but also different attenuation properties with distance.

When a disturbance is applied in an elastic half-space, the initial energy released from the source is spread over an increasing volume of the medium, and thus the intensity of the wave decreases with distance. This geometrical attenuation is usually expressed by means of a coefficient of attenuation, which is a function of the distance r from the source. The coefficient of attenuation depends on the wavefront propagation, which is hemispherical for body waves and cylindrical for Rayleigh waves.

The Rayleigh wave decays by a factor of $1/\sqrt{r}$, while the body wave amplitude decays as $1/r^2$ along the free-surface and as $1/r$ along depth (Figure 2.2) [69]. As a result, Rayleigh waves can travel longer distance than body waves.

The geometrical attenuation is not sufficient to describe the phenomenon of attenuation of seismic wave energy. The decrease in the amplitude is also due to intrinsic attenuation, which comprises anelastic processes and internal frictions occurring during the wave propagation in solid media [71]. In a linear, viscoelastic medium, the magnitude of intrinsic attenuation is quantified by the dimensionless parameter η, called quality factor, which is material dependent and equals the fractional elastic energy dissipated per each cycle [72]:

$$\eta = -\frac{\Delta E_n}{2\pi E_n} \tag{2.20}$$

where ΔE_n is the energy loss at each cycle and E_n is the peak strain energy. The quality factor is generally frequency dependent. The amplitude A of a seismic wave in viscoelastic medium decays according to the following expression:

$$A(x,t) = A_0 \cdot \mathrm{e}^{\left[\frac{-\omega \cdot x \cdot \eta}{2 \cdot c_m} + \mathrm{i}\omega\left(t - \frac{x}{c_m}\right)\right]} \tag{2.21}$$

where x is the space measured along the propagation direction, A_0 is the initial wave amplitude, ω is the angular velocity, c_m is the wave speed in the medium and t represents time.

Equation (2.21) is equivalent to the following wider expression of wave propagation:

$$A(x,t) = A_0 \cdot \mathrm{e}^{\mathrm{i}\left(\omega t - k^* x\right)} \tag{2.22}$$

where $k^* = k(1 + \mathrm{i}\xi)$ is the complex wavenumber, and $\xi = \eta / 2$ is the damping ratio.

For a constant value of η, higher frequencies will decrease earlier: this is due to the fact that high frequency waves will go through more oscillations than low frequency waves in the same time, i.e. high frequency waves have a shorter wavelength. For a constant value of η and ω, Rayleigh wave undergoes faster intrinsic attenuation than body wave due to being the slowest wave.

2.4 Wave Propagation in a Layered System

In a horizontally layered system, the propagation of waves follows laws that are more complicated. When body waves reach the interface between two layers, several phenomena occur [62, 66, 73]:

- Generation of refracted and reflected body waves;
- Generation of surface waves;

As introduced in section 2.2, each incident shear wave can be decomposed in its two components, a SV-wave that polarizes in a plane perpendicular to the plane of the interface, and a SH-wave that polarizes in a plane parallel to the interface. Thus, each incident P-wave generates a reflected P-wave and SV-wave and a refracted P-wave and SV-wave in the incident point of the boundary. In addition to compressional wave, each incident SV-wave creates reflected P-wave and SV-wave and a refracted P-wave and SV-wave. Incident SH-wave generates a refracted SH-wave and a reflected SH-wave. Therefore, in a horizontal, two-layered system, three incident body waves result in the generation of ten new waves.

P-waves and S-waves are refracted and reflected with different angles, according to the Snell's law (Figure 2.3(a)):

$$\frac{\sin(\alpha)}{V_{p,A}} = \frac{\sin(\beta_1)}{V_{s,A}} = \frac{\sin(\alpha_1)}{V_{p,A}} = \frac{\sin(\beta_2)}{V_{s,B}} = \frac{\sin(\alpha_2)}{V_{p,B}}, \tag{2.23}$$

$$\frac{\sin(\beta)}{V_{s,A}} = \frac{\sin(\beta_1)}{V_{s,A}} = \frac{\sin(\alpha_1)}{V_{p,A}} = \frac{\sin(\beta_2)}{V_{s,B}} = \frac{\sin(\alpha_2)}{V_{p,B}}, \tag{2.24}$$

where α,β are the incident angles, with respect to a vertical axis, for the P-wave and the S-wave respectively, α_1,β_1 are the reflected angles, with respect to a vertical axis, for the P-wave and the S-wave respectively, α_2,β_2 are the refracted angles, with respect to a vertical axis, for the P-wave and the S-wave respectively, $V_{s,A}$,$V_{p,A}$ are the shear wave velocity and body wave velocity in medium A, $V_{s,B}$,$V_{p,B}$ are the shear wave velocity and body wave velocity in medium B.

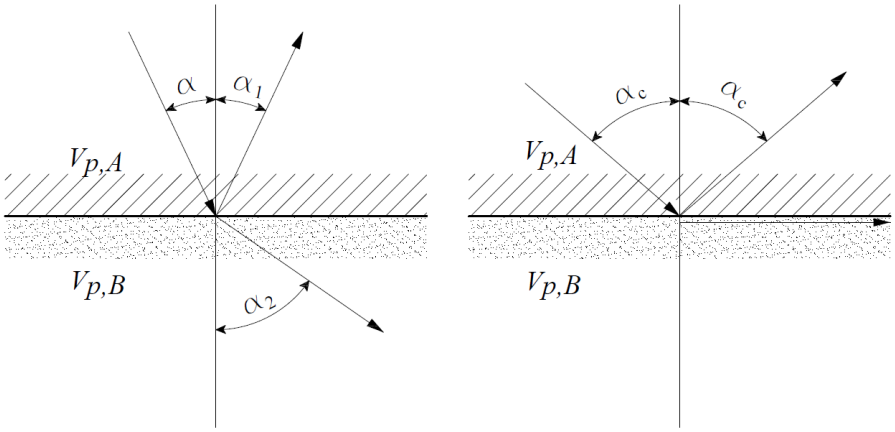

(a) (b)

Figure 2.3: Snell's law for compressional wave (a) and incident angle (b).

Refraction occurs up to a critical incident angle α_c , for which the refracted wave travels parallel to the interface, so that (Figure 2.3(b)):

$$\alpha_c = \sin^{-1}\left(\frac{V_{p,A}}{V_{p,B}}\right) \tag{2.25}$$

2.5 Analytical Solution of Wave Propagation in a Layered System

The solution of the wave propagation problem in a layered medium used in this work is based on the use of stiffness matrices in the frequency-wavenumber domain [63, 67]. Since the details of the solution are well known and established, for sake of brevity only the principle of the method is reported herein. The explicit notation of the solution in case of SV-P waves is given in Appendix B. The solutions are given for in-plane line loads. The transfer matrix method provides exact solutions for the wave propagation problem: the method assumes that the profile consists of a set of homogeneous layers with infinite extension in the longitudinal direction, while the last layer is usually considered a homogeneous half-space. In the transfer matrix approach the displacements, the shearing and the normal stress components at a given layer interface define the state vector, which is related through the transfer matrix to the state vectors at the preceding ones by:

$$\mathbf{z}_{j+1} = \mathbf{H}_j \mathbf{z}_j \tag{2.26}$$

where $\mathbf{z}_j$ is the state vector of the j-th layer and $\mathbf{H}_j$ is the transfer matrix of the j-th layer. If the analysis is restricted to a plane strain condition (i.e. plane waves), stresses and displacements in the state vector relate to in-plane components. The transfer matrix is a function of the angular frequency ω, the wavenumber k, the soil properties and the thickness of the layer.

If a single layer is isolated, preserving the equilibrium leads to the following relationship between forces and displacements:

$$\mathbf{p} = \mathbf{K}\mathbf{u} \tag{2.27}$$

where $\mathbf{K}$ is the dynamic stiffness matrix of the layer, $\mathbf{p}$ is the external "load vector" and $\mathbf{u}$ is the displacement vector. It can be noticed that $\mathbf{K}$ is symmetric. In the case of a system consisting of several layers, the global stiffness matrix is assembled in the finite element sense by overlapping the contribution of each layer matrices as shown in Appendix B.

Hence, the displacements at any layer interface are obtained by the formal inversion of the global stiffness matrix, as follows:

$$\mathbf{u} = \mathbf{K}^{-1}\mathbf{p} \tag{2.28}$$

2.5.1 Eigenvalue Problem

The natural modes of propagation of the system are obtained solving the eigenvalue problem, i.e. setting the load vector of equation (2.27) equal to zero. However, the problem itself is transcendental if the exact solution is used, i.e. it has infinite solutions.

To obtain the eigenvector, the soil is assumed as a multi-layered system over a rigid base and a discrete solution is used instead. When using a discrete solution for the wave propagation problem, the associated eigenvalue problem is algebraic in k, hence has a finite number of solutions and can be solved by standard techniques [63].

In the case of thin layers, i.e. when the thicknesses are small compared to the wavelength of interest the layer stiffness matrices in the discrete case may be obtained as:

$$\mathbf{K} = \mathbf{A}k^2 + \mathbf{B}k + \mathbf{G} - \omega^2\mathbf{M} \tag{2.29}$$

The quadratic eigenvalue problem can be written as:

$$\left(\mathbf{A}k^2 + \mathbf{B}k + \mathbf{G} - \omega^2\mathbf{M}\right)\boldsymbol{\varphi} = 0 \tag{2.30}$$

where $\mathbf{A,B,G,M}$ are the matrices given in Appendix C and involve only the material properties of the layers, and $\boldsymbol{\varphi}$ is the vector of eigenvectors. This problem yields $4N_L$ eigenvalues and eigenvectors in the case of plane strain waves, with N_L being the total number of layers. Then only positive propagating waves are considered, hence the negative-going waves and the non-propagating waves (i.e. evanescent) are discarded. This method is also known as the "Thin-Layer Method" [74].

In a layered system, surface waves are dispersive due to the variation of the stiffness properties of soil with depth. Moreover, the eigenvalue problem has multiple solutions, corresponding to multiple Rayleigh waves, thus higher order modes of Rayleigh wave occur.

Different modes carry a different amount of energy, depending on the stratigraphy, on the depth and on the type of source utilized [36]. The fundamental mode (mode0) is often dominant at low frequencies, but in many situations higher order modes become dominant playing an important role: hence, they should not be neglected. Different modes have different velocity of propagation: hence, in the time domain, they separate at a great distance from the source. Otherwise, they superimpose onto one another [36].

2.6 Near-Field and Far-Field Effects

As shown in the previous chapter, a seismic survey usually comprises the use of one (or more) source of wave and multiple receivers lined up along an imaginary array. Depending on the geometry of the deployment, the distance from the source and the size of the spacing between sensors, problems in the recoding of waves may arise.

Until surface-type waves travel a distance called near-field, they are not distinguishable from body-type waves and hence there are mutual interferences between the different waves. Within the near-field distance, which is dependent on the wave velocities, different waves are not separated and the influence of body waves on the propagation pattern cannot be neglected [6, 75]. Moreover, the cylindrically spreading wavefront has not travelled sufficiently to appear as a plane wavefront [76]. The effects resulting from working in the near-field distance are called near-field effects. An empirical rule of thumb to avoid near-field effect is widely proven to be:

$$x_1 \geq 0.5 \cdot \lambda_{max}, \tag{2.31}$$

where x_1 is the offset between source and the first receiver and λ_{max} is the maximum desired wavelength, i.e. the wavelength at the lowest frequency of interest.

Fundamental mode (mode0) of surface wave usually carries the biggest amount of energy among all the other modes, if the soil profile is regular (i.e. R- wave velocity increases with depth). Higher order modes of R-wave and body waves tend to dominate over the fundamental mode of surface waves at far offsets and at high frequencies. According to the intrinsic attenuation equation (2.21), since body waves and higher order modes of surface waves travel faster than the fundamental mode, their amplitude is likely to dominate high frequencies. The contamination of the signal by body wave components due to the intrinsic attenuation of high frequency components of surface wave is called far-field effect. Far-field effect leads to an overestimation of the apparent phase velocity, and in a decrease in the coherence values at high frequencies [6, 33, 77, 78].

Spacing between sensors D depends on the maximum and minimum desired wavelength to be measured and on the elastic properties of the soil to be tested. In terms of spatial distribution of receivers, the most accepted empirical rule of thumb is the following [9, 15]:

$$\frac{\lambda_{max}}{3} \leq D \leq 2\lambda_{min} \tag{2.32}$$

The lower bound is due to the precision of the instrumentation, which creates a physical limitation that governs the spacing between geophones. The upper bound is an empirical criterion tailored to avoid the far-field effect. Far-field effects limit the highest frequency at which the phase angle can be still measured without incurring in any errors, so the upper bound of receiver spacing should be tailored to insure that the Rayleigh-wave energy does not decay excessively [6].

While the lower bound of equation (2.32) seems to be too conservative, the upper limit for the frequency range seems to be too high. A newer widespread rule of thumb is the sequent [79]:

$$\frac{\lambda_{max}}{16} \leq D \leq \lambda_{min} \tag{2.33}$$

The receiver spacing is also governed by the equivalent in the space domain of the Nyquist sampling criterion, in order to avoid spatial aliasing:

$$D \leq \frac{\lambda_{min}}{2} \tag{2.34}$$

Therefore, although many authors proposed different empirical criteria there is not a standard about the experimental set-up for dispersion measurement [35]. The debate over the optimum configuration contributes to the lack of standardization of surface-wave methods, slowing down their use.

2.7 Depth Resonances of Surface-Breaking Cracks

One of the sources of data for the estimation of the depth of surface-breaking cracks is their frequency response. Defects like cracks and notches act like a source of acoustic scattering when illuminated by an incident pulse. A scattering wave, which contains the information about the crack that generated it, radiates off the crack. Various experimental results and studies have shown that the crack response has a resonance-type feature that occurs periodically at certain frequencies and has found to be associated with the depths of the cracks [53-55].

Ayter and Auld [53] developed the resonance theory for a surface-breaking crack in the case of Rayleigh wave normally incident to the illuminated face of a crack normal to the surface of a homogeneous, isotropic half-space. They demonstrated that when the depth of the crack is a multiple of a half-wavelength long, there is a maximum in the reflection coefficient of the incident wave as the crack exhibits little displacement of its top edge. The depth resonant frequencies are found to be:

$$f_{res} \leq \frac{d_i \cdot V_R}{C \cdot h} \tag{2.35}$$

Where f_{res} is the resonant frequency, h is the depth of the vertical surface-breaking crack, d_i is the mode integer index and C is a coefficient equal to 2.

2.8 Ellipticity of Rayleigh Wave

Ellipticity (also recalled as H/V in this thesis) is the dimensionless ratio of the vertical and horizontal frequency components of displacement of the Rayleigh wave. The vertical component of displacement is normal to the direction of propagation; the horizontal component is parallel to the direction of propagation. The ellipticity is an important parameter which reflects fundamental properties of the elastic material [39]. As mentioned in Section 2.2, the Rayleigh wave particle motion is elliptical, thus the spectral ratio of the horizontal to the vertical components depends on the velocity profile of the medium. The dependence of the ellipticity of Rayleigh waves on frequency is very sensitive to the material properties of the propagation medium. The exact analytic formulae of the ellipticity are known for the half-space case and for the layer over half-space case [39].

For the half-space case, ellipticity is consistent with frequency and only dependent on the ratio between the R-wave and the S-wave velocity, or in other terms, on the Poisson's ratio [39], as it follows:

$$\Upsilon = \frac{2 \cdot \sqrt{1 - \frac{V_R^2}{V_S^2}}}{2 - \frac{V_R^2}{V_S^2}} \tag{2.36}$$

In case of multi-layered systems, the ellipticity shows a strong frequency dependency and its character is strongly dependent on the velocity contrast of the layers of the propagation medium. For normally dispersive profiles, i.e. when velocity increases with depth, the resonant frequency of the H/V is often assumed to correspond to the so-called "shear wave resonance" of the top layer. That means, it is assumed that the singularity occurs for such frequencies where the layer's thickness is one quarter of the wavelength of the shear wave within the layer [39]. Other authors [23, 24] suggested minima in the ellipticity curve to be associated with the phenomenon of mode osculation in not normally dispersive systems. They observed that the osculation frequency, where the energy shifts between two modes, occurs at the same frequency at which the ellipticity curve shows a minimum. Ellipticity increases with increasing velocity contrasts: in the absence of sharp velocity

contrasts, modes are well separated and the ellipticity curve is almost flat, while in the presence of strong velocity contrast, the distance between modes is reduced and the ellipticity shows one or more peaks. Their experimental and numerical tests shown that the osculation frequency, where the energy shifts between the fundamental to higher order modes and/or viceversa, occurs at the same frequency at which the two modes have similar ellipticity and predominantly vertical motion, i.e. the frequency at which ellipticity presents local minima. Ellipticity in the numerical and experimental investigations of this thesis is averaged in space.

2.9 Summary

The theory of elastic wave propagation in infinite, semi-infinite and layered media was reviewed in this chapter by focusing on the mechanical propagating waves and on their properties. An analytical solution for the wave propagation in layered system was proposed and it will be utilized in the forthcoming chapters. Finally, some basics regarding the ellipticity of the Rayleigh wave and the depth resonances of surface-breaking cracks were introduced.

Chapter 3: Signal Processing and Numerical Model

Signal processing methods are applied to seismic data in order to extract relevant information and to compare experimental measurement with numerical results. This chapter presents an overview of existing methods for the dispersion calculation in the frequency domain.

To study the wave propagation along multi-layered media, a two-dimensional finite element model of the ground is assembled in the *x-y* plane. Finite element modelling of seismic waves has practical applications in simulating seismic measurement. A two-dimensional model at this stage is chosen for being quicker and easier to implement than a full three-dimensional model. With a two-dimensional model, it is possible to exploit the axial symmetry of the problem with respect to the propagation of mechanical waves. Moreover, the plane-strain approximation is adopted, i.e. the strain normal to the two-dimensional plane is assumed very small. A finite element model requires appropriate mesh dimension and attenuation parameters, which will be discussed in this chapter. The accuracy and resolution of the model and hence its limitations are affected by the spatial-temporal discretization within the mesh, which is discussed in the following sections. The numerical model is then validated through analytical solutions introduced in the previous chapter.

The data obtained through numerical simulations will be analyzed with the signal processing methods introduced in this chapter and extensively utilized in the forthcoming chapters to understand and explain some of the key issues with surface wave dispersion in layered media.

3.1 Frequency Domain Operations

Any time series data, such as $x(t)$, can be transformed into its frequency components via a Fourier transform. The way of representing a periodic signal in terms of its frequency component is called linear spectrum and it is used to identify all the frequencies and their absolute amplitudes and phases.

Signals from two records, $x(t)$ and $y(t)$, can be compared in terms of cross-power spectrum, which measures the inter-relationship between two signals in the frequency domain and is defined as the average of the product of the spectrum of $x(t)$ and the complex conjugate spectrum of $y(t)$.

$$S_{xy}(f) = \lim_{T\to\infty} \frac{1}{T} \mathbf{E}\left[S_x(f) \cdot S_y(f)^*\right] \tag{3.1}$$

where $x(t)$ and $y(t)$ are the time histories of the signals, $S_x(f)$, $S_y(f)$ are the Fourier transforms of the signals, **E** denotes the expected value and (…)* denotes the complex conjugation operation. The cross-power spectrum carries the information of the relative phase between the two signals at each frequency within the bandwidth. The units of the Fourier transforms are EU (engineering units), whereas the units of the cross-power spectrum are EU^2 over frequency, and they are usually expressed in a decibel scale.

The auto-spectrum $S_{xx}(f)$ is the cross spectrum between the same signal $x(t)$. It describes how a random signal's power is decomposed as a function of frequency, e.g. it can be used to determine which band of frequencies makes the largest contribution to a signal.

The time delay between two signals for each frequency component is then simply computed through the following expression, for each frequency:

$$t(f) = \frac{\phi(f)}{2\pi f} \tag{3.2}$$

where $\phi(f)$ is the phase difference between two signals at two different positions, i.e. the phase of the cross-power spectrum.

To reduce the background noise that obscure a signal coming from *in-situ* testing, averaging is a common and reliable practice. Averaging is possible as long as the system is or can be considered linear. This is generally the case of the ground for small level of strains (typically less than $100\mu\varepsilon$) [2, 9]. It has been noticed that, in general, the arithmetic average of at least five signal records gathered under constant conditions is required [42], although others suggest an averaging among 20 signals [1] or up to 100 [80].

The coherence function is defined as:

$$c_{xy}^2 = \frac{|S_{xy}(f)|^2}{S_{xx}(f) \cdot S_{yy}(f)} \tag{3.3}$$

The coherence function is an absolute measure of how well two signals $x(t)$ and $y(t)$ are linearly related. A coherence value close to unity corresponds to a perfect correlation between the two signals, while a coherence value close to zero means that the two signals are totally unrelated. Coherence is the most common method to perform real time quality checks, e.g. to see the level of noise contamination [15].

3.2 Cross-Power Spectral Method

The Cross-Power Spectral Method is the traditional approach to obtain the dispersion curve from the measurement coming from SASW or MASW tests. It relies on the main assumption that only one type of wave or one mode of propagation dominates in the frequency range of interest. For each sensor spacing D, the apparent phase velocity is calculated as follows:

$$V_{ph} = \frac{D}{t(f)} = \frac{D \cdot 2\pi \cdot f}{\phi(f)} \tag{3.4}$$

To form the final dispersion curve, i.e. the plot of the apparent phase velocity vs. frequency, the contribution of each pair of sensors of the deployment is added. The apparent phase velocity is a velocity that does not necessarily correspond to the velocity of one mode of propagation or one wave, but it is rather an average value among different types. The dispersion curve can be quickly converted into the shear velocity-depth curve considering the effective depth of investigation equal to one third of the wavelength, under the assumption of the Rayleigh wave to be predominant.

One of the main problems of the cross-power spectral method is the unwrapping of the cross-power spectrum phase: in fact, the presence of low frequency noise can prevent the extraction of reliable information from the signal. Inclusion of external noise can cause the estimation of the unwrapped phase more difficult, which reflects in fictitious jumps in the wrapped phase [15]. Moreover, the estimation of the unwrapped phase is affected by the presence of higher dominating modes in the wave motion, since the phase belonging to different modes may be incorrectly used [21, 36]. To mitigate this unwanted phenomenon, usually data with low coherence value (e.g. lower than 0.9) are filtered and discarded from the survey, even though numerical and empirical observations suggest that phase angle is reliable also for lower coherence values [81]. The data points are eventually reduced with arithmetic average to obtain a single value of phase velocity for each frequency. Typically, five or more measurements are averaged for each sensor spacing in order to reduce the inclusion of noise (stacking).

It is clear that this technique is unable to isolate the contribution of different types of wave and different modes of propagation of the R-wave. The dispersion measurement is rather an average dispersion that takes into account all the phenomena occurring in the surveyed medium and hence a superposition of different waves and modes of propagation [17, 21]. The apparent phase velocity is that of the superposed mode resulting from the combination of fundamental and higher modes of propagation. Therefore the spectral method is a reliable method for R-wave velocity measurement as long as the first fundamental R-wave mode is dominant among all the other modes and waves in

terms of energy, which is likely to happen in homogeneous soils, when the stiffness does not vary abruptly with depth [18, 19, 32].

The spectral method is then a simplistic approach to dispersion measurement and can be not accurate in case of irregular stratifications or whenever the fundamental Rayleigh mode is not dominant among the others. Figure 3.1 shows a typical example of dispersion curve obtained with the Cross-Power Spectral Method. Each point is associated to a frequency and its relative phase velocity, obtained after an arithmetic average of all the values obtained via equation (3.4).

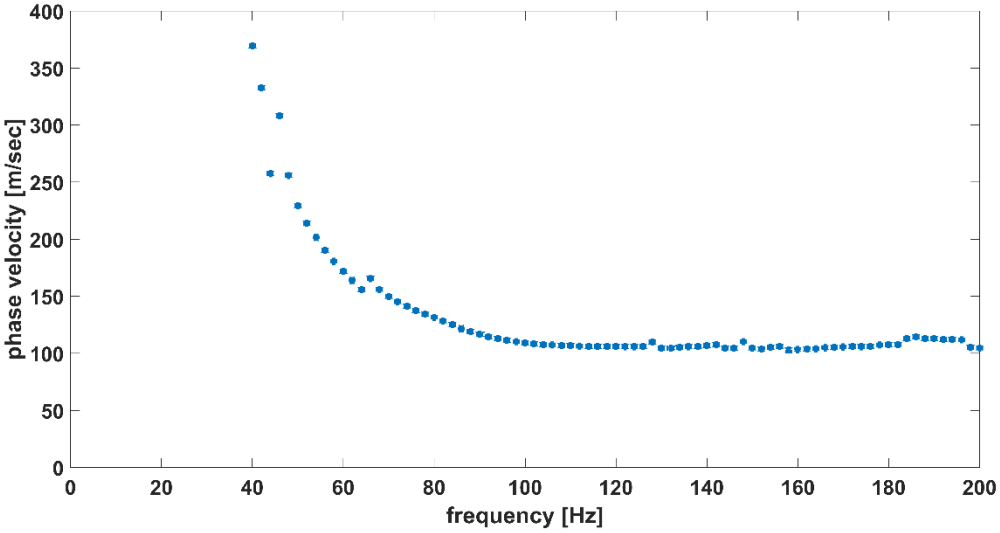

Figure 3.1: Experimental dispersion curve obtained from the Cross-Power Spectral Method. The figure shows a dispersion curve obtained on a soil site, using a shaker as a continuous vertical source and an array of 7 geophones (following the configuration displayed in section 5.2.1).

3.3 Frequency-Wavenumber Transformation

The frequency-wavenumber transformation (*f-k*) is a signal processing method of seismic data coming from a MASW or a MISW test to obtain a dispersion curve. It consists of a two-dimensional Fourier Transform: the time history is transformed into frequency components and the spatial data is transformed into wavenumber components [15-18].

Considering the discrete space-time domain representation $u(x,t)$ of a multichannel survey, being $u(x,t)$ vertical displacements varying in space and time, the Fourier Transformation can be applied to the time axis of $u(x,t)$ to obtain:

$$U(x,\omega) = \int u(x,t) \cdot e^{i\omega t} dt \tag{3.5}$$

A second Fourier transform can then be applied to the space axis of the normalized spectrum $U(x,\omega)$, to obtain:

$$U(k,\omega) = \int e^{ikx} \frac{U(x,\omega)}{|U(x,\omega)|} dx \tag{3.6}$$

where $k = \omega / c_\omega$, ω is the angular frequency and c_ω is the phase velocity associated with the frequency ω. Normalization is accomplished in the space and frequency directions, using the maximum value on the space axis and on the frequency axis respectively. In fact, dividing by the magnitude compensates for the effects of the geometrical and intrinsic attenuation of the wavefield, i.e. the attenuation along space and frequency. In the experimental investigations of this thesis, the transfer function between the output and the input signal (source) is used in equation (3.7). The spectrum $U(x,\omega)$ is divided by the frequency spectrum of the input signal, recorded using an accelerometer. This has the effect of reducing the noise, triggering the recorded signal with the excitation and in general augmenting the confidence of the measurements.

This leads to the representation of the wavefield in the *f-k* domain, where peaks of the $U(k,\omega)$ spectrum are associated with the biggest energy and hence to the vibrational modes of propagation. Recalling that the phase velocity c_ω is given by the ratio between frequency and wavenumber, the dispersion curve can be estimated. Typically, five or more measurements are averaged in order to reduce the inclusion of noise (stacking). The *f-k* spectra obtained within this thesis are normalised by their maximum absolute values of energy, since for the aims of this work absolute magnitude is not important.

The *f-k* transform can discriminate between direct positive going waves (characterized by positive wavenumbers) and reflected negative going waves (characterized by negative wavenumbers), but cannot distinguish between direct and reflected positive going waves [16, 82].

Examples of *f-k* representations of multichannel records are shown in Figure 3.7 and Figure 3.8.

3.3.1 Aliasing

The frequency-wavenumber representation can potentially suffer from spatial and temporal aliasing, which is the consequence of spatial or temporal undersampling. Temporal and spatial aliasing follows the Nyquist's sampling criterion and shows up when [16, 83]:

$$f > \frac{1}{2\Delta t} \tag{3.7}$$

$$k > \frac{2\pi}{2D} \tag{3.8}$$

where $\Delta t, D$ are respectively the temporal and spatial sampling intervals. Aliasing manifests as fictitious phenomena spread across the two dimensions. However, spatial aliasing does not occur as long as equation (2.34) is satisfied.

3.3.2 Resolution

Resolution Δf in the frequency domain is inversely proportional to the length of the signal:

$$\Delta f = \frac{1}{L_f} \tag{3.9}$$

where $L_f = n\Delta t$ is the length of the signal, n is the number of points in time, Δt is the temporal interval and $f_s = 1/\Delta t$ is the sampling frequency.

Resolution Δk in the wavenumber domain is inversely proportional to the length of the sensor line. The half-width between the neighbouring minima is:

$$\Delta k = \frac{2\pi}{L_s} \tag{3.10}$$

where $L_s = ND$ is the length of the sensor line, N is the number of sensors and D is the sensors spacing (spatial interval) [16, 60]. Both $u(x,t)$ and $U(x,\omega)$ are usually zero padded in the time direction and in the space direction respectively, to artificially increase their length. The Fourier Transform assumes that the signal is periodic. Adding a group of zeros at the end equals to treat the signal as if the original signal is followed by silence, and that whole thing is repeated on to infinity. Zero padding does not add any additional information to the survey, but only improves the reading of the spectrum. Zero padding does not increase the resolution of the spectrum. In this thesis, numerical traces are zero padded usually up to 10k points in both the space and time domains, experimental traces are zero padded up to 1k points only in the space domain.

Resolution of the *f-k* domain is a key aspect for the separation of different modal contributions: often a peak in the *f-k* domain is not associated with a single mode, but is rather a superposition of several different modes. Often different modes have close phase velocities: hence, in the time domain they separate at great distance from the source. Figure 3.2 shows the difference of the effective wavenumber resolution of the dispersion curve: two slices of *f-k* spectrum corresponding to a certain frequency are reported. Figure 3.2(a) shows the case when the fundamental mode is the one carrying more energy, while Figure 3.2(b) shows the case of higher order modes playing a relevant role in the propagation. In the case only one mode of propagation is dominant (Figure 3.2(a)), low and high resolution lead to the location of one main peak. In the case of multiple modes dominating the propagation pattern, with poor resolution (24 receivers, short deployment) it is possible to locate only a single peak, which could be erroneously associated with a single mode of propagation (Figure 3.2(b)); with high resolution (256 receivers, long deployment), the different modes are well separated and detected. Hence, once a certain array configuration has been adopted to carry out a survey, and the sampling frequency and duration of acquisition is chosen, it is impossible to improve the real resolution of the spectrum [15].

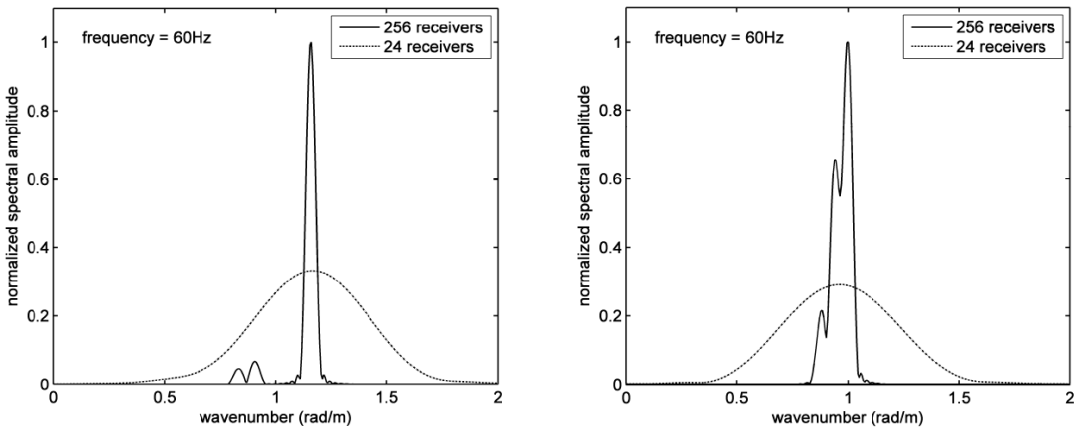

(a) (b)

Figure 3.2: Influence of the resolution on the separation of different modes on propagation [17]: when one mode of propagation is dominant (a); when three modes of propagation are dominant (b).

3.4 Introduction to Finite Element Modelling of the Soils

Alongside the experimental investigation, and as a validation of it, a two-dimensional finite element model of the ground is assembled through the Abaqus/CAE software, in the "vertical" plane, to study the wave propagation in half-spaces and layered systems. The solver used for the FEM model in this thesis is the explicit dynamic solution method: it is one of the approaches used in numerical analysis for obtaining numerical approximations to the solutions of time-dependent, ordinary and partial

differential equations (PDE), as is required in computer simulations of physical processes [84]. Explicit dynamics is a mathematical technique for integrating the equation of motion through time using the Euler method. Explicit dynamics was chosen because it provides the capability to analyse short-duration, dynamic problems [85].

This model is subject to the assumptions that the medium's layers are elastic and isotropic. The biggest issue with numerical simulation of wave propagation in soils/multi-layered systems is to avoid, or at least minimize, the effects of reflection of the wavefronts from the boundaries, and hence to properly model P-wave, S-wave and R-wave [86]. One possible approach could be that of having a model big enough to avoid the occurrence of reflections with respect of the time of simulation, but this sometimes leads to big computational efforts. Another way of dealing with reflections is the use of infinite elements in combination with finite elements to allow unbounded problems to be modelled without reflections from the domain boundaries. The infinite elements behave as many infinitesimal dashpots that are oriented normally and tangentially with respect to the boundary. The elements are designed to absorb plane waves in three orthogonal directions. Hence, the distributed equivalent dampers on the boundary are chosen to satisfy:

$$\begin{cases} \sigma_{xx} = -\rho \cdot V_P \cdot \dot{u}_x \\ \sigma_{xy} = -\rho \cdot V_S \cdot \dot{u}_y \\ \sigma_{xz} = -\rho \cdot V_S \cdot \dot{u}_z \end{cases} \tag{3.11}$$

where $\sigma_{xx}, \sigma_{xy}, \sigma_{xz}$ are stresses, $\dot{u}_x, \dot{u}_y, \dot{u}_z$ are velocities and ρ is the material density. Infinite elements only give perfect absorption for waves that impinge perpendicularly to the boundary [85]. They are particularly useful when modelling high velocity layers: smaller and computationally lighter models are possible.

A two-dimensional model at this stage is chosen for being quicker and easier to implement than a full three-dimensional model. With a two-dimensional model, it is possible to exploit the axial symmetry of the problem with respect to the propagation of mechanical waves. Moreover, plane-strain, isotropic, finite elements have been used for the ground simulation. This means that the strain normal to the *x*-*y* plane, ε_z, and the shear strains γ_{xz} and γ_{yz}, are assumed to be very small. Hence plane-strain elements represent an infinitely long structure in the *z*-direction. They have two degrees of freedom (DoF): the translation in the *x* and *y* direction. One limitation of the two-dimensional model is the plane wave approximation of seismic waves.

In this thesis, both finite and infinite elements are used in combination for the ground model: a 3-node bilinear triangle and a 4-node bilinear quadrilater. A 3-node, triangular element was chosen for

being computationally more accurate than elements with higher order nodes [87]. They are listed in Table 1.

TYPE	NAME	DESCRIPTION	DoF
Finite	CPE3	3-node linear plane-strain triangle	Translation in direction *x*,*y*
Infinite	CINPE4	4-node bilinear plane-strain quadrilater	Translation in direction *x*,*y*

Table 1: Elements used in the numerical model.

3.5 Model Accuracy and Stability

With finite elements methods, two discretization constraints should be adopted in order to achieve appropriate spatial and temporal resolution. The spatial condition assures that a sufficient number of points in space are sampled in order to recreate the wave, or in other words, that the element size l_{max} is small enough (it is the analogue of the Nyquist's criterion in the time domain) [82, 88].

$$l_{max} \leq \chi \lambda_S \tag{3.12}$$

where $\lambda_S = \frac{V_S}{f_{max}}$ is the minimum shear wavelength, f_{max} is the maximum desired frequency and the constant χ must be less than 0.5 because of the Nyquist's limit. Rearranging (3.12) we obtain a relationship between the element size and the upper limit of the frequency range:

$$f_{\max} \leq \chi \frac{V_R}{l_{\max}} \tag{3.13}$$

The temporal constraint must be set after the spatial, to ensure that the wavefront does not travel faster than the temporal sampling interval Δt. This is achieved using the Courant-Friedrichs-Lewy condition [82, 89, 90], here rearranged for two-dimensional problems:

$$\Delta t_{\max} \leq \frac{1}{V_P \sqrt{\frac{1}{l_{\max}^2}}} \tag{3.14}$$

Damping in numerical simulations is usually related to the hysteretic damping of equation (2.20) by means of the classic Rayleigh damping: it uses a system damping matrix $\mathbf{C}$ proportional to the mass matrix $\mathbf{T}$ and to the stiffness matrix $\mathbf{S}$ as follows [82, 91]:

$$\mathbf{C} = \alpha_d \mathbf{T} + \beta_d \mathbf{S} \tag{3.15}$$

where α_d is the mass-proportional damping coefficient and β_d is the stiffness-proportional damping coefficient. Relationships between the modal equations and orthogonality conditions (modal decomposition) allow this equation to be rewritten as:

$$\xi = \frac{1}{2\omega}\alpha_d + \frac{\omega}{2}\beta_d \tag{3.16}$$

It can be noticed that the damping ratio varies with the frequency of excitation. Rayleigh damping allows the damping ratio to be considered constant only in a range of frequency, if both mass and stiffness damping are considered, or to avoid big damping at low frequencies, by setting the mass damping to zero. The values of α_d and β_d are usually selected, according to engineering estimations, such that the critical damping ratio is given at two known frequencies. A deep insight on the effects of the mass-proportional and the stiffness-proportional damping, and on their choice for the numerical simulations within this thesis is given in section 3.7.1. Figure 3.3 shows the mathematical meaning of equation (3.1). The model is unconstrained to avoid reflections that may occur by constraining the nodes of the finite elements.

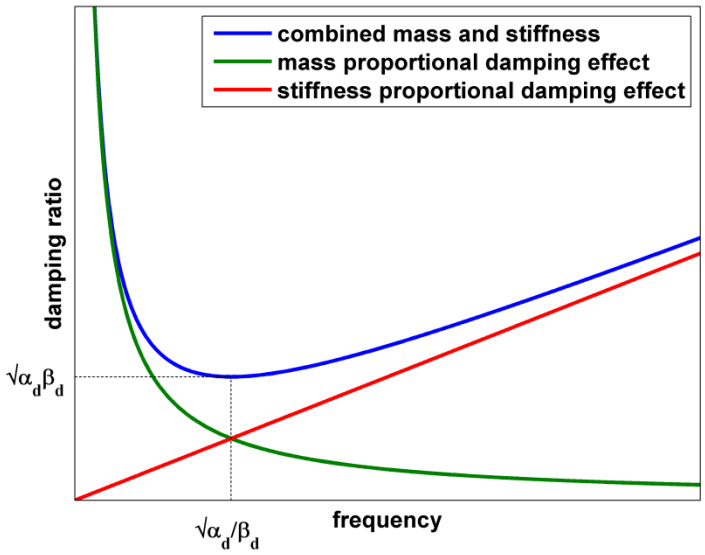

Figure 3.3: Relationship between mass-proportional and stiffness-proportional damping.

3.6 Features of the 2-D Model

The choice of the shape of the model was made with the aim of avoiding reflections from the boundary: since infinite elements only give perfect absorption for perpendicularly impinging waves, the vector components of the wavefront should always be normal to the boundary. Two models are developed and exploited in this work: the first (model "1") is a semi-circle, the second (model "2") is a semi-ellipse, both with infinite elements applied at their boundaries. In the first case, the boundaries are normal with respect to the wavefront of body waves; in the second case, the elliptical shape is a compromise that ensures the boundaries to be almost normal to both the body wave's and surface wave's wavefronts. Model "1" is used for simulations on a half-space; model "2" is used to model layered systems. Forthcoming simulations were run with different profiles, mechanical properties, damping, loads and sampling frequencies. Table 2 shows the values of the parameters used to run the simulations for the two models. Mechanical parameters and damping ratios were chosen to be close enough to typical values of soils and asphalts, and were not so different from that used in [57, 86, 92, 93]. The mass damping was equal to zero in all the simulations, following [60, 92] (refer to later section).

PARAMETER	Half space	Layered models
Young's Modulus, E	100 MPa	variable
Poisson ratio, ν	0.33	
Mass damping, α_d	0	
Stiffness damping, β_d	$0.2/200 \cdot 2\pi$	variable
Mass density, ρ	2000 kg/m^3	
Maximum element size at the surface, l_{max}	0.05 m	0.05 m
Radius/Semi-major and semi-minor axis	50 m, 50 m	10 m, 7.5 m
Sampling frequency, f_s	20 kHz	20 kHz or 50 kHz
Duration of the simulation T	0.25 sec	0.10 sec

Table 2: Parameters for model "1" and model "2".

Following the work of Zerwer [82], since we have only interest in surface wave measurements, the mesh elements are smaller near the surface, where R-wave propagates, with an element size equal to $l_{\max}$, then progressively increasing with depth. In this work, two mesh designs are used: model "1" has a graded mesh in both vertical and horizontal direction, model "2" has a graded mesh only in the vertical direction. This choice is motivated by two factors. Firstly, the higher frequencies travel at the shallow surface, where a certain mesh size is required. Lower frequencies travel at lower depths with bigger wavelength, so a bigger mesh size is acceptable. Secondly, the R-wave decays

exponentially with depth, i.e. most of the R-wave energy is located within the depth of one wavelength. Infinite elements permit a relevant reduction of the size of the model, since we can ignore the reflection from the boundaries, especially in the case of high stiffness values and hence fast seismic waves' velocities. The element dimensions of model "1" are between 5 mm and 3 m in the vertical direction; the element dimensions of model "2" are between 5 mm and 25 mm in the vertical direction. Figure 3.4 and Figure 3.5 depict the dimensions and the mesh distribution of the two models.

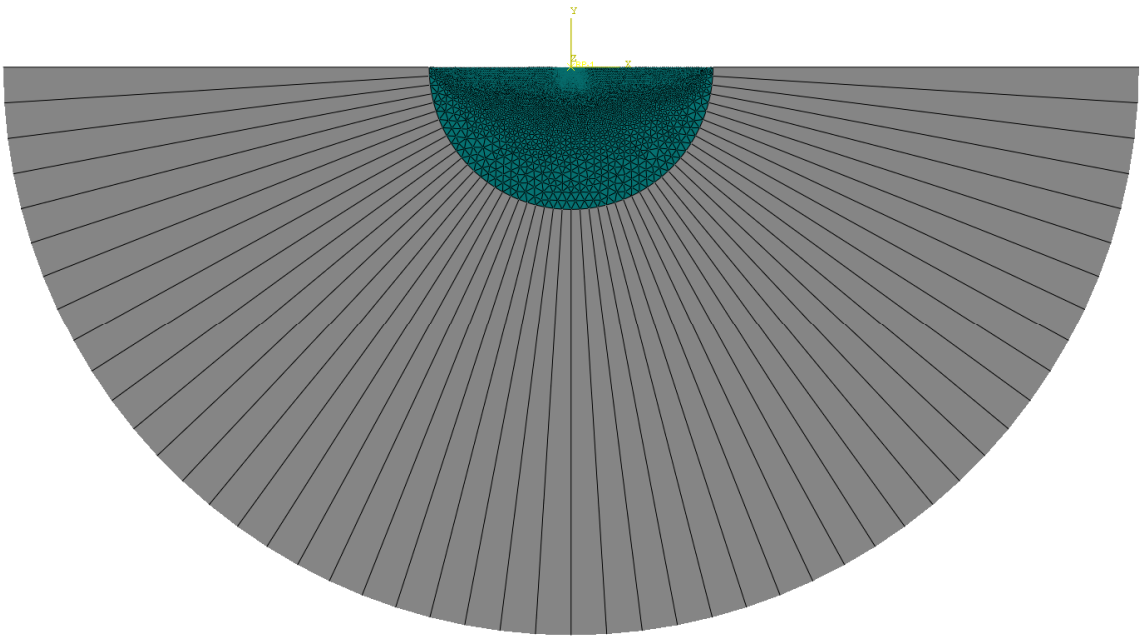

(a)

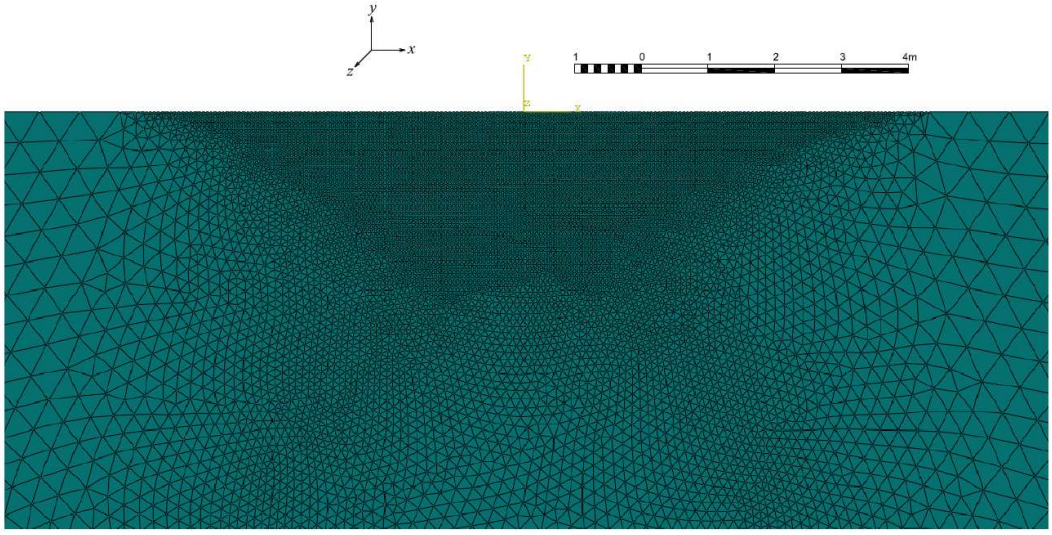

(b)

Figure 3.4: Geometry of model "1", with both finite and infinite elements (a) and view of the graded mesh of the central region of model "1" (b). Finite elements are coloured in green, whereas infinite elements are coloured in grey.

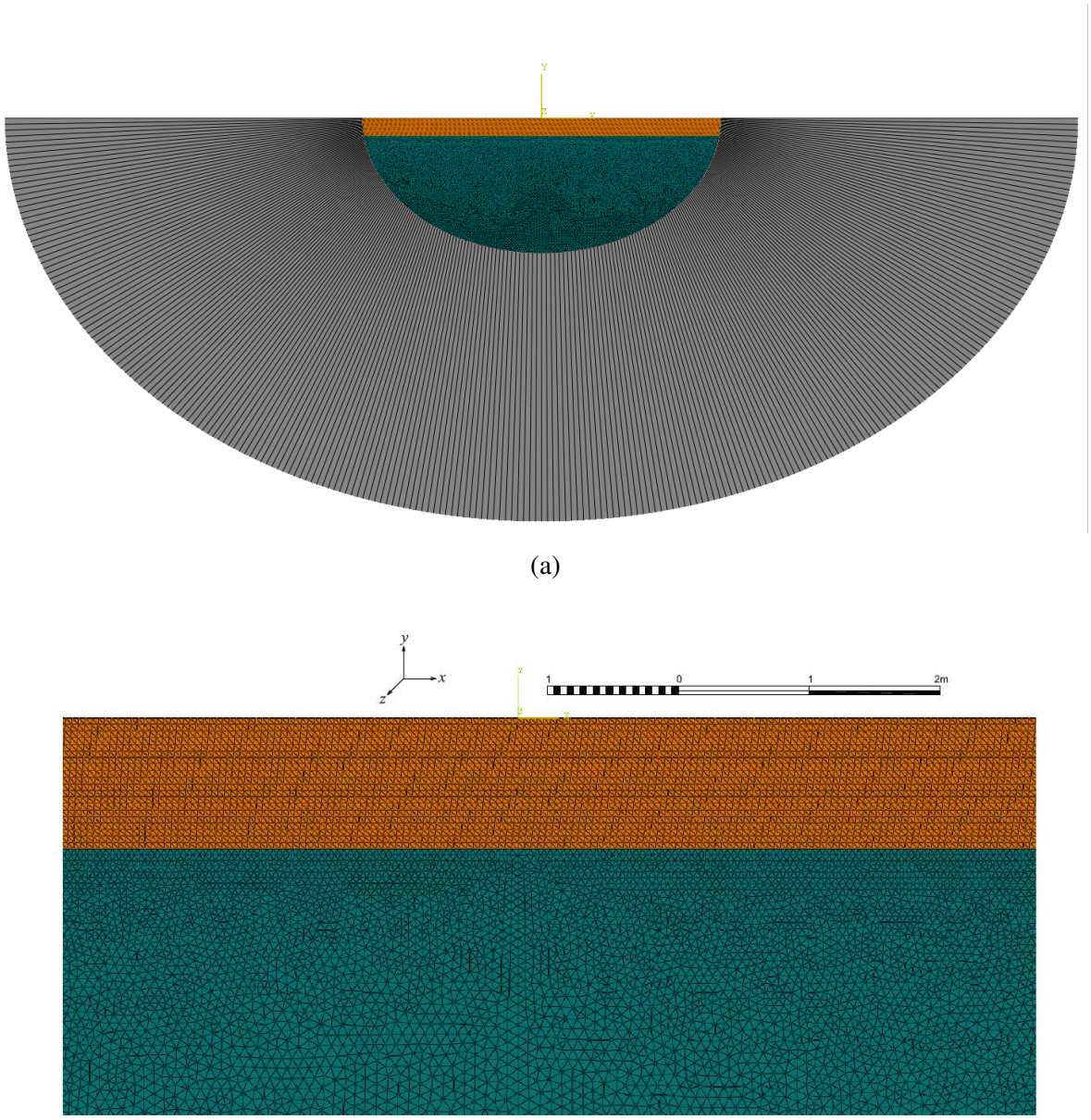

(a)

(b)

Figure 3.5: Geometry of model “2”, with both finite and infinite elements (a) and view of the graded mesh of the central region of model “2” (b). Finite elements belonging to the first layer are coloured in orange; finite element belonging to the half-space are coloured in green; infinite elements are coloured in grey.

3.7 Validation of the Model

Model “1” and “2” were validated through a direct comparison with the analytical proposed solutions for wave propagation in layered media (see section 2.5), in the frequency-wavenumber (*f*-*k*) domain.

The FEM simulations were run with a force normally applied on a strip of 0.10 m. Different waveforms were used as loads for the simulations of this thesis, for which energy was distributed among different frequency bandwidths. The time histories and the auto-spectra of the loads used in the forthcoming simulations for model "1" and model "2" are depicted in Figure 3.6.

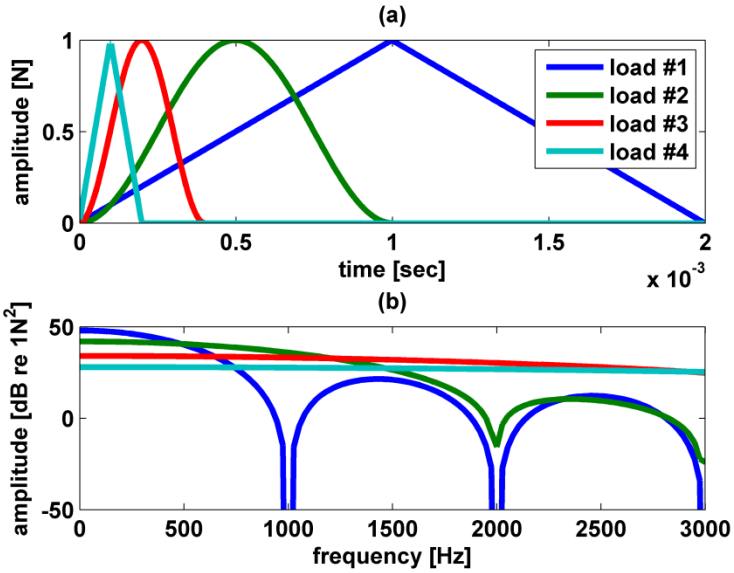

Figure 3.6: Time histories (a) and auto-spectra (b) of the impulsive loads used in the simulations.

Figure 3.7(a) shows the wavefront in the *f-k* domain obtained compiling the vertical signals coming from 198 points equally spaced by 0.05 m, using model "1" and load #1. The slope of the black line indicates the velocity of the R-wave in the half-space, whilst the slope of the green line indicates the velocity of the compressional wave. The parameters are the same shown in Table 2. The presence of energy for zero wavenumber is linked to finite element modelling: the model sinks showing permanent deformation since the problem is unconstrained. Figure 3.7(b) depicts the wavefront in the same half-space in the frequency-wavenumber domain, obtained through the analytical solutions for a vertical unit line load. The spectral image has a resolution Δf of 1 Hz and Δk of 0.025 rad/m. The damping ratio is the same as used in the FEM simulations. Again, the black and green lines represent the Rayleigh and compressional wave propagation modes. Both images are normalized by their respective maximum absolute values of energy.

Comparison of the dispersion spectra in the *f-k* domain shows a good agreement between the finite element results with model "1" and the analytical solutions. In fact, the energy maxima in both spectra follow the black line, which indicates the dispersive relationship in the half-space. Moreover, the geometrical and intrinsic attenuation of the R-wave in the numerical model seems to match that of the analytical solution. In fact, the energy has the same distribution in the two spectra, although there is a disagreement in the value of the magnitude due to the normalization process.

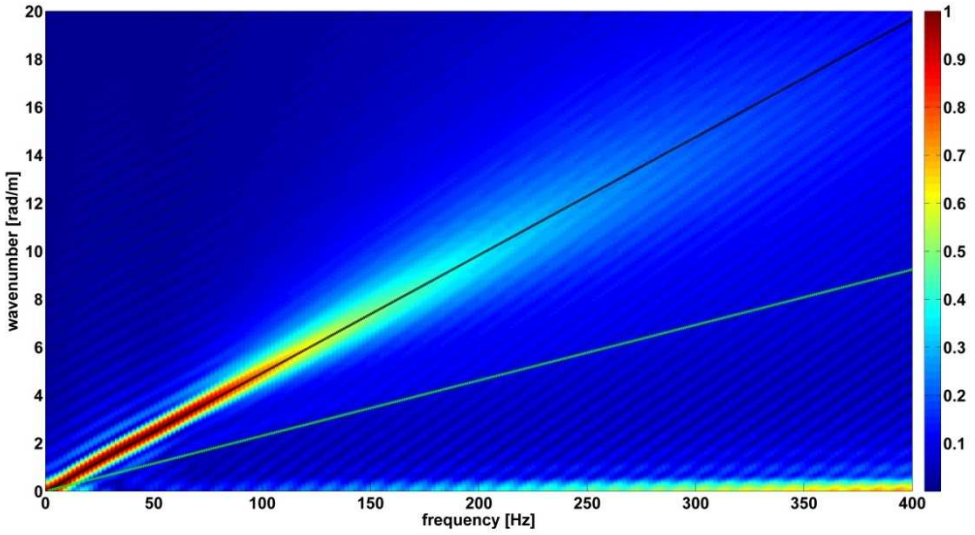

(a)

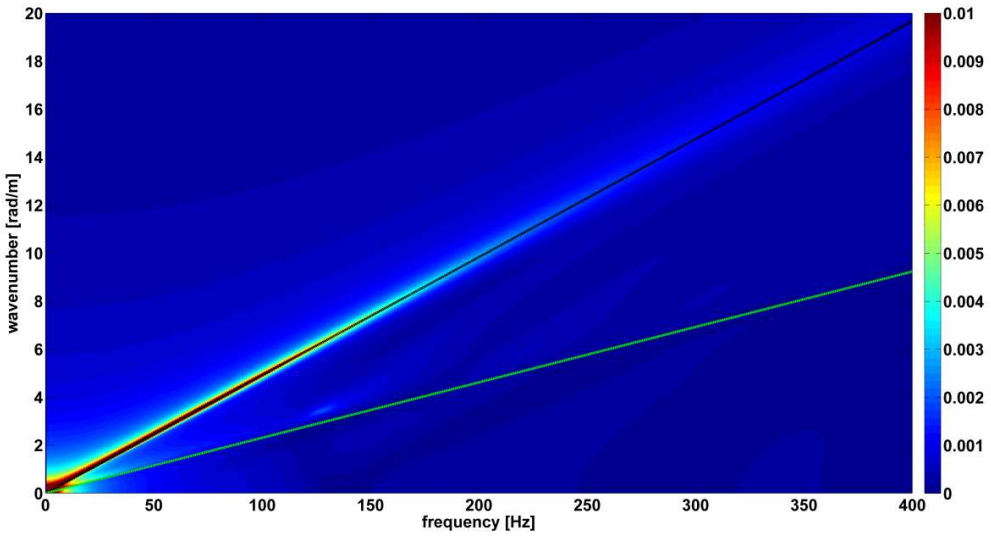

(b)

Figure 3.7: Vertical *f-k* spectra in a half-space from FEM (a) and from analytical solutions (b). The slope of the black lines indicates the velocity of the R-wave in the half-space, while the slope of the green lines indicates the velocity of the P-wave.

Figure 3.8(a) shows the wavefront in the *f-k* domain obtained compiling the vertical signals coming from 198 points equally spaced by 0.05 m, using model "2", load #2 and a sampling frequency of 20 kHz. The multi-layered system is composed as in Table 3. The parameters are the same shown in Table 2. The slope of the two black lines indicates the velocity of the R-wave in the upper layer and in the half-space. The presence of energy for zero wavenumber is again linked to finite element modelling. Figure 3.8(b) depicts the wavefront in the same multi-layered system in the *f-k* domain, obtained through the analytical solutions for a vertical unit line load. The spectral image has a resolution Δf of 1 Hz and Δk of 0.025 rad/m. The damping ratio is the same as used in the FEM

simulations. The slope of the two black lines indicates the R-wave velocity in the upper layer and in the half-space. Both images are normalized by their respective maximum absolute values of energy.

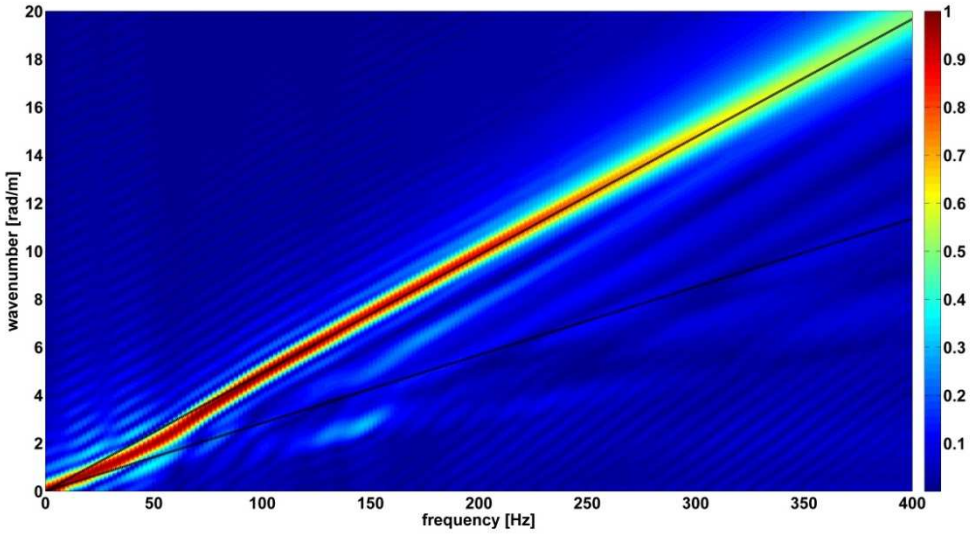

(a)

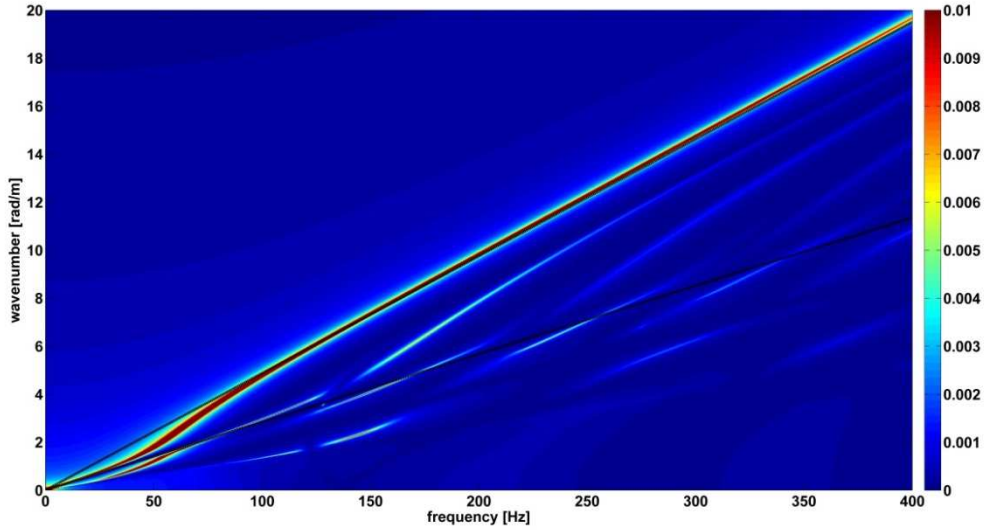

(b)

Figure 3.8: Vertical *f-k* spectra in a multi-layered system from FEM (a) and from analytical solution (b). The slope of the two black lines indicates the velocity of the R-wave in the upper layer and in the half-space.

One can notice again that model "2" matches well the analytical results. In fact, the energy maxima in both spectra follow the same propagation pattern, which indicates the dispersive relationship in the layered model. Moreover, the geometrical and intrinsic attenuation of the R-wave in the numerical model seems to match that of the analytical solution. In fact, the energy seems to have the same distribution in the two spectra, although there is a disagreement in the value of the magnitude due to the normalization process.

According to the aforementioned results, the two-dimensional model, as developed in this work, represents a reliable tool for simulation of wave propagation in half-spaces and in multi-layered systems.

Layer	Thickness [m]	Poisson's ratio	Density [kg/m3]	Young's modulus [MPa]	Rayleigh damping, β	V_P [m/s]	V_S [m/s]	V_R [m/s]
1	1	0.33	2000	100	$0.025/200 \cdot 2\pi$	272.2	137.1	127.8
2	∞	0.33	2000	300	$0.025/200 \cdot 2\pi$	471.4	237.5	221.3

Table 3: Characteristics of the multi-layered system.

3.7.1 Effect of Mass-Proportional and Stiffness-Proportional Damping

The influence of mass-proportional and stiffness-proportional damping on the finite element model simulations were investigated running different simulations with model "1" and load #2, in which their values were progressively changed. The value of mass-proportional and stiffness-proportional damping (from now on simply recalled as mass and stiffness damping) were chosen such that the value of the critical damping is known at the frequency of 200 Hz, following equation (3.1).

The values chosen for the simulations are listed in Table 4.

	Stiffness damping	No damping	Mass damping	Mass and stiffness damping
Mass damping α_d	0	0	125.66	83.78
Stiffness damping β_d	0.000159	0	0	0.000106
Damping ratio (at 200 Hz)	0.1	0	0.05	0.1

Table 4: Mass and stiffness damping values chosen for the simulations and total damping ratio at 200 Hz.

Then, the vertical components of displacement at the surface at a distance of 0.75 m from the point of excitation, the amplitude and the phase angle of the cross-power spectra between two signals at the surface 0.75 m and 0.80 m far from the excitation point, were obtained from the four simulations. The results were directly compared in the time and in the frequency domains.

Simulations without damping (Figure 3.9(b)) and with only mass damping (Figure 3.9(c)) show disturbed displacements in the time domain, with lots of unwanted and unreal vibrations. Similarly to this results, various authors like Zerwer [82], observed the presence of several extraneous

numerical (parasitic) modes in the time-space and in the frequency-wavenumber domain at the high frequencies, when no damping or only mass damping is used in combination with uniform or graded mesh. Simulations with both stiffness and mass damping (Figure 3.9(d)) and with only stiffness damping (Figure 3.9(a)) show smoother displacements. The use of stiffness damping removes the parasitic modes since it adds more damping at the high frequencies.

Looking at the linear spectra, when no damping and only mass damping is used (Figure 3.10(b) and Figure 3.10(c)), higher frequencies are excited (up to 1 kHz), while the energy decays around 250 Hz when stiffness damping is used (Figure 3.10(a)) and around 400 Hz when both stiffness and mass damping are used (Figure 3.10d).

The phase increases with a linear trend up to 500 Hz with no damping, only mass damping and both mass and stiffness damping (Figure 3.11(b), Figure 3.11(c) and Figure 3.11(d)), while has a linear trend only up to a frequency of 250 Hz in case only the stiffness damping is used (Figure 3.11(a)). This is due to the different values of damping chosen for the simulations. The effect of stiffness damping is more pronounced for high frequencies than the effect of the mass damping.

The simulations in the forthcoming chapters are carried out with mass damping set equal to zero, following the work of Zerwer [60] and of Jou-Yi Shih [92], in the attempt to avoid high damping at low frequencies and the presence of numerical parasitic modes.

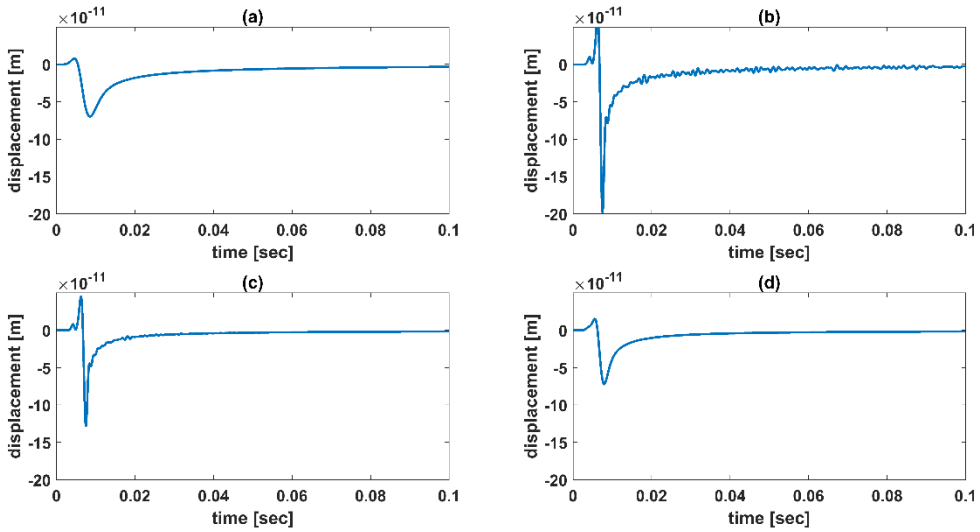

Figure 3.9: Vertical displacements at the surface 0.75 m from the source. Simulations carried out with stiffness damping (a), no damping (b), mass damping (c) and mass and stiffness damping (d).

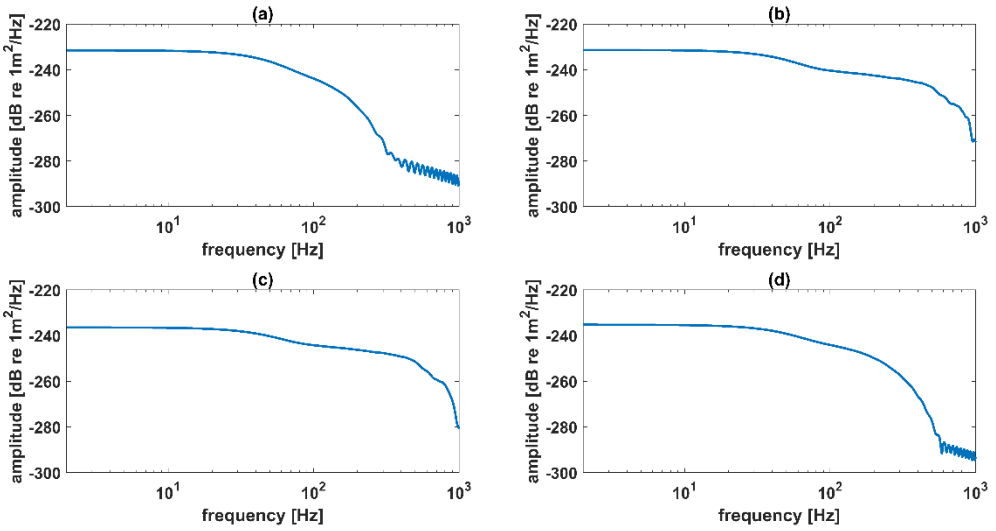

Figure 3.10. Amplitude of cross-power spectra between vertical signals at the surface 0.75 m and 0.80 m far from the source. Simulations carried out with stiffness damping (a), no damping (b), mass damping (c) and mass and stiffness damping (d).

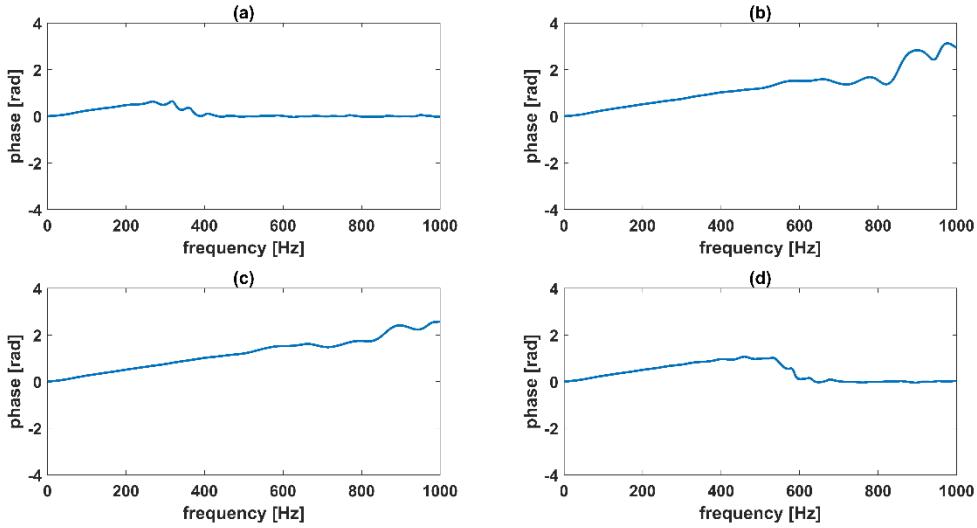

Figure 3.11: Phase of cross-power spectra between vertical signals at the surface 0.75 m and 0.80 m far from the source. Simulations carried out with stiffness damping (a), no damping (b), mass damping (c) and mass and stiffness damping (d).

3.8 Summary

This chapter presented the traditional frequency domain operations and transformations of seismic data. The cross-power spectrum method relies on the assumption of one type of wave or one mode of propagation dominating in the frequency range of interest. Hence, it is incapable of distinguishing different waves and modes of propagation. The frequency-wavenumber transformation presented

herein instead allows the separation of different modes and waves contributions in the seismic signal. This ability is limited by the resolution of the spectrum.

A two-dimensional finite element model of the ground was assembled through the Abaqus/CAE software, in the "vertical" plane, to study the wave propagation in half-spaces and multi-layered systems. Finite elements together with infinite elements were used for modelling the propagation of ground-borne seismic waves. Infinite elements were used with the aim of avoiding or at least minimizing spurious reflections from the boundaries of the model.

Two models were developed and exploited in this work: the first with was a semi-circle, the second was a semi-ellipse, both with infinite elements applied at their boundaries. In the first case the boundaries were normal with respect to the wavefront of body waves, in the second case the elliptical shape was a compromise and ensured the boundaries to be almost normal to both the body wave's and surface wave's wavefronts. Spatial and temporal discretizations assured the operational frequency range to be tailored to the purposes of this work. The mesh element size progressively increased in the downward vertical direction and the mass-proportional damping was set to zero.

The model was affected by permanent deformation in the vertical direction since the problem was unconstrained. The presence of energy for zero wavenumber was linked to finite element modelling: the model sank showing permanent deformation.

The model proved to be consistent with the analytical solutions for wave propagation in half-spaces and layered media. Hence, it proved to be a reliable tool for the simulation of seismic waves' propagation.

Chapter 4: Spectral Convolution Method and Wave Decomposition Method

This chapter introduces and explains two new methods for the signal processing of seismic data. The new methods aim at addressing some of the limitations of the existing ones and to extract more significant information from the seismic survey. Particularly, the new spectral convolution method aims at augmenting the resolution and the accuracy of the frequency-wavenumber (*f-k)* spectrum in both the frequency and wavenumber domains. It is based on the joint use of the vertical and of the horizontal components of displacement of a ground-borne R-wave. The new wave decomposition method aims at detecting, locating and assessing the depth of surface-breaking vertical cracks in layered media. It is based on the calculation of reflection and transmission coefficients of an R-wave.

The rationale belonging to both methods is introduced and explained in section 4.1 for the spectral convolution method and in section 4.2 for the wave decomposition method. Numerical simulations complement the analytical explanation and show the benefits of the new methods.

Section 4.3 introduces the problem of the inversion of seismic dispersion spectra and the proposed method for inversion. It will be used for the forthcoming experimental investigations. Finally, some conclusions are discussed in section 4.4.

The two methods are described in this chapter for sake of convenience, albeit they address diverse problems.

4.1 Spectral Convolution Method

A new signal processing method of seismic data coming from a multichannel survey is introduced in this section. The aim of the new spectral convolution method is to enhance the global resolution and accuracy of the spectral image in the *f-k* domain by jointly using the vertical and horizontal components of displacement of a seismic event. In the spectral convolution method, the mutual product between the vertical and the horizontal components is performed in the time domain and it is used as the time-space representation $p(x,t)$ of a multichannel survey, as follows:

$$p(x,t) = u(x,t) \cdot w(x,t) \tag{4.1}$$

where $u(x,t)$ and $w(x,t)$ are the vertical and horizontal space-time representations.

Then the new space-time representation $p(x,t)$ is transformed using equation (3.5) and (3.7), leading to a spectral image in the frequency-wavenumber domain.

This method exploits the feature of the vertical (the component of displacements traditionally used in shallow seismic applications) and of the horizontal components of motion of the surface wave, which are $\pi/2$ out-of-phase. This method assumes the R-wave energy to be the strongest energy component of a seismic event at the surface compared to other wave components or events, such as body waves, background noise or backscatter waves, when a vertical excitation is used (see section 2.2).

The product between the vertical and the horizontal signals in time domain can be seen as a convolution between spectra in the frequency domain. By multiplying the time histories, every wave component that is strong in both signals will become stronger in the convoluted spectrum; conversely, energy that is weak in the input signals will be weaker in the output spectrum.

A simplified mathematical approach is used here to explain the rationale belonging to this methodology. Under the assumption that the seismic event is only composed by the R-wave, its vertical components $u(x,t)$ and its horizontal components $w(x,t)$ of displacement can be expressed as wave packets, i.e. a summation of different travelling waves over a finite frequency bandwidth:

$$u(x,t) = \int_{i=1}^{N_f} A_i \cdot \sin(\omega_i t - k(\omega_i)x)\mathrm{d}\omega_i \tag{4.2}$$

$$w(x,t) = \int_{j=1}^{N_f} B_j \cdot \cos(\omega_j t - k(\omega_j)x)\mathrm{d}\omega_j \tag{4.3}$$

Where N_f is the frequency bandwidth, ω is the angular frequency, k is the wavenumber, which is associated with the phase velocity c_ω through the dispersive relationship:

$$k(\omega) = \frac{\omega}{c_\omega(\omega)} \tag{4.4}$$

The phase velocity can be frequency dependent or can be constant.

The analytical product between the vertical and the horizontal component of the displacement, called $p(x,t)$, is displayed in the following equation (4.5):

$$\begin{aligned} & p(x,t) = u(x,t) \cdot w(x,t) = \\ & = \int_{i=1}^{N_f} A_i \cdot \sin(\omega_i t - k(\omega_i)x)\mathrm{d}\omega_i \cdot \int_{j=1}^{N_f} B_j \cdot \cos(\omega_j t - k(\omega_j)x)\mathrm{d}\omega_j = \\ & = \int_{i=1}^{N_f} \int_{j=1}^{N_f} A_i \cdot B_j \cdot \begin{bmatrix} \sin\left((\omega_i + \omega_j)t - (k(\omega_i) + k(\omega_j))x\right) + \\ + \sin\left((\omega_i - \omega_j)t - (k(\omega_i) - k(\omega_j))x\right) \end{bmatrix} \mathrm{d}\omega_i \mathrm{d}\omega_j \end{aligned} \tag{4.5}$$

It consists of two members. In this case, the second member is equal to zero due to the destructive superposition of the different waves, since the sin function is odd. In fact, $\sin(-x) = -\sin(x)$. The first member is a wave with doubled frequency and wavenumber but with an unaffected dispersive relationship with respect to the original horizontal and vertical waves. In order to restore the original time and space variation, the matrix needs to be compressed by a factor of two in both frequency and wavenumber domains. The cross-product terms are negligible in the frequency-wavenumber domain, .i.e. once the double Fourier transform is performed in time and space, due to destructive superposition. The spectral convolution *f-k* spectrum, $P(k,\omega)$, obtained from $p(x,t)$ after applying equation (3.5) and equation (3.6), has a doubled resolution in the frequency and wavenumber domain with respect to the vertical or horizontal *f-k* spectra $U(k,\omega)$ and $W(k,\omega)$. Appendix E shows several analytical investigations that led to the development of the spectral convolution method and helps to understand the features of equation (4.5).

Remembering equation (4.5), the spectral convolution method artfully "lengthens" by a factor of two the survey line and the length of the signal, adding the information carried by the horizontal displacements, thus improving the resolution by the same factor. Let $u(t)$ and $w(t)$ be the time histories in the horizontal and vertical direction respectively, $U(\omega)$ and $W(\omega)$ be the linear spectra of $u(t)$ and $w(t)$. Recalling the width property of convolution, if $U(\omega)$ and $W(\omega)$ have length of L_1 and L_2 respectively, than the length of the convoluted signal is $L_1 + L_2$. If $L_1 = L_2$, the convoluted signal has double length but the same frequency content, hence the resolution is doubled. The extension of this property to the space axis causes the resolution to increase in both the frequency and the wavenumber domains. A gain in resolution was accompanied by a proportional reduction in the frequency bandwidth: the aliasing occurred for half the value obtained with equation (3.). This drawback can be easily overtaken by adopting a small temporal discretization. However, spatial aliasing is primarily governed by equation (2.34).

For a comparison with the outcome of equation (4.5), the analytical self-product of the vertical (or horizontal) component of the displacement, called $z(x,t)$, is displayed in the following equation (4.6):

$$\begin{aligned} & z(x,t) = u(x,t) \cdot u(x,t) = \\ & \int_{i=1}^{N_f} A_i \cdot \sin(\omega_i t - k(\omega_i)x)\mathrm{d}\omega_i \cdot \int_{j=1}^{N_f} A_j \cdot \sin(\omega_j t - k(\omega_j)x)\mathrm{d}\omega_j = \\ & = \int_{i=1}^{N_f} \int_{j=1}^{N_f} A_i \cdot A_j \cdot \begin{bmatrix} \cos\left((\omega_i + \omega_j)t - (k(\omega_i) + k(\omega_j))x + \pi\right) + \\ + \cos\left((\omega_i - \omega_j)t - (k(\omega_i) - k(\omega_j))x\right) \end{bmatrix} \mathrm{d}\omega_i \mathrm{d}\omega_j \end{aligned} \tag{4.6}$$

Again, this consists of two members. The first member has the same properties of the first member of equation (4.5). In this case, the second member is not equal to zero but it represents a wave with a different dispersive relationship than the original wave, destructively interacting with the first member of the equation. The second wave has the same frequency bandwidth of $u(x,t)$. Hence the self-product of the vertical component (or the horizontal), i.e. the product of two in-phase waves, produces instead a second wave that alters the original dispersive relationship (this is shown in Appendix E). For these reasons the product between the vertical and the horizontal components of motion, and not the self-product, is applied for the spectral convolution method in this thesis.

4.1.1 Introduction to Numerical Simulations

The benefits of the spectral convolution method are shown comparing the vertical, horizontal and spectral convolution dispersion curves in the *f-k* and phase velocity-frequency domains. Three cases of soil stratification, as depicted in Figure 4.1, were analysed and compared using the components of displacement coming from FEM simulations (chapter 3), obtained with model "2". The first case was the half-space case, the second case was a normally dispersive system, and the third case was a layered system with velocity inversion (i.e. shear velocity not increasing with depth) and a strong impedance contrast (e.g. loose sediments on bedrock). A sampling frequency of 20 kHz was used for the numerical simulations.

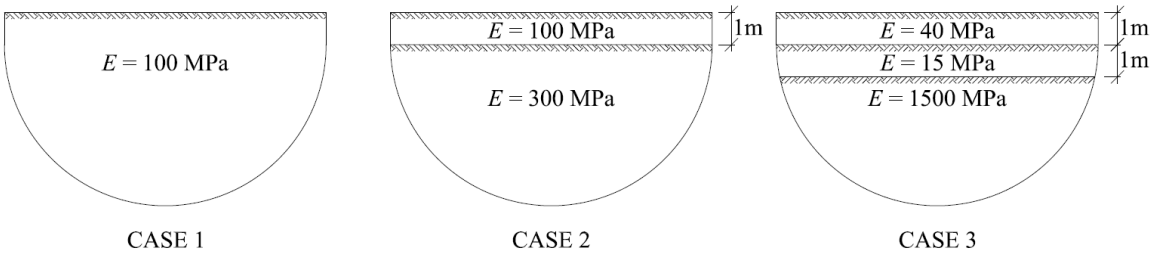

Figure 4.1: Analysed soil profiles.

4.1.2 Numerical Simulations on Half-Space

In this section, the spectral convolution method was applied on data coming from the numerical simulation on a half-space.

Figure 4.2(a), Figure 4.2(b) and Figure 4.2(c) depict respectively the vertical, horizontal and spectral convolution *f-k* spectrum of case 1 profile from a deployment of 198 surface receivers equally spaced 0.05 m, the source being 0.05 m far from the deployment (load #1). A stiffness-proportional damping of $0.025/(200 \cdot 2\pi)$ was used for the numerical simulations. The red areas indicate the propagation pattern of the Rayleigh wave. In the three cases, the slope of the black lines indicates the velocity of the direct R-wave in the half-space, while the slope of the green lines indicates the velocity of the direct compressional wave.

The vertical and horizontal spectra only differ for a bigger quantity of energy comprised between the R-wave and the P-wave velocity, observed in the horizontal spectra. The vertical spectrum shows the presence of energy for zero wavenumber since the problem of FEM is unconstrained in the vertical direction. The gain in resolution achieved with the spectral convolution approach can be easily perceived looking at Figure 4.2(c): the energy peaks are concentrated in a narrower area in the spectral convolution spectrum. The spectral convolution spectrum does not show permanent deformation in the vertical direction because of the product between horizontal and vertical displacements.

The amplitude of the ellipticity, displayed in Figure 4.3, is consistent in the range of excited frequencies (0-100 Hz), showing no dependency on frequency as it was expected for the half-space case. The value of the ellipticity in the half-space case is only dependent on the Poisson's ratio: in this case the value is consistent to that of [39] and it is highlighted by a red line in Figure 4.3. The phase of the ellipticity curve shows that the vertical displacements are $\pi/2$ out-of-phase with the horizontal displacements in the range of excited frequencies (0-100 Hz).

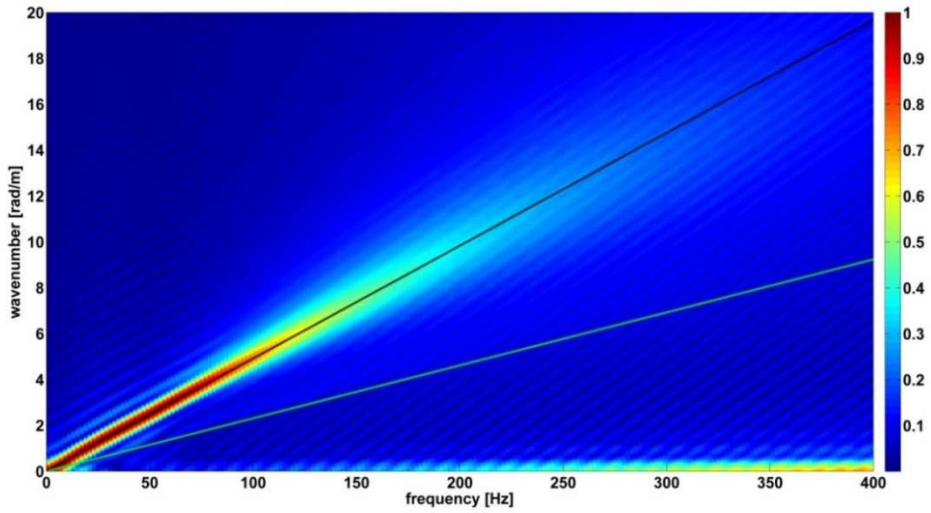

(a)

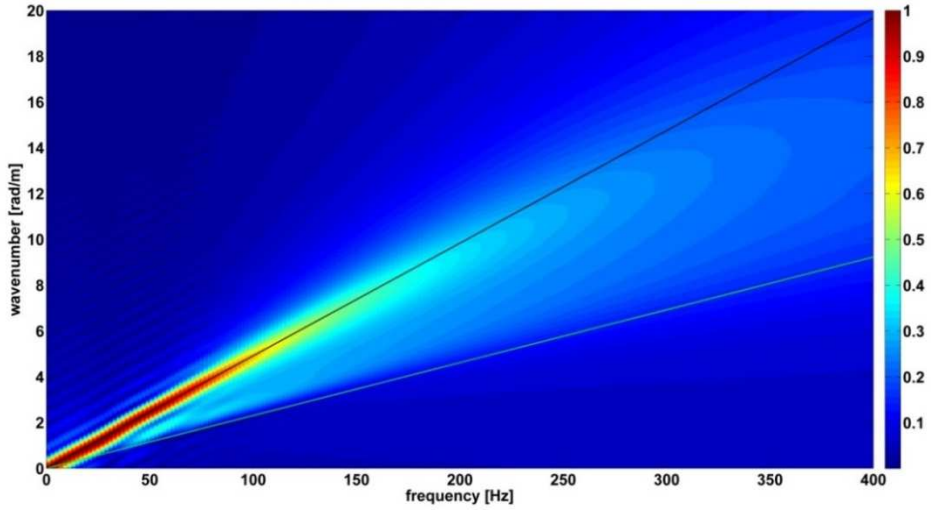

(b)

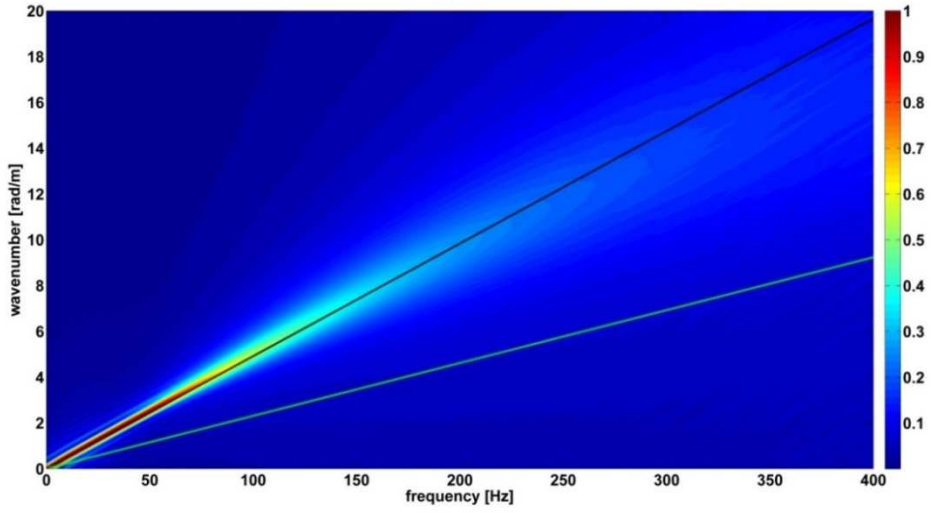

(c)

Figure 4.2: *F-k* spectrum with vertical (a), horizontal (b) and spectral convolution (c) traces for case 1 profile of Figure 4.1 ($L_s = 9.90\text{m}, N = 198$). The slope of the black lines indicates the velocity of the direct R-wave in the half-space, while the slope of the green lines indicates the velocity of the direct P-wave.

Figure 4.4 displays the amplitude of the vertical, horizontal and spectral convolution displacements 8.20 m far from the source in the time domain: the shift of $\pi/2$ between the horizontal and vertical displacements descending from the retrograde elliptical motion is evident, since horizontal displacements peak when the vertical displacements are zero. The vertical trace shows a certain amount of permanent deformation, due to the unconstrained problem of FEM analysis. Moreover, the spectral convolution signal contains reduced compressional and shear wave energy with respect to R-wave energy. In fact, the amplitude of the signal up to the major peak, which is associated with the R-wave, can be considered due to body waves and it is lower in the spectral convolution signal compared to the vertical and horizontal signals. The arrivals of the P-wave, S-wave and R-wave are highlighted by straight lines in Figure 4.4. The spectral convolution trace, being a product in time between the horizontal and vertical components, does not suffer from the unconstrained problem, i.e. there is no permanent deformation.

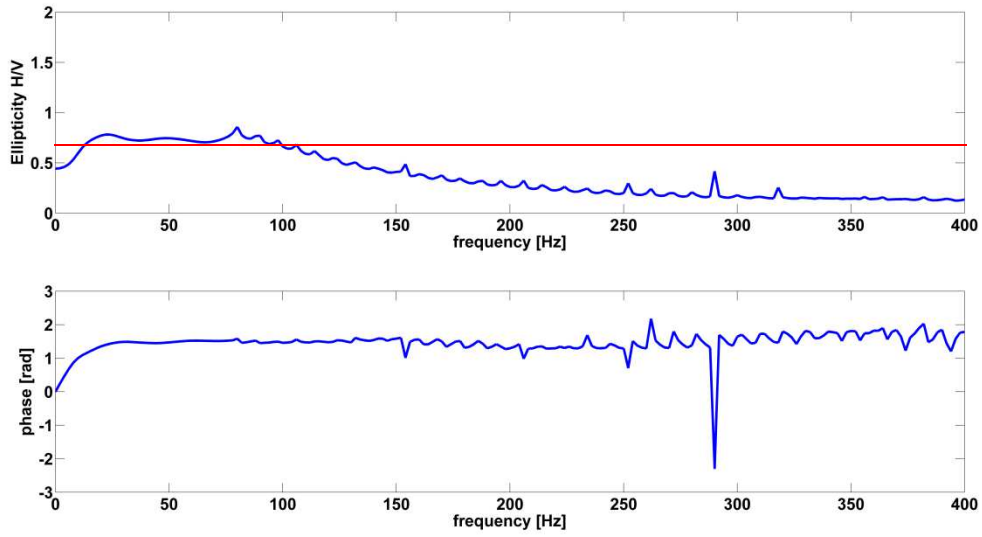

Figure 4.3: Amplitude and phase of the ellipticity curve for case 1 profile. The ellipticity is consistent in the range of excited frequencies (0-100 Hz), showing no dependency on frequency. The red line indicates the value of the ellipticity for a perfect half-space with Poisson's ratio of 0.33.

By looking at the amplitude of the *f-k* spectra at the frequency of 50 Hz (Figure 4.5), which can be seen as a slice of the *f-k* spectrum at the chosen frequency, it can be observed that the energy peak of the spectral convolution spectrum is sharper and narrower compared to that of the vertical spectrum. It can be noticed that the distance between two neighbouring minima, as explained in equation (3.), is halved, i.e. the wavenumber resolution is doubled.

The spectral convolution method improved the accuracy and the resolution of the spectral image in the *f-k* domain in the case of a homogeneous half-space.

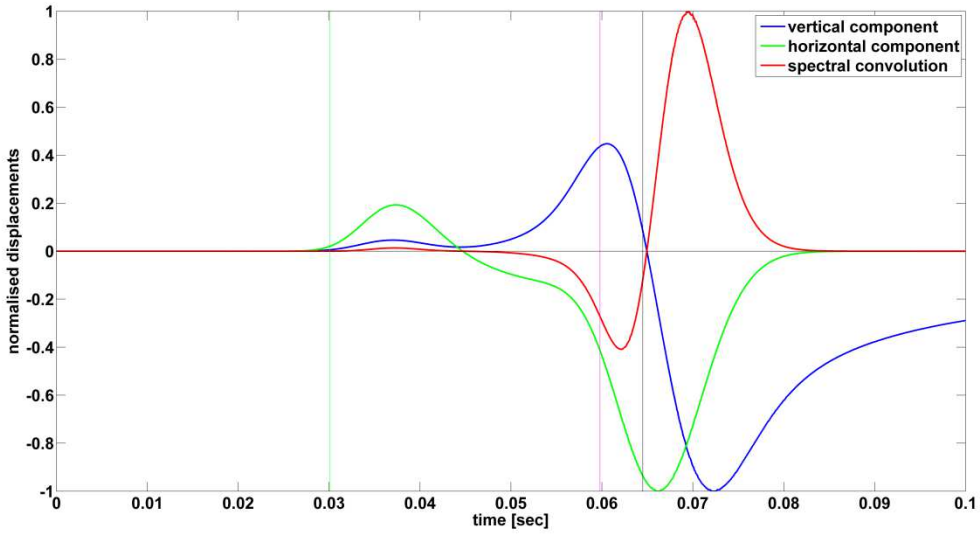

Figure 4.4: Displacements at 8.20 m from the source, case 1 profile.

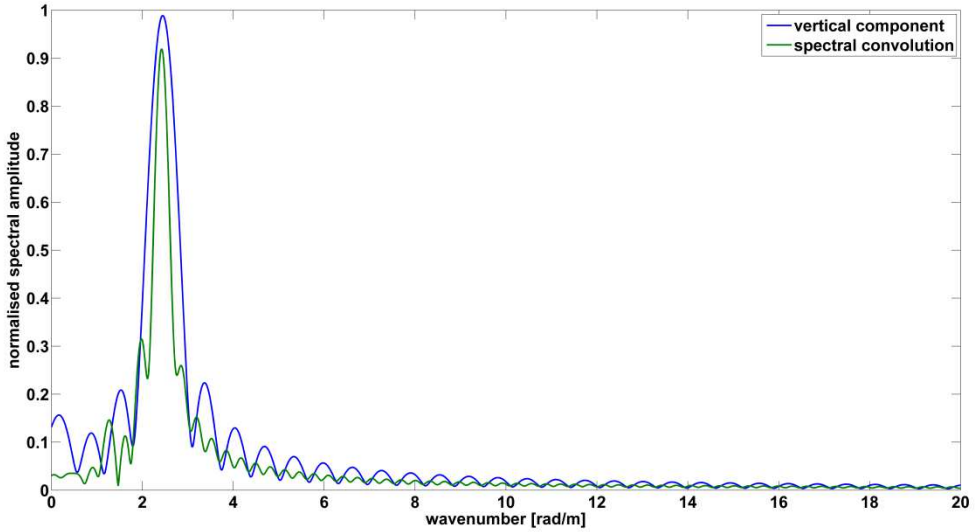

Figure 4.5: Amplitude of *f-k* spectra for case 1 profile ($L_s = 9.90\text{m}, N = 198$), at frequency of 50 Hz.

4.1.3 Numerical Simulations on Normally Dispersive Medium

In this section, the spectral convolution method was applied on data coming from the numerical simulation on a normally dispersive medium, i.e. a layered medium in which the shear velocity increases with depth.

Figure 4.6(a), Figure 4.6(b) and Figure 4.6(c) depict respectively the vertical, horizontal and spectral convolution *f-k* spectrum of case 2 profile from a deployment of 50 surface receivers equally spaced

0.05 m, the source being 5.00 m far from the deployment (load #2). A stiffness-proportional damping of $0.025/(200 \cdot 2\pi)$ was used for both analytical and numerical simulations. The black dots indicate the extracted energy maxima of the *f-k* spectrum; the red superimposed lines indicate the eigenvalues obtained from the analytical solution solving equation (2.30).

The fundamental mode (mode0) is the most energetic and predominant mode due to case 2 profile being normally dispersive. High frequency components of the fundamental mode travel with the velocity of the upmost layer, low frequency components with the velocity of the half space: the shift of the velocity starts at the frequency of approximately 100 Hz as can be seen by looking at the eigenvalues of Figure 4.6. Nonetheless, vertical and horizontal *f-k* spectra fail in the identification of the fundamental mode, especially at the low frequencies, since they describe a mode with consistent velocity or with a slight change. The resolution increases as a factor of two in both the frequency and wavenumber domain in the spectral convolution spectrum: it can be easily observed by comparing the images of Figure 4.6. Some outliers are present in Figure 4.6(c): they are probably caused by numerical errors or parasitic modes introduced with the FEM model.

Figure 4.7 shows the dispersion curves in the phase velocity-frequency domain extracted from the peaks of energy of vertical, horizontal and spectral convolution spectra. While the vertical and horizontal spectra fail in revealing the fundamental mode, especially regarding the low frequencies, the dispersion curve from the spectral convolution spectrum adheres to the fundamental mode with better accuracy.

The amplitude of the ellipticity curve, depicted in Figure 4.8, shows a resonant peak at the frequency of approximately 35 Hz: for normally dispersive profiles, the peak corresponds to the "shear wave resonance" of the top layer. Following (3.4), the layer's thickness is one quarter of the wavelength of the shear wave within the layer. The ellipticity is then consistent in the remaining range of excited frequencies, showing no relevant local minima or resonant peaks: this is consistent with the spectral convolution spectrum of Figure 4.6(c), which shows neither mode jumps nor osculation points (see definition in section 2.8). The phase of the ellipticity curve shows that the vertical displacements are $\pi/2$ out-of-phase with the horizontal displacements in the range of excited frequencies (0-400 Hz).

Figure 4.9 depicts the vertical, horizontal and spectral convolution displacements obtained 6.25 m far from the source, from the simulation of case 2 profile. It is evident again the shift of $\pi/2$ between the horizontal and vertical R-wave components of the signal, since horizontal displacements peak when the vertical displacements are zero and viceversa. The relative amplitude of body waves is reduced when the spectral convolution approach is adopted. In fact, the amplitude of the signal up to the major peak, which is associated with the R-wave, can be considered due to body waves. It is lower in the spectral convolution signal compared to the vertical and horizontal signals.

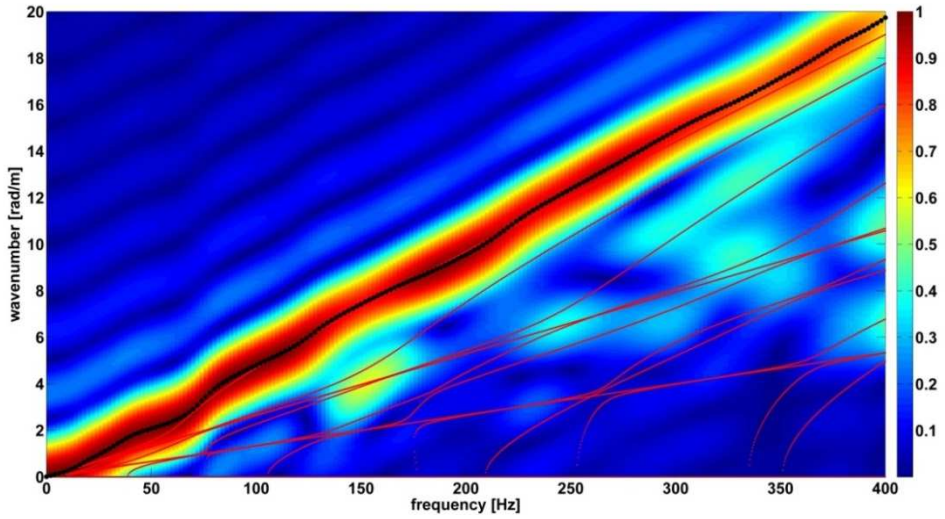

(a)

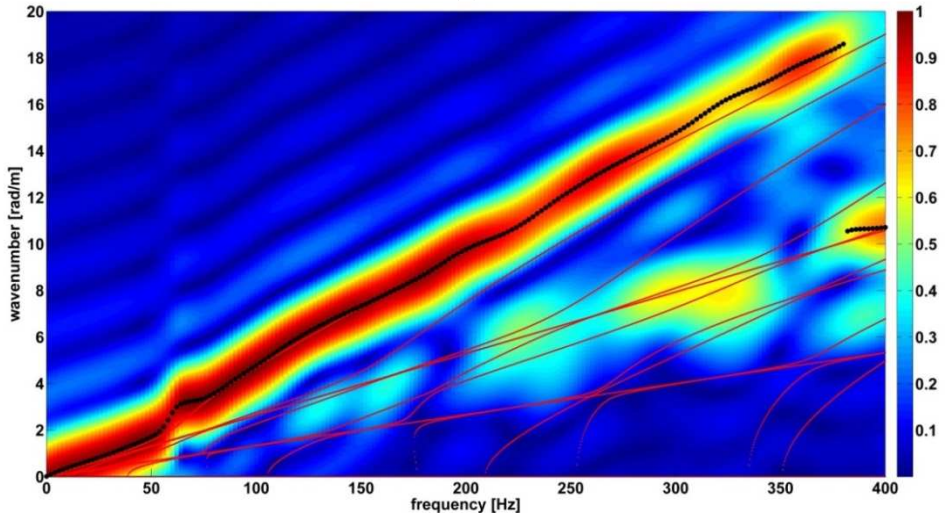

(b)

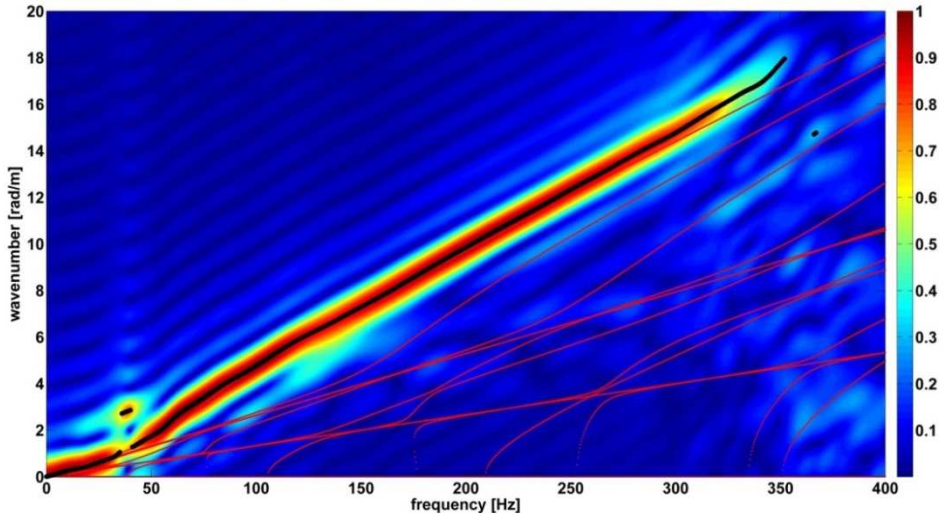

(c)

Figure 4.6: *F-k* spectrum with vertical (a), horizontal (b) and spectral convolution (c) traces for case 2 profile of Figure 4.1 ($L_s = 2.50\text{m}$, $N = 50$). The black dots indicate the extracted energy maxima of the *f-k* spectrum; the red superimposed lines indicate the eigenvalues obtained from the analytical solution solving (2.30).

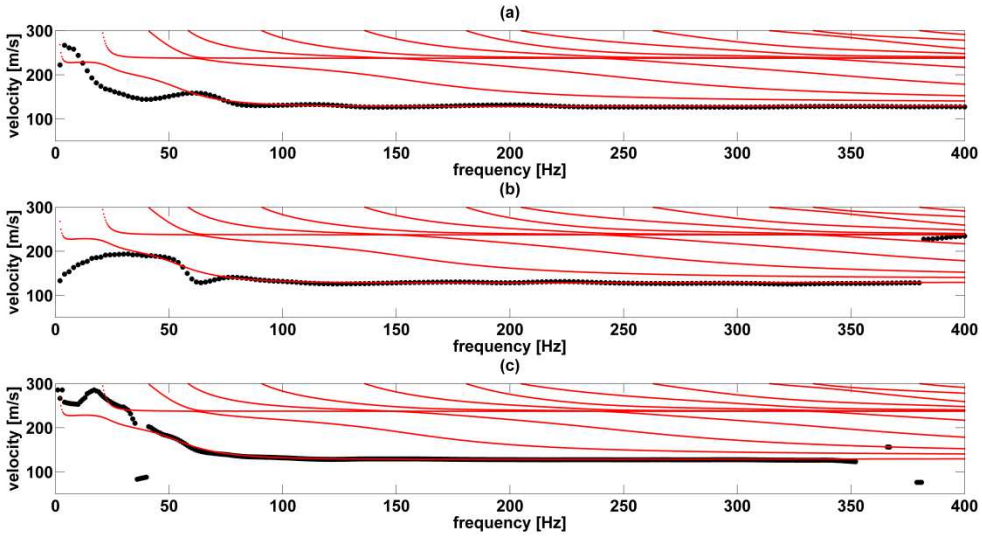

Figure 4.7: Dispersion curves for case 2 profile: from vertical (a), horizontal (b) and spectral convolution (c) spectra in the *f-k* domain. The black dots indicate the extracted peaks of energy of the *f-k* spectrum; the red superimposed lines indicate the eigenvalues obtained from the analytical solution solving (2.30). Dispersion curve (c) adheres to the fundamental mode with better accuracy.

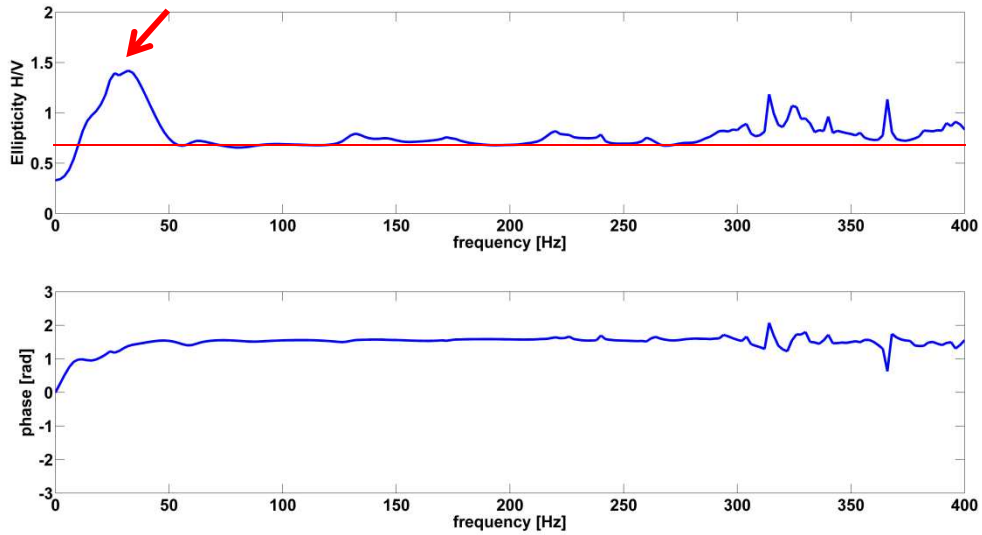

Figure 4.8: Amplitude and phase of the ellipticity curve for case 2 profile. It is possible to notice a resonant peak at the frequency of approximately 35 Hz, highlighted by a red arrow, which corresponds to the "shear wave resonance" of the top layer. The amplitude of the ellipticity is consistent and flat in the remaining range of excited frequencies. The red line indicates the value of the ellipticity for a perfect half-space with Poisson's ratio of 0.33.

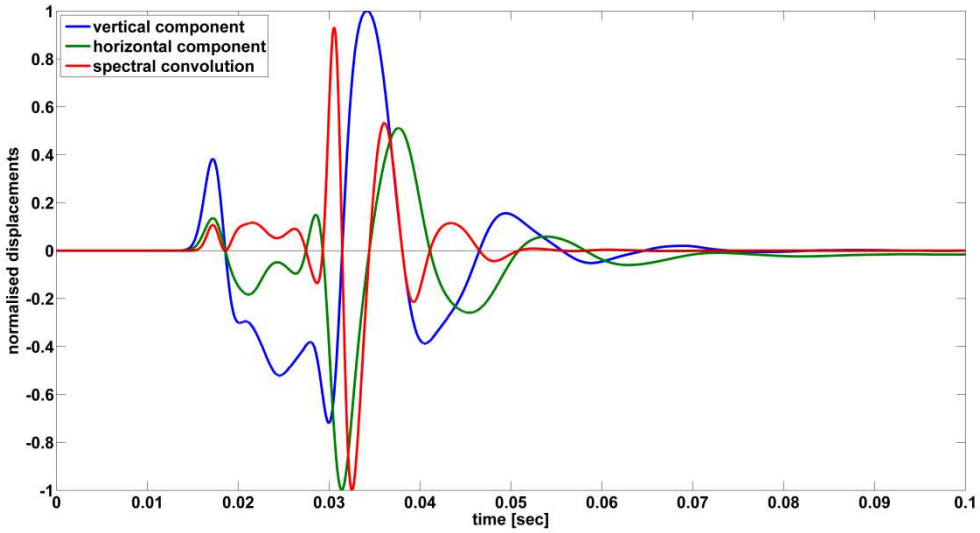

Figure 4.9: Displacements at 6.25 m from the source, case 2 profile.

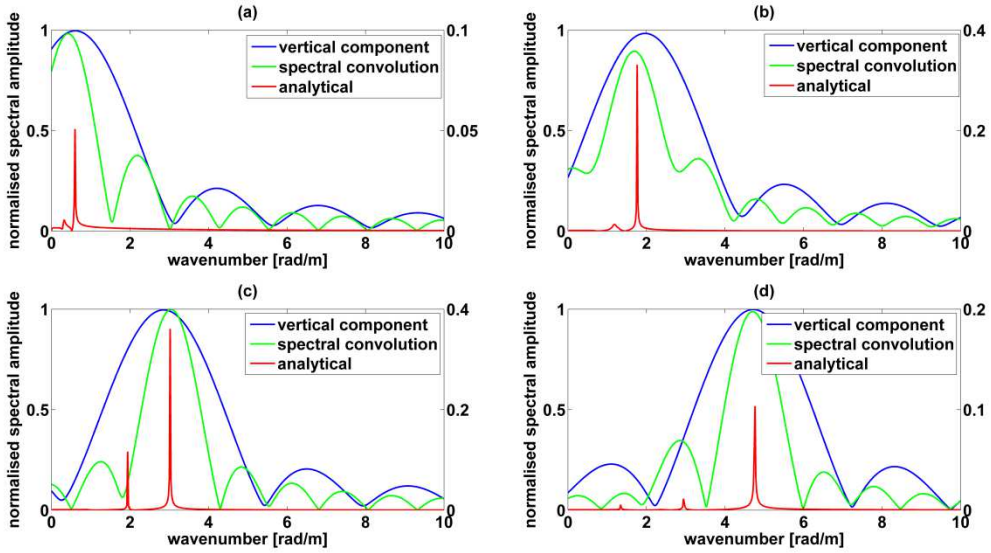

Figure 4.10: Amplitude of *f-k* spectra for case 2 profile ($L_s = 2.50\text{m}$, $N = 50$), at frequencies of 20 Hz (a), 50 Hz (b), 70 Hz (c) and 100 Hz (d).

The amplitudes of the *f-k* spectra of Figure 4.10 at the frequencies of 20 Hz, 50 Hz, 70 Hz and 100 Hz, which can be seen as slices of the *f-k* spectrum at a certain frequency, are compared with the analytical solution for the vertical component, with resolution Δf of 1 Hz and Δk of 0.025 rad/m. With the spectral convolution method the half-width between the neighbouring minima Δk is halved with respect to the spectrum obtained with vertical traces. In addition, the spectral convolution method leads to an improvement in the accuracy: in fact, the spectrum obtained with the spectral

convolution method and with the analytical solution peak at approximately the same wavenumber, while the position of the peaks of the spectrum obtained with vertical traces seems inaccurate.

The spectral convolution method improved the accuracy and the resolution of the spectral image in the *f-k* domain in the case of a normally dispersive layered medium.

4.1.4 Numerical Simulations on Medium with Velocity Inversion

In this section, the spectral convolution method was applied on data coming from the numerical simulation on a not normally dispersive medium, i.e. a layered medium in which the shear velocity does not always increase with depth. Particularly, a layered medium with a soft layer sandwiched between two stiffer layer and with strong impedance contrast was chosen for the forthcoming simulations.

Figure 4.11(a), Figure 4.11(b) and Figure 4.11(c) depict respectively the vertical, horizontal and spectral convolution *f-k* spectrum of case 3 profile from a deployment of 40 surface receivers equally spaced 0.25 m, the source being 0.05 m far from the deployment (load #2). A stiffness proportional damping of $0.005/(200 \cdot 2\pi)$ was used for both analytical and numerical simulations. The black dots indicate the extracted energy maxima of the *f-k* spectrum; the red superimposed lines indicate the eigenvalues obtained from the analytical solution solving equation (2.30).

The *f-k* spectrum obtained with vertical displacements (Figure 4.11(a)) only shows evidence of the first mode of propagation. The second and third modes of propagation are merged into the same energy peaks, leading to a misinterpretation of the seismic survey. The superposition of the eigenvalues for the aforementioned layered system proves that despite the first mode being consistent, the energy peaks above the frequency of 50 Hz do not correspond to the actual modes of propagation. The resolution of the spectra is not high enough to separate different modal contributions, which are camouflaged under the same fictitious mode of propagation. The *f-k* spectrum obtained with horizontal displacements (Figure 4.11(b)) only shows evidence of the first and the third mode of propagation. There is no evidence of the second mode of propagation, leading again to a misinterpretation of the seismic survey. The spectral convolution *f-k* spectrum (Figure 4.11(c)) clearly shows the first three modes of propagation, which are well distinct and defined. A superposition of the eigenvalues for the aforementioned layered system proves that the energy peaks correspond to the first three modes of propagation. Osculation frequencies at around 40 Hz, 75 Hz and 120 Hz are clearly detectable by observing the spectrum in the *f-k* domain (see definition in section 2.8). The number of osculation points expected to see is dependent on the number of mode switches and hence on the velocity profile.

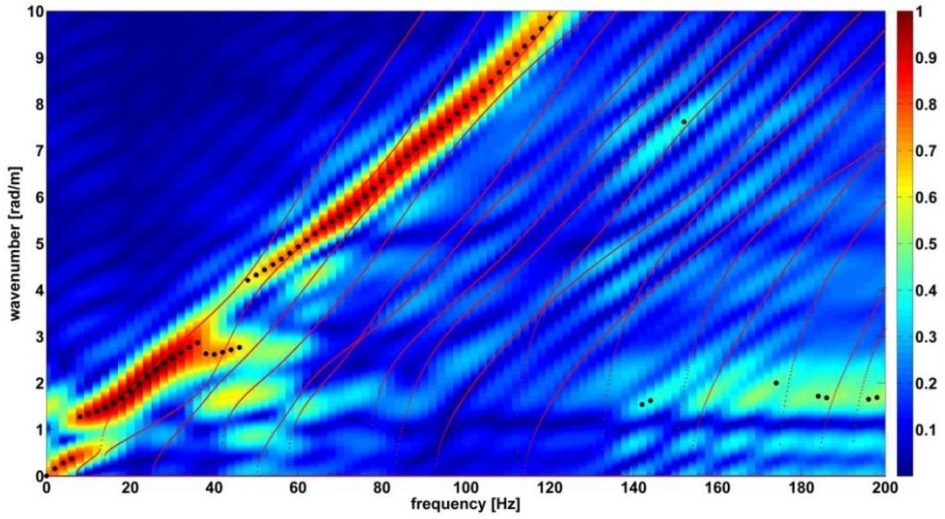

(a)

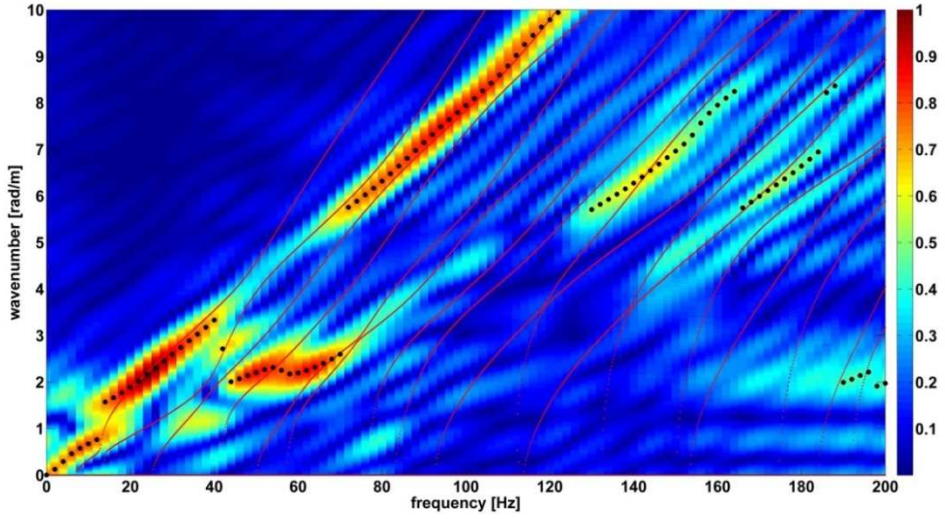

(b)

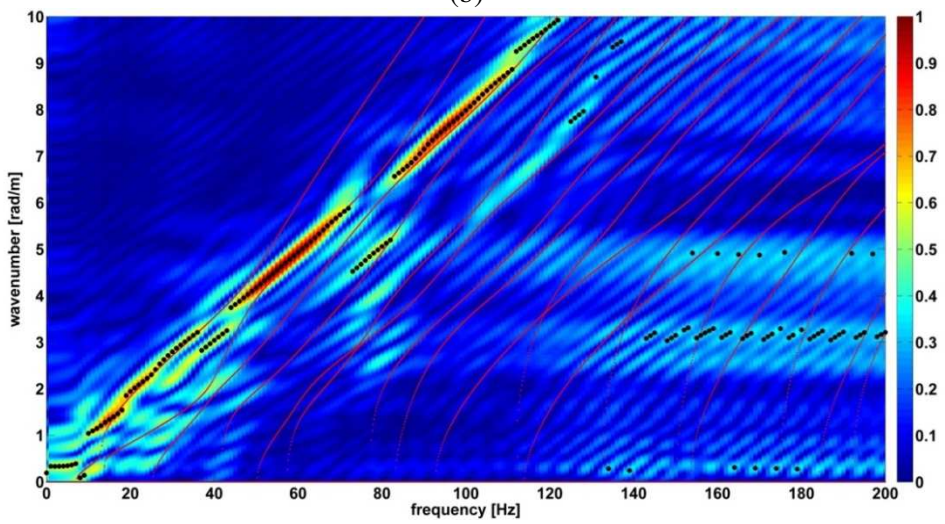

(c)

Figure 4.11: *F-k* spectrum with vertical (a), horizontal (b) and spectral convolution (c) traces for case 3 profile of Figure 4.1 ($L_s = 10.00\text{m}, N = 40$). The black dots indicate the extracted energy maxima of the *f-k* spectrum; the red superimposed lines indicate the eigenvalues obtained from the analytical solution solving (2.30).

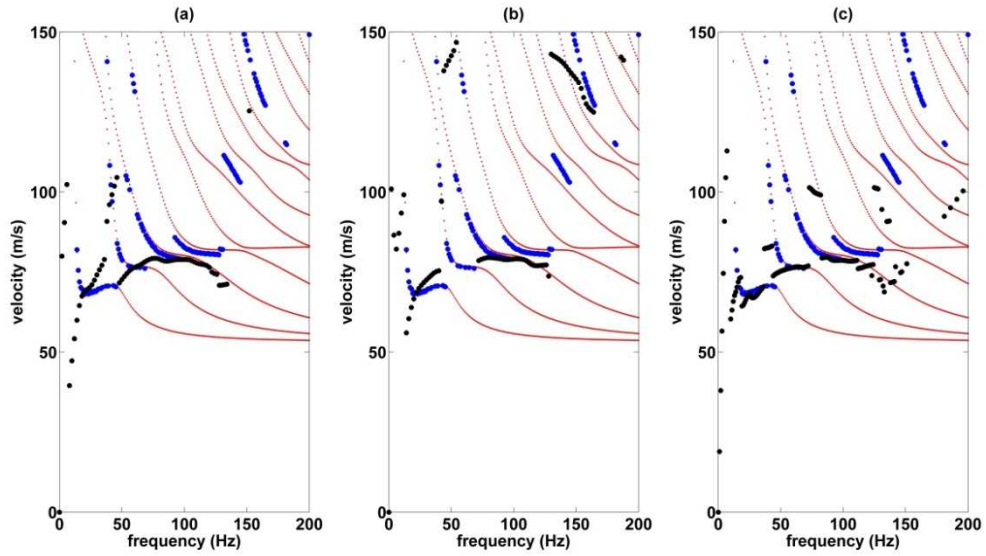

Figure 4.12: Dispersion curves for case 3 profile: from vertical (a), horizontal (b) and spectral convolution (c) spectra in the *f-k* domain. The black dots indicate the extracted peaks of energy of the *f-k* spectrum. The red superimposed lines indicate the eigenvalues obtained from the analytical solution solving (2.30). The blue dots indicate the peaks of energy obtained with the analytical solution with a resolution Δf of 1 Hz and Δk of 0.025 rad/m.

Figure 4.12 shows the dispersion curves in the phase velocity-frequency domain extracted from the peaks of energy of vertical, horizontal and spectral convolution spectra. The black dots indicate the extracted peaks of energy of the *f-k* spectrum. The red superimposed lines indicate the eigenvalues obtained from the analytical solution solving equation (2.30). The blue dots indicate the peaks of energy obtained with the analytical solution for the vertical component, with a resolution Δf of 1 Hz and Δk of 0.025 rad/m. The analytical solution shows a specific trend in which moving from the low to the high frequency, the energy splits to higher and higher modes. The dispersion curve from vertical traces (Figure 4.12(a)) shows evidence of the first mode of propagation but it is not possible to separate the contribution of the second and third mode, which seem to be reunited under the same fictitious mode. Moreover, the phase velocity of the first mode is overestimated. The dispersion curve from horizontal traces (Figure 4.12(b)) again only shows evidence of the first and of the third mode of propagation. There is no evidence of the second mode of propagation and the phase velocity of the first mode is overestimated. The dispersion curve from spectral convolution traces (Figure 4.12(c)) shows evidence of the first three modes of propagation, which are well separated and defined. It is possible to pick out the osculation frequencies, at which the velocity of two modes is close and the energy shifts from one mode to another, at the frequencies of approximately 40 Hz, 72 Hz and 120 Hz. The phase velocity of the first three modes of propagation coincides with that of the analytical solution.

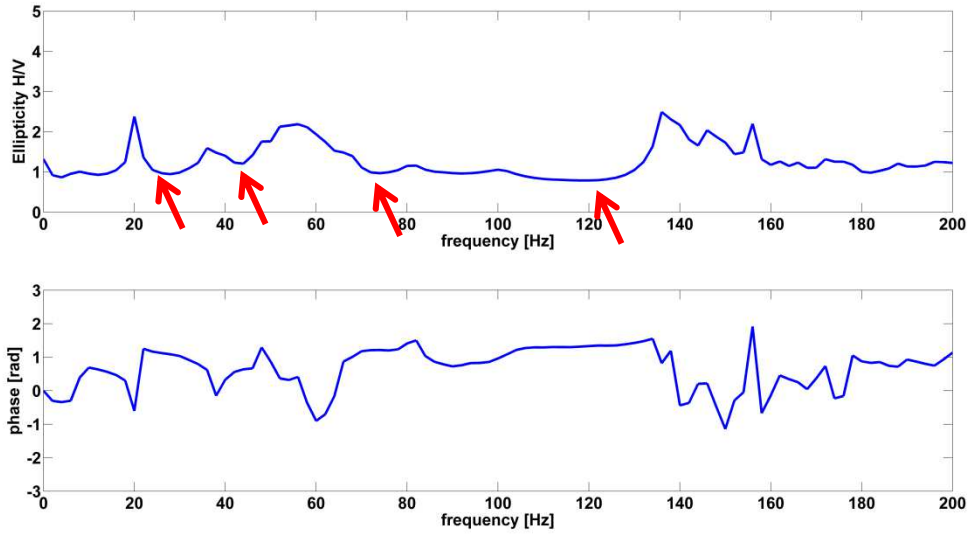

Figure 4.13: Amplitude and phase of the ellipticity curve for case 3 profile. It is possible to notice several resonant peaks and several local minima at the frequencies of approximately 27 Hz, 43 Hz, 73 Hz and 120 Hz. Local minima are highlighted by red arrows. The first biggest peak corresponds to the "shear wave resonance of the top layer".

The amplitude of the ellipticity curve depicted in Figure 4.13 has several local minima, at the frequencies of approximately 27 Hz, 43 Hz, 73 Hz and 120 Hz. These minima in the R-wave ellipticity occur at the osculation frequencies, where the velocity of two modes is close and the energy shifts from one mode to another. The minima in the ellipticity are consistent with the osculation points observed in the spectral convolution *f-k* spectrum, which displays a specific trend in which moving from the low to the high frequencies, the energy splits to higher and higher modes ("mode splitting", [22]). The ellipticity shows several resonant peaks. The first peak shows up at the frequency of approximately 20 Hz. Its high value confirms the presence of a strong shallow impedance contrast between the soil and the stiffer deep layer. The first resonant peak is sharper than the other successive peaks and probably corresponds to the "shear wave resonance" of the top layer. In fact, following equation (3.4) and assuming a shear velocity of 87 m/s the thickness of the top layer is 1.08 m. The phase of the ellipticity is not consistent throughout the range of excited frequencies. Several phase jumps are observable: they seem to occur at the frequencies at which resonances in the ellipticity curve occur, and in any case very close to the frequencies at which the osculation points occur.

The spectral convolution method improved the accuracy and the resolution of the spectral image in the *f-k* domain in the case of a layered medium with velocity inversion.

4.1.5 Summary of the Spectral Convolution Method

The new spectral convolution method was introduced in this chapter. It was based on the simultaneous exploitation of the vertical and the horizontal components of a seismic event and it showed to improve the resolution and the overall accuracy of the spectral image in the frequency-wavenumber (*f-k*) domain. The multiplication between the vertical and the horizontal component created a new wave that preserved the original dispersive relationship, doubling the wavenumber and the frequency. This result was obtained exploiting the feature of the vertical component of motion, being $\pi/2$ out-of-phase with the horizontal component of motion. The cross-product terms were negligible in the frequency-wavenumber domain, i.e. once the double Fourier transform is performed in time and space, due to destructive superposition (as shown in Appendix F). Conceptual analysis and numerical investigation proved the benefits of the spectral convolution method.

The product between vertical and horizontal signals in time domain can be seen as a convolution between spectra in the frequency domain. By multiplying the time histories, every wave component that is strong in both signals will become stronger in the convoluted spectrum; conversely energy that is weak in the input signals will be weaker in the output spectrum. Thus, adopting the product between vertical and horizontal displacements has a dual benefit: it lowers the content of the noise and unwanted waves and it enhances the R-wave content.

The numerical simulation displayed in this chapter proved that the energy maxima of the *f-k* spectrum were sharper (i.e. the bandwidth of each peak is smaller) when the spectral convolution method was used, helping the separation of different normal Rayleigh modes and the identification of osculation points, where the energy shifts between two modes. The spectral convolution method was beneficial especially in layered media where the stiffness was not regular, i.e. when higher order modes played a relevant role in the wave propagation and the fundamental one was not anymore the mode carrying more energy (see section 4.1.4). The spectral convolution method can be seen as a filter that enhances the R-wave energy of a signal coming from a seismic survey, lowering the other unwanted components and enhancing the overall accuracy of the survey.

Based on the outcome of the numerical simulations it was also found that the spectral convolution method improved the accuracy of the dispersion curves at the lower frequencies, since the new multichannel record was equivalent to a record with doubled length in space (see section 4.1.3 and section 4.1.4). The spectral convolution method also addressed the disadvantage of long deployments of sensors, which are likely to consider lateral inhomogeneity and variations from the main assumption of horizontality (see section 1.4.2). In fact, in order to keep the same resolution in the *f-k* domain by employing both the horizontal and vertical component of the seismic event, the length of the deployment is halved. This has the effect of halving the probability of lateral heterogeneities

to occur. Hence, it is advantageous in such cases when the area to survey is difficult to access, small, or whenever a long deployment of sensors is impossible or unwanted.

A gain in resolution was accompanied by a proportional reduction in the maximum detectable frequency: the aliasing occurred for half the value obtained with equation (3.). This drawback can be easily overtaken by adopting a small temporal discretization. However, spatial aliasing is primarily governed by equation (2.34).

The spectral convolution method proved to be effective for short transient pulse load, e.g. the loads utilized in the numerical simulations and shown in section 3.7, but the effectiveness was not proven for other types of signal, e.g. white noise.

For all the aforementioned reasons, the spectral convolution method was a valid multimode separation technique, able to augment the accuracy of the dispersion measurement by doubling the resolution of the spectral image with respect to the classical single-component testing.

4.2 Wave Decomposition Method

Here a new technique for the measurement of the amplitudes of the direct and reflected surface wave from a vertical discontinuity in asphalt layers is proposed. The aim of the wave decomposition method is the assessment of location and depth of vertical discontinuities, by means of the amplitude and phase of positive and negative going R-wave components propagating in the top layers of a complex system, e.g. a road pavement system. Particularly, the resonant peak frequencies of the reflection coefficient and the cut-off frequencies of the transmission coefficient are exploited to get the information about the depth of a vertical discontinuity. The phase of the reflection coefficient is used instead to get the information about the location of the crack (refer to section 2.7). The decomposition of the wave is provided by filtering the outputs of an array of sensors: a similar technique is currently applied to waveguided systems as beams and pipes, using two receivers [94, 95].

This method relies on the main assumption that the entire signal is composed only of one type of wave. This is certainly true for waveguides, like beams or rods. The challenge in applying the wave decomposition method in tarmac layers is that of the presence of multiple types of wave and mode. In addition, problems caused by intrinsic attenuation, geometrical spreading and vertical layering (dispersion) may occur. The key points of this new method are the use of a number of measurements much bigger than the number of unknown and the application of a wave method in a heterogeneous dispersive material. The latter needs the dispersive relationship to be an *a-priori* information for the entire range of frequency. Hence, the estimate is accomplished in the frequency domain exploiting

the wavenumber solutions coming from one of the dispersion methods (spectral, frequency-wavenumber and/or spectral convolution methods) previously discussed.

4.2.1 Methodology

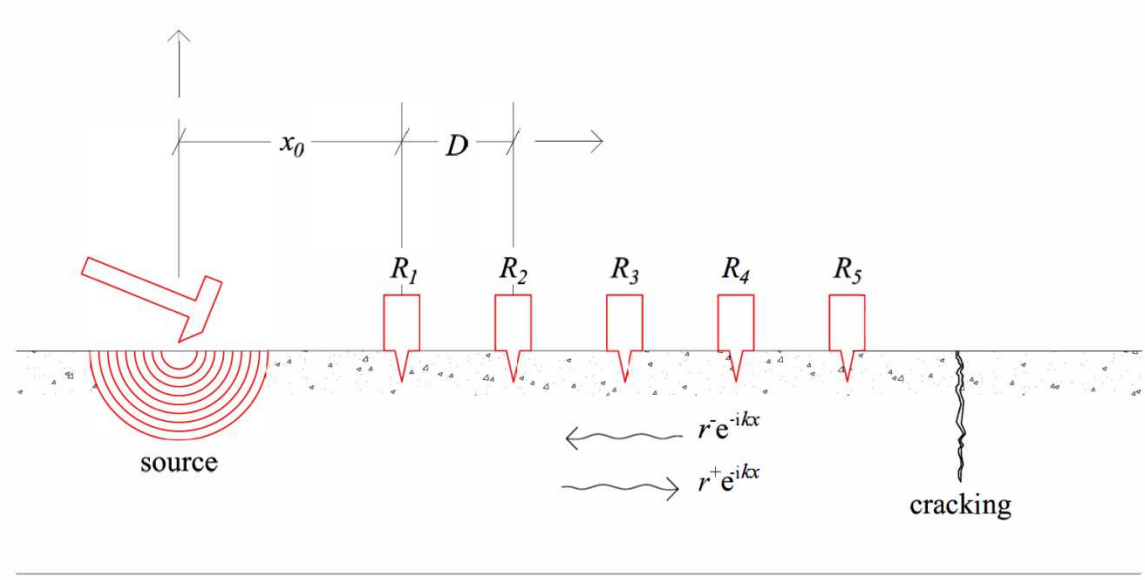

Figure 4.14: One-dimensional waves in the top layer of a road pavement system in the presence of a discontinuity and wave decomposition experimental set-up.

Looking at Figure 4.14, the wave decomposition test comprises a set of two or more receivers, disposed on the road surface with an equal spacing along a survey line, and a source of seismic energy (the set-up configuration does not differ at all from that of a typical MASW survey, (section 1.4.2)). According to Figure 4.14, in the case of a two-receiver set-up, the amplitude of the signal at two different locations (R_1) and (R_2) can be written, for each frequency, as:

$$\begin{cases} U(R_1) = r^+ e^{+ikx_0} + r^- e^{-ikx_0} \\ U(R_2) = r^+ e^{+ik(x_0+D)} + r^- e^{-ik(x_0+D)} \end{cases} \tag{4.7}$$

where the time and frequency dependence is omitted for convenience, k is the wavenumber, x_0 is the distance from a reference point (in this case the distance from the source), D is the receiver spacing, $U(x)$ is the space-frequency representation of the wavefield at a fixed frequency and r^+ and r^- are the amplitudes of the positive and negative going waves, respectively.

Hence:

$$\begin{Bmatrix} U(R_1) \\ U(R_2) \end{Bmatrix} = \begin{bmatrix} e^{+ikx_0} & e^{-ikx_0} \\ e^{+ik(x_0+D)} & e^{-ik(x_0+D)} \end{bmatrix} \begin{Bmatrix} r^+ \\ r^- \end{Bmatrix} \tag{4.8}$$

Then, by inverting the matrix, it is possible to find the values of r^+ and r^- for each value of frequency and for each associated value of wavenumber.

A very common practical problem encountered in almost every experimental measurement is that of measurement error. Experimental measurements are naturally affected by observation error. To tackle this problem linear systems are usually solved with a greater number of measurements than the number of unknowns. In this thesis, the wave decomposition method uses a greater number of receivers than the number of unknowns. Moreover, more than two sensors are needed to obtain the dispersive relationship for the entire range of frequency of the survey. Hence, the system of equations is overdetermined and generally does not have an exact solution. In the case of *N* receivers, the system (3) becomes:

$$\begin{Bmatrix} U(R_1) \\ U(R_2) \\ U(R_3) \\ \cdots \\ U(R_N) \end{Bmatrix} = \begin{bmatrix} e^{+ikx_0} & e^{-ikx_0} \\ e^{+ik(x_0+D)} & e^{-ik(x_0+D)} \\ \cdots & \cdots \\ e^{+ik(x_0+ND)} & e^{-ik(x_0+ND)} \end{bmatrix} \begin{Bmatrix} r^+ \\ r^- \end{Bmatrix} \tag{4.9}$$

The method of ordinary least square can be used to find an approximate solution that minimizes the error of the system of equations, i.e. the best possible solution [96]. For the system:

$$\mathbf{A_w x^*} = \mathbf{r} \tag{4.10}$$

where $\mathbf{x}^*$ is the vector of the approximate solution, $\mathbf{r}$ is the amplitude vector, $\mathbf{A_w}$ the matrix of constant terms, the solution of the least square formulae can be written as follows:

$$\mathbf{x}^* = \left(\mathbf{A_w^T} \cdot \mathbf{A_w}\right)^{-1} \mathbf{A_w^T} \cdot \mathbf{r} \tag{4.11}$$

where the matrix $\left(\mathbf{A_w^T} \cdot \mathbf{A_w}\right)^{-1} \mathbf{A_w^T}$ is called the pseudo-inverse matrix of $\mathbf{A_w}$.

The solution descending from (4.11) is complex and allows the computation of the reflection and the transmission coefficients. The phase angle of the complex solution contains the information about

the distances travelled by the direct positive going R-wave and by the negative going R-wave. The phase angle, as descending from equation (4.11), is also susceptible to any phase change occurring at the boundaries and edges of the discontinuity. In the following numerical and experimental investigations, the condition number of the matrix $\mathbf{A}_w$ will always be close to unity (always smaller than 5).

4.2.2 Introduction to the Numerical Simulations

The wave decomposition method was applied on data coming from five different numerical models of various layered systems and vertical surface-breaking discontinuities. Model "A", "B" and "C" consisted of a half-space, with various mechanical parameters and crack depths. Model "D" and "E" consisted of a two-layered system. The first simulation was performed on a half-space with low mechanical properties and a crack with exaggerated depth: the purpose was to check the effectiveness of the method and to understand the resonant-type feature of surface-breaking cracks. The second simulation was performed on a half-space with a different receiver configuration: the purpose was to highlight the influence of the number of receivers and of the distance from the crack on the wave decomposition method. Following simulations on the half-space and on multi-layered media were performed with more realistic mechanical properties and crack sizing.

Model	Layer	Thickness [m]	Poisson's ratio	Density [kg/m³]	Young's modulus [MPa]	Stiffness proportional damping	Load	Sampling frequency [kHz]	Crack depth [m]
A	1	∞	0.33	2000	100	$0.025/200 \cdot 2\pi$	2	20	3.00
B	1	∞	0.33	2000	100	$0.025/200 \cdot 2\pi$	2	20	3.00
C	1	∞	0.33	2000	1000	$0.005/200 \cdot 2\pi$	4	50	1.00 0.50 0.20
D	1	0.2	0.33	2000	6000	$0.01/200 \cdot 2\pi$	3	50	1.00
	2	∞	0.33	2000	1000	$0.025/200 \cdot 2\pi$			
E	1	0.2	0.33	2000	2000	$0.01/200 \cdot 2\pi$	3	50	0.18
	2	∞	0.33	2000	1000	$0.025/200 \cdot 2\pi$			

Table 5: Parameters of the FEM model for crack detection with the wave decomposition method. Loads refer to Figure 3.6.

In the next numerical and experimental investigations, usually the first one or two closest sensors to the source were excluded from the calculation in order to avoid the near-field effects to negatively

affect the results. Since the wave velocities were bigger in models “C”, “D” and “E”, a different sampling frequency was chosen in order to respect the Courant condition (equation (3.)). Mechanical parameters, density and damping ratios were chosen to be close to typical values of soils and asphalts, and were similar to those used in [57, 93]. The different models’ properties are summarized in Table 5.

4.2.3 Numerical Simulations on Half-Space

In this section, the wave decomposition method was applied to numerical data coming from simulation with model “A”, “B” and “C”. Figure 4.15 illustrates the set-up and the dimensions of the numerical simulations with the three models. The discontinuity consisted of a 0.01 m wide and 3.00 m deep vertical notch for models “A” and “B”. Different crack depths were utilized in model “C”: the first with a depth of 0.20 m, the second with a depth of 0.50 m and the third with a depth of 1.00 m. The crack was simulated with absence of matter.

For model “A”, the deployment consisted of 60 sensors on the left end side of the crack. Sensors were equally spaced by 0.05 m, covering a length L_s of 3 m. The source was 5 m distant from the deployment of sensors (Figure 4.15(a)). For model “B”, the deployment consisted of 50 sensors on the left end side of the crack, equally spaced by 0.05 m. The deployment was 2.50 m distant from the source and 3 m distant from the crack, covering a length L_s of 2.50 m (Figure 4.15(b)). For model “C” the crack was within the deployment of sensors, which consisted of 12 sensors on the left end side and 12 sensors on the right end side of the notch, equally spaced by 0.05 m (Figure 4.15(c)). The length of the deployment of sensors L_s was 0.60 m. The source was 0.05 m far from the deployment of sensors. For each crack depth, the simulations were repeated moving apart the source by an equal length L_s three times. In the simulations with model “A” and “B” a great number of sensors were used to have a high resolution and to evaluate the effects of the deployment of sensors from the crack. The simulations with model “C” were performed choosing the size of the crack, mechanical parameters of the half-space and number of sensors such as to model realistic scenarios.

The reflection coefficient was computed as the amplitude ratio of the negative going wave to the positive going wave at the reference node. The transmission coefficient was computed only for the case of the crack within the deployment of sensors (model “C”). It was evaluated as the amplitude ratio of the direct positive going wave on the right end side of the notch to the direct positive going wave on the left end side of the notch, evaluated at their respective reference nodes.

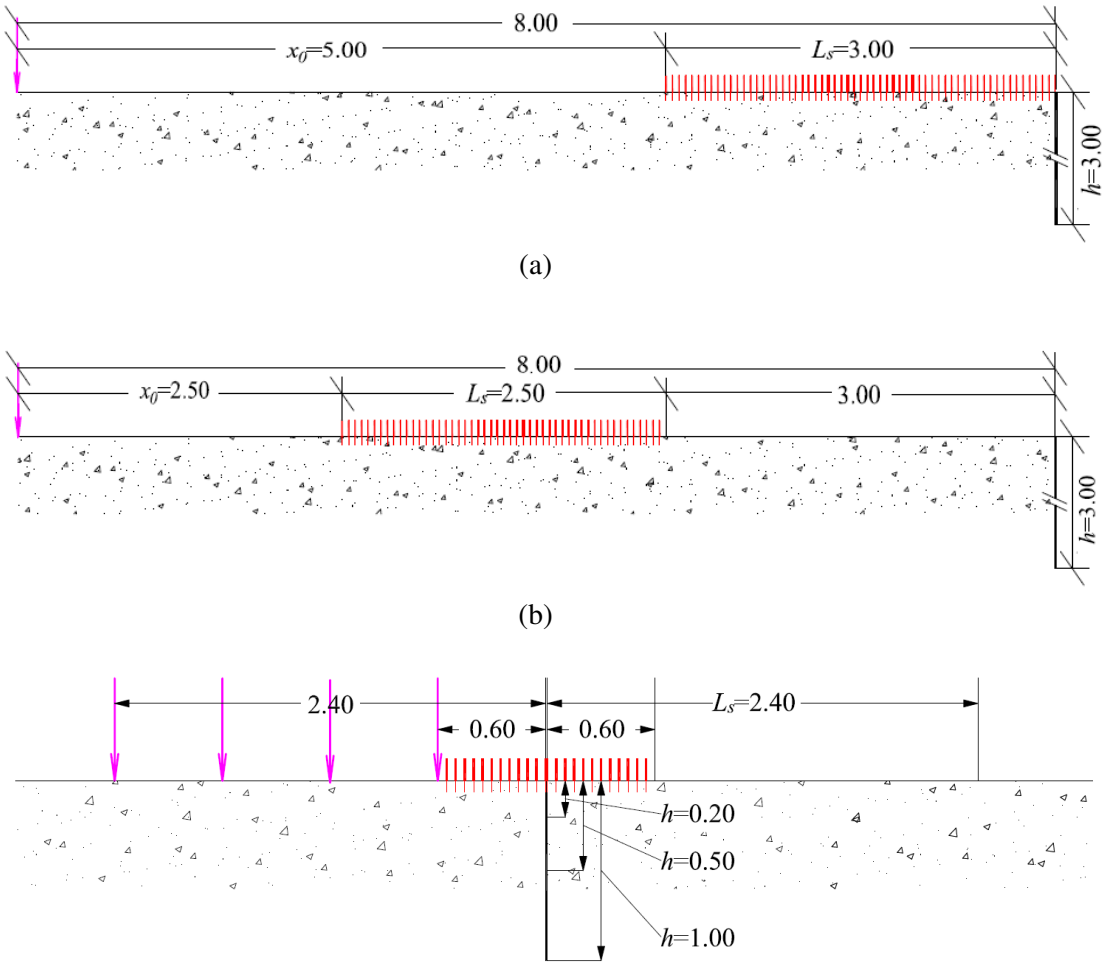

Figure 4.15: Set-up and dimensions for the numerical simulations with model "A" (a), with model "B" (b) and with model "C" (c). The pink arrow indicates the source position; the red lines indicate the sensors. Distances are shown in metres.

Simulations with model "A" and with model "B" were performed on half-spaces with low mechanical properties (far from the real mechanical properties of the asphalts) and a crack with exaggerated depth: the purpose was to check the effectiveness of the method and to understand the resonant-type feature of surface-breaking cracks. The combination of a low Young's modulus and of a high crack depth should cause the resonant-type behaviour to happen at the low frequencies (range 0-200 Hz). To highlight the influence of the number of receivers and of the distance from the crack on the wave decomposition method, difference receiver configurations were chosen.

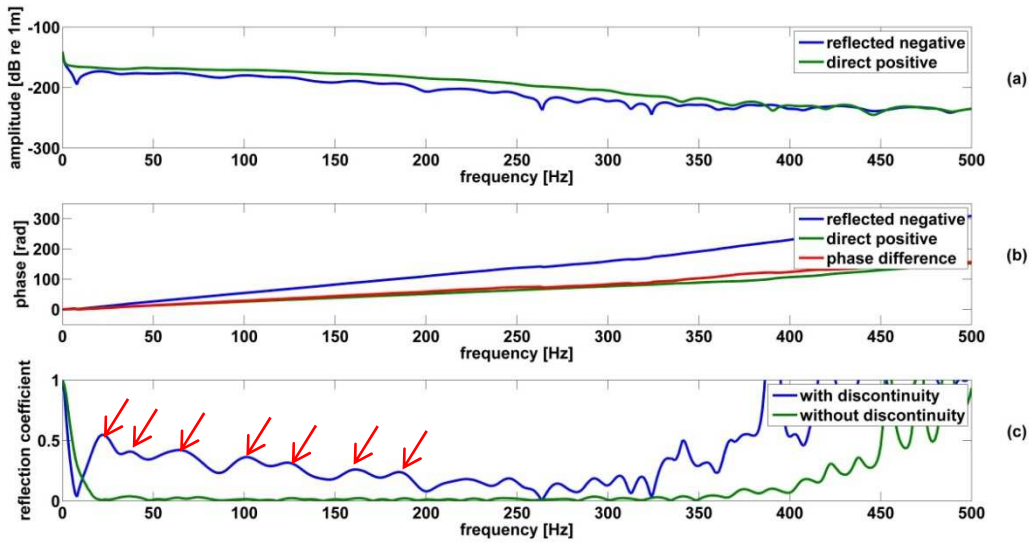

Figure 4.16: Amplitude (a) and phase (b) of reflected negative going and of direct positive going R-wave and reflection coefficient of R-wave with and without discontinuity (c), for numerical simulation with model "A". The resonant peaks in the reflection coefficient are highlighted with red arrows.

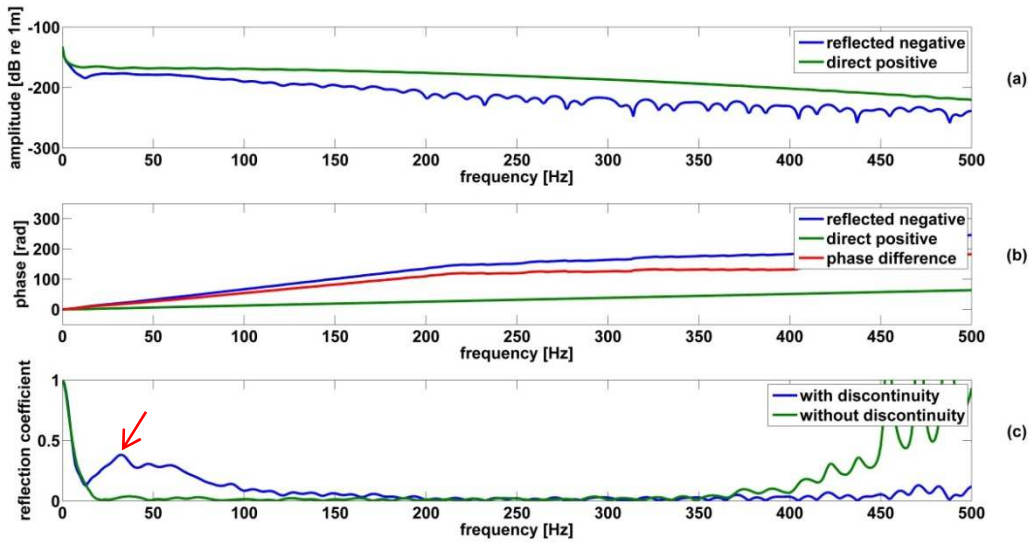

Figure 4.17: Amplitude (a) and phase (b) of reflected negative going and of direct positive going R-wave and reflection coefficient of R-wave with and without discontinuity (c), for numerical simulation with model "B". The resonant peak in the reflection coefficient is highlighted with a red arrow.

For both simulations with model "A" and with model "B", the amplitude of the direct wave is always larger than that of the reflected wave, especially at the low frequencies (less than 30 Hz). The amplitude of both direct and reflected R-wave decreases moving from the low to the high frequencies

due to intrinsic attenuation (Figure 4.16(a) and Figure 4.17(a)). The phase of the direct and reflected R-wave, and their difference, have a linear trend and carry the information of the distance travelled by the waves with respect to the reference node, which in both cases is the first receiver from left to right (Figure 4.16(b) and Figure 4.17(b)). For model "A", the reference node is 5 m distant from the source and 3 m distant from the discontinuity. Given the dimensions of Figure 4.15, the direct wave travels 5 m, while the negative wave travels 11 m: the phase difference gives the doubled distance between the reference sensor and the discontinuity, which in this case is 6 m. For model "B" the reference node is 2.50 m distant from the source and 5.50 m distant from the discontinuity. Given the dimensions of Figure 4.15, the direct wave travels 2.50 m, while the negative wave travels 13.50 m: the phase difference gives the doubled distance between the reference sensor and the discontinuity, which in this case is 11 m. Table 6 shows the distances estimated from the phase angle of the direct and reflected wave at two different frequencies, after applying equation (3.4). The estimation obtained from the phase angle appears to be very close to the actual values, with only minor discrepancies. Despite the distance of the deployment of sensors from the crack in model "B", the estimation obtained from the phase angle still appears very close to the actual values, with only minor discrepancies. The latter could be due to the discretization of the FEM model and to non-linear effects occurring at the faces of the discontinuity where the wave is reflected.

Frequency		**Model "A"**			**Model "B"**		
		Estimated	**Actual**	**Error**	**Estimated**	**Actual**	**Error**
150 Hz	Direct wave	4.99 m	5.00 m	-0.2%	2.47 m	2.50 m	-0.6%
	Reflected wave	10.68 m	11.00 m	-2.9%	13.15 m	13.50 m	-2.6%
	Phase difference	5.68 m	6.00 m	-5.3%	10.68 m	11.00 m	-2.9%
75 Hz	Direct wave	5.17 m	5.00 m	+3.4%	2.46 m	2.50 m	-1.6%
	Reflected wave	10.81 m	11.00 m	-1.7%	12.81 m	13.50 m	-5.1%
	Phase difference	5.65 m	6.00 m	-5.8%	10.35 m	11.00 m	-5.9%

Table 6: Actual and estimated distances travelled by the direct and the reflected wave, model "A" and model "B".

The reflection coefficient in the presence of a discontinuity (Figure 4.16(c) and Figure 4.17(c)), decreases and increases again rapidly for low frequencies, showing a major peak at the frequency of approximately 21 Hz for model "A" and of approximately 33 Hz for model "B". Remembering equation (2.35), the first resonant peak is associated with the modal index d_i equal to 1 and to a depth of the crack h equal to 3 m for model "A" and to 2 m for model "B". Hence, the depth of the

discontinuity is underestimated with the location of sensors of model "B", probably due to the distance of the deployment of sensors from the crack. This makes the amplitude of the reflected wave significantly lower than the case of model "A". Model "B" also uses fewer sensors compared to model "A": this probably causes the least square optimization to be less accurate. After the major resonant peak, the reflection coefficient in both cases smoothly decreases due to the intrinsic attenuation of R-wave, with the high frequencies decaying faster than the low frequencies. Model "A" shows other minor peaks at the frequencies of approximately 35 Hz, 63 Hz, 102 Hz, 123 Hz, 161 Hz and 185 Hz: they are associated with the modal indexes d_i equal to 2, 3, 5, 6, 8, and 9. The peaks associated with the modal indexes 4 and 7 are not visible and are probably masked in the reflection coefficient due to the solution being an approximation. The reflection coefficient obtained with model "B" instead does not show other relevant resonant peaks. This is probably again due to the distance from the crack, which makes the amplitude of the reflected wave significantly lower than the case of model "A". The resonant peaks are highlighted with red arrows in Figure 4.16(c) and Figure 4.17(c). The image also shows the reflection coefficient in absence of a discontinuity for comparison: in this case, the reflection coefficient only decreases and rapidly approaches the zero value.

Since the method was established and proved effective, simulations with model "C" were run with parameters that are more realistic. The asphalt stiffness and realistic crack depths were modelled. For each crack depth, the wave decomposition method was applied to the deployment of sensors on the left end side of the notch to compute the reflection coefficient and then to the deployment of sensors on the right end side of the notch to compute the transmission coefficient. Since for each crack depth the simulations were repeated moving apart the source by an equal length L_s three times, the result was the average among four simulations.

The reflection and transmission coefficients are shown in Figure 4.18 for the three different crack depths. The reflection coefficient in all the cases shows a trend in which it quickly decreases and augments moving from the low to the high frequencies, with one or more resonant peaks. The peaks are consistent with the resonant behaviour of surface-breaking cracks, and are associated with the depth of the crack, as per equation (2.35). The transmission coefficient in all the cases has a high value at low frequency, dropping down with a steep trend up to a cut-off frequency, where it approaches the zero value. Sometimes more than one cut-off is visible, with a trend in which the value of the transmission coefficient decreases and increases while tending to the zero value. This behaviour reflects the effect of a surface-breaking crack on the R-wave propagation: the finite depth blocks shorter-wavelength (higher frequency) Rayleigh waves, allowing only the longer wavelength (lower frequency) to move on, thus acting as a low-pass filter. The cut-off frequency of the transmission coefficient is also believed to be associated with the depth of the crack, following

equation (2.35). As can be perceived by looking at Figure 4.18, as a general trend the deeper the crack is, the lower the resonant and the cut-off frequencies are. Moreover, when the reflection coefficient shows a peak, the transmission coefficient shows a local minimum: hence, resonances and cut-offs occur approximately at the same frequency.

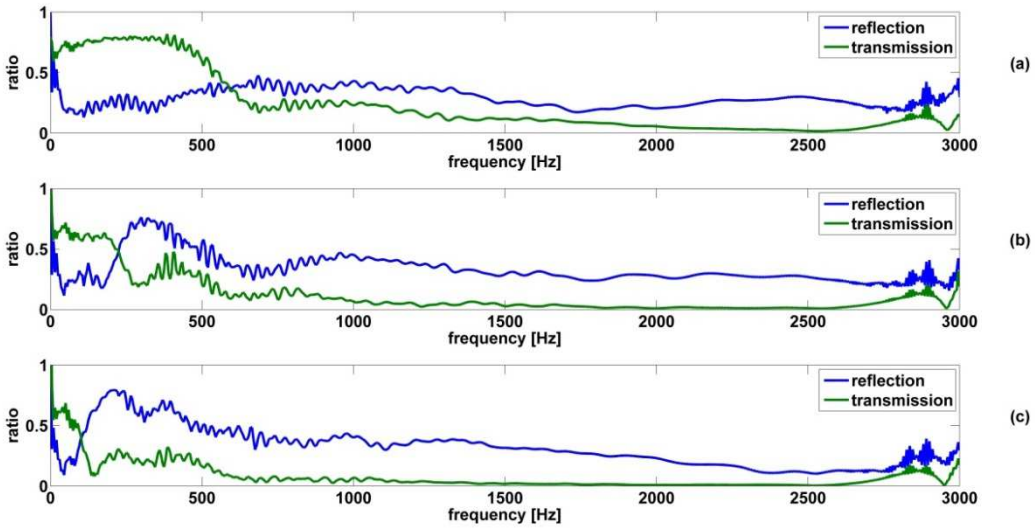

Figure 4.18: Reflection and transmission coefficients for the vertical crack with depth of 0.20 m (a), of 0.50 m (b) and of 1.00 m (c). The result is the average among four simulations.

In case of a 0.20 m crack (Figure 4.18(a)), the reflection coefficient shows a resonant peak at the frequency of approximately 685 Hz, while the transmission coefficient has cut-off frequency at approximately 690 Hz. The resonant peak of the reflection coefficient and the cut-off of the transmission coefficient occur at approximately the same frequency, which is associated with the modal index d_i equal to 1 and a crack depth h of 0.29 m.

In case of a 0.50 m crack (Figure 4.18(b)), the reflection coefficient shows a resonant peak at the frequency of approximately 300 Hz, associated with the modal index d_i equal to 1 and a crack depth h of 0.66 m. A second and a third resonant peak at approximately 500 Hz and 900 Hz are barely visible. They are associated with the modal index 2 and 3 according to equation (2.35). The transmission coefficient shows a first cut-off frequency at approximately 320 Hz, associated with a crack depth of 0.63 m. A second and a third cut-off shows up at approximately 600 Hz and 900 Hz. Again, resonant peaks of the reflection coefficient and cut-offs of the transmission coefficient occur at approximately the same frequency.

In case of a 1.00 m crack (Figure 4.18(c)), the reflection coefficient shows a resonant peak at the frequency of approximately 200 Hz, associated with the modal index d_i equal to 1 and a crack depth h of 1.00 m. A second resonant peak at approximately 400 Hz is clearly visible. It is associated with

the modal index 2 according to equation (2.35). The transmission coefficient shows a first cut-off frequency at approximately 150 Hz, associated with a crack depth of 1.34 m. A second and a third cut-off shows up at approximately 400 Hz and 800 Hz.

Table 7 summarizes the resonant and cut-off frequencies as extracted from the reflection and transmission coefficients of the three cases, and the depth estimated as per equation (2.35). As can be seen by looking at Table 7, the crack depth was generally overestimated by more than 25% if the wave decomposition method was used to compute the reflection and transmission coefficients. The parameter C of equation (2.35) set equal to 2.5 would correct the overestimation.

	Estimated crack depth, h	**Actual crack depth**	**Error**
Resonant frequency = 685 Hz	h = 0.29 m	0.20 m	+45%
Cut-off frequency = 690 Hz	h = 0.29 m		+45%
Resonant frequency = 300 Hz	h = 0.66 m	0.50 m	+32%
Cut-off frequency = 320 Hz	h = 0.63 m		+26%
Resonant frequency = 200 Hz	h = 1.00 m	1.00 m	+0%
Cut-off frequency = 150 Hz	h = 1.34 m		+34%

Table 7: Resonant and cut-off frequencies, estimated and actual crack depths for simulations with model "C".

The wave decomposition method proved to be a reliable technique for the calculation of reflection and transmission coefficients in the presence of an anomaly or a vertical discontinuity for a half-space, thus allowing estimating its depth and location. Particularly, the resonances of the reflection coefficient and the cut-offs of the transmission coefficient were associated with the depth of the crack. The phase of the direct and of the reflected wave gave an indication of the location of the crack with respect to the chosen reference point. Media with constant velocity were investigated at this stage, i.e. the dispersive behaviour was not considered. The influence of the distance of the deployment of sensors from the relevant crack seemed to affect the accuracy of the depth estimation, whereas the influence on the phase of the direct and reflected wave was less pronounced. The number of the measurement affected the final results of the wave decomposition method: the more measurements were taken, the more accurate the approximate solution was. From now on, the phase angle will not be considered and the attention will be focused on the computation of the reflection and transmission coefficients for crack interrogation.

4.2.4 Numerical Simulations on Layered Systems

In this section, the wave decomposition method was applied to numerical data coming from simulations with multi-layered models "D" and "E" in the presence of a vertical discontinuity. The following simulations were performed with more realistic layered systems and number of sensors. The biggest challenge in the application of the wave decomposition method on layered systems is that the medium is dispersive, i.e. the phase velocity is not consistent with respect to the frequency, but it varies with a specific trend due to the properties of the system. Hence, the dispersive relation is an *a-priori* information for the wave decomposition method.

Figure 4.19 illustrates the set-up and the dimensions of numerical simulations with model "D" and "E". The discontinuity consisted of a vertical notch with a width of 0.01 m and a depth of 1.00 m for model "D" and a depth of 0.18 m for model "E". The deployment consisted of 6 sensors, the crack being in the exact middle of the deployment of sensors, equally distant from the third and the fourth sensor. The crack was simulated with absence of matter. Sensors were equally spaced by 0.10 m, covering a length L_s of 0.60 m. The number of sensors was chosen to match the number of sensors available for the experimental investigations.

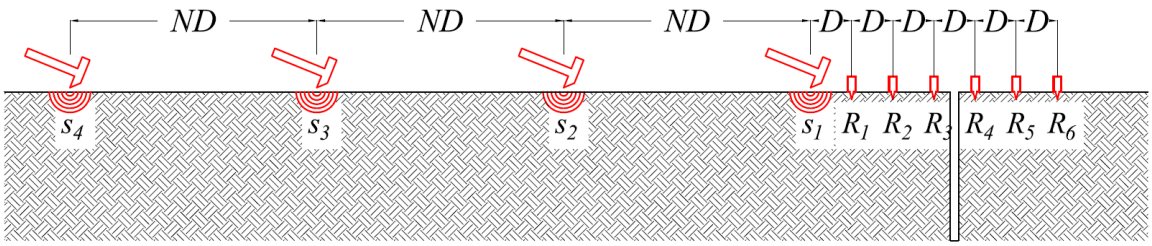

Figure 4.19: Set-up configuration for numerical simulations with model "D" and "E" on layered systems. The crack is in the exact middle of the deployment of sensors, equally distant from the third and the fourth sensors. Crack depth is 1.00 m for model "D" and 0.18 m for model "E".

Since the wavenumber solutions are *a-priori* information for the wave decomposition method, the wavenumber and phase velocity were extracted from the vertical *f-k* representation of the multichannel record obtained with the MISW technique, on the same isotropic layered medium with absence of discontinuity, with the set-up configuration of Figure 4.19. Figure 4.20 shows the dependency from frequency of the wavenumber and of the phase velocity for the layered model "D" and "E", as obtained from the vertical *f-k* spectra.

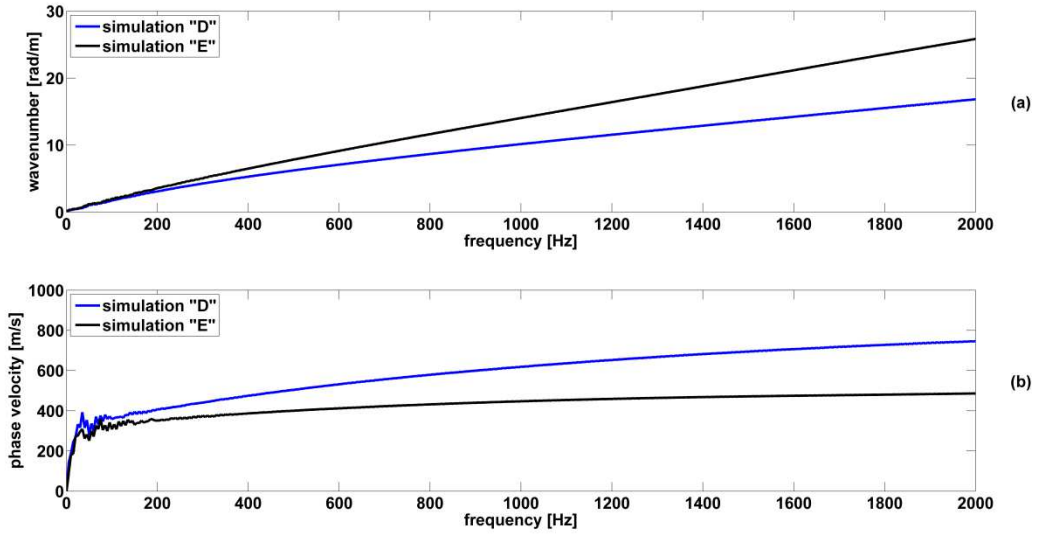

Figure 4.20: Wavenumber (a) and phase velocity (b) against frequency for layered model "D" and "E".

For each simulation, the wave decomposition method was applied to the deployment of sensors on the left end side of the notch to compute the reflection coefficient, and then to the deployment of sensors on the right end side of the notch to compute the transmission coefficient. The reflection coefficient was evaluated as the amplitude ratio of the negative going wave to the positive going wave at the reference node of the left end side deployment of sensors (geophone #1). The transmission coefficient was evaluated as the amplitude ratio of the direct positive going wave on the right end side of the notch to the direct positive going wave on the left end side of the notch, evaluated at their respective reference nodes (geophone #1 and geophone #4). Since for each crack depth the simulations were repeated moving apart the source by an equal length L_s three times, the result was the average among four simulations.

The reflection and transmission coefficients are shown in Figure 4.21 for the two simulations. The reflection coefficient in both cases shows a trend in which it quickly decreases and augments moving from the low to the high frequencies, with one or more resonant peaks. The transmission coefficient in both cases has a high value at low frequency, dropping down with a steep trend up to a cut-off frequency, where it approaches the zero value. The deeper the crack is, the lower the resonant and the cut-off frequencies are. Moreover, when the reflection coefficient shows a peak, the transmission coefficient shows a local minimum: hence, resonances and cut-offs occur approximately at the same frequency.

For simulation with model "D" (Figure 4.21(a)), the reflection coefficient displays its first and second resonant peaks at the frequencies of approximately 175 Hz and 425 Hz. The peaks are associated with the depth of the crack and to the modal index d_i respectively equal to 1 and 2, as per equation

(2.35). They are highlighted by red arrows in Figure 4.21(a). Following equation (2.35) and choosing the phase velocity of 388 m/s and of 481 m/s from Figure 4.20, the first peak is associated with a crack depth of 1.11 m and the second peak to a crack depth of 1.13 m. The two values are consistent and very close to the actual crack depth for simulation with model "D", albeit leading to a slight overestimation of the crack depth. The transmission coefficient for simulation with "D" has a cut-off at the frequency of approximately 180 Hz: it occurs when the reflection coefficient peaks and it is again associated with the depth of the crack. The transmission coefficient then slightly increases, showing a second cut-off at the frequency of approximately 500 Hz. Cut-off frequencies of the transmission coefficient are highlighted by black arrows in Figure 4.21(a).

For simulation with model "E" (Figure 4.21(b)), the reflection coefficient displays its first and second resonant peaks at the frequencies of approximately 890 Hz and 1955 Hz. The peaks are associated with the depth of the crack and to the modal index d_i respectively equal to 1 and 2, as per equation (2.35). They are highlighted by red arrows in Figure 4.21(b). Following equation (2.35) and choosing the phase velocity of 439 m/s and of 485 m/s from Figure 4.20, both resonant peaks are associated with a crack depth of 0.25 m. The crack depth is very close to the actual depth, albeit it is slightly overestimated. It is also worth to notice the presence of a small hump in the reflection coefficient that shows up at approximately 200 Hz: it is probably a phenomenon associated with a mode switch in the wave propagation pattern rather than linked to the presence of the crack, since for the same value of frequency the transmission coefficient shows a high value. The transmission coefficient for simulation with model "D" has the first cut-off at the frequency of approximately 900 Hz: it occurs when the reflection coefficient peaks and is again associated with the depth of the crack. The transmission coefficient than slightly increases, showing a second cut-off at the frequency of approximately 1900 Hz. Cut-off frequencies of the transmission coefficient are highlighted by black arrows in Figure 4.21(b).

The wave decomposition method proved to be a reliable technique for the calculation of reflection and transmission coefficients in the presence of an anomaly or a vertical discontinuity, in layered systems. It demonstrated to be able to cope with the heterogeneities and the dispersive nature of layered systems, thus making possible to detect and assess the depth of surface-breaking cracks. As it happened for the half-space case, the crack depth in layered systems was generally overestimated by 25% if the wave decomposition method was used to compute the reflection and transmission coefficients. The parameter C of equation (2.35) set equal to 2.5 would correct the overestimation.

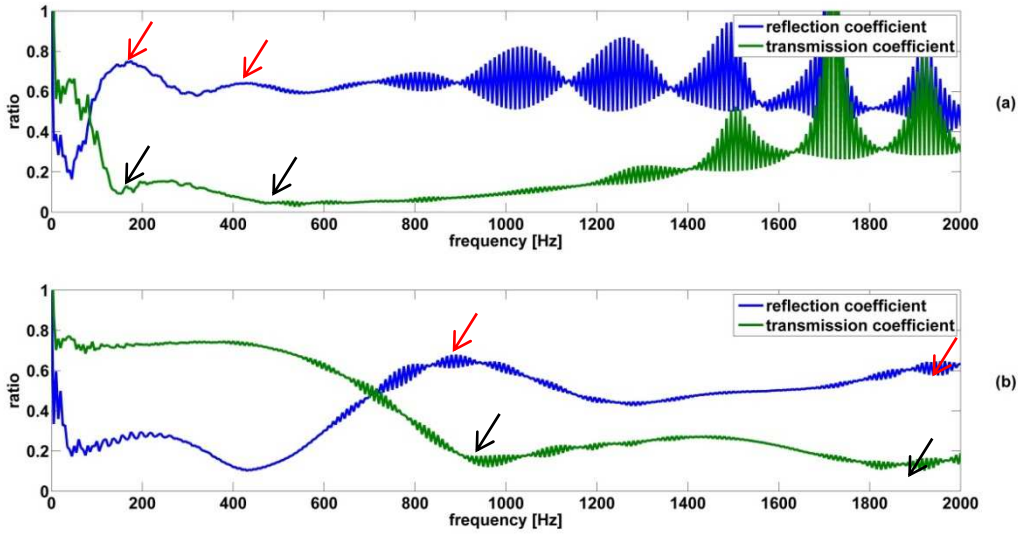

Figure 4.21: Reflection and transmission coefficients for simulation with model "D" (a) and with model "E" (b).

4.2.5 Summary of the Wave Decomposition Method

A new wave decomposition method for crack interrogation in asphalt was presented in this chapter. The wave decomposition method consisted of a signal processing algorithm capable of computing the direct and reflected waves amplitudes and phase angles from the signals of a deployment of sensors. It employed a number of measurements much bigger than the number of unknowns, tackling the measurement errors naturally present in experimental data by finding a least square approximate solution with the help of the pseudo-inverse matrix for overdetermined systems.

Knowing the amplitude of the positive and negative going R-wave could lead to a better understanding of the phenomenon of reflection and then could help in the detection of cracks and discontinuities in the shallow subsurface.

Numerical simulations proved the wave decomposition method to be effective for the assessment of the location and of the depth of surface-breaking cracks in the half-space and in layered systems. Particularly, the resonances of the reflection coefficient and the cut-offs of the transmission coefficient were associated with the depth of the crack. The phase of the direct and of the reflected wave gave an indication of the location of the crack with respect to the chosen reference point. The influence of the distance of the deployment of sensors from the relevant crack seemed to affect the accuracy of the depth estimation, whereas the influence on the phase of the direct and reflected wave was less pronounced. The number of measurements affected the final results of the wave decomposition method: the more measurements were taken, the more accurate the approximate solution was. Hence, a configuration that maximizes the number of sensors and minimizes the

distance of the deployment from the crack has to be chosen for the best results with the wave decomposition method.

The crack depth was generally overestimated by more than 25% if the wave decomposition method was used to compute the reflection and transmission coefficients. The parameter C of equation (2.35) set equal to 2.5 would correct the overestimation.

The wave decomposition made possible the detection and the assessment of the depth of surface-breaking cracks in dispersive and heterogeneous layered systems.

4.3 Inversion of Seismic Data

In the next chapters, experimental *f-k* spectra obtained with the spectral convolution method will be inverted in order to obtain a shear wave profile of the investigated ground and to compare the experimental spectra with the analytical spectra obtained after the inversion. For these reasons, an inversion algorithm is proposed and introduced in this section.

The inversion of seismic dispersion measurement in this work will be accomplished directly in the *f-k* domain, without subjectively extraction of any dispersion curve. The experimental spectrum is directly compared to analytical spectra in the *f-k* domain, to find the best possible match between the measured (observed) and the modelled (predicted) spectrum. The analytical model used in this work is based on the use of stiffness matrices in the frequency-wavenumber domain [63, 67], giving the response of the system due to a time harmonic line load. The principals of the analytical model used in this thesis are introduced in section 2.5.

Before comparing the experimental and the analytical spectra, the latter is corrected to account for the cylindrical spreading of the R-wave and to overcome the plane wave approximation of the analytical solution. The analytical predicted spectrum $U(x,\omega)_{pred}$ is obtained through an inverse Hankel transformation, with the same offset range as used for the measured data. The Hankel function is used instead of the plane-wave approximation to consider the cylindrical spreading of the R-wave. It also allows the characterization of the source of excitation. The Hankel function accounts for the near-field effect and introduces a nonlinear phase shift at near offsets [32, 46, 97, 98]. The inverse Hankel transformation used to obtain the frequency-space representation $U(x,\omega)_{pred}$ is the following:

$$U(x,\omega)_{pred} = \int_0^N J(kx)U(k,\omega)_{an}\,kdk \tag{4.12}$$

where $J(kx)$ is the Bessel function of the first kind of order 1; $U(k,\omega)_{an}$ is the surface vertical displacement in the frequency-wavenumber domain due to a unit surface loading, obtained from the analytical model. Eventually, the analytical predicted spectrum $U(k,\omega)_{pred}$ is obtained from equation (3.6), zero padding the space domain in order to match the resolution of the experimental spectrum. This can now be compared directly with the experimental observed spectrum, minimizing the following error algorithm:

$$M = \sum_{i=1}^{n}\sum_{j=1}^{N}\left(\left\|P(k_j,\omega_i)_{obs}\right\| - \left\|U(k_j,\omega_i)_{pred}\right\|\right)^2 \tag{4.13}$$

where M represents the mismatch between the two *f-k* spectra. The analytical and experimental spectra are both normalized by their respective maximum values and have the same aperture of 0-200 Hz for the frequencies and of 0-4 π rad/m for the wavenumbers.

The inversion is accomplished fixing the number of layers of the model, the values of the density, damping and Poisson's ratio for each layer, and then varying the thicknesses and the Young's modulus of each layer in a Montecarlo simulation, in order to find the global minimum of the function M. Whenever a global minimum is found, if the mismatch is considered not enough small, a new inversion is performed with finer values and the Montecarlo simulation is repeated. The main benefit of this proposed inversion procedure is that the raw data can be entirely processed without any subjective user input and extractions to identify discrete dispersion curves.

4.3.1 Summary of Inversion of Seismic data

Inversion in this thesis will be achieved without any subjective extraction of dispersion curves. A full waveform inversion will be accomplished in the frequency-wavenumber domain, directly comparing the experimental and the analytical spectra. To account for the cylindrical spreading of Rayleigh waves and for the near field effects, the Hankel function is used instead of the plane-wave approximation.

4.4 Summary

The spectral convolution method introduced in this chapter tried to bridge the problems and limitations of the traditional methods used for the imaging of seismic data. The dispersion curves are usually affected by a non-negligible amount of uncertainty. Often multiple modes are masked under the same energy band in the spectral images, or often only one direction of the motion shows the existence of a certain mode of propagation. In general, the dispersion curve obtained with the frequency-wavenumber transformation (see section 3.3) suffers from resolution problems. The spectral convolution methods tried to overcome all these issues by simultaneously employing the vertical and the horizontal component of motion before the imaging process, and not at the end by jointly fusing the results obtained with the two directions of motion. It consisted of a convolution in the frequency domain between the vertical and horizontal spectra. The new spectral image obtained had a doubled resolution in the frequency and wavenumber domain. The accuracy of the dispersion curve was also improved, since the spectral convolution method led to a more robust signal than the single-axis signal. The numerical investigations showed in this chapter and in the Appendix F highlighted the advantages of the spectral convolution method. It improved the resolution and the accuracy of the dispersion curves of the R-wave.

The ellipticity curve (see section 2.8) showed a minimum when the energy in the propagation pattern shifted from one mode to the higher one. The spectral convolution method helped the separation of modes with similar velocities, and to spot osculation points, especially if used in conjunction with the ellipticity curve.

The spectral convolution method improved the accuracy of the dispersion curves at lower frequencies, since the new multichannel record was equivalent to a record with doubled length in time and space (see section 4.1.3 and section 4.1.4). A gain in resolution was accompanied by a proportional reduction in the maximum detectable frequency: the aliasing will occur for half the value obtained with equation (3.). This drawback can be easily overtaken by adopting a small temporal discretization. However, spatial aliasing is primarily governed by the equation (2.34).

There are currently no standard methods for the detection of cracks and the monitoring control of the roads. This chapter proposed a linear system for the interrogation of surface-breaking asphalt cracks based on a wave decomposition method and on the computation of the reflection and the transmission coefficients of the R-wave. Insight into practical application for detection and crack sizing in asphalt descends from the observations of the measurement shown in this paper. A possible strategy for the interrogation of cracks would be to always collect data, where possible, with the deployment across the discontinuity. This assures the estimation of both the reflection and the transmission coefficients, the summation of which should always be approximately less than one for each frequency. To avoid

misinterpretation of the results of the wave decomposition (e.g. to avoid picking out a resonance due to other causes than a vertical crack), the two coefficients should be used synergistically: in fact, the transmission coefficient should present a cut-off at approximately the same value of frequency at which the resonance occurs. Alternatively, a comparison with the results coming from a section without discontinuities would also be helpful at excluding misinterpretations.

In the case the location of the crack is unknown, the phase angle would help in the localisation of the crack with respect to the deployment of sensors, but at this stage a wider investigation for the interrogation of bottom-up cracks, which are not visible from the surface, is needed.

Chapter 5: Surface Wave Dispersion Measurements: Experimental Investigations and Inversions

This chapter describes the experimental investigations and inversions accomplished on both soils and asphalts. The first part of the chapter describes the results of an experimental study on the differences in the generation of seismic waves in soils with respect of different ground excitation methods. It also shows the drawbacks and limitation of the cross-power spectral method in the presence of multiple waves and/or multiple R-wave modes. The second part of this chapter focusses on the experimental validity of the spectral convolution method for seismic surveys of shallow soils and asphalts. Section 5.1 focusses on the calibration of the tri-axial geophones that will be employed in the experimental investigation. Section 5.2 focusses on the different ways of ground excitation, and on the subsequent differences on phase velocity estimations. The experimental results are compared and validated with the aid of numerical simulations. Section 5.3 displays the results of two ground investigations using the MASW method. Spectral images were obtained using vertical, horizontal and spectral convolution signals. Numerical inversions of the spectral convolution spectra were performed and the results are displayed and discussed. Furthermore, DCP test curves and ellipticity of the R-wave helped in the interpretation of the results and were used to constrain the problem. Section 5.4 shows the preliminary application of surface wave dispersion measurements on asphalt using the MISW method. Vertical, horizontal and spectral convolution signals were used to obtain the spectral images. Ellipticity of the R-wave helped in the interpretation of the results.

5.1 Calibration of Geophones

This section displays the results of a calibration session of the geophones that will be employed in the forthcoming experimental tests. Geophones are usually preferred to accelerometers in soil testing since they are more reliable and do not show resonances in the frequency range of interest of ground testing (10-1000 Hz). Requirement for geophones is a natural resonant frequency ω_n outside the range of interest of seismic *in-situ* tests, to avoid possible phase changes occurring at resonance. In order to compute the phase angle difference, the geophones should be of the same type or at least share the same dynamic behaviour [3, 7, 25].

A geophone behaves as an absolute velocity sensor above some resonant frequency depending on the mechanical structure of the transducer [99]. A model with this behaviour comprises a spring-dashpot-mass system attached to the sensor frame and connected to one independent moving-coil

transducer, used as velocity sensor (Figure 5.1). According to Preumont [99], the transfer function between the output voltage and the absolute frame velocity is the following:

$$\frac{V_{out}}{i\omega \cdot x_a} = \frac{-T_2 \cdot \frac{m}{Re_1} \cdot \omega^2 \cdot Re_2}{\left(I \cdot i\omega + Re_2\right) \cdot \left[-\frac{m}{Re_1} \cdot \omega^2 + \left(d_r + \frac{T_2}{I \cdot i\omega + Re_2} \right) \cdot \frac{i\omega}{Re_1} + 1 \right]} \tag{5.1}$$

where V_{out} is the output of the geophone (the drop voltage in the resistor), m is the moving mass, x_a is the absolute displacement of the frame, Re_1 is the internal resistance, T_2 is the transducer constant, I is the inductance of the sensor, Re_2 is the electrical resistance, and d_r is the damping.

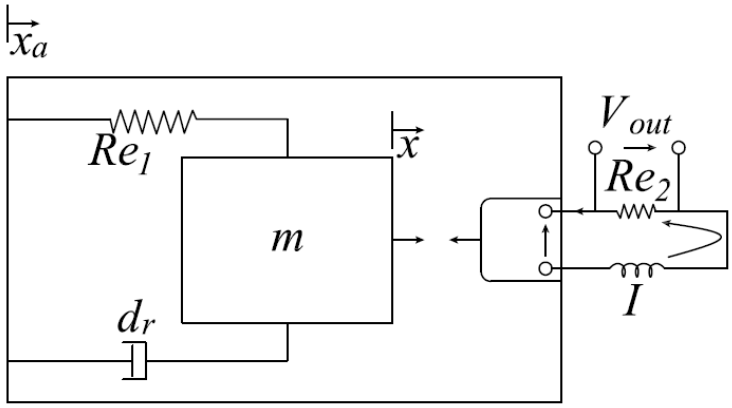

Figure 5.1: Geophone involving one-moving coil transducer. The figure is modified from [99].

In the following experimental investigations within this thesis, the data was acquired using a ProSig P8020 data acquisition unit and a laptop. All the tests were repeated and recorded 5 times with a sample frequency of 8 kHz (or 20 kHz in some cases), under the same input conditions, and then averaged in the frequency domain. For the purposes of this work, tri-axial geophones SM-24 from ION Sensor Nederland with a cut-off frequency of approximately 1 kHz and miniature single-axis accelerometers from PCB Piezotronics were used. Thus, a calibration session was carried out, in order to find the sensitivity for each geophone and to check their response. Each geophone was vertically excited via a shaker, using a white noise up to a frequency of 1 kHz, and at the same time the acceleration was registered through an accelerometer previously calibrated, hence with known sensitivity.

Table 8 contains the values for the aforementioned quantities, according to the measurements taken and to the SM-24 ION Sensor Nederland geophone's specifications sheet.

Electrical resistance, Re_2	405 Ω
Inductance of the geophone, I	26 mH
Moving mass of the geophone, m	0.0111 kg
Transducer constant, T_2	21 $\frac{\text{V·s}}{\text{rad}^2\text{·m}}$
Damping of the geophone, d_r	0.25 kg · rad/s
Natural resonant frequency of the geophone, $\frac{\omega_n}{2\pi} = \sqrt{\frac{Re_1}{m}}$	10 Hz
Internal resistance of the geophone, $Re_1 = \omega_n^2 \cdot m$	44 N/m

Table 8: values of the SM-24 ION Sensor Nederland geophone's parameters.

Figure 5.2(a) depicts a comparison between the vertical transfer function of the first six geophones and the Frequency Response Function (FRF) coming from equation (5.1), in a linear scale. Figure 5.2(b) depicts the comparison between the behaviour of the first six geophones and the behaviour expected from the model, in a linear scale, in terms of the unwrapped phase angle of the vertical FRF. For the sake of illustration, only the first six geophones were reported in the following graphs.

The frequency response curves for the geophones are nearly identical up to 1 kHz and are approximately linear up to a frequency of about 500 Hz. A natural resonant frequency at approximately 10 Hz is visible for all the tested geophones as a pick in the magnitude of the FRF. The unwrapped phase shows a decrement with frequency, due to the inductance. The calibration factor ranges between 20 and $22\,\text{Vs/m}$ for the frequency range 0-500 Hz, although an exact calibration is not necessary, since we are interested in wave propagation velocity (and not in absolute particle displacement).

Both the FRF and the unwrapped phase show good agreement with the expected behaviour of geophones coming from the analytical model. The geophones' unwrapped phase shows the same vertical behaviour with frequency of the analytical model of equation (5.1), so they are suitable for seismic surveys up to a frequency of 1 kHz. The amplitude of the sensitivity curve (Figure 5.2(a)) is nearly identical with the analytical model of equation (5.1), up to a frequency of approximately 500Hz: for higher frequencies, the actual behaviour separates from the analytical model. We ignored this behaviour since the geophones had the same dynamic behaviour with frequency and the unwrapped phase of the vertical FRF followed the trend of the analytical model.

A calibration with a swept sine ranging from 1 Hz to 10 kHz and a sampling frequency of 20 kHz was carried out in an attempt to check the upper limit of the reliable frequency range of usage. Figure

5.3 shows the unwrapped phase of the vertical transfer function between the output voltage and the absolute frame velocity. These results show that the geophones are not suitable for measurements of frequencies higher than 1 kHz.

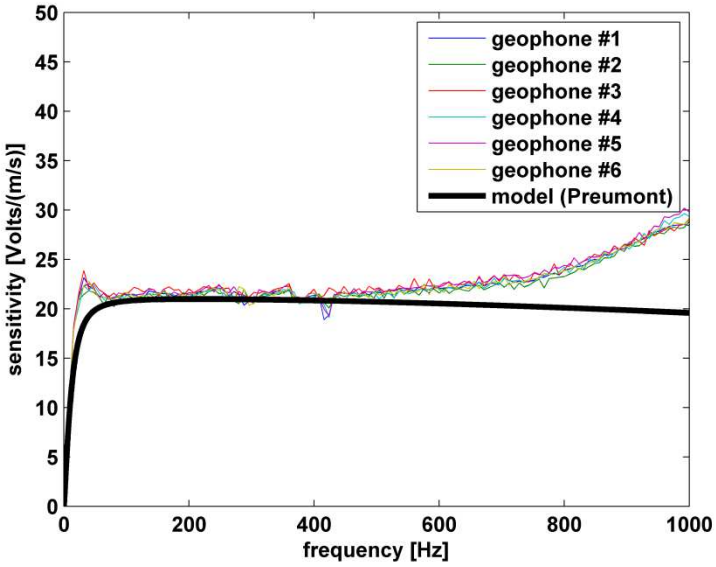

(a)

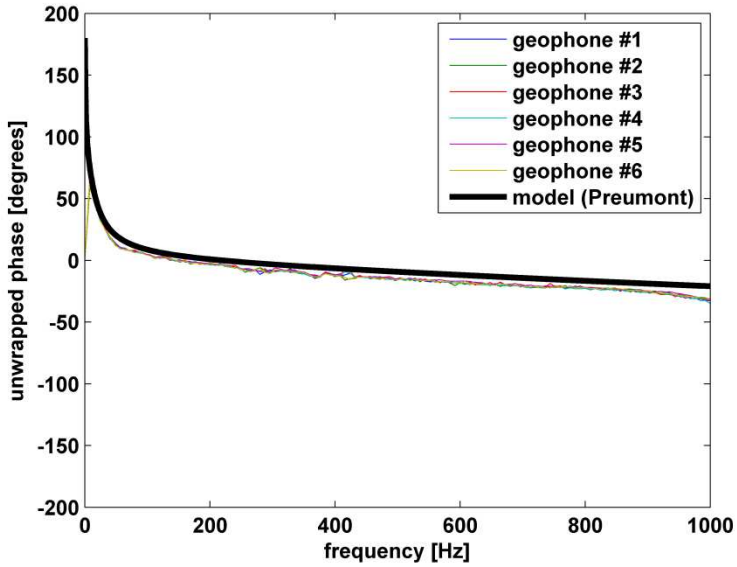

(b)

Figure 5.2: Geophones' vertical sensitivity (a) and geophones' phase angle (b).

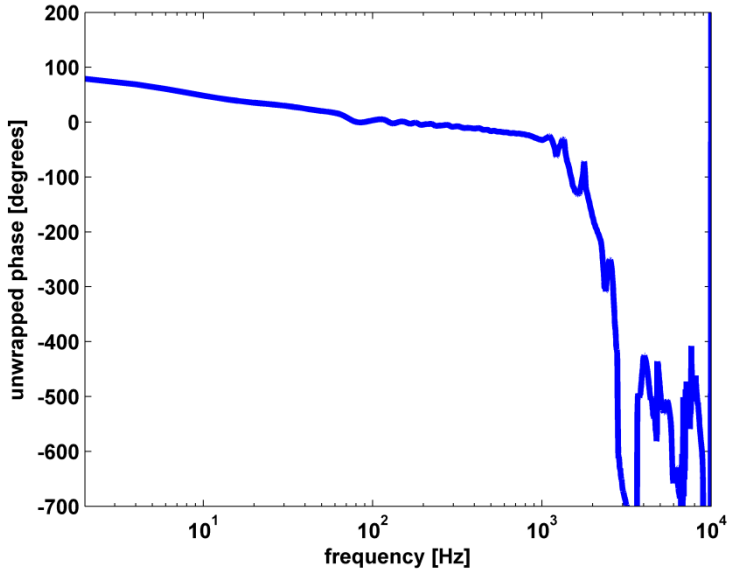

Figure 5.3: Geophones' phase angle up to 10 kHz, in a logarithmic scale.

Each geophone will be coupled with the soil by means of three metallic spikes, which penetrate the ground and assure the stability of the geophone. The coupling with the asphalt surface will be achieved substituting the spikes with curved-shaped metallic feet: each geophone will simply rest on the asphalt surface.

5.2 Comparison of Soil Excitation Methods for Surface Wave Dispersion Measurements

This section introduces and describes the results of two experimental sessions carried out in order to study the phenomenon of generation of stress waves on soils with respect to different types of source, directions of excitation, source sizes and source-to-ground couplings. It also aims at highlighting the drawbacks and the limitations of using the cross-power spectral method for the processing of seismic data. For this purpose, a private test site belonging to the University of Southampton, based on the northern side of the town (Chilworth) was exploited. The test site soil was mainly composed of a soft loose sediment layer over bedrock. In order to validate the experimental results, a numerical investigation was also carried out with the aid of the finite element model on half-space.

The dispersion curves associated with each excitation method were obtained following the cross-power spectral method (see section 3.2), using the vertical component of motion. For the determination of dispersion curves, the following filters of data were applied:

- Data points with coherence value lower than 0.3 were identified and discarded;
- Data points with negative phase velocities were identified and discarded;

- Data points with frequency value under the natural frequency of the geophones (i.e. 35 Hz), were identified and discarded;

- The upper limit of frequency was chosen equal to 200 Hz for the first experimental sessions and equal to 300 Hz for the second experimental session, following equation (2.34).

5.2.1 Comparison of Directions of Excitation

This experimental session aimed at assessing and at comparing the effects on the dispersion curves obtained with the cross-power spectral method, of different directions of excitation and source-to-ground couplings on soils.

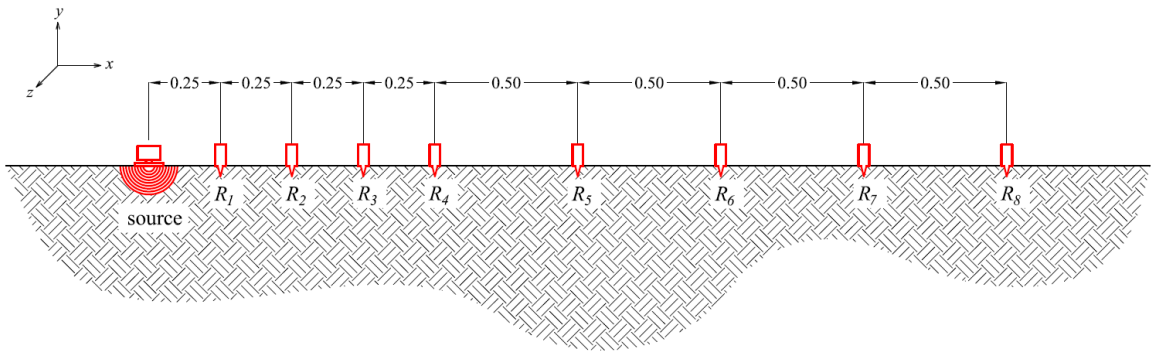

Figure 5.4: Experimental set-up for the comparison of directions of excitation, *R* refers to a geophone and the number identifies the position. Distances are shown in metres (the symbol represents the shaker in its vertical arrangement).

The experimental set-up consisted of a source and an array of 8 tri-axial geophones, disposed as in Figure 5.4. The duration of the signal L_f was 2 sec.

An IV40 Data Physics inertial shaker was used as continuous source. Different types of continuous sources, source-to-ground couplings and directions of excitation were used for experimental purposes. Different steel platforms were used in order to assess different couplings:

- One rectangular L-shaped aluminium platform, consisting of a horizontal 16.0x16.0x1.5 cm plate and a vertical 10.0x16.0x1.5 cm plate. To ensure a good source-to-ground coupling, this platform had 2 spike rakes attached, 7.5cm each long, which penetrated into the ground and could be alternatively oriented parallel or orthogonally to the sensors array, or completely removed. The shaker could be bolted to the rectangular platform in two different ways, in the horizontal and in the vertical direction with respect to the ground surface (Figure 5.5).

- One aluminium circular plate with 15.0cm diameter and 1.5cm thickness, resting on the ground surface. The shaker could only be attached vertically to the circular plates (Figure 5.6(b)).

- One aluminium circular plate with 30.0cm diameter and 1.5cm thickness, resting on the ground surface. The shaker could only be attached vertically to the circular plates (Figure 5.6(a)).

The differences in the coupling between source and ground were evaluated also placing a layer of mono-granular sand between the circular platforms and the ground.

(a) (b)

Figure 5.5: Rectangular platform with IV40 shaker attached horizontally (a) and vertically (b), the rakes are orthogonal with respect to the direction of the sensors array.

(a) (b)

Figure 5.6: Large (a) and small (b) circular platform with IV40 shaker attached vertically.

The magnitude of the load was measured through a force gauge mounted between the platform and the shaker, and by means of an accelerometer directly mounted on the bottom of the shaker chassis.

The nominal moving mass of the IV40 body was 1.21 kg, so the force could be easily computed as the product of the moving mass times the acceleration.

The time extended signal was a white noise, with a unit variance and low pass filtered at 4 kHz, in order to avoid aliasing. The peak force value was about 0.015 N. Figure 5.7 lists the excitation methods tested in this session.

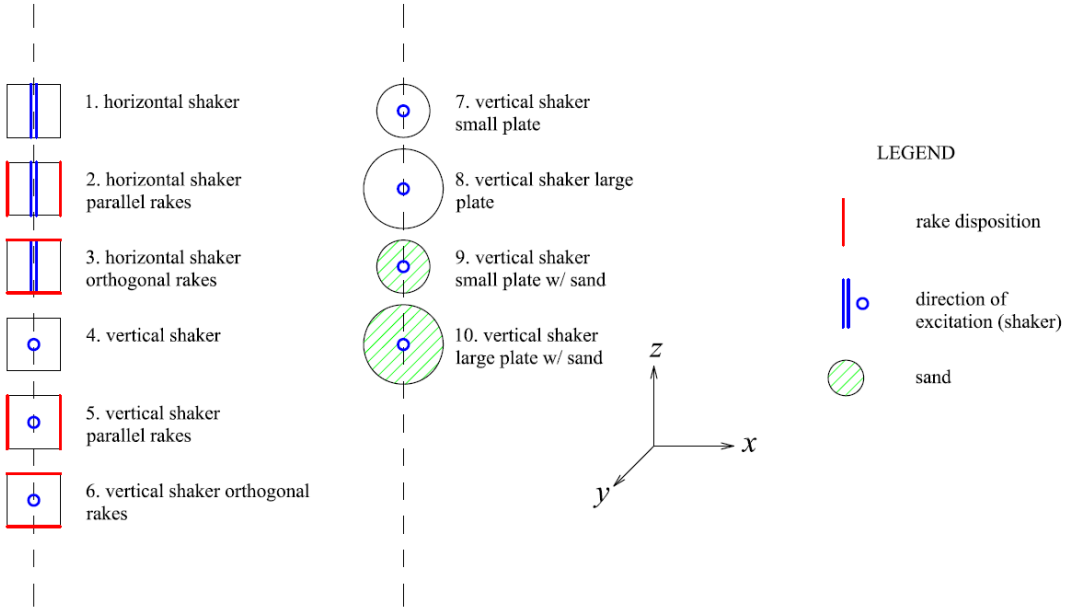

Figure 5.7: Excitation methods tested at the experimental session for the comparison of directions of excitation (top view).

Figure 5.8, Figure 5.9 and Figure 5.10 show a comparison between the dispersion curves obtained with vertical and horizontal excitation methods. One can notice that horizontal excitation methods always lead to a higher estimation of the phase velocity compared to vertical excitation methods. Horizontal excitation methods produce a bigger amount of body wave energy. It results in a higher estimation of the phase velocity compared with vertical excitation methods, if the cross-power spectra method is utilized. In fact, it is incapable to separate the contribution of different waves and/or different modes of propagation (see section 3.2).

As can be seen in the Appendix D, the coherence being close to 1 is a guarantee of linear behaviour of soil. The coherence is low for frequencies lower than 40 Hz: the lowest limit is imposed by the length of the array of sensors. In this case the distance between geophone 1 and geophone 7 is 2.75 m, which, given a R-wave velocity of 100 m/s, allows to correctly acquiring down to the frequency of approximately 72 Hz.

There are no big differences in the phase velocity estimation with respect to the orientation of the rakes in the rectangular platform, since the estimation of the phase velocity with parallel and orthogonal rakes is almost identical (Figure 5.9 and Figure 5.10).

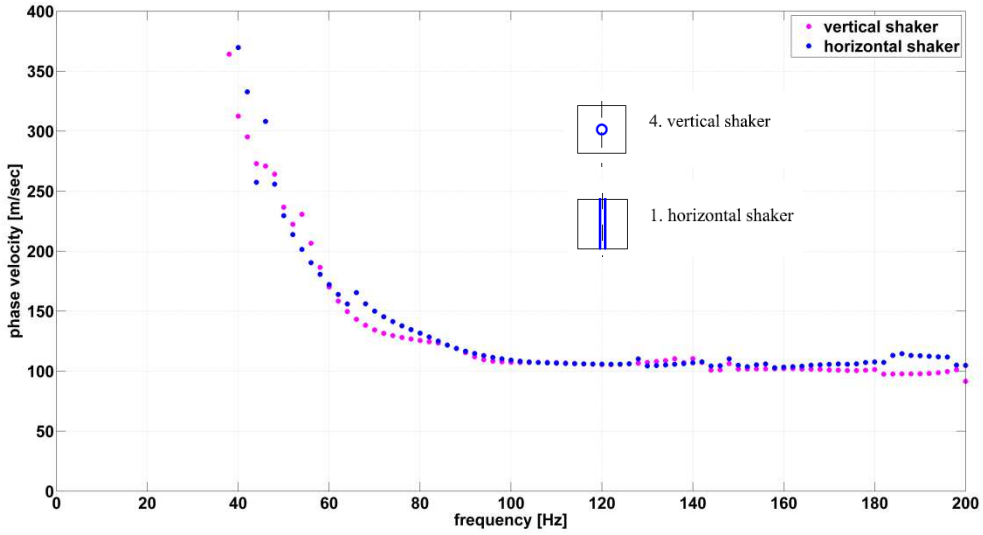

Figure 5.8: Dispersion curves with excitation methods 1 and 4.

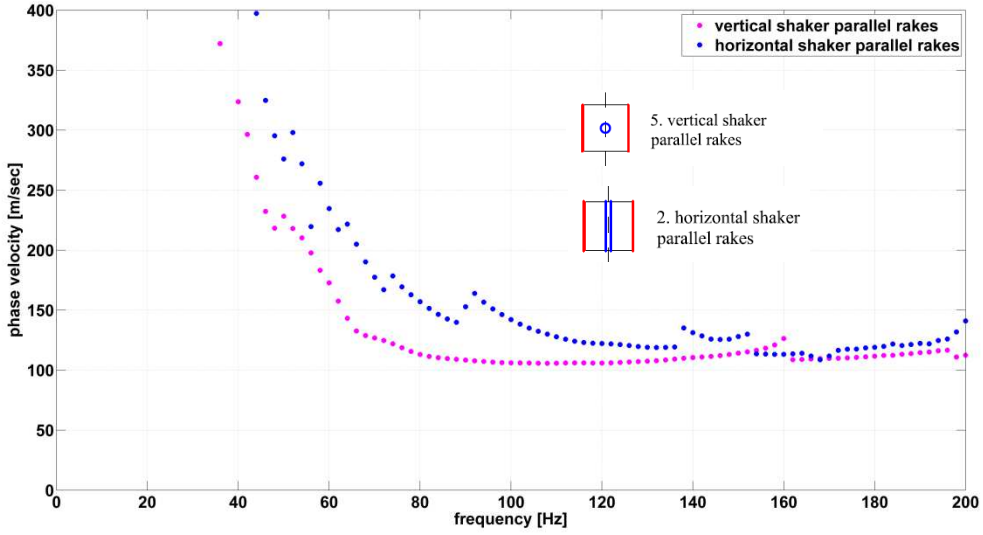

Figure 5.9: Dispersion curves with excitation methods 2 and 5.

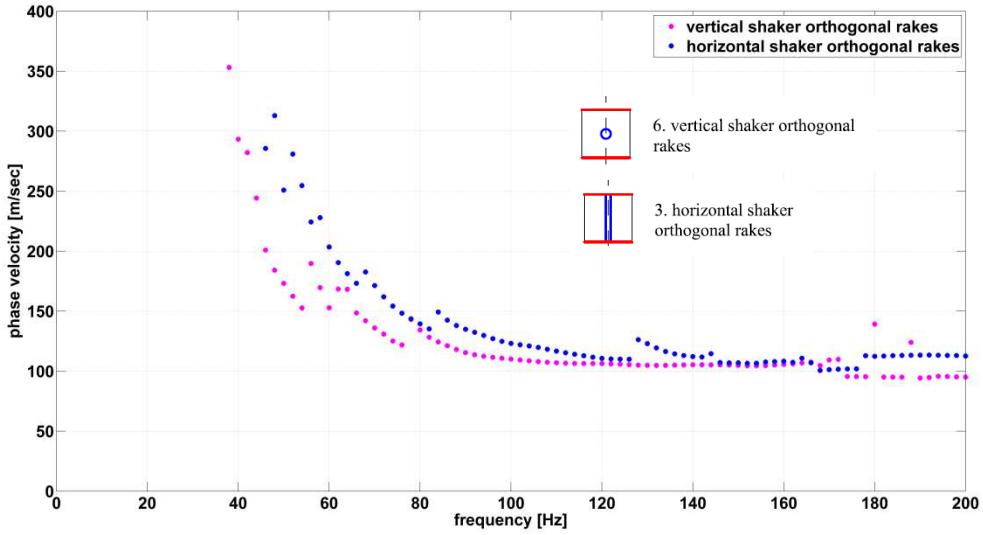

Figure 5.10: Dispersion curves with excitation methods 3 and 6.

Figure 5.11 and Figure 5.12 depict the comparison between dispersion curves obtained using the same direction of excitation, but different sizes of the circular coupling. It can be noticed that the estimation of the phase velocity is also sensitive to the change of the source-to-ground coupling, since the small circular plate seems to lead to a generation of a bigger amount of body waves at high frequencies, and hence to a higher estimation of the actual phase velocity. Thus, a stiffer (i.e. a circular plate with bigger diameter) source-to-ground coupling is preferable for generation of Rayleigh waves.

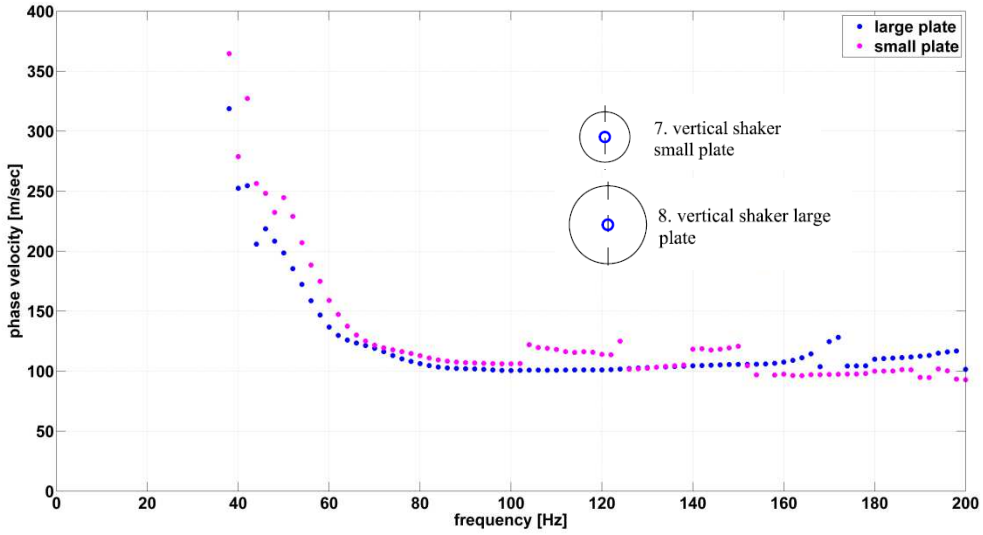

Figure 5.11: Dispersion curves with excitation methods 7 and 8.

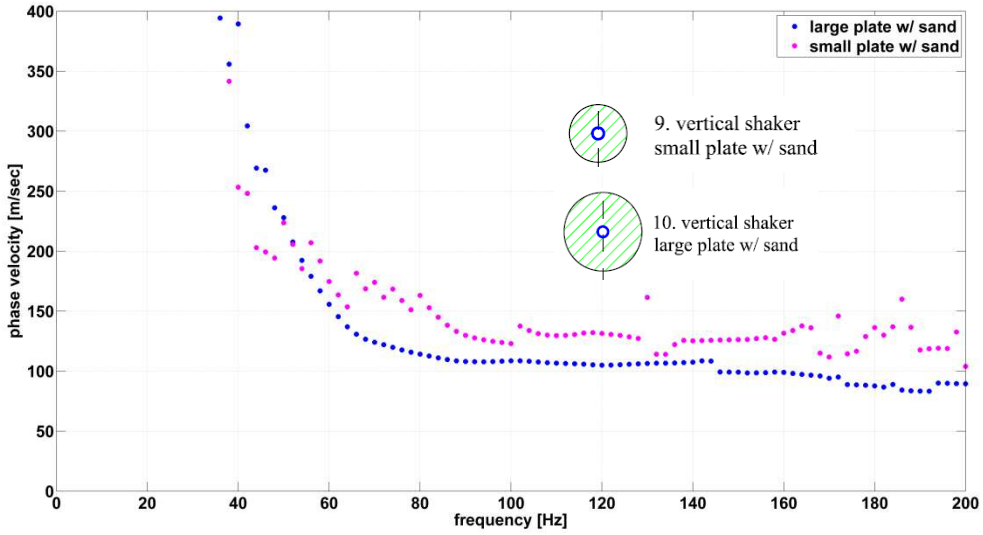

Figure 5.12: Dispersion curves with excitation methods 9 and 10.

5.2.2 Comparison of Shaker Sizes

This experimental session aimed at assessing and at comparing the effects on the dispersion curves obtained with the cross-power spectral method, of different shaker sizes and different directions of excitation. The experimental set-up consisted of a source and an array of 7 tri-axial geophones, disposed as in Figure 5.13. The duration of the signal L_f was 2 sec. The time extended signal was a white noise, with a unit variance and low pass filtered at 4 kHz, in order to avoid aliasing.

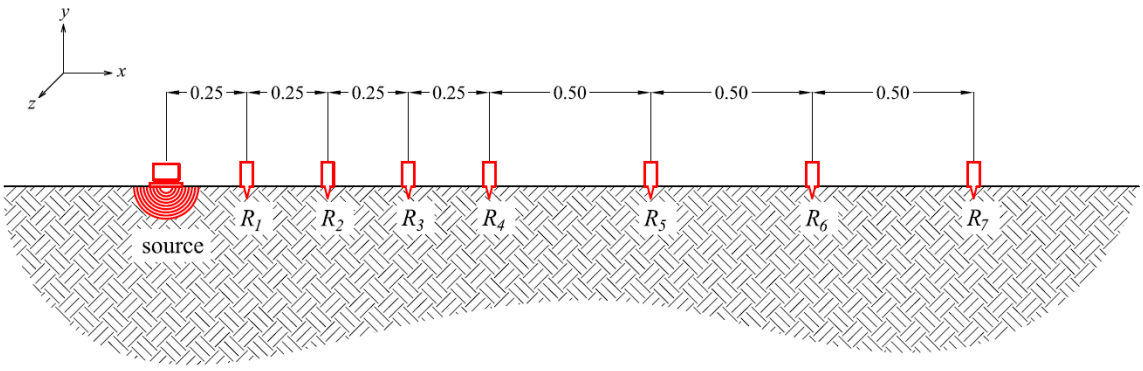

Figure 5.13: Experimental set-up for comparison of shaker sizes, *R* refers to a geophone and the number identifies the position. Distances are shown in metres (the symbol represents the shaker in its vertical arrangement).

In this experimental session, two shakers with different sizes were utilized:

- IV40 Data Physics inertial shaker, with a nominal moving mass of 1.21 kg, which will be recalled as “small” shaker.

- IV45 Data Physics inertial shaker, with a nominal moving mass of 4.20 kg, which will be recalled as “big” shaker.

The same steel platforms used in the experimental session of section 5.2.1 were used in order to assess different couplings, with its rakes bolted in the parallel arrangement. Figure 5.14 lists the excitation methods tested in this session.

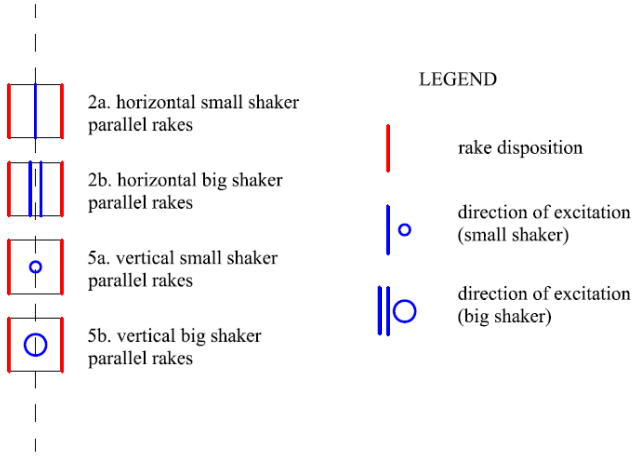

Figure 5.14: Excitation methods tested at the experimental session for the comparison of shaker sizes (top view).

Figure 5.15 and Figure 5.16 show a comparison between the dispersion curves obtained with vertical and horizontal excitation methods. One can notice again that horizontal excitation methods lead to an overall higher estimation of the phase velocity, while the velocity estimated through vertical excitation is generally lower. For the sake of brevity, only the comparison between horizontal and vertical excitation methods is reported herein.

As can be seen in the Appendix D, the coherence being close to 1 is a guarantee of linear behaviour of soil. The coherence though is low for frequencies lower than 100 Hz, where the dispersion curves do not show relevant information: the lowest limit is imposed by the length of the array of sensors. In this case the distance between geophone 1 and geophone 7 is 2.25 m, which, given a R-wave velocity of 150 m/s, allows to correctly acquiring down to the frequency of approximately 140 Hz.

It can be noticed that the estimation of the phase velocity is affected by the size of the shaker. By comparing the estimation of the phase velocity obtained with the small and the big shakers in their vertical arrangement (Figure 5.15 and Figure 5.16) it can be observed that the use of the IV40 (small) shaker generally leads to a higher estimation of the phase velocity. This is again linked to a different

amount of body wave energy produced in the process of ground excitation: the IV45 (big) shaker seems to be able to better generate Rayleigh waves.

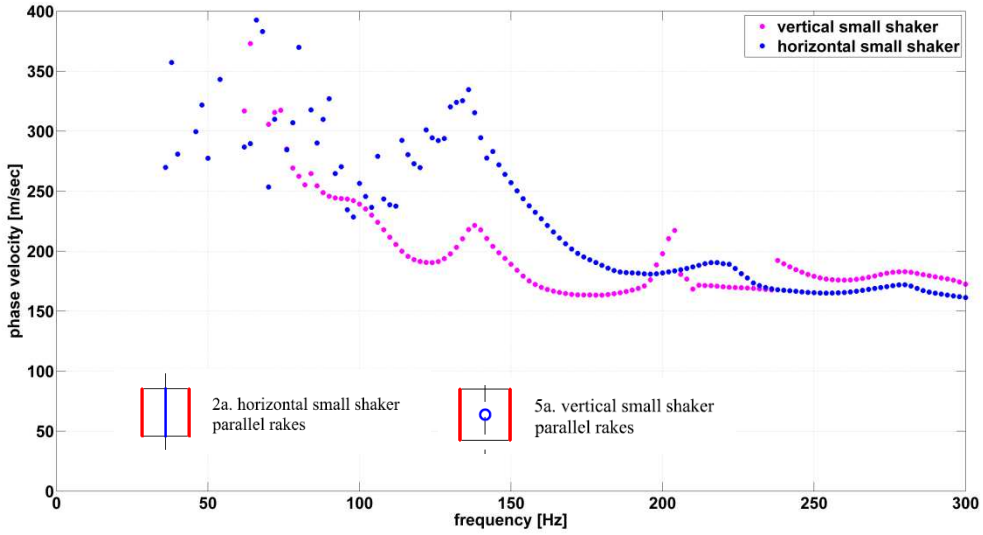

Figure 5.15: Dispersion curves with excitation methods 2a and 5a.

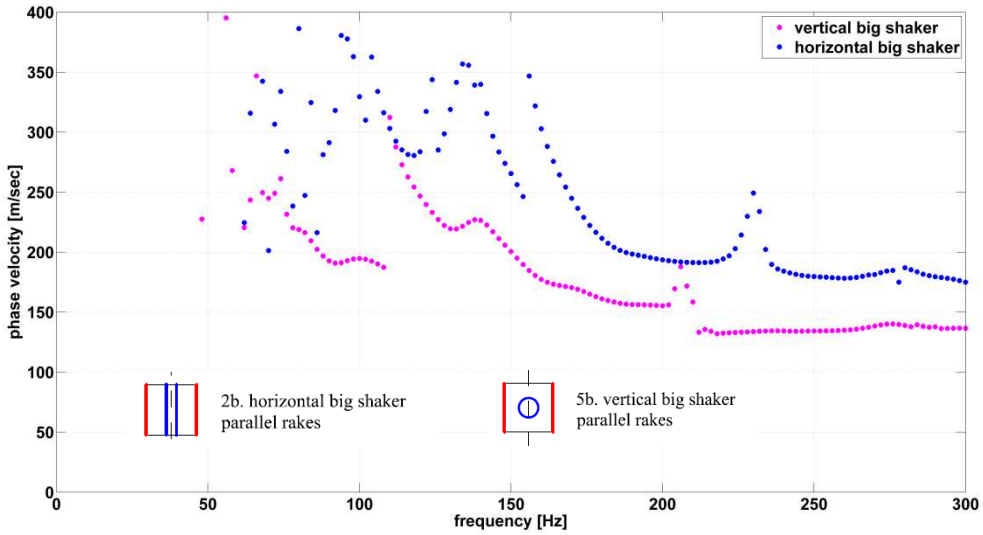

Figure 5.16: Dispersion curves with excitation methods 2b and 5b.

It is possible to observe a jump in the phase velocity trend at a frequency of approximately 150 Hz: this is compatible with a mode switch in the propagation pattern. This behaviour of the dispersion curve might suggest a layered soil system for the shallow surface, with a big velocity contrast between the layers' stiffness.

As observed in the previous investigation (section 5.3.1), horizontal methods produced a bigger amount of body waves which resulted in a higher estimation of the phase velocity if the cross-power

spectral density method was utilized to produce the dispersion curve. The size of the shaker affected the estimation of the phase velocity: a small shaker in the vertical arrangement was found to be capable of producing more body wave energy compared to a heavier one.

5.2.3 Numerical Simulations

A numerical investigation was carried out to compare and validate the results coming from the experimental sessions. For this purpose, simulations were accomplished with the model of a half-space (model "1") using the same parameters reported in section 3.6. Load #1 was evenly distributed along a surface line of 0.10 m.

When simulating the vertical load, load #1 was applied normally to the surface, while when simulating the horizontal load, load #1 was applied tangentially to the surface. A moment $x(t) = b \cdot y(t)$, acting normally to the *z*-direction, was also applied to the centre of the surface, where b is the arm of the moment and is equal to 0.05 m, and $y(t)$ is the time history of load #1.

The excitation source was 0.25 m apart from the deployment of sensors, which consisted of 36 nodes spaced 0.05 m each other.

Hence, the dispersion curves associated with each direction of excitation were obtained following the cross-power spectral method (see section 3.2), using vertical traces coming from each of the 36 nodes of the survey array. The results are shown in the following Figure 5.17, where the red horizontal line indicates the actual R-wave velocity of the half-space.

The estimation of the phase velocity varies according to the different adopted directions of ground excitation. The estimation of the phase velocity with the spectral method is highly influenced by the presence of multiple waves. In the case of the vertical excitation method, the amount of body waves can be neglected, although the R-wave velocity is slightly overestimated. In the case of the horizontal excitation method, the amount of body wave energy is bigger, leading to an overestimation of the R-wave velocity, which can be clearly observed in Figure 5.17. Numerical results were hence consistent with the experimental results: the horizontal excitation produced a bigger amount of body wave energy causing a relevant overestimation of the phase velocity.

Albeit simulations were run on a half-space, the phase velocity seemed to have a dependency on frequency and it showed a gradient: this effect was likely to be linked to the far-field effect. The body waves became predominant at far offsets and for the high frequencies, causing a bigger overestimation at high frequencies if the cross-power spectral method was used to assess the wave speed.

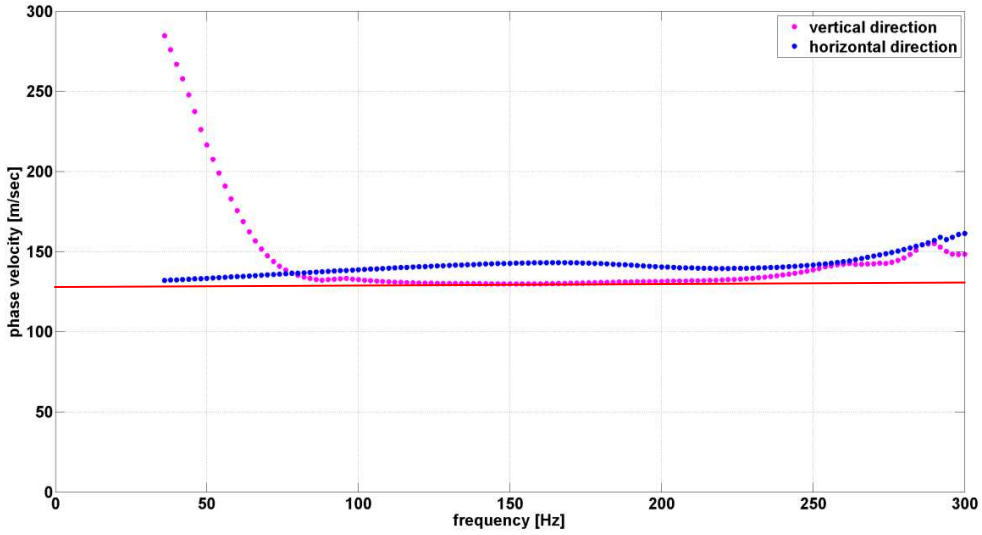

Figure 5.17: Dispersion curves from simulations on a half-space with vertical and horizontal excitation methods. Horizontal excitations produce a bigger amount of body waves, causing an overestimation of the R-wave velocity with the cross-power spectral method. The red horizontal line indicates the actual analytical R-wave velocity in the half-space.

5.2.4 Summary of the Comparison of Soil Excitations

The results from two experimental sessions were presented in this section. They were carried out in order to see the effects of different types of excitation, directions of excitation, source sizes and source-to-ground couplings, on the estimation of the phase velocity of soils. They also had the aim at highlighting the drawbacks and limitations of the use of the cross-power spectral method for the processing of seismic data. The generation of seismic waves in a soil was found to be influenced by all of the aforementioned variables.

Vertical continuous sources exhibited good reliability as R-wave sources in soils. In fact, we know that 2/3 of the energy of a vertical source is converted into R-wave (section 2.2). Horizontal continuous sources produced also a significant amount of body wave energy, which became predominant at far offsets. This caused a different estimation of the phase velocity if the cross-power spectral method was used for processing the data: horizontal methods generally led to a higher estimation of the phase velocity. The stiffer was the coupling between the source and the ground, the more reliable was the source in terms of R-wave generation. Plates ensuring a wider contact surface with the ground were found to be better for the generation of Rayleigh waves. A heavy shaker (4.20 kg) exciting vertically was found to be more reliable than a lighter shaker (1.21 kg) exciting in the same direction, in terms of R-wave generation.

Nonetheless, in the next experimental sessions a 4-oz mallet striking on a circular metallic plate of 0.15 m diameter will be used as a source of excitation, since it ensured more energy in the frequency range 0-200 Hz, which is the typical range of interest in seismic soil surveys, and for being fast and practical to use.

Cross-power spectral method proved to be unable to discern different type of waves and different modes of propagation of Rayleigh waves. The dispersion measurement obtained with the spectral technique was rather an average dispersion of different waves and modes of propagation showing up in the surveyed medium. In the next experimental tests within this thesis, the seismic data will be processed with the frequency-wavenumber transformation, as explained in section 3.3.

5.3 Surface Wave Dispersion Measurement of Soil

This section details the results and the physical interpretation of two soil dispersion measurements executed via the MASW technique and processed in the *f-k* domain using vertical, horizontal and spectral convolution signals. Spectral convolution spectra were inverted using the information gathered through the DCP investigations to constrain the problem.

The two investigations, although carried out both in urban settings, differ in the soil stratification: the first soil seems to show the presence of a thin soft layer sandwiched between two stiffer layers while the second soil seems to be loose sediment over a stiffer layer.

The next experimental investigations aimed at highlighting the differences that may occur between the vertical and horizontal spectra, and hence the danger in choosing (or excluding) one direction from the seismic survey. It also aimed at showing and describing the advantages of the spectral convolution method for seismic surveying of soils, compared to the fashions using only one direction at time.

5.3.1 Dispersion Measurement of Soil at Birmingham

The experimental set-up consisted of a source and an array of 21 tri-axial geophones, disposed as shown in Figure 5.18, covering a length L_s of 5.25 m. The duration of the signal L_f was 3 sec. The source consisted of a 4-oz metallic mallet striking on a circular aluminium plate of 0.15 m diameter and 1.5cm thickness, resting on the ground surface. The data acquisition was triggered with respect to the hammer impact.

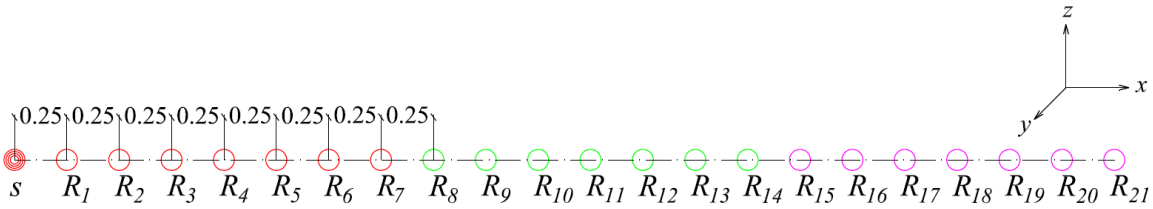

Figure 5.18: Experimental set-up for the Birmingham test site. *R* refers to a geophone, *s* refers to source and the number identifies the position. Distances are shown in metres (top view).

The choice between a vertical continuous source and a vertical transient source was based on the analysis of the signal power in the frequency domain. A 4-oz metallic mallet striking on a circular metallic plate of 0.15 m diameter and a 4.20 kg inertial shaker vertically bolted on the same circular plate were compared in terms of power of their auto-spectrum. The time extended signal for the shaker was a sweep sine ranging from 1 Hz to 1 kHz, low pass filtered at 4 kHz. The signal was acquired via an accelerometer attached onto the surface of the circular plate. The 4-oz mallet has was chosen since it ensured more energy in the frequency range 0-200 Hz, which is the typical range of interest in seismic soil surveys, as shown in Figure 5.19, and for being fast and practical to use.

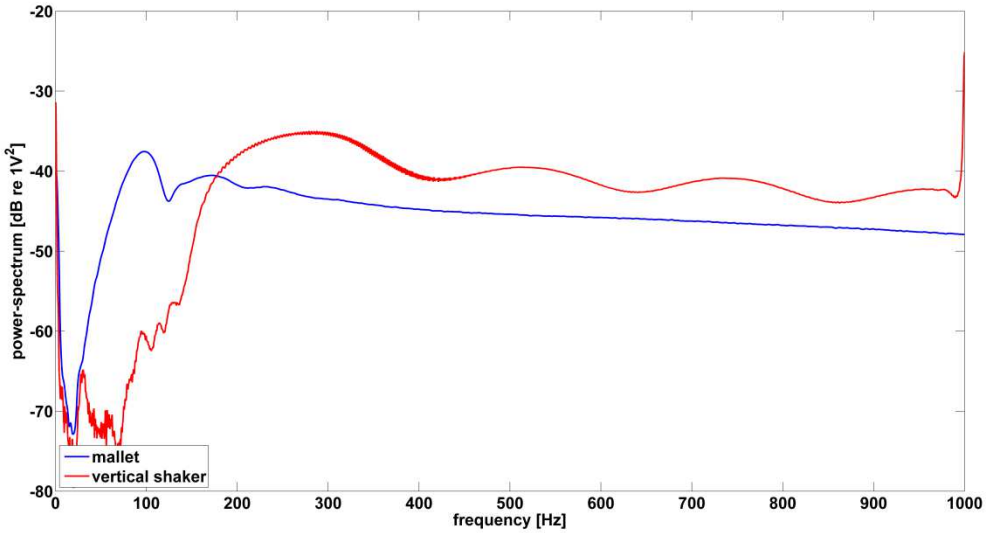

Figure 5.19: Comparison of the auto-spectrum of the signal by a 4-oz mallet and by a 4.20 kg inertial shaker on circular metallic plate of 0.15 m diameter.

Figure 5.20(a), Figure 5.20(b) and Figure 5.20(c) depict respectively the vertical, horizontal and spectral convolution *f-k* spectra, in which the black dots indicate the extracted energy maxima of the *f-k* spectra. Due to the anisotropy of the material tested, the vertical and the horizontal components of motion give different information for the evaluation of the dispersive relation. In fact, two modes

seem to appear in the spectrum obtained with the vertical traces (Figure 5.20(a)): the energy is distributed to one slower mode (probably the fundamental mode) up to a frequency of approximately 50 Hz, then switching to one higher order and more energetic mode (for lower wavenumbers). In the spectrum obtained with horizontal traces (Figure 5.20(b)) instead, the maxima remain predominantly on the fundamental (mode0). There is lack of energy at around 60 Hz and 80 Hz, where the motion is prevalently vertical. Considering only the vertical motion could lead to a misidentification of the fundamental mode and to an overestimation of the shear velocity of the soil deposit. The spectrum obtained with the spectral convolution method (Figure 5.20(c)), clearly details the presence of two, if not three, modes of propagation: the energy is distributed in the fundamental mode up to the frequency of approximately 70 Hz, when it switches to the first order mode, then probably switching back to the fundamental from the frequency of approximately 160 Hz to 200 Hz. The energy seems to be distributed to the second order mode from the frequency of 40 Hz onward, and the fundamental and first order mode are close together. The spectral convolution spectrum has narrower energy peaks, i.e. a superior resolution in both the frequency and the wavenumber domain. It presents a better mode separation, allowing the detection of the first two clearly separated and well defined modes of propagation. The spectral convolution spectrum also contains information in the low frequency range (frequencies lower than 35 Hz), where is possible to notice clear energy peaks, while it is impossible to extract this information from the vertical and horizontal spectra. Hence, the spectral convolution method helps in the definition of the long wavelengths since it is equivalent to a multichannel record with doubled length in space. The spatial Nyquist's criterion limits the maximum value of frequency to approximately 200 Hz.

Figure 5.21 details the dispersion curves in the phase velocity-frequency domain as obtained from the extraction of the peaks of energy of the *f-k* spectra. The fundamental mode of propagation and the first order mode are visible in the vertical dispersion curve, with a mode switch at approximately 50 Hz. The horizontal dispersion curve seems to show mainly parts of the fundamental mode of propagation. The spectral convolution dispersion curve shows a trend in which the energy distributes in the fundamental mode up to the frequency of approximately 60 Hz and then it switches to the higher order mode of propagation. The spectral convolution dispersion curve overlaps the vertical dispersion curve up to the frequency of 60 Hz and for a portion of the higher order mode.

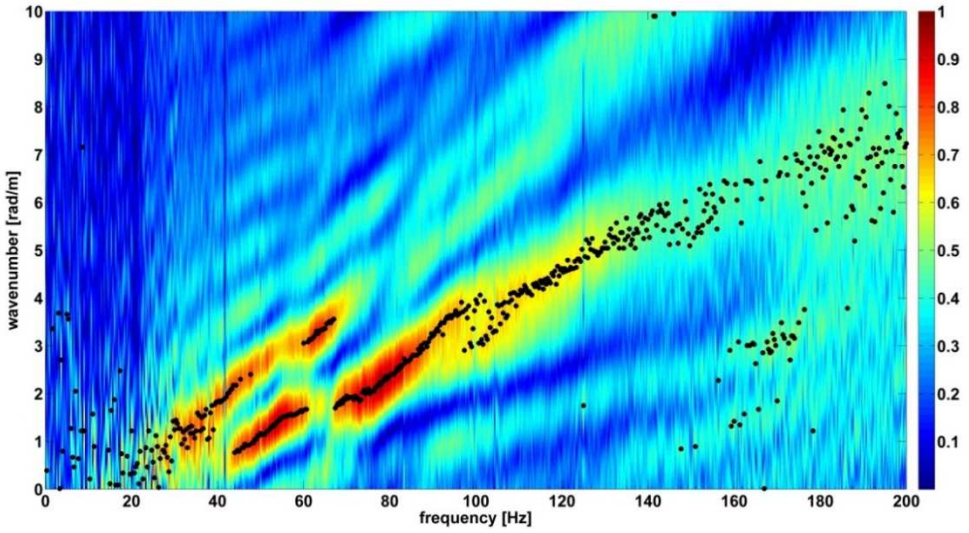

(a)

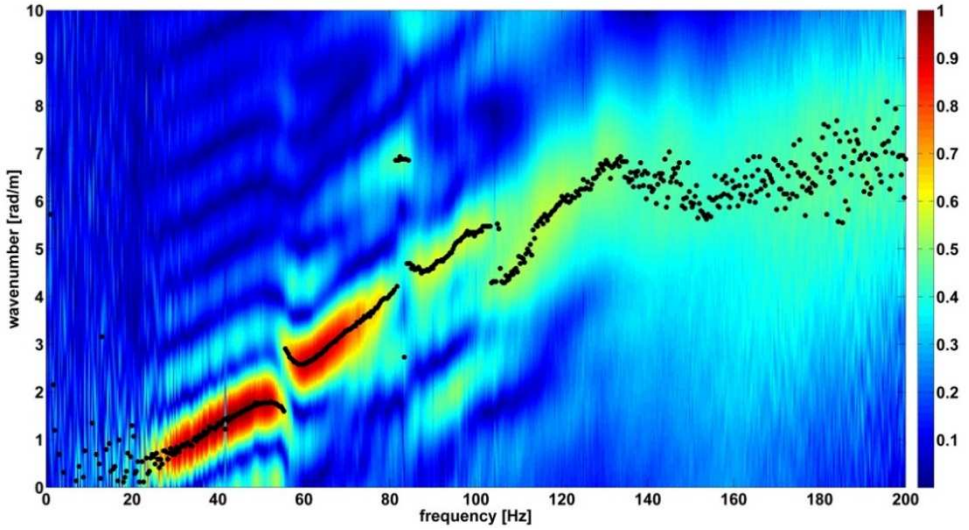

(b)

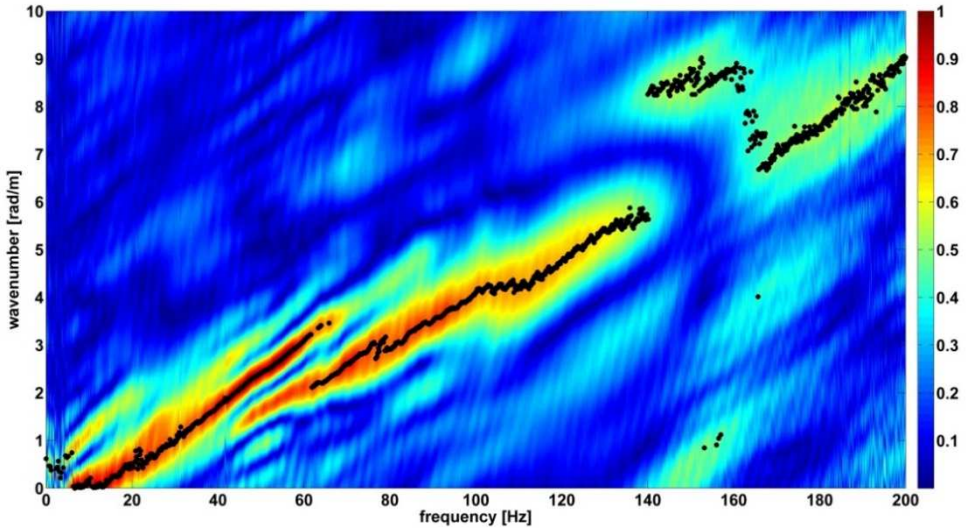

(c)

Figure 5.20: *F-k* spectrum with vertical (a), horizontal (b) and spectral convolution (c) traces for the dispersion measurement of soil at Birmingham ($L_s = 5.25\text{m}, N = 21$). The black dots indicate the extracted energy maxima of the *f-k* spectrum.

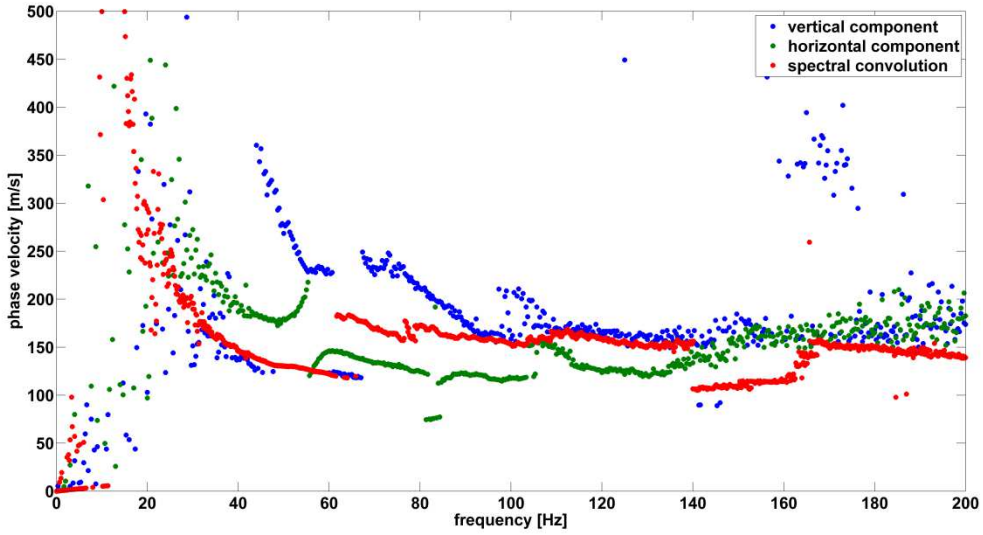

Figure 5.21: Vertical, horizontal and spectral convolution dispersion curves in the phase velocity-frequency domain, dispersion measurement of soil at Birmingham.

The ellipticity curve depicted in Figure 5.22 is almost consistent in the range of excited frequencies, with the horizontal to vertical ratio oscillating around the value of 4. It is not possible to identify any major peaks or local minima. The shape of the ellipticity curve suggests a profile with no big impedance contrast between shallow layers and substrate, and modes of propagation distant and separated. The phase of the ellipticity curve does not display any relevant information within the range of excited frequencies.

The DCP investigation was executed along the survey line, where geophone 6 is located (see Figure 5.18). The DCP field curve is depicted in Figure 5.23. The stiffness of the soil can be related to the slope of the DCP curve, which is generally consistent up to a depth of 0.40 m, where a change in the slope can be observed. This is compatible with the presence of a soft layer sandwiched between two stiffer layers. From the depth of 0.70 m onward, the slope of the DCP curve remains consistent, suggesting the presence of a third layer. The trend of the DCP is consistent with the physical interpretation of the ellipticity: the stiffness does not show abrupt changes along the profile depth.

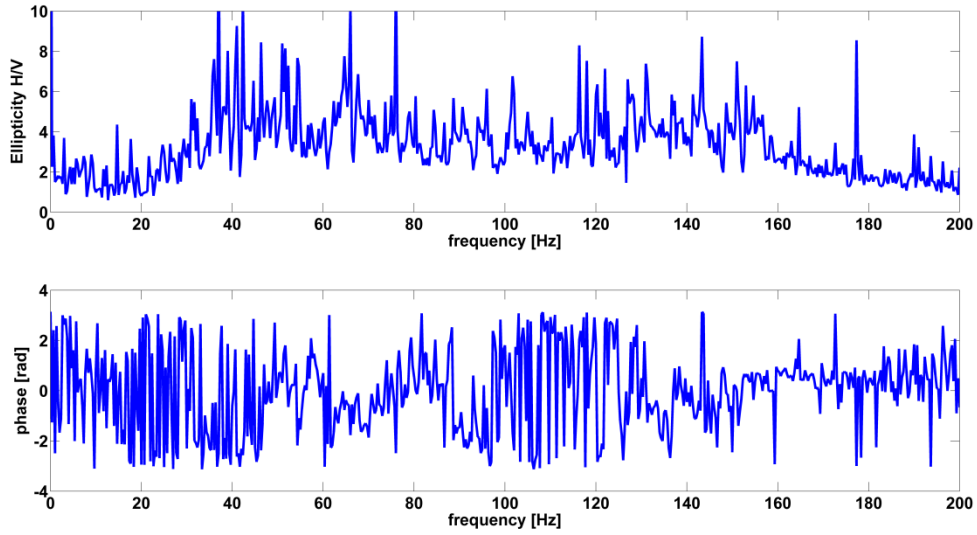

Figure 5.22: Amplitude and phase of the ellipticity curve for the Birmingham test site. The ellipticity is consistent and flat in the range of excited frequencies.

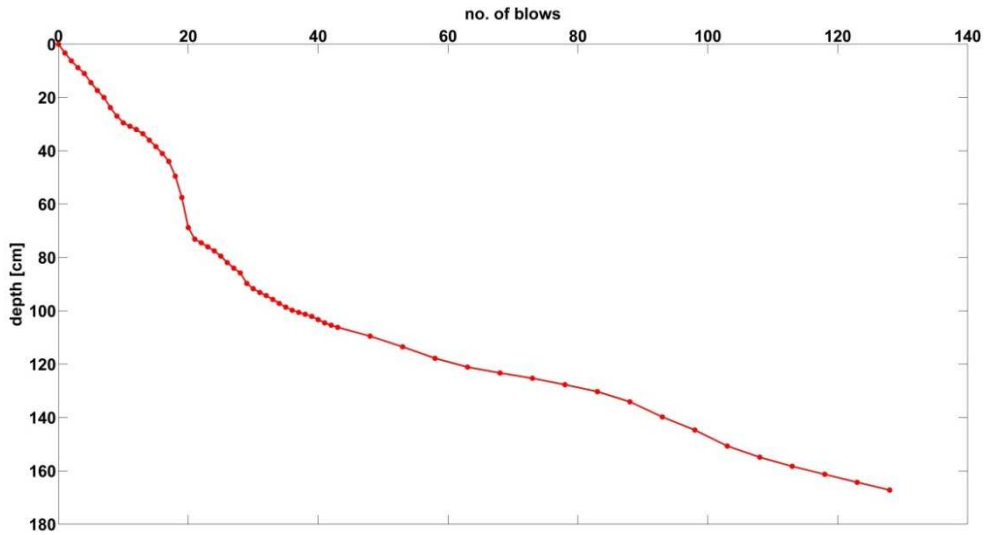

Figure 5.23: DCP field curve for the Birmingham test site. The curve might suggest the presence of a three-layered system, with a slight change in the material stiffness at the depth of approximately 0.40 m, compatible with the presence of a soft layer sandwiched between two stiffer layers.

The information extracted from the spectral convolution spectrum, the ellipticity curve and the DCP curve concur to infer a layered system with no big velocity contrasts, with possibly a softer layer sandwiched between two layers with similar stiffness between the depths of 0.40 m and 0.70 m. Therefore, the ground appears not to be normally dispersive. This is quite a usual case for many urban and man-made settings.

5.3.2 Dispersion Measurement of Soil at Chilworth

The experimental set-up consisted of a source and an array of 21 tri-axial geophones, disposed as shown in Figure 5.24, covering a length L_s of 5.25 m. The duration of the signal L_f was 1 sec.

The shallow soil was very moist due to the heavy rain fallen the days prior the survey.

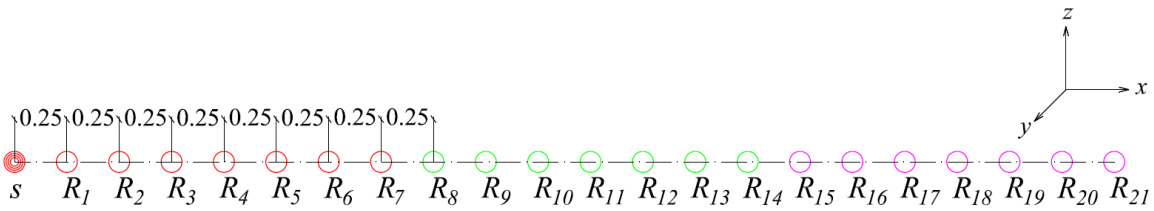

Figure 5.24: Experimental set-up for the Chilworth test site. *R* refers to a geophone, *s* refers to source and the number identifies the position. Distances are shown in metres (top view).

The source consisted of a 4-oz metallic mallet striking on a circular plate of 0.15 m diameter and 1.5cm thickness, resting on the ground surface. The data acquisition was triggered with respect to the hammer impact. Figure 5.25(a), Figure 5.25(b) and Figure 5.25(c) depict respectively the vertical, horizontal and spectral convolution *f-k* spectra, in which the black dots indicate the extracted energy maxima of the *f-k* spectra. Again, due to the anisotropy of the material tested, the vertical and the horizontal components of motion give different information for the evaluation of the dispersion relation. In the vertical spectrum (Figure 5.25(a)) just one mode appears, probably not the fundamental but one of the higher order modes corresponding to the surveyed layered system. It could also be a superposition of two or more modes, which appear as one mode in the spectrum due to lack of resolution. In the horizontal spectrum (Figure 5.25(b)), two modes of propagation are clearly observed, with a mode jump at the frequency of about 70 Hz. The faster mode is probably the same mode of propagation detected with the vertical motion, while at lower frequencies a lower order mode or again a superposition of two modes is present. Considering only the vertical spectrum would lead to misidentify its energy maxima for the fundamental mode, leading to a complete erroneous interpretation of the seismic survey. The spectral convolution spectrum (Figure 5.25(c)) displays a specific trend in which moving from the low to the high frequencies, the energy splits to higher and higher modes (“mode splitting”, [22]).

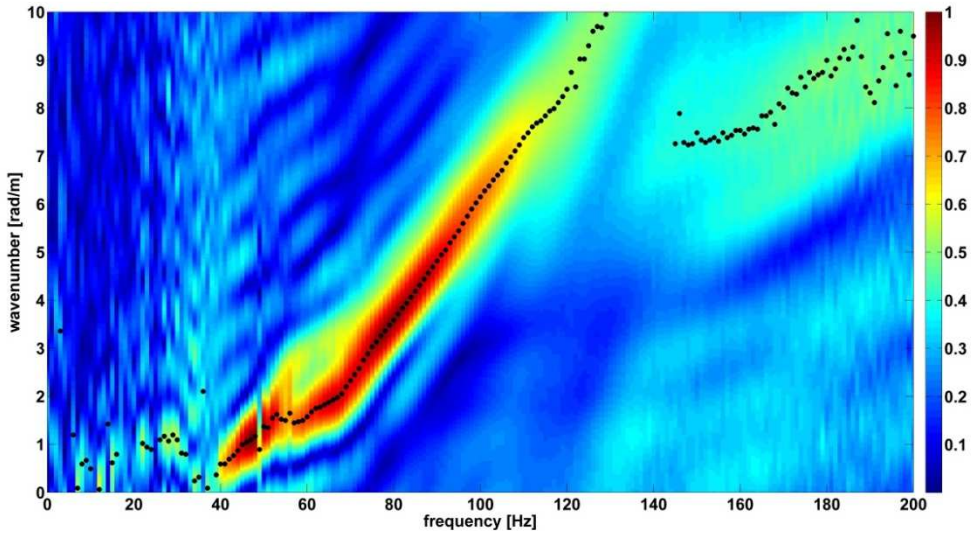

(a)

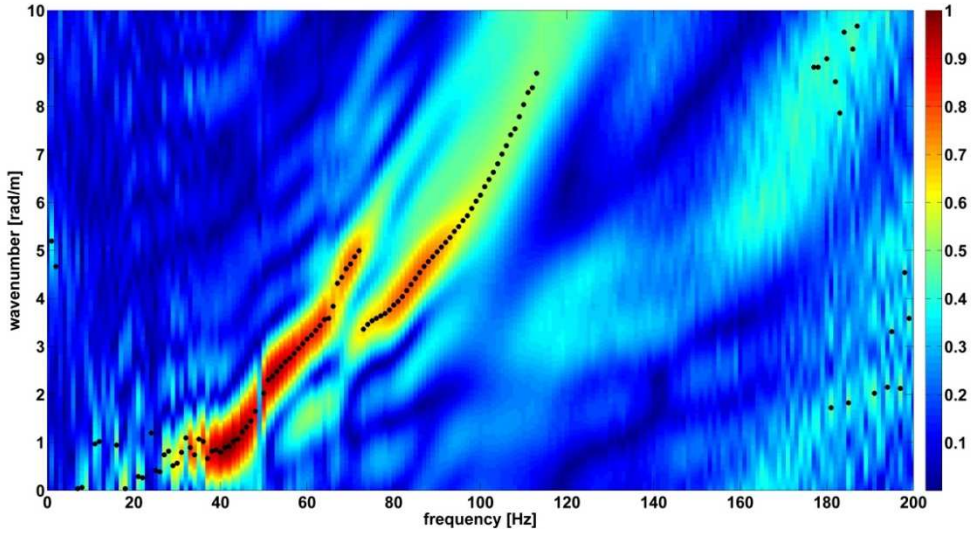

(b)

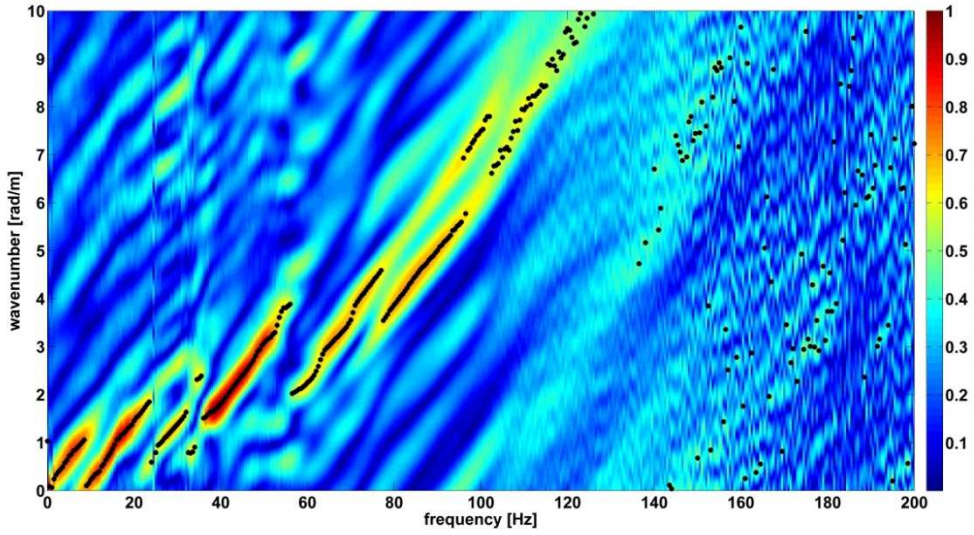

(c)

Figure 5.25: *F-k* spectrum with vertical (a), horizontal (b) and spectral convolution (c) traces for the dispersion measurement of soil at Chilworth ($L_s = \mathbf{5.25m}$, $N = 21$). The black dots indicate the extracted energy maxima of the *f-k* spectrum.

The propagation modes in the spectral convolution spectrum are very close each other and the energy switches from the fundamental to the higher order modes, as it happens in the case of velocity inversions or a strong impedance contrast. The spectral convolution spectrum has narrower energy peaks, i.e. a superior resolution in both the frequency and the wavenumber domain. It presents a better mode separation, allowing the detection of the first five clearly separated and well defined modes of propagation.

The spectral convolution spectrum also contains information in the low frequency range (frequencies lower than 35 Hz), where is possible to notice clear energy peaks, while it is impossible to extract this information from the vertical and horizontal spectra. Hence, the spectral convolution method helps in the definition of the long wavelengths since it is equivalent to a multichannel record with doubled length in space. The spatial NY Quist criterion limits the maximum value of frequency to approximately 140 Hz.

Figure 5.26 details the dispersion curves in the phase velocity-frequency domain as obtained from the extraction of the energy maxima of the *f-k* spectra. Consistently with the *f-k* spectra, only one of the higher order modes is visible in the vertical dispersion curve. This can be misled for the fundamental mode if the vertical signal is only used for the characterization of the medium. Two modes are observed in the horizontal dispersion curve. The higher one overlaps the mode observed in the vertical dispersion curve; the slower one is possibly a combination of two modes with very close velocities. The spectral convolution dispersion curve shows evidence of five modes in the range of excited frequencies, with a specific trend in which the energy switches from the fundamental mode to higher order modes.

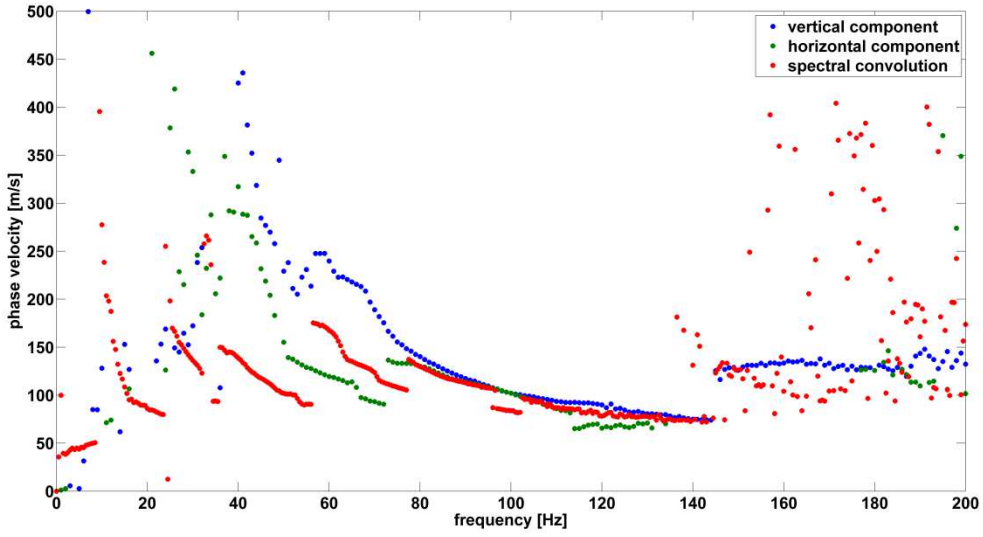

Figure 5.26: Vertical, horizontal and spectral convolution dispersion curves in the phase velocity-frequency domain, for the dispersion measurement of soil at Chilworth.

The amplitude of the ellipticity curve, depicted in Figure 5.27, shows several local minima, at the frequencies of approximately 22 Hz, 35 Hz, 50 Hz and 90 Hz. These minima in the R-wave ellipticity occur at the osculation frequencies, where the velocity of two modes is close and the energy shifts from one mode to another. The minima in the ellipticity are consistent with the *f-k* spectrum obtained with the spectral convolution method, which displays a specific trend related to the so-called "mode splitting". The local minima of the ellipticity curve are consistent with the osculation points visible in the spectral convolution dispersion curve of Figure 5.26. The ellipticity shows several peaks, the first and sharpest peak shows up at the frequency of approximately 38 Hz: it is consistent with the presence of a strong shallow impedance contrast between the soil and the stiffer deep layer. The first sharpest resonant peak probably corresponds to the "shear wave resonance" of the top layer. In fact, following equation (3.4) and assuming a shear velocity of 150 m/s (extracted from the dispersion curve depicted in Figure 5.26), the thickness of the top layer is about 1 m. Moreover, the high value of the horizontal to vertical ratio at the resonance peak (larger than 10) suggests the presence of a strong velocity contrasts between the horizontal layers of the surveyed medium. The phase of the ellipticity is not consistent throughout the range of excited frequencies, as it happened for the numerical simulation of section 4.1.1. Several phase jumps are observable: they seem to occur at the frequencies at which peaks in the ellipticity curve occur, and in any case very close to the frequencies at which the osculation points occur. In the frequency ranges between 40 Hz and 50 Hz, between 60 Hz and 70 Hz and between 80 Hz and 100 Hz the phase assumes almost a constant value.

A DCP investigation on the same site, although executed in a different experimental session and in different weather conditions, could be representative of the soil deposit profile. The DCP investigation (see section 1.7) was executed along the survey line, between the location of geophone 3 and geophone 4. The DCP investigation depicted in Figure 5.28 clearly shows the presence of a two-layered system, with a big velocity contrast between the top layers, up to a depth of 1 metre, and the subsoil. In the first metre, it is possible to notice a first stiffer layer of approximately 0.50 m overlaying a softer layer of 0.50 m, although the difference of stiffness between the first two layers is very subtle.

Hence the results extracted from the spectral convolution spectrum, the ellipticity curve and the DCP curve are consistent and suggest a layered system with a big impedance contrast between the shallow layers and the subsoil.

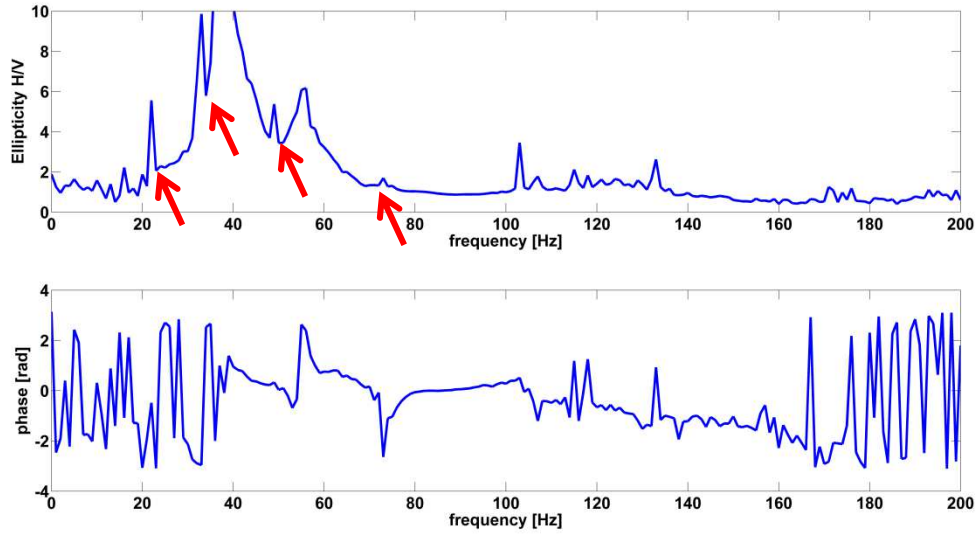

Figure 5.27: Amplitude and phase of the ellipticity curve for the Chilworth test site. The ellipticity shows several resonant peaks and several local minima at the frequencies of approximately 22 Hz, 35 Hz, 50 Hz and 90 Hz. Local minima are highlighted by red arrows. The first biggest peak corresponds to the “shear wave resonance of the top layer”.

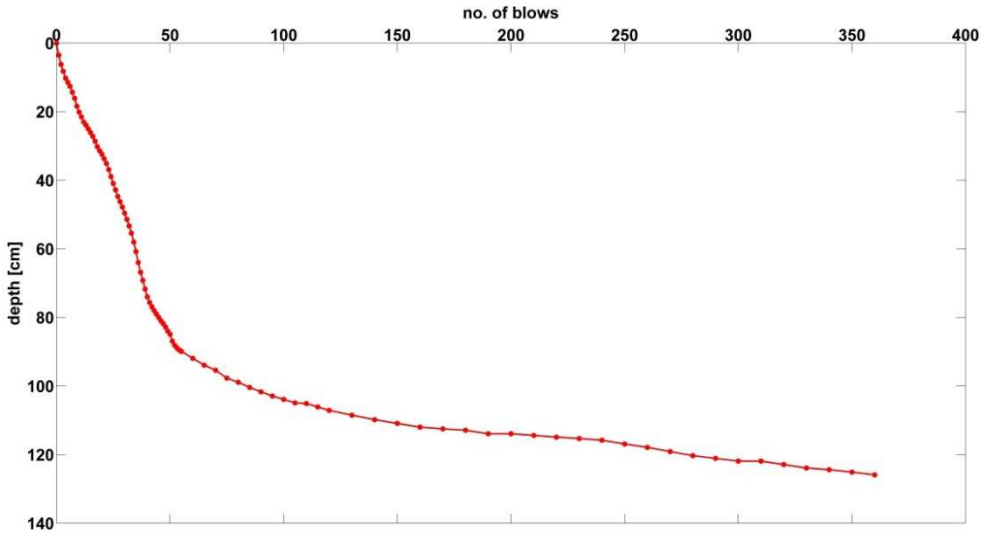

Figure 5.28: DCP field curve for the Chilworth test site. The test curve suggests a two-layer system for the soil deposit with a clear change in the stiffness at around one metre of depth. The test curve displays a big impedance contrast between the top layers and the subsoil.

5.3.3 Numerical Inversions

This section displays the results of two numerical inversions performed on the spectral convolution spectra of section 5.3.1 and 5.3.2. The results of the inversions aim at qualitatively characterize the investigated soils and do not affect the validity of the spectral convolution method. As explained in section 1.7, numerical inversion is a difficult, ill-posed problem for which different assumptions need to be defined beforehand. Hence, the outcomes need to be interpreted bearing in mind all the different assumption that they are subjected to. The results are dependent on various parameters, one of which is the weather conditions that the soil site experienced on the day of the survey. The error of the inversion process is more sensitive to the thickness and the mechanical parameters of the shallow layers and less sensitive to deeper layers' properties. For these reasons, the shallow layers' parameters had a smaller range but a finer step than those of the half-space. The sensitivity of Poisson's ratio and damping ratio was very small and almost negligible, and so they were fixed for each inversion's iteration.

The numerical inversions were carried out as described in section 4.3, choosing a layered model over an half-space and fixing the value of density equal to 2000 kg/m^3, the value of Poisson's ratio to 0.33 and the damping ratio to $0.25/200 \cdot 2\pi$ for each layer. The spectral convolution spectra were directly compared to vertical analytical spectra in the *f-k* domain, following equation (4.13), with the same aperture of 0-200 Hz for frequencies and of 0-4 π rad/m for wavenumbers.

PARAMETER	**RANGE**		**STEP**
	Birmingham	**Chilworth**	
Thickness third layer	1 m, 5 m, 10 m, 20 m		
Elastic modulus top layer	100÷500 MPa	10÷100 MPa, 200 MPa, 300 MPa	100 MPa
Elastic modulus second layer	10÷100 MPa	10÷100 MPa, 1 MPa, 2 MPa, 3 MPa, 4 MPa, 5 MPa, 6 MPa, 7 MPa, 8 MPa, 9 MPa	10 MPa
Elastic modulus third layer	100÷500 MPa		100 MPa
Elastic modulus half-space	500÷3000 MPa	500÷5000 MPa	500 MPa

Table 9: Parameters, ranges and steps used in the inversion process for the Birmingham and the Chilworth test sites.

For the Birmingham test site, the inversion process was carried out choosing a three layer over half-space system, fixing the thickness of the first two layers to 0.40 m and to 0.30 m respectively, and varying five parameters (the thicknesses of the third layer and the Young's modulus of the layers and of the half-space), according to the ranges and steps displayed in Table 9. For the Chilworth test site, the inversion process was carried out choosing a two layer over half-space system, fixing the thickness of the first two layers to 0.50 m, and varying the Young's modulus of the layers and of the half-space according to the ranges and steps displayed in Table 9. These assumptions were based on the outcomes of the *f-k* spectra, the ellipticity curve and the DCP curve.

Figure 5.29 depicts the physical model obtained after the inversion of the spectral convolution spectra. For the Birmingham test site, it consists of a soft shallow layer of 30 MPa of stiffness sandwiched between two layers of 400 MPa and 200 MPa each. The total thickness of the first three layers is 1.70 m. The half-space has stiffness of 500 MPa. For the Chilworth test site, it consists of a shallow layer with stiffness of 60 MPa overlaying a softer layer of 2 MPa and stiffer half-space with a stiffness of 500 MPa. The total thickness of the two shallow layers is 1 m.

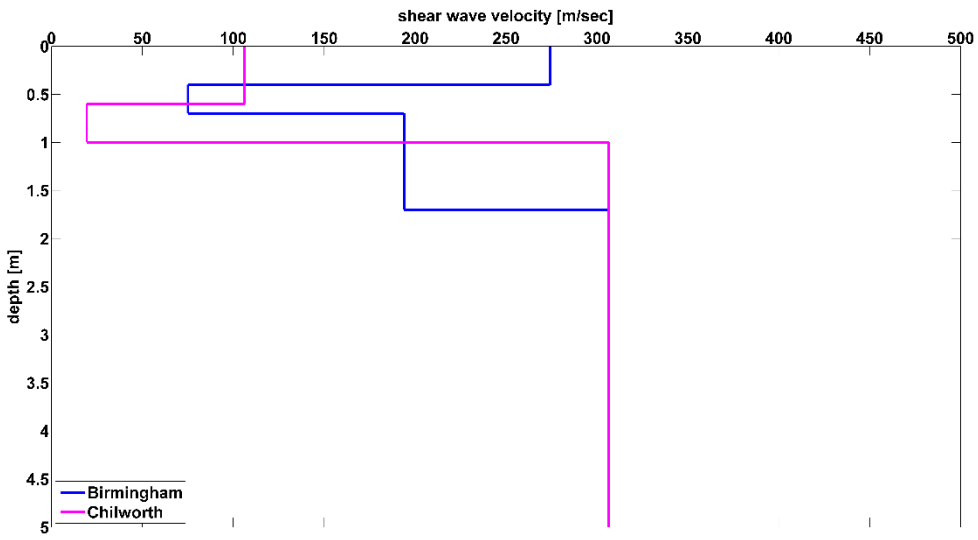

Figure 5.29: Shear wave velocity profile for Birmingham and Chilworth test sites, after inversion of the spectral convolution spectra.

Figure 5.30(a) displays the spectral convolution spectrum obtained experimentally, whereas Figure 5.30(b) the analytical, vertical spectrum of the stratification obtained from the inversion, for the Birmingham test site. The red superimposed lines in the latter indicate the different modes of propagation obtained from the equation (2.30). In the model obtained with the inversion the first fundamental mode is the most energetic up to a frequency of approximately 140 Hz. This behaviour is consistent with the information extracted from the ellipticity (Figure 5.22), which highlights neither mode jumps nor big velocity contrasts between layers. In the experimental spectral image,

the energy is also spread into the second mode of propagation, as discussed in section 5.4.1, then switching back to the fundamental mode at the frequency of approximately 120 Hz.

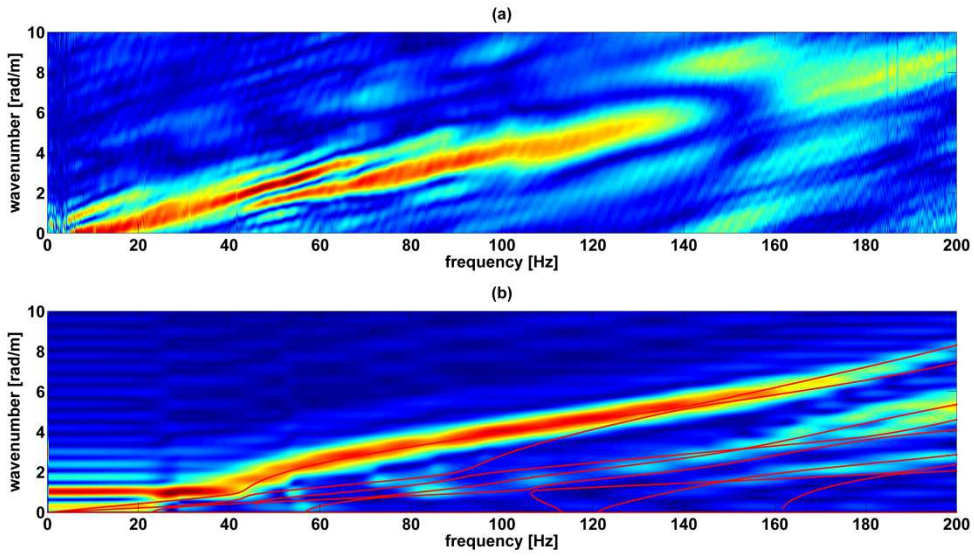

Figure 5.30: *F-k* spectral convolution spectrum obtained experimentally (a) and *f-k* analytical, vertical spectrum obtained from inversion (b), Birmingham test site.

Figure 5.31(a) displays the spectral convolution spectrum obtained experimentally, whereas Figure 5.31(b) the analytical, vertical spectrum of the stratification obtained from the inversion, for the Chilworth test site. The red superimposed lines in the latter indicate the different modes of propagation obtained from the equation (2.30). In the model obtained with the inversion, moving from the low to the high frequencies, the energy switches to higher and higher modes. The behaviour of the model is consistent with that observed experimentally and discussed in section 5.4.2. Particularly, it is consistent with the information extracted from the ellipticity (Figure 5.27), which shows several local minima and hence several mode jumps in the frequency range of investigation.

The inversions in this thesis were carried out fixing the values of density and of Poisson's ratio, and fixing the number of layers and their thicknesses' and elastic modulus' scopes based on some available *a-priori* information (DCP curves, ellipticity curves). The results from inversions displayed in this section reflect all the assumption and limitation described in section 1.7, section 4.3 and those descending from the choice of the parameters of Table 9, as well as the inversion algorithm proposed in section 4.3. Bearing in mind all their limitations, different algorithms and different assumptions could lead to different results and/or to less ambiguous layered models.

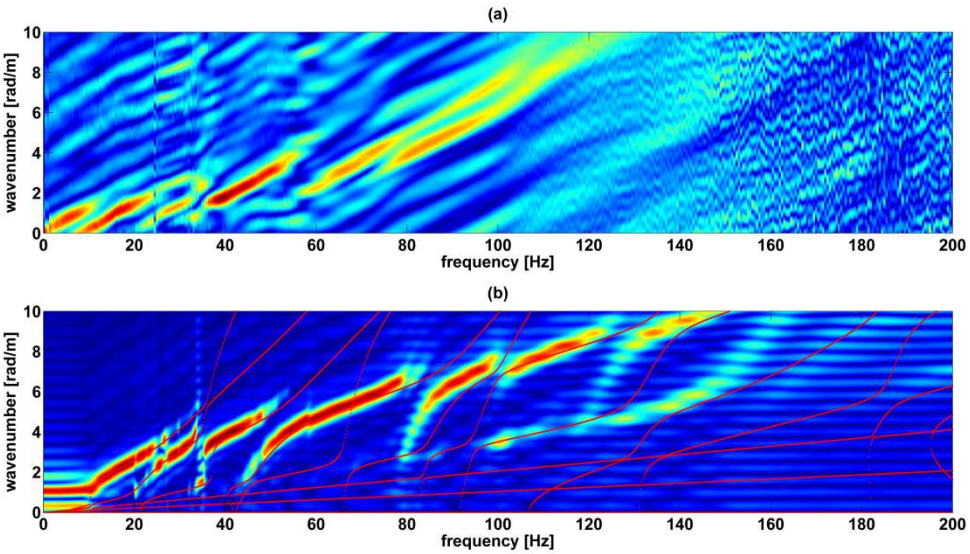

Figure 5.31: *F-k* spectral convolution spectrum obtained experimentally (a) and *f-k* analytical, vertical spectrum obtained from inversion (b), Chilworth test site.

5.3.4 Summary of the Surface Wave Dispersion Measurement of Soil

In this section, two soil deposits were surveyed via the MASW technique. Vertical, horizontal and spectral convolution spectra were obtained and compared.

Often some modes of propagation were superimposed and camouflaged under the same energy peaks due to lack of resolution. Sometimes the vertical and the horizontal components of motion showed a different distribution of energy among different modes: often one component only showed evidence of one mode (the fundamental or some higher order mode), while the other was a mixture of fundamental and higher order modes. The spectral convolution method tackled these issues by improving the resolution and the accuracy of the *f-k* spectrum. The results coming from the ellipticity curves, the DCP curves and the inversions were consistent with the spectral convolution spectra. Moreover, the spectral convolution method led to a higher resolution of the spectral image at the low frequencies and hence it opened up the possibility to survey bigger depths.

5.4 Surface Wave Dispersion Measurement of Asphalt

One experimental session was carried out in order to obtain preliminary dispersion measurement of surface waves in asphalt. It was executed with the MISW technique. For this purpose, experimental tests were performed in the parking area of the University of Southampton Glen Eyre Campus. The test site was expected to be composed by a base of asphalt over a foundation layer, each of which is 0.10 thick as reported in Mott MacDonald's Survey Report [100]. The results were displayed in the

form of vertical, horizontal and spectral convolution spectra. The data was acquired using a ProSig P8020 data acquisition unit and a laptop.

This experimental investigation also aimed at showing and describing the advantages of the spectral convolution method for seismic survey of roads, with respect to the traditional single component survey.

5.4.1 Dispersion Measurement of Asphalt

The experimental set-up consisted of a source and an array of 6 tri-axial geophones, arranged as in Figure 5.32 and Figure 5.33, covering an overall length L_s of 0.50 m. The duration of the signal L_f was 1 sec.

The source consisted of a 4-oz metallic mallet striking directly onto the surface. The auto-spectrum computed as per equation (3.1) from the signal of an accelerometer attached to the tip of the mallet showed a flat response up to a frequency of approximately 1 kHz, as depicted in Figure 5.34. The multichannel record was obtained with the MISW technique (section 1.4.3), subsequently moving apart the source by 0.60 m four times, resulting in a multichannel record of 24 traces and length L_s of 2.40 m.

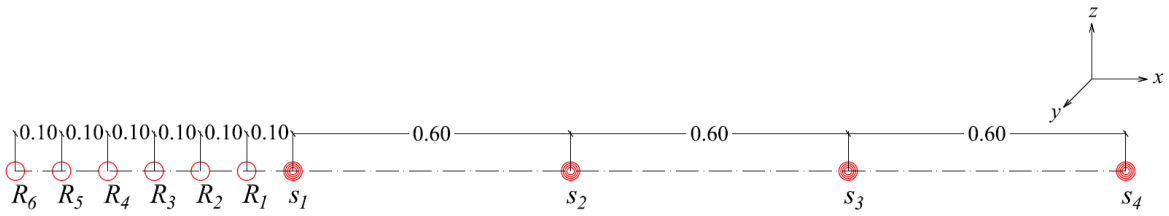

Figure 5.32: Experimental set-up for the dispersion measurement of asphalt. *R* refers to a geophone, *s* refers to source and the number identifies the position. Distances are shown in metres (top view).

Figure 5.33: Experimental set-up for the dispersion measurement of asphalt.

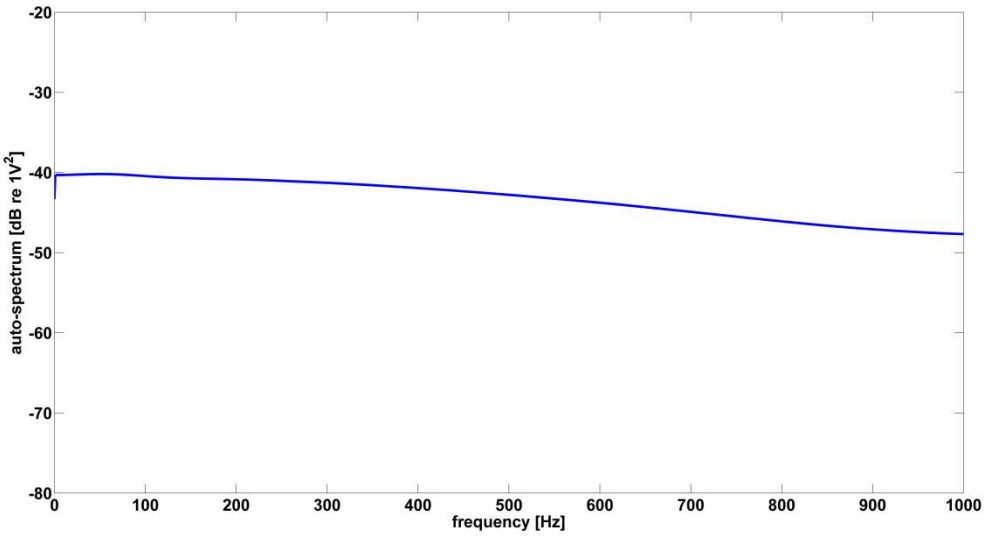

Figure 5.34: Auto-spectrum of the signal of an accelerometer mounted on top of the body of the mallet.

Figure 5.35(a), Figure 5.35(b) and Figure 5.35(c) depict respectively the vertical, horizontal and spectral convolution *f-k* spectra obtained as described in Chapter 4, in which the black dots indicate the extracted energy maxima of the *f-k* spectra. The vertical spectrum (Figure 5.35(a)) shows continuous peaks associated with the red bands, for the whole range of excited frequencies, with a trend that can be linked to the R-wave propagation pattern in irregular profiles. Peaks are less energetic at the frequency of approximately 620 Hz, showing an osculation point presumably due to a mode jump in the R-wave propagation pattern.

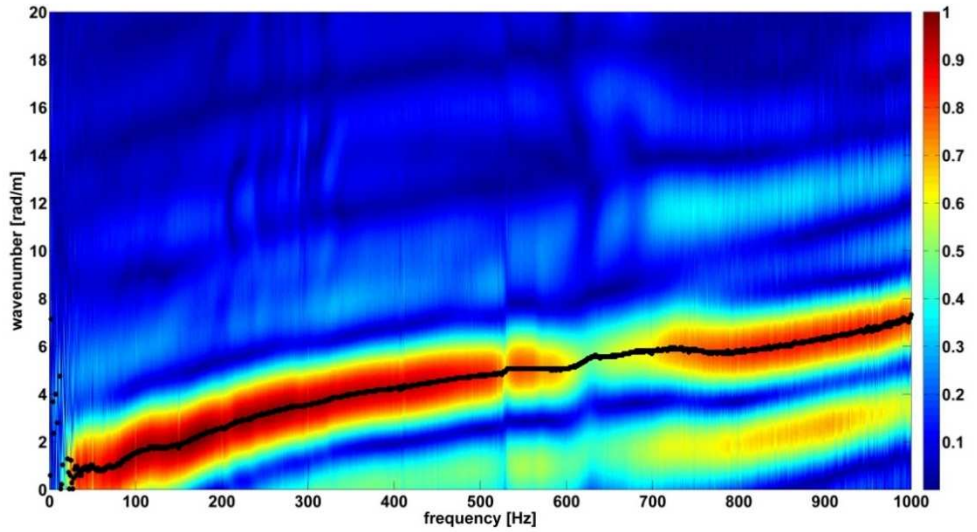

(a)

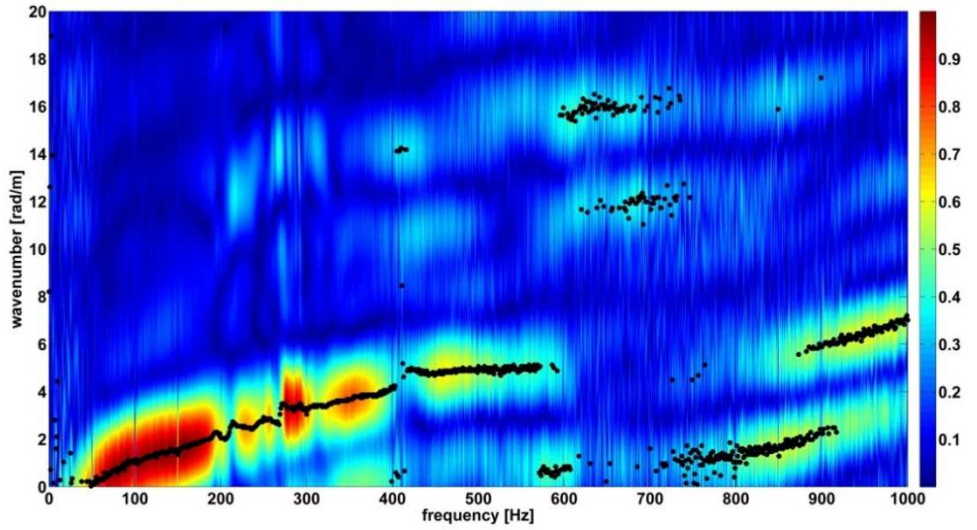

(b)

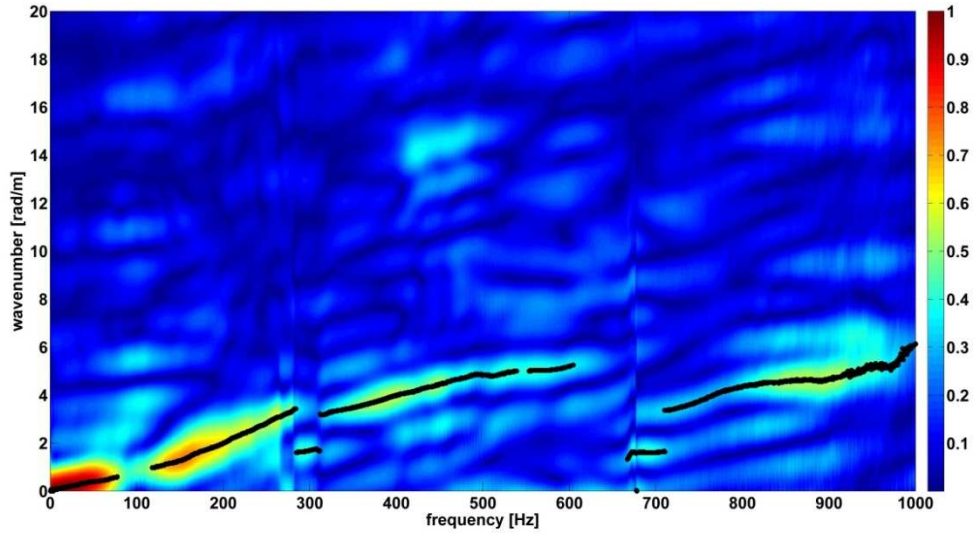

(c)

Figure 5.35: *F-k* spectrum with vertical (a), horizontal (b) and spectral convolution (c) traces for the dispersion measurement of asphalt ($L_s = 2.40\text{m}, N = 24$). The black dots indicate the extracted energy maxima of the *f-k* spectrum.

Such behaviour is consistent with not normally dispersive system, where the energy is expected to switch from the fundamental mode to some higher and faster modes. In the horizontal spectrum (Figure 5.35(b)), the energy does not show the same distribution as in the vertical one and the pattern of propagation is less regular. Particularly, less energy is observed in the interval 200-280 Hz and from the frequency of 320 Hz onward. No relevant energy seems to show up from the frequency of 600 Hz onward. The spectral convolution spectrum (Figure 5.35(c)) shows four detached segments with relevant peaks and possibly three osculation points at the frequency of 100 Hz, 290 Hz and 620 Hz. The spectral convolution spectrum has narrower energy peaks and allows better mode detection and definition since the resolution of the spectrum has doubled in both the frequency and the wavenumber domain.

Figure 5.36 details the dispersion curves in the phase velocity-frequency domain as obtained from the extraction of the peaks of energy of the *f-k* spectra. All the three dispersion curves show a change of phase velocity at the frequency of approximately 100 Hz, compatible with a mode switch. They differ in the phase velocity estimation up to the frequency of approximately 300 Hz, when they overlap, leading to the estimation of the same R-wave velocity. The horizontal and spectral convolution dispersion curves seem not to be reliable from the frequency of approximately 620 Hz onward. The spectral convolution dispersion curve shows evidence of three osculation points, at 100 Hz, 290 Hz and 620 Hz, consistently with the spectral convolution spectrum of Figure 5.35(c).

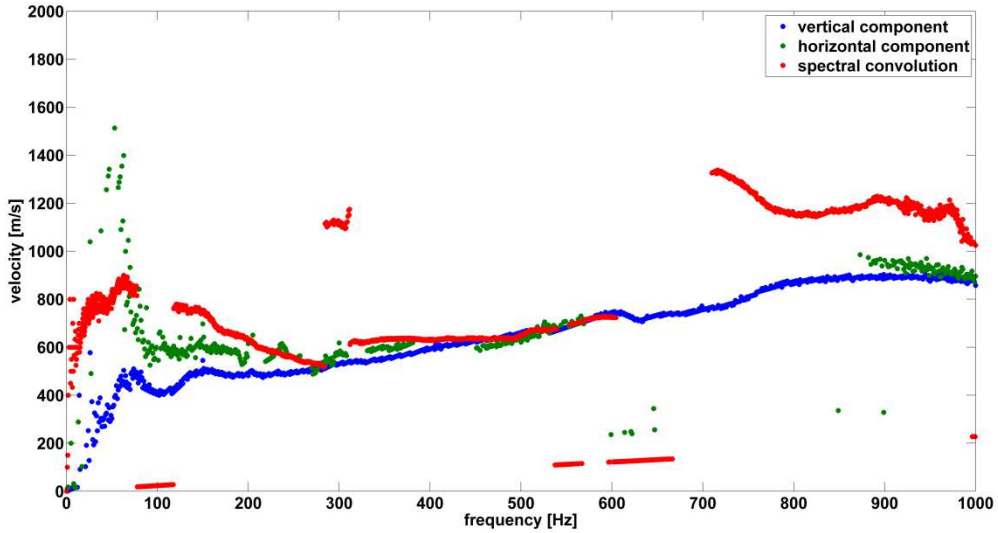

Figure 5.36: Vertical, horizontal and spectral convolution dispersion curves in the phase velocity-frequency domain, dispersion measurement of asphalt.

The amplitude of the ellipticity curve of Figure 5.37 shows one local minimum at 290 Hz and possibly two other local minima at 100 Hz and 620 Hz (highlighted by red arrows). These are compatible with the osculation points observed in the spectral convolution spectrum. Looking at the

ellipticity curve, the osculation point at 100 Hz occurs at the same frequency at which the fundamental and the first higher mode have similar velocity and a predominant vertical motion. Hence, is easy to speculate that the osculation point at 280 Hz occurs at the frequency at which the energy switches from the first to the second order mode. Similarly, a mode switch is related to the osculation point at 620 Hz. The first resonant peak at approximately 250 Hz has found not to be related to the thickness of the top layer since the medium is not normally dispersive. The phase of the ellipticity curve is constant up to the frequency of approximately 250 Hz. Then two sudden phase jumps occurs. These are related to the peaks in the ellipticity curve and to the phenomenon of the mode jump.

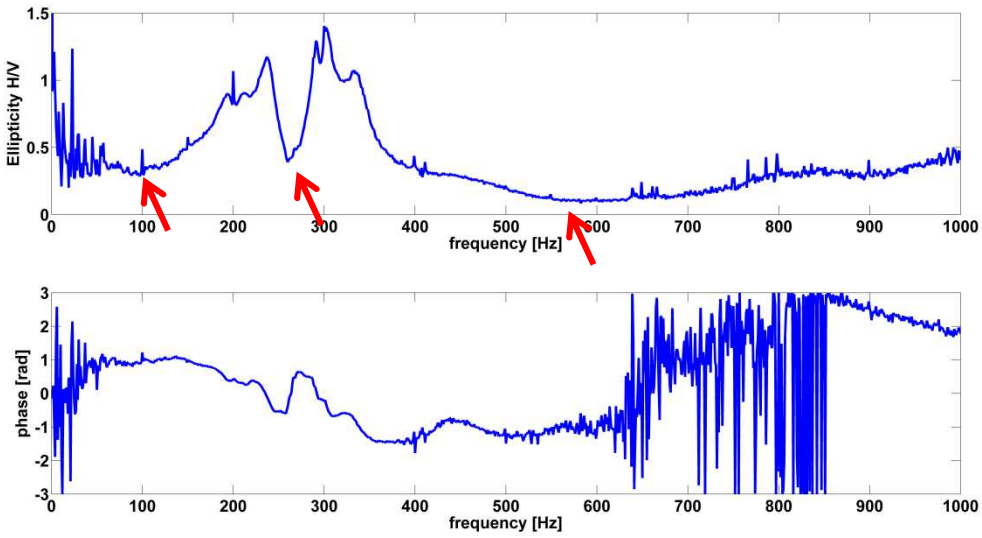

Figure 5.37: Amplitude and phase of the ellipticity curve for the dispersion measurement of asphalt. The ellipticity curve shows three local minima at 100 Hz, 280 Hz and 620 Hz. These are compatible with the osculation points also visible in the spectral convolution spectrum and are highlighted by red arrows.

5.4.2 Summary of the Surface Wave Dispersion Measurement of Asphalt

This section described the preliminary experimental dispersion measurement accomplished on asphalt. The MISW method was used and it was found to be appropriate for surveys of flexible road systems. The exploitation of both vertical and horizontal traces of a seismic event in a spectral convolution fashion could help to obtain a better resolution and to distinguish different Rayleigh modes of propagation, but further investigations based on inversions of different *f-k* spectra are needed. The use of geophones did not allow to record frequencies higher than 1 kHz.

The main issue at this stage of the investigation seemed that of the excitation and measurement of high frequencies in asphalt and that of the sensor-to-asphalt coupling. An increase of the stiffness of

the coupling between source and surface (e.g. using a rigid plate interposed between the surface and the mallet) could lead to the generation of higher frequency energy. That implies the use of different types of transducers, capable of high frequency detectability, and different asphalt-to-sensor couplings, capable of assuring a reliable recording of the signal. An investigation on different ways to couple single-axis accelerometers with the asphalt surface will be shown in Chapter 7.

5.5 Summary

This chapter showed the experimental validation of the spectral convolution method introduced in Chapter 4 as a signal processing tool for seismic data. Section 5.2 detailed a brief explanation of the sensor used in the experiments, and their calibration. Section 5.3 consisted of a set of preliminary experiments on soils, which aimed at highlighting the differences on the phase velocity estimation with the use of different type of sources, direction of excitation and source-to-ground couplings. The cross-power spectral method was found to be incapable of distinguishing different waves and different modes of propagation, and hence it proved to be a simplistic approach to dispersion measurement. For these reasons, it was abandoned in favour of the more robust frequency-wavenumber imaging technique. In addition, a 4-oz mallet striking on a circular plate was chosen as a reference source for the next experimental investigations.

Section 5.3 described the experimental investigations on soils. The data was processed using the vertical and horizontal components of motion separately, and using the new spectral convolution method proposed in Chapter 4. The experimental investigations showed that often some modes of propagation were superimposed and camouflaged under the same energy peaks due to lack of resolution. Sometimes the vertical and the horizontal components of motion showed a different distribution of energy among different modes: often one component only showed evidence of one mode (the fundamental or some higher order mode), while the other was a mixture of fundamental and higher order modes. This section aimed at highlighting the potential risks at favouring one direction with respect to the other, and the lack of resolution if the traditional imaging techniques are adopted. The spectral convolution method tackled these issues by improving the resolution and the accuracy of the *f-k* spectrum. The ellipticity curve showed local minima were energy in the spectral image switched from one mode to another. In addition, the DCP curves helped to interpret the spectral images and to constrain the inversion problem. The inversions accomplished with the images obtained with the spectral convolution method are more robust and less prone to ambiguities. The spectra obtained after inversions showed to be consistent with the spectra obtained experimentally.

Section 5.4 described a first preliminary experimental investigation on asphalt. Vertical, horizontal and spectral convolution imaging was obtained, as in the case of soil. The investigation showed that the spectral convolution method helped the recognition of osculation points and the separation of

different modes, especially if used in conjunction with the ellipticity curve. The investigation was limited by the type of sensors employed, which had a cut-off frequency of 1 kHz. The employment of sensors with a wider range of frequency and the generation of high-frequency energy were the main issues at this stage of the investigation.

Chapter 6: Detection and Assessment of Cracks in Asphalt: Numerical Investigations

This chapter focuses on the novel application and combination of diverse surface wave methods for the detection and the assessment of surface-breaking cracks in asphalt. Particularly, two existing spectral methods, the MASW and the MISW methods (see section 1.4), are synergistically used for crack interrogation. The fundamental principle is to exploit the differences between the spectral images obtained with the two methods to detect the presence of a vertical discontinuity and to assess its depth. This chapter aims at introducing the application of the two aforementioned seismic methods for the detection of surface-breaking cracks in half-spaces and in multi-layered media. It also aims at showing the results with a particular focus on the differences between the MASW and the MISW method for detection of cracking. Spectral methods could be used in conjunction with other methods, like the wave decomposition method (see chapter 4), with which they share the set-up configuration, or the time-space analysis, in the form of seismograms. The chapter guides the interpretation of the spectral images, reflection and transmission coefficients, and seismograms for crack interrogation purposes.

The investigation in this chapter was accomplished with the aid of numerical simulations of various crack detection scenarios. The mechanical parameters, density and damping ratio used in the simulations were chosen to be close to typical values of asphalts.

The problem of the presence of vertical discontinuities in layered media is faced exploring consequently the four main circumstances that are likely to be encountered (see Figure 6.1):

A. Discontinuity located external to the array of sensors. The discontinuity can be located after the source and the deployment of sensors: in this case, the positive going direct wave and the negative going reflected wave are present (Figure 6.1(a)). Section 6.1 describes the numerical investigation of this special case.

B. Discontinuity located external to the array of sensors. The location can be located before the source and the deployment of sensors: in this case the positive going direct and reflected waves are present (Figure 6.1(b)).

C. Discontinuity within the array of sensors: in this case a reflected negative going wave and a direct positive going wave are present. The discontinuity acts like a low-pass filter, thus the direct wave exhibits a cut-off frequency when the wavefront passes by the vertical discontinuity (Figure 6.1(c)). Section 6.2 describes the numerical investigation of this special case.

D. Discontinuity located in between the source and the deployment of sensors: in this case, the wavefield is low-pass filtered when it is recorded by the receivers (Figure 6.1(d)). Section 6.3 describes the numerical investigation of this special case.

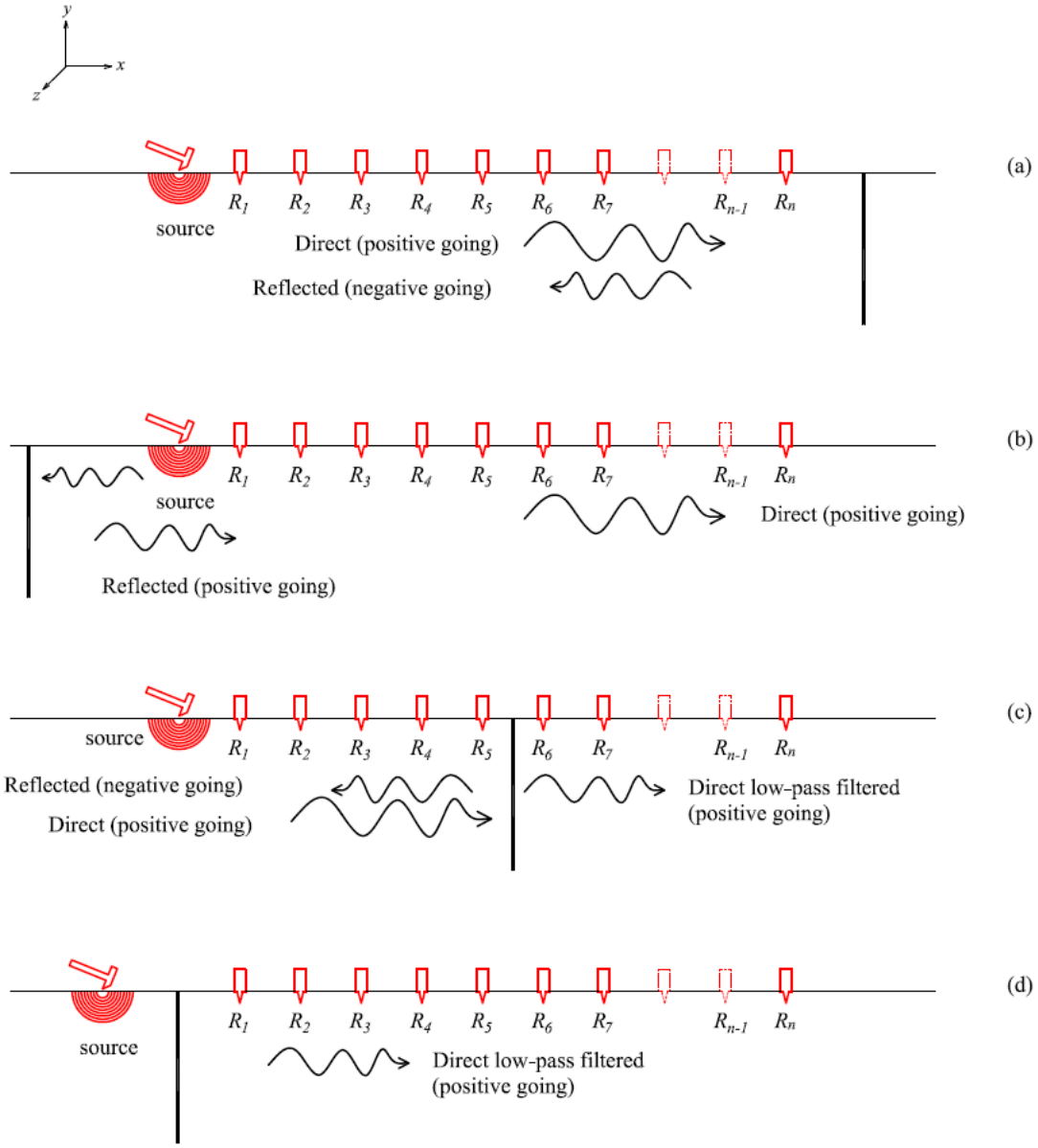

Figure 6.1: Four possible circumstances to be encountered in detection of vertical discontinuities: when the crack is external to the deployment of sensors and it is possible to look at the reflected negative going wave (a); when the crack is external and it is possible to look at the reflected positive going wave (b); when the crack within the deployment, and the direct wave is low-pass filtered (c); when the crack is in between the source and the deployment of sensors and the direct wave is low-pass filtered (d).

Section 6.4 describes then the numerical investigation of the combination of the case depicted by Figure 6.1(a) and the case depicted by Figure 6.1(b), for which two vertical surface-breaking cracks

outside the deployment of sensors are present. The parameters of the models used in the forthcoming simulations are displayed in Table 5.

6.1 Crack outside the Deployment of Sensors

The simulations displayed in this section have the aim of seeing the effects on the spectral images obtained with the MASW and the MISW method, of a discontinuity located outside the deployment of sensors. Simulations were executed with model "E" (see section 4.2.2) and with the configuration shown in Figure 6.2, where the spacing D was equal to 0.05 m. The discontinuity consisted of a surface-breaking vertical notch 0.18 m deep and 0.01 m wide.

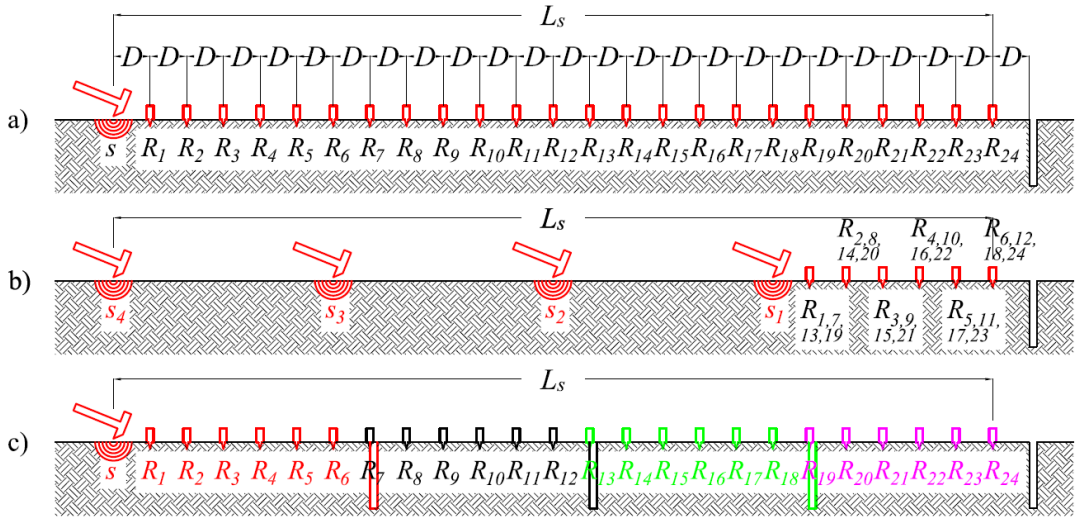

Figure 6.2: MASW set-up configuration (a) and MISW set-up configuration (b) adopted for the numerical and experimental investigation in the case of a discontinuity located outside the deployment of sensors. The source was consecutively moved along the survey line to get the MISW equivalent configuration (c). *R* refers to a geophone, *s* refers to a source, *D* is the receiver spacing and L_s is the length of the deployment of sensors.

With presence of a vertical discontinuity outside the deployment of sensors, the *f-k* spectrum obtained with a MASW technique shows peaks corresponding to the direct Rayleigh modes of propagation (Figure 6.3(a)). These peaks carry the biggest amount of energy and are then associated with the red band in the spectrum. One can notice the presence of the negative going R-wave reflected by the boundaries of the anomaly, characterized by negative wavenumbers and highlighted by the black arrow in Figure 6.3(a). The energy associated with the reflected negative going wave is very weak and the reflection shows limited duration with the higher frequencies decaying very fast.

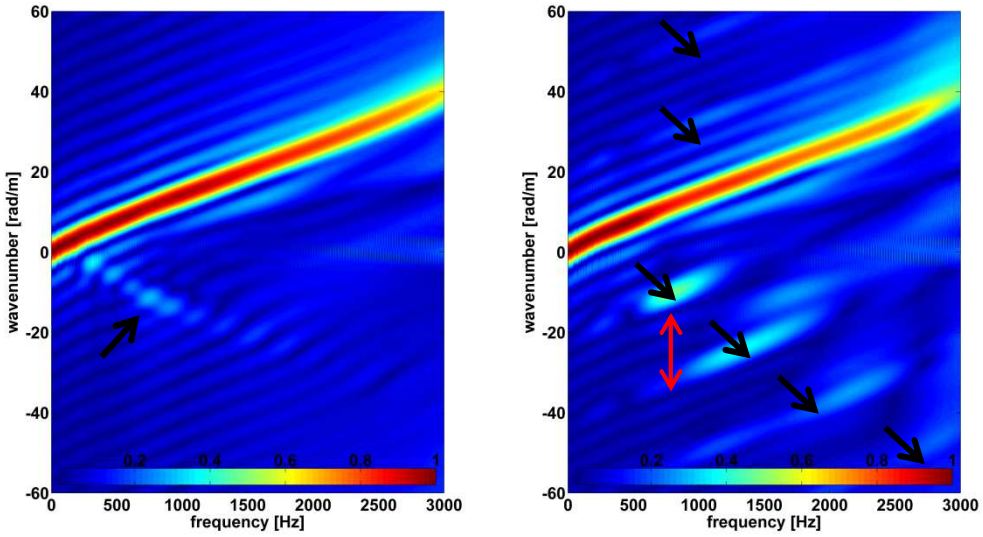

(a) (b)

Figure 6.3: *F-k* spectrum obtained with MASW (a) and with MISW technique (b) from FEM simulations with a crack external to the array of sensors. The direct Rayleigh modes of propagation correspond to the red peaks. The black arrows highlight energy peaks produced by reflections from the faces of the vertical discontinuity. The red double arrow highlights the offset Δp .

The *f-k* spectrum obtained with a MISW technique shows peaks corresponding to the direct Rayleigh modes of propagation, as with the MASW technique (Figure 6.3(b)), associated with the red band in the spectrum. One can notice the presence of additional energy peaks in the negative wavenumbers quadrant. They are parallel to the direct R-wave and they are produced by the reflections from the faces of the vertical discontinuity. These energy peaks are distributed such as to follow the slope of the reflected negative going wave (negative wavenumbers). Moving the source and keeping the sensors in a fixed position adds a periodicity in the system (see Figure 6.2) resulting in fictitious energy peaks also in the positive wavenumber region. These peaks are highlighted by arrows in Figure 6.3(b) and they are spaced by an offset Δp proportional to the length L_s of the sensor deployment, as follows:

$$\Delta p = \frac{2\pi}{L_s} \tag{6.1}$$

In this simulation $\Delta p = 20.94$ rad/m . The offset Δp is highlighted by a double red arrow. In addition, energy peaks in the positive wavenumber quadrant are visible: those are related to the use of the MISW technique, which adds a periodicity to the system. If the MISW technique is adopted, the sensors are closer to the discontinuity. This has the effect of magnifying the reflections in the spectral image, as can be noticed from a comparison between the two *f-k* spectra.

A vertical discontinuity was detected since the spectral images obtained with MISW and MASW were different. It was possible to locate it outside the deployment of sensors

Reflection coefficients were computed with the wave decomposition method from the data acquired with the MASW and the MISW methods. They are displayed in Figure 6.4. The trend of the reflection coefficient obtained from MISW shows three peaks at the frequencies of approximately 800, 1600 and 2400 Hz. These peaks are associated with the crack depth and with the mode integer index d_i of 1, 2, and 3, respectively. Adopting an R-wave velocity of 420 m/s and a value of the coefficient C equal to 2.5, the first resonant frequency leads to a depth of the crack of approximately 0.21 m, according to equation (2.35). If MASW is used, the reflection coefficient quickly drops to low values without showing any relevant peaks. In fact, the reflection coefficient computed from MASW remains consistent below a value of 0.2. This is due to the sensors being too far from the crack, when MASW is used. The wave decomposition method helped for the assessment of the depth of the crack located outside the deployment of sensors.

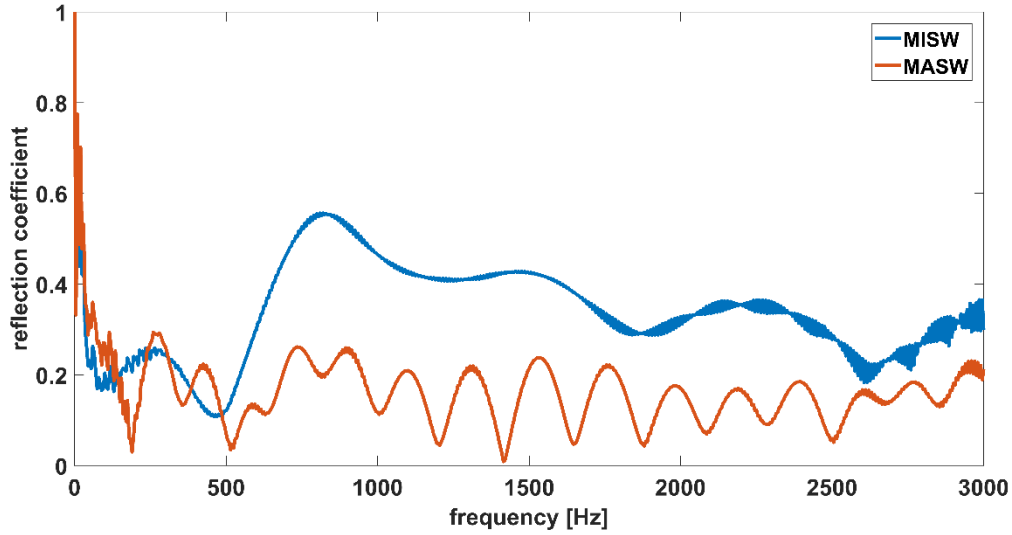

Figure 6.4. Reflection coefficients obtained with the wave decomposition method from MASW and MISW data, from FEM simulations with a crack external to the array of sensors.

6.2 Crack within the Deployment of Sensors

In this section, model "E" was considered to see the effects on the spectral images obtained with the MASW and the MISW methods, of a crack located within the array of sensors. Simulations were executed with the configuration displayed in Figure 6.5, where the spacing D was equal to 0.10 m. Moreover, the ultimate goal was to prove the effectiveness of the MISW technique for detection of a vertical crack and for the evaluation of the crack depth. The discontinuity consisted of a surface-breaking vertical notch 0.18 m deep and 0.01 m wide.

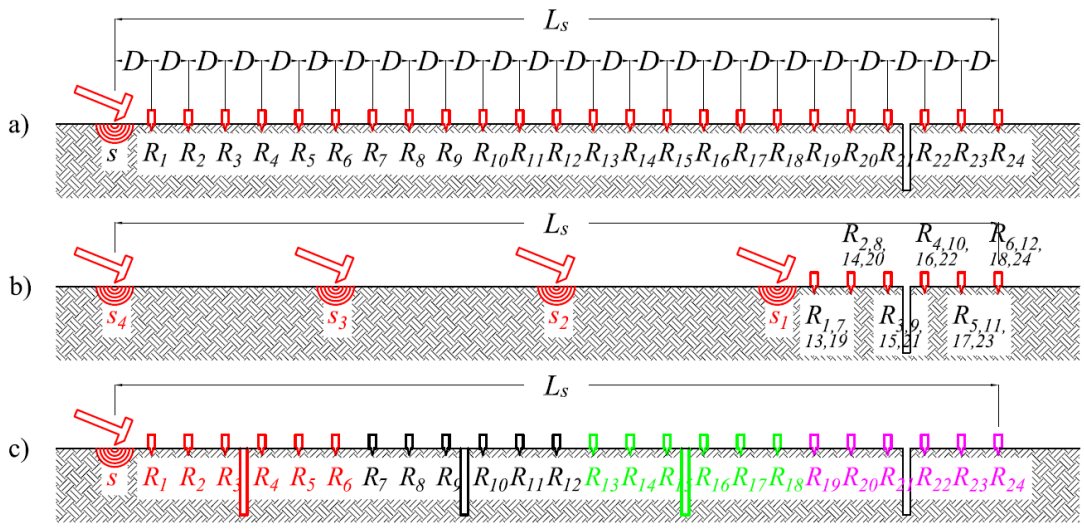

Figure 6.5: MASW set-up configuration (a) and MISW set-up configuration (b) adopted for the numerical and experimental investigation in the case of a discontinuity located within the deployment of sensors. The source is consecutively moved along the survey line to get the MISW equivalent configuration (c). *R* refers to a geophone, *s* refers to a source, *D* is the receiver spacing and L_s is the length of the deployment of sensors.

As in the previous simulations, the *f-k* spectrum obtained with a MASW technique (Figure 6.6(a)) shows peaks corresponding to the direct Rayleigh modes of propagation (red band). Very weak reflected energy is present and visible in the form of energy peaks in the negative wavenumbers quadrant (black arrow). By looking at the spectrum of Figure 6.6(a), although it is probably possible to discern the presence of some sort of discontinuity (due to the presence of reflected energy in the negative wavenumber quadrant), it is impossible to infer its location and depth. The *f-k* spectrum obtained with the MISW technique (Figure 6.6(b)) also shows peaks corresponding to the direct Rayleigh modes of propagation, associated with the red areas. The presence of the energy peaks parallel to the direct R-wave, as discussed in section 6.1, is an indicator of the presence of the vertical discontinuity. These peaks are spaced by an offset Δp , following equation (6.1), and are highlighted by black arrows in Figure 6.6(b). In this simulation $\Delta p = 10.50$ rad/m . The offset Δp is highlighted by a double red arrow. Energy associated with reflection is much higher than the MASW case, helping with the detection of the vertical notch. Moreover, the energy associated with the direct R-wave, although noticeable until the frequency of approximately 2 kHz, it becomes abruptly weaker from the frequency of 1 kHz. This cut-off frequency is highlighted in the spectrum by a red arrow. The discontinuity acts as a low-pass filter, reflecting short-wavelength waves and allowing the passage of long-wavelength waves. This phenomenon indicates that the discontinuity is somewhere located inside the deployment of sensors, and its cut-off frequency could potentially suggest the depth of the discontinuity. Bearing in mind equation (2.35), it is possible to estimate a depth of about 0.18

m for the vertical notch, if a cut-off frequency of 1 kHz, the V_R of 450 m/s, the mode integer index d_i equal to 1 and the coefficient C equal to 2.5 are assumed. The R-wave velocity has chosen from the peaks of energy of the spectral image of Figure 6.3. Hence, the estimation accomplished from the spectral image using the MISW technique is very accurate.

A vertical discontinuity was detected since the spectral images obtained with MISW and MASW were different. Moreover, the presence of the cut-off frequency in the spectral image obtained with MISW suggested the presence of a crack within the array of sensors. Its depth could be estimated from the value of the frequency of cut-off.

The reflection and the transmission coefficients were computed with the wave decomposition method from the data acquired with the MISW method. They are displayed in Figure 4.21(b). The major peak of the reflection coefficient and the first cut-off of the transmission coefficient occur at the frequency of approximately 900 Hz. The latter, as explained in section 4.2.4, is associated to the depth of the crack and it is consistent with the cut-off frequency identified with the spectral image obtained from the MISW method. The wave decomposition method complemented the results obtained with the imaging techniques. It confirmed the presence and the depth of the crack, improving the robustness of the results.

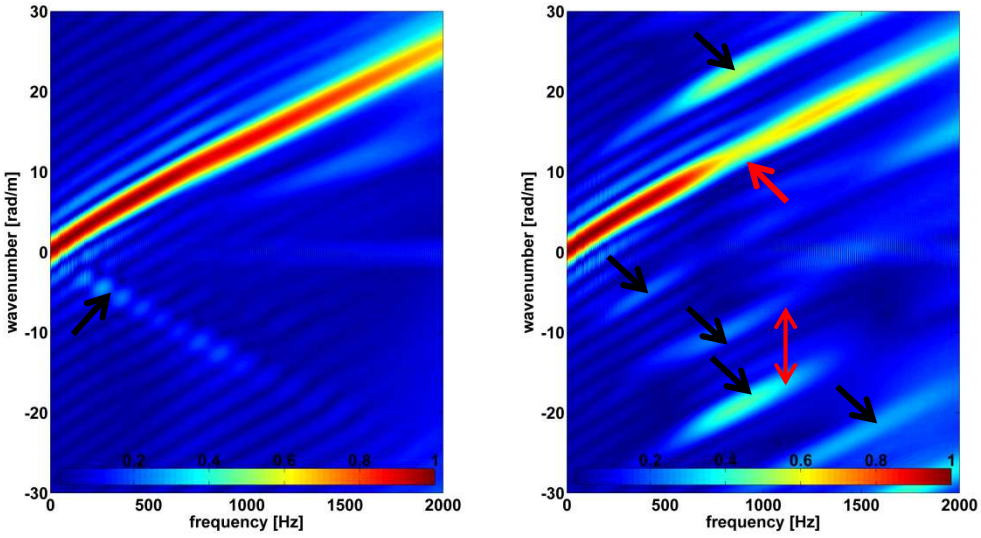

(a) (b)

Figure 6.6: *F-k* spectrum obtained with MASW (a) and with MISW technique (b) from FEM simulations with a crack within the array of sensors. The direct Rayleigh modes of propagation correspond to the red peaks. The black arrows highlight energy peaks produced by reflections from the faces of the vertical discontinuity. The red arrow highlights the cut-off frequency due to the presence of the crack. The red double arrow highlights the offset Δp .

6.3 Crack between the Source and the Deployment of Sensors

Model "C" was used in this section to study the effects of the crack depth on the spectral images obtained with the MASW and the MISW methods. In these cases, the crack was located between the source and the deployment of sensors. Simulations were executed with the configuration displayed in Figure 6.7, where the spacing D was equal to 0.05 m. The aim of the simulation was of identifying the cut-off frequency due to the presence of the surface-breaking crack, in the *f-k* domain. The cut-off frequency was associated with the depths of the cracks as per equation (2.35). The discontinuity consisted of a surface-breaking vertical notch 0.01 m wide. Three crack depths were progressively simulated as per Table 5.

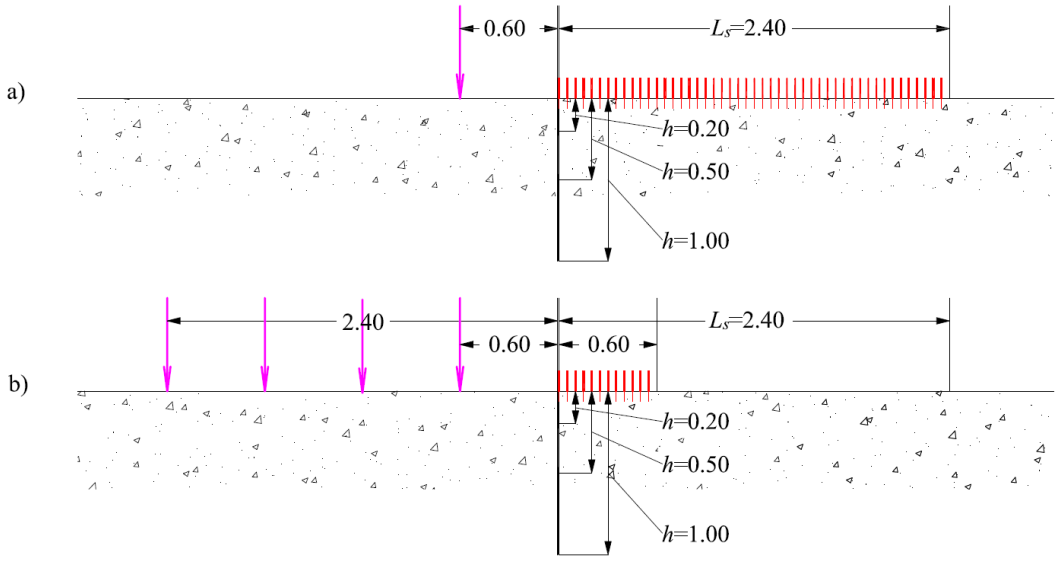

Figure 6.7: Set-up and dimensions for numerical simulation of a vertical crack between the source and the deployment of sensors, with MASW (a) and MISW (b) technique. Three crack depths were progressively simulated: 0.20 m, 0.50 m and 1.00 m. The notch was 0.01 m wide. The pink arrow indicates the source position; the red lines indicate the sensors. Distances are shown in metres.

The *f-k* spectra obtained with the MASW technique show peaks of energy, corresponding to the direct Rayleigh mode of propagation, associated with the red bands of Figure 6.8. It is possible to notice a clear cut-off frequency for the case of the 0.20 m crack (Figure 6.8(a)): the energy associated with the mode of propagation of the R-wave suddenly drops to a zero value and then increases again at approximately 700 Hz. It is highlighted by a red arrow. The surface-breaking crack acts like a low-pass filter, blocking the shorter wavelengths and allowing the longer wavelengths to propagate further. The cut off frequency is difficult to spot for the case of the 0.50 m crack (Figure 6.8(b)),

where it should happen at approximately 300 Hz, according to equation (2.35), and it is even more difficult for the case of the 1.00 m crack (Figure 6.8(c)).

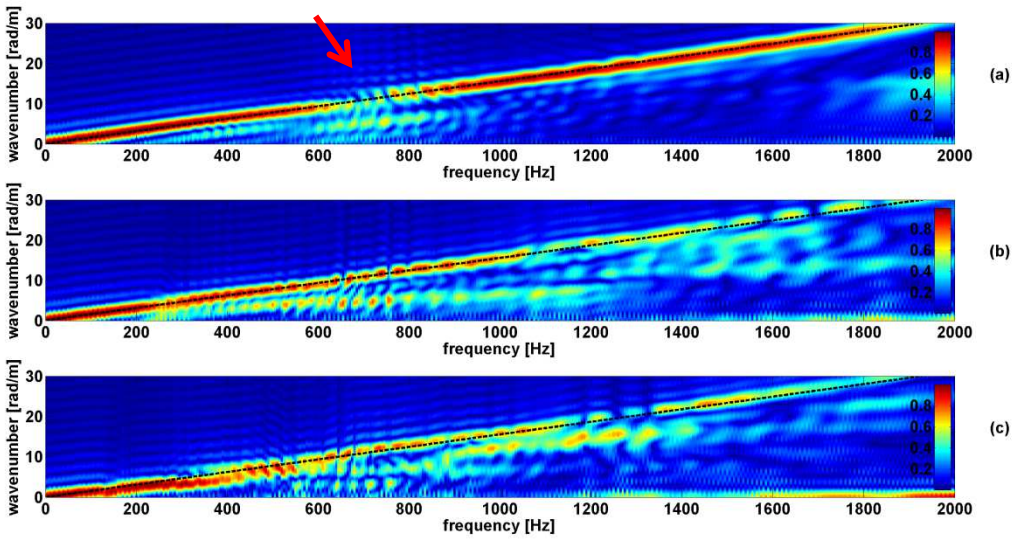

Figure 6.8: *F-k* spectra obtained with MASW technique from FEM simulations in the case of a surface-breaking crack situated between the source and the deployment of sensors. The crack depth was 0.20 m (a), 0.50 m (b) and 1.00 m (c). The red arrow highlights the cut-off frequency due to the presence of the 0.20 m crack.

The *f-k* spectra obtained with the MISW technique show peaks of energy, corresponding to the direct Rayleigh mode of propagation, associated with the red areas in Figure 6.9. Contrary to the MASW case, with MISW it is possible to clearly identify the cut-off frequencies for all the three crack depths. The energy associated with the mode of propagation of the R-wave drops suddenly due to the presence of the surface-breaking crack that acts like a low-pass filter. The cut-off is at approximately 700 Hz for the 0.20 m crack, at approximately 300 Hz for the 0.50 m crack and at approximately 150 Hz for the 1.00 m crack. They are highlighted by red arrows in Figure 6.9. These cut-off frequencies are consistent with the cut-off frequencies identified with the wave decomposition method in section 4.2.1 and are associated with each crack depth.

The transmission coefficients were computed with the wave decomposition method from the data acquired with the MISW method. They are shown in Figure 4.18 and in Table 7. It can be noticed that the cut-off frequencies of the transmission coefficients match those identified from the spectral images of Figure 6.9. The wave decomposition method complemented the results obtained with the imaging techniques. It confirmed the presence and the depth of the crack, improving the robustness of the results.

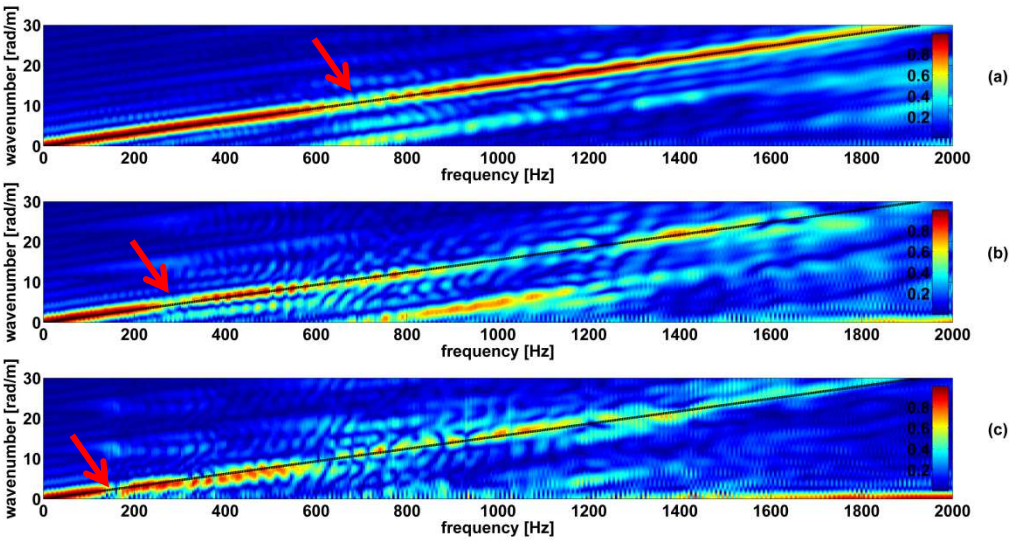

Figure 6.9: *F-k* spectra obtained with MISW technique from FEM simulations in the case of a surface-breaking crack situated between the source and the deployment of sensors. The crack depth was 0.20 m (a), 0.50 m (b) and 1.00 m (c). The red arrows highlight the cut-off frequencies due to the presence of the cracks.

6.4 Space-Normalised Seismogram for the Localization of Two Cracks outside the Deployment of Sensors

The aim of this section is to show the effect of different normalizations on the seismic seismogram. In the seismogram (sometimes also recalled as shot gather), each vertical trace is offset vertically to represent the spatial separation of each sensor. Each trace in space is traditionally normalised to its maximum amplitude along the time axis to compensate for the geometrical attenuation. The seismogram displays the wavefield in the time-space domain and it is useful to detect different waves and their speed. The gradient of wave-groups in the time-space domain is associated with the speed of the different waves [16, 41, 101]. It generally gives better results with numerous and close receivers. This section introduces the situation in which two surface-breaking cracks are located outside the deployment of sensors. The numerical simulation was executed with model "A" and with the configuration displayed in Figure 6.10, where the spacing D was equal to 0.05 m. The geometry of the problem consisted of two discontinuities that were 7.60 m apart each other: the crack on the left-hand side was 0.01 m wide and 1.00 m deep, the crack on the right-end side coincided with the edge of the finite element model and hence had theoretically an infinite depth. Between the two discontinuities, sensors were placed with a step of 0.05 m. The source was placed 1.00 m apart from the crack on the right-end side. The aim of this simulation is to detect the presence of the two cracks by looking at the reflected positive and negative going waves in the time-space domain.

In this case, a frequency-wavenumber transformation would lead to a spectral image similar to that of Figure 6.3(a) and of Figure 6.6(a), from which no relevant information about the presence or the extension of the two cracks can be extrapolated. For these reasons, the seismic data here was treated in a different fashion and analysed in the time-space domain.

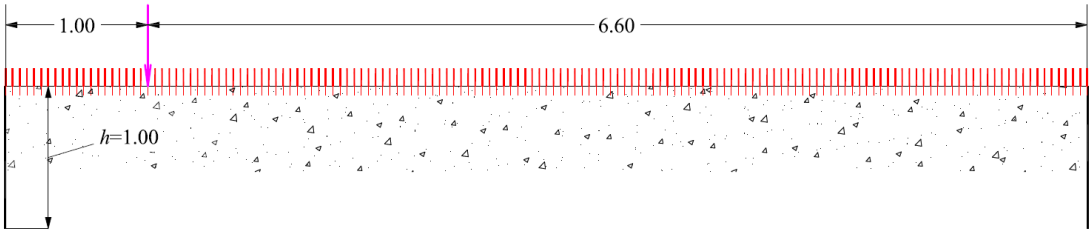

Figure 6.10: Set-up and dimensions for numerical simulation of multiple cracks external to the deployment of sensors. The geometry of the problem consisted of two discontinuities 7.60 m apart: the crack on the left-hand side was 0.01 m wide and 1.00 m deep; the crack on the right-end side coincided with the edge of the finite element model and hence had theoretically an infinite depth. The pink arrow indicates the source position; the red lines indicate the sensors. Distances are shown in metres.

The seismogram shown in Figure 6.11(a) is obtained by normalizing each trace in space along the time axis. The time-normalised seismogram displays the direct positive going (highlighted with a red arrow) and the direct negative going waves (highlighted with a black arrow), both starting at the offset of 1 m. Remembering the velocity of the half space (Table 5), the direct positive going wave hits the edge of the model at 0.0163 sec. The direct negative going wave is reflected by the boundaries of the notch at 0.005 sec and it starts to propagate in the opposite direction, reaching the edge of the model at 0.0213 sec. It can be clearly seen in the time-normalised seismogram as it travels parallel to the direct positive going wave (i.e. with the same wavespeed) and it is highlighted by a green arrow in Figure 6.11(a).

The seismogram shown in Figure 6.11(b) is instead obtained by normalizing along the space axis. Each trace in time is normalised to its maximum amplitude along the space axis. As it happens with the time-normalised seismogram, the space-normalised seismogram displays the direct positive going (highlighted with a red arrow) and the direct negative going waves (highlighted with a black arrow), both starting at the offset of 1 m. Remembering the velocity of the half space (Table 5), the negative going wave is reflected by the boundaries of the notch at 0.005 sec and it starts to propagate with a direct direction. It can be also seen in the space-normalised seismogram as it travels parallel to the direct positive going wave and it is highlighted by a green arrow in Figure 6.11(b).

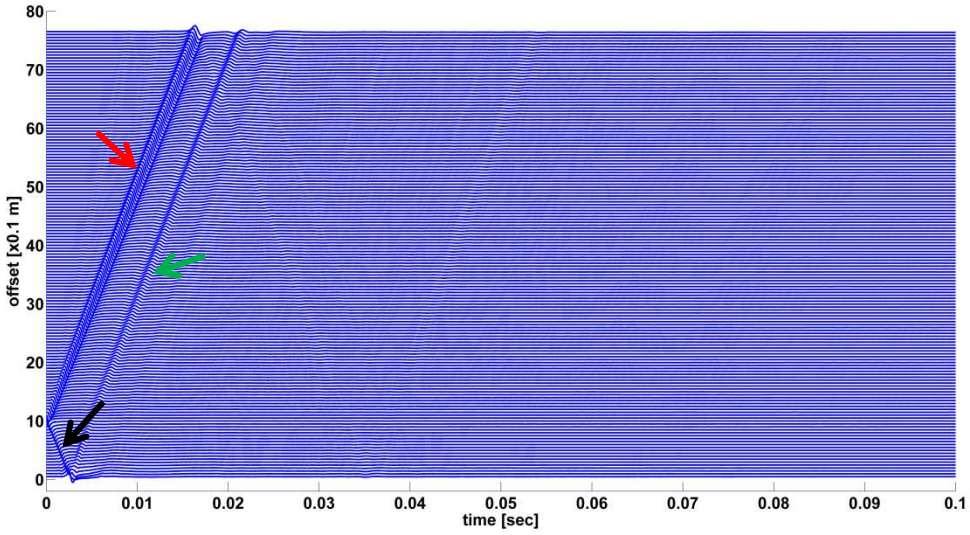

(a)

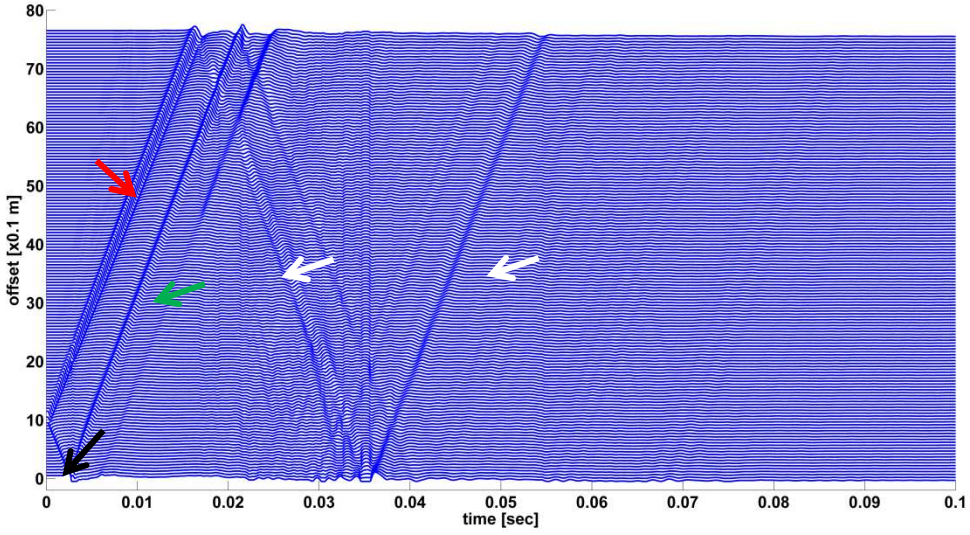

(b)

Figure 6.11: Time-normalised (a) and space-normalised (b) seismogram from numerical simulation on a half-space. By looking at (a), only the direct positive and direct negative going waves and the reflected positive going wave from the crack on the right-end side are visible. They are respectively highlighted by red, black and green arrows. By looking at (b), it can be observed that the direct positive going wave is reflected back from the edges of the model at the offset of 7.60 m and then from the crack a second time. The reflections experienced by the direct positive going wave are only visible in (b) and are highlighted by white arrows.

Moreover, additional information can be picked out by looking at the space-normalised seismogram. The two direct positive going waves are reflected back by the edges of the model: the first at 0.0163 sec and the second at 0.0213 sec. It can be clearly seen that the first direct wave, with bigger amplitude, travels back and hits the vertical notch at 0.0376 sec, then propagating in the positive

direction and hitting the edges of the model at the offset of 7.60 m for the second time at 0.054 sec. The reflections experienced by the direct positive going wave are only visible in the space-normalised seismogram and are highlighted by white arrows. To some extent, also the pattern of the second direct positive going wave is observed up to its second reflection.

Hence, while with the time-normalised seismogram would be impossible to spot the presence of a second crack external to the deployment of sensors, the space-normalised seismogram allowed the detection and the assessment of its location. A space normalised seismogram helped in the detection of reflections and hence of vertical anomalies. Particularly, it identified the reflected positive going wave caused by a vertical anomaly which was outside the deployment of sensors (case (a) and (b) of Figure 6.1). In this case, the spectral image would have not been sensitive to the reflected positive going wave (as explained in section 3.3).

6.5 Summary

This chapter proposed the synergistic application of two standard spectral methods for the interrogation of surface-breaking asphalt cracks, based on the exploitation of Rayleigh wave reflected from their surfaces. The aim was to highlight the potential of extracting information about the state of the road from spectral images in the frequency-wavenumber domain. Insight into practical application for detection and crack sizing in asphalt descends from the observations of the measurements shown in this chapter. A possible detection strategy would be to combine the MASW and the MISW measurements, and then process the data with the wave decomposition method. Firstly, any relevant differences in the spectral images obtained with MASW and MISW would be an indicator of the presence of a vertical discontinuity. This might be located either externally or internally to the deployment of sensors. The second step consists in repeating the MISW measurement at different locations with the aim of obtaining spectral images like that of section 6.2 and section 6.3. This has the aim to locate and to assess the depth of the crack. The final step of the survey is the computation of the reflection coefficient and, where possible, of the transmission coefficient with the wave decomposition method, with the final aim to complement and enhance the fidelity of the survey.

MASW and MISW did not lead to the same *f-k* spectrum, if used in the presence of transversal anomalies. Any relevant differences in the spectral images obtained with the two methods were an indicator of some kind of vertical anomaly. Once the presence of a crack was detected, MISW was the spectral method to adopt for the assessment of its location and depth. In fact, MISW enhanced the visibility of reflected waves in the *f-k* spectrum: the sensors close to the discontinuity magnified the content of the reflections in the signal allowing a more efficient detection of a vertical discontinuity in asphalt. In the presence of a discontinuity, MISW added a periodicity in the system,

which appeared as peaks of energy parallel to the main propagation mode in the spectral image. This phenomenon was enhanced the closer the sensors were to the discontinuity.

A vertical discontinuity acted like a low-pass filter, allowing the passage of longer wavelengths, but blocking the passage and reflecting the short ones. By looking at the *f-k* spectrum of a low-pass filtered Rayleigh wavefield obtained with the MISW approach, when the sensors were across the crack, it was possible to extract information regarding the location and depth of the cracking.

The wave decomposition method (introduced in Chapter 4) could complement a seismic survey conducted synergistically using the MASW and the MISW method. The reflection and, where possible, the transmission coefficients computed with the wave decomposition from MISW, were a valid tool to validate and to augment the robustness of the results obtained with the imaging techniques.

Moreover, a space-normalised seismogram helped in the detection of the reflections caused by vertical discontinuities since it displayed more information than the traditional time-normalised seismogram. It could be a useful tool to support and complement the spectral methods, particularly to detect the reflected positive going wave caused by a vertical anomaly outside the deployment of sensors (case (a) and (b) of Figure 6.1).

A wider investigation for the interrogation of bottom-up cracks, which are not visible from the surface, with spectral methods is needed.

Chapter 7: Detection and Assessment of Cracks in Asphalt: Experimental Investigations

This chapter displays the experimental investigations accomplished for cracks and flaws interrogation in asphalt, exploiting the propagation of surface waves. The novel combination of diverse surface wave methods for the analysis of the seismic data is applied with the aim of crack detection and interrogation. For each test site, the MASW and/or the MISW spectral methods are exploited to confirm or exclude the presence of a crack. In addition, the reflection and the transmission coefficients computed with the wave decomposition method are used to get the information about the depth of the crack and to confirm the findings obtained from the spectral images.

Section 7.1 describes the application of the spectral methods and of the wave decomposition method to a real case of a pristine asphalt, with absence of crack. The ellipticity curve is added for a qualitative description of the test site. Section 7.2 describes a real case of a crack external to the deployment of sensors. Section 7.3 introduces a real case of a crack internal to the deployment of sensors. The use of geophones to accomplish seismic survey in asphalt limits the upper detectable frequency. For this reason, a comparison among a variety of different couplings between the seismic sensors (accelerometers) and the medium (asphalt) surface is described in section 7.4.

7.1 Asphalt without Crack

This section details the results and the physical interpretation of two dispersion measurements in asphalt executed via the MASW and the MISW technique and processed in the *f-k* domain using vertical signals, in the absence of a discontinuity. Moreover, the wave decomposition method (see section 4.2) was applied to experimental data. The aim of this experimental session was to prove that the MASW and the MISW techniques lead to the same spectral image in a real case of absence of transversal discontinuities. It also had the scope to show the trend of the reflection coefficient in a real case if no discontinuities are present.

The MASW experimental set-up consisted of a source and an array of 24 geophones, arranged as in Figure 6.2(a) with the spacing D equal to 0.10 m, covering an overall length L_s of 2.40 m.

The MISW experimental set-up consisted of a source and an array of 6 geophones, arranged as in Figure 6.2(b) and Figure 7.1 with the spacing D equal to 0.10 m, covering a length L_s of 0.60 m. The source was moved apart by 0.60 m four times, resulting in a multichannel record of 24 traces

covering an overall length L_s of 2.40 m. The surface of the medium did not show evidence of any sort of transversal discontinuity.

The source consisted of a 4-oz metallic mallet striking on a circular plate of 0.15 m diameter, resting on the surface of the road. The auto-spectrum computed from the signal of an accelerometer attached to the surface of the plate showed that the energy was evenly distributed over a range of frequencies varying from 10 Hz to 1 kHz, as depicted in Figure 7.7.

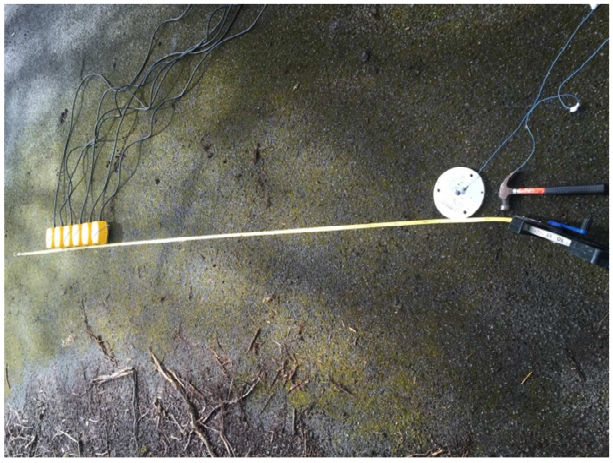

Figure 7.1: MISW experimental set-up configuration for the asphalt test site without crack. At the bottom of the figure, the mallet and the aluminium plate used as a source are shown. In addition, it can be observed that the surface of the medium does not show evidence of any transversal discontinuity.

The *f-k* spectra obtained utilizing the vertical signals obtained from the MASW technique and from the MISW technique are shown in Figure 7.2(a) and in Figure 7.2(b) respectively.

In both spectra, the biggest amount of energy corresponds to the direct Rayleigh wave propagation modes and it is associated with the red bands. The behaviour of the propagation modes of the Rayleigh wave follows that of layered irregular systems, i.e. system where the shear velocity decreases with depth. In this case there is a very visible mode jump, associated with a change in the slope, at the frequency of approximately 250 Hz, which suggests a two-layered system with one stiff layer overlaying a softer layer. The frequency at which the mode jump occurs is likely to be related to the thickness of the upper layer. In fact, the Rayleigh wave starts to propagate on the upper layer from a frequency of approximately 220 Hz: assuming a Rayleigh wave phase velocity of 190 m/s for the subgrade layer, the associated wavelength is 0.95 m. Bearing in mind that the representative depth of ground roll is one third of its wavelength, the upper layer can be assumed to be approximately 0.30 m thick. No reflected energy is visible in the negative wavenumber quadrant for both the MASW and the MISW case. This excludes the presence of a reflected wave from the boundaries of vertical discontinuities. The two spectral image, albeit obtained with two different surface wave techniques,

are almost identical. Hence, the MASW and the MISW lead to the same spectral image if used in a medium with absence of transversal discontinuities.

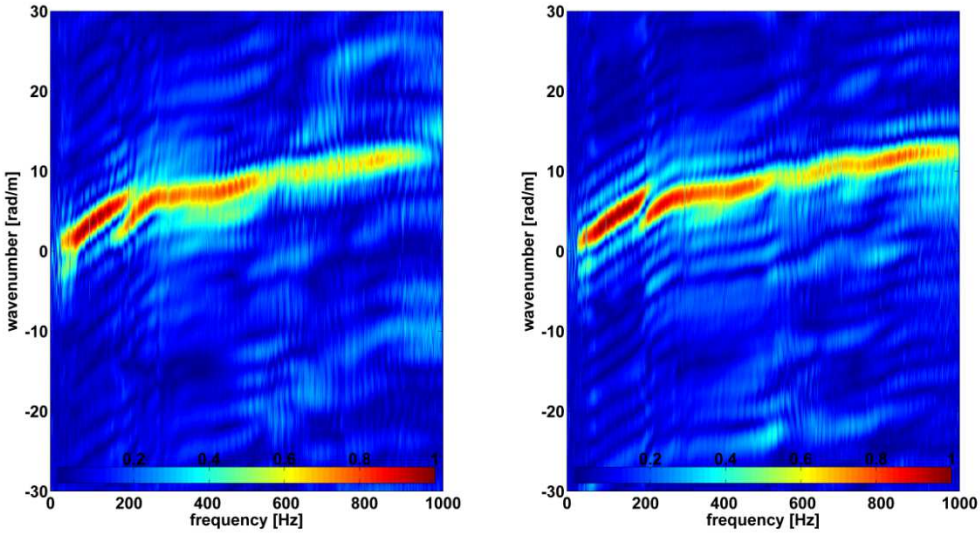

(a) (b)

Figure 7.2: *F-k* spectrum obtained with MASW (a) and with MISW technique (b) from the experimental investigation with no presence of crack. The MASW and the MISW lead to the same spectral image if used in a medium with absence of transversal discontinuities.

The ellipticity curve depicted in Figure 7.3 shows one major global minimum in the range from 0 to 1 kHz at the frequency of approximately 220 Hz. It is associated with an osculation point that is also clearly visible in the *f-k* spectra, where the velocities of two modes become very close. Moreover, the high value of the horizontal to vertical ratio at the resonance peak (higher than 14) suggests the presence of a strong velocity contrasts between the horizontal layers of the surveyed medium. This behaviour is consistent with the structure of the surveyed medium, composed by a stiff asphalt layer presumably overlaying a much softer layer. The phase of ellipticity shows a sudden jump at the frequency of approximately 220 Hz, i.e. at the same frequency at which the local minimum occurs: it can be related to the mode jump that is clearly detectable from both the amplitude of the ellipticity (its local minimum) and from the *f-k* spectra. The phase jump is likely to be related to the phenomenon of the mode jump and to the motion becoming predominantly vertical.

The wave decomposition method was applied to the data coming from the deployment of sensors for both the MASW and the MISW case, as explained in section 4.2. The reflection coefficient was evaluated as the amplitude ratio of the negative going wave to the positive going wave at the reference sensor position (in this case the first sensor moving from the left to the right). For the MISW case, since the experiment was repeated moving apart the source by an equal length L_s three times, the result was the average of four tests.

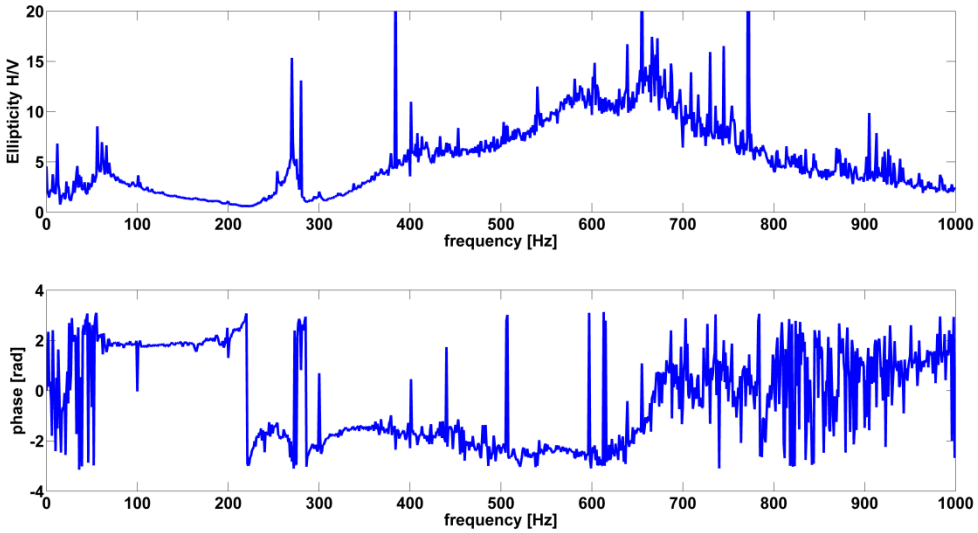

Figure 7.3: Amplitude and phase of the ellipticity curve for the asphalt test site without crack. The ellipticity curve shows one major minimum at approximately 220 Hz, which is compatible with the osculation points also visible in the *f-k* spectrum. The phase shows a sudden jump at the same frequency the local minimum occurs.

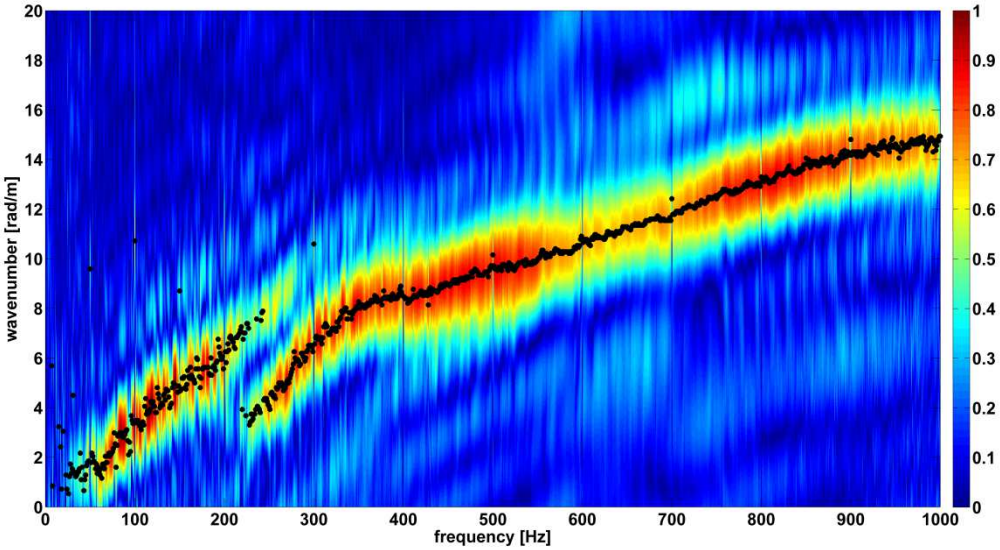

Figure 7.4: *F-k* spectrum with absence of discontinuity obtained with MISW. The direct Rayleigh modes of propagation correspond to the red peaks. The black dots indicate the extracted energy maxima of the *f-k* spectrum used in the wave decomposition method.

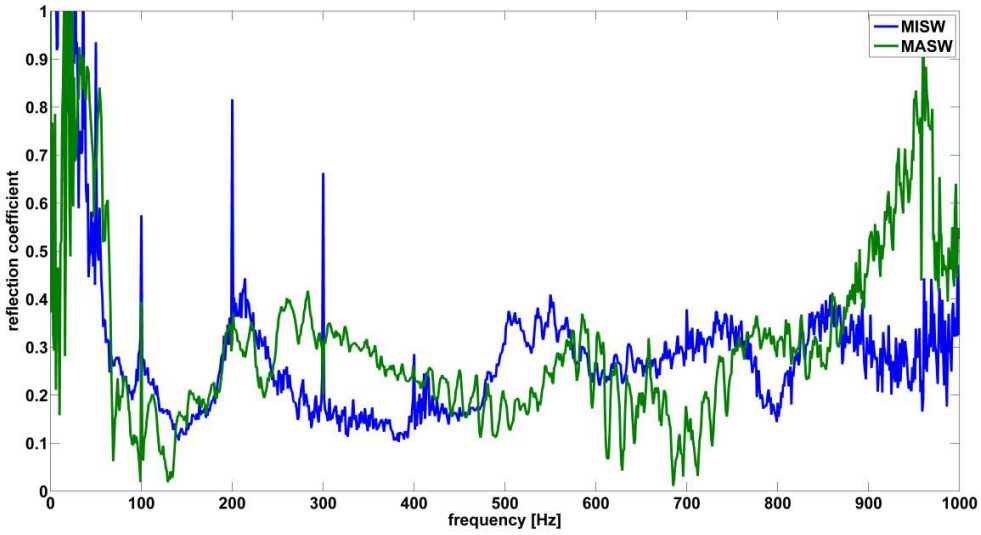

Figure 7.5: Reflection coefficients obtained with the wave decomposition method from MASW and MISW data. No resonant peaks are observable in the reflection coefficient, as the surface of the medium does not show evidence of any sort of transversal discontinuity.

The wavenumber and phase velocity are extracted from the vertical *f-k* spectra obtained with the MISW technique displayed in Figure 7.4. The black dots indicate the extracted energy maxima and used as *a-priori* information in the wave decomposition method. Some outliers are present but they do not disturb the overall application of the wave decomposition method.

The reflection coefficients obtained with the wave decomposition method from MASW and from MISW data are displayed in Figure 7.5. The reflection coefficient obtained with the two surface wave techniques has the same trend as it quickly decreases up to being close to the zero value and then being consistent towards the value equal to 0.3 from the frequency of 200 Hz onward. No relevant peaks are recognizable in the aspect of the reflection coefficient, albeit a small peak can be observed at approximately 220 Hz, when the wave decomposition method is applied to MISW data. It is probably associated with the mode jump and not to the resonance due to the presence of a vertical crack. The surface of the medium does not show evidence of any sort of transversal discontinuity and so does the reflection coefficient computed from MISW and MASW data.

7.2 Asphalt with Crack External to the Deployment of Sensors

This section details the results and the physical interpretation of two dispersion measurements in asphalt executed via the MASW and the MISW technique and processed in the *f-k* domain using vertical signals, in the presence of a discontinuity. In this case, the vertical discontinuity was located outside the deployment of sensors and it consisted of the transversal edge of the road. Moreover, the wave decomposition method (see section 4.2) was applied to experimental data to assess the depth

of the surface-breaking crack. The aim of this experimental session was to highlight the differences between the two techniques with respect to the detection of vertical discontinuities and to prove the effectiveness of the wave decomposition method for the assessment of the depth of surface-breaking cracks.

The MASW experimental set-up consisted of a source and an array of 24 geophones, arranged as in Figure 6.2(a) with the spacing D equal to 0.10 m, covering an overall length L_s of 2.40 m.

The MISW experimental set-up consisted of a source and an array of 6 geophones, arranged as in Figure 6.2(b) and Figure 7.6 with the spacing D equal to 0.10 m, covering a length L_s of 0.60 m. The source was moved apart by 0.60 m four times, resulting in a multichannel record of 24 traces covering an overall length L_s of 2.40 m. Both deployments of sensors were 0.10 m distant from a vertical discontinuity represented in this case by the transversal edge of the asphalt wearing course of the road.

Figure 7.6: MISW experimental set-up configuration for the asphalt test site, with the discontinuity outside the array of sensors (in this case the edge of the road pavement).

The source consisted of a 4-oz metallic mallet striking on a circular plate of 0.15 m diameter, resting on the surface of the road. The auto-spectrum computed from the signal of an accelerometer attached to the surface of the plate showed that the energy was evenly distributed over a range of frequencies varying from 10 Hz to 1 kHz, as depicted in Figure 7.7.

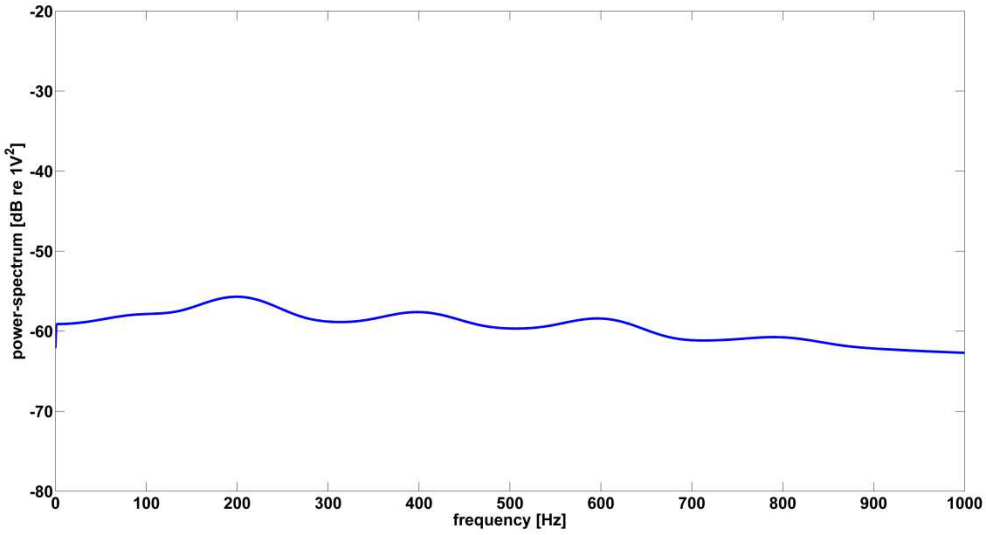

Figure 7.7: Auto-spectrum of the signal of an accelerometer attached onto the surface of the aluminium plate.

The *f-k* spectra obtained utilizing the vertical signals obtained from the MASW technique and from the MISW technique are shown in Figure 7.8(a) and in Figure 7.8(b) respectively.

In both spectra, the biggest amount of energy corresponds to the direct Rayleigh wave propagation modes and it is associated with the red bands. The behaviour of the propagation modes of the Rayleigh wave follows that of layered irregular systems, i.e. where the shear velocity decreases with depth. In this case, there is a very visible mode jump associated with a change in the slope at the frequency of approximately 200 Hz, which suggests a two-layered system with one stiff layer overlaying a softer layer. The frequency at which the mode jump occurs is likely to be related to the thickness of the upper layer. In fact, the Rayleigh wave starts to propagate on the upper layer from a frequency of approximately 200 Hz. Assuming a Rayleigh wave phase velocity of 190 m/s (from the energy maxima at the frequency of 200 Hz) for the subgrade layer, the associated wavelength is 0.95 m. Bearing in mind that the representative depth of ground roll is one third of its wavelength, the upper layer can be assumed to be approximately 0.30 m thick. With the MASW technique, only weak reflected energy is visible (black arrow in Figure 7.8(a)). It is not possible to realize the presence of a discontinuity by only looking at the spectrum of Figure 7.8(a).

For the MISW test, additional peaks parallel to the ones associated with the direct wave are visible. The presence of the energy peaks parallel to the direct Rayleigh wave in the negative wavenumber quadrant are an indicator of the presence of the vertical discontinuity. These peaks are spaced by an offset Δp, following equation (6.1), and are highlighted by black arrows in Figure 7.8(b). In this case $\Delta p = 10.50$ rad/m . The offset Δp is highlighted by a double red arrow. The reflections are enhanced when MISW is used in the proximity of a discontinuity, helping the detection of a vertical

discontinuity. In addition, energy peaks in the positive wavenumber quadrant are visible: those are related to the use of the MISW technique adding a periodicity to the system and changing the uniformity of the sensors spacing if the source is not precisely moved by the wanted distance.

A vertical discontinuity was detected experimentally since the spectral images obtained with MISW and MASW are different. This investigation located the crack outside the deployment of sensors.

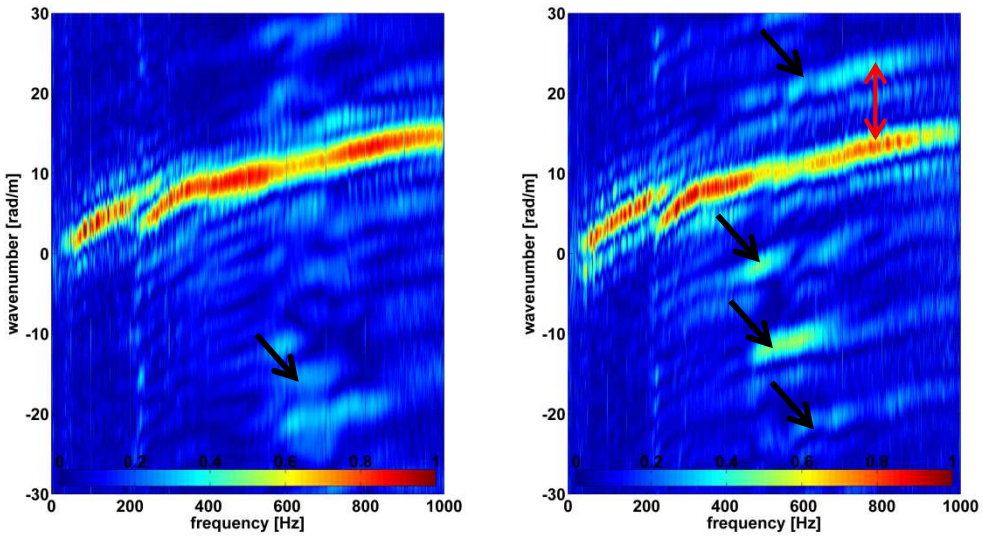

(a) (b)

Figure 7.8. *F-k* spectrum obtained with MASW (a) and with MISW technique (b) from the experimental investigation with a crack external to the array of sensors. The direct Rayleigh modes of propagation correspond to the red peaks. Black arrows highlight energy peaks produced by reflections from the faces of the vertical discontinuity. The red double arrow highlights the offset Δp.

The wave decomposition method was applied to the data coming from the deployment of sensors for both the MASW and the MISW case. The reflection coefficient was evaluated as the amplitude ratio of the negative going wave to the positive going wave at the reference sensor position (in this case the first sensor moving from left to right). For the MISW case, since the experiment was repeated moving apart the source by an equal length L_s three times, the result was the average of four tests. The wavenumber and phase velocity are extracted from the vertical *f-k* spectra obtained with the MISW technique displayed in Figure 7.4, which was conducted in a pristine area in the proximity of the location of this experiment. The black dots indicate the extracted peaks of energy, which are used as *a-priori* information in the wave decomposition method.

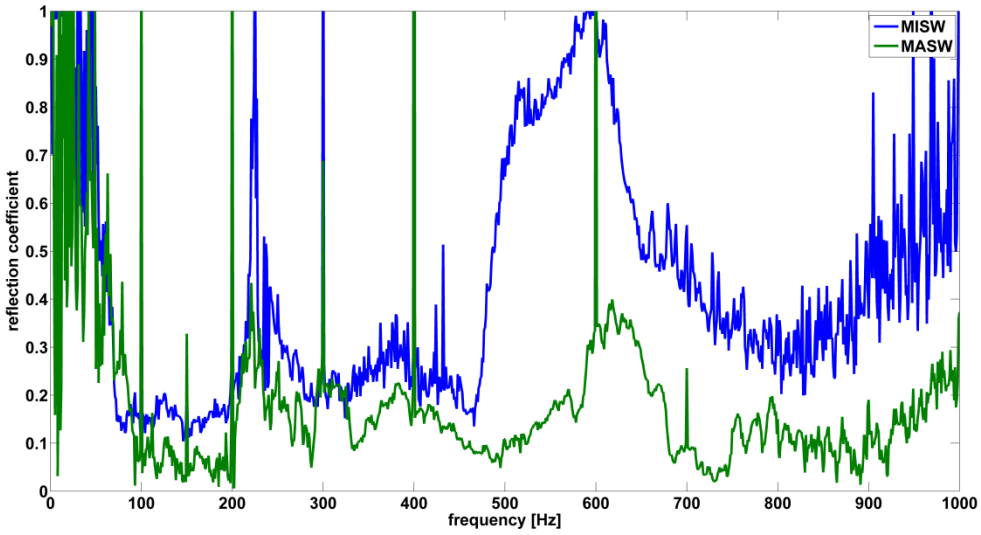

Figure 7.9: Reflection coefficients obtained with the wave decomposition method from MASW and MISW data. The vertical discontinuity is external to the deployment of sensors.

The reflection coefficients obtained with the wave decomposition method from MASW and from MISW data are displayed in Figure 7.9. The reflection coefficient is very high for the low frequencies, quickly decreasing up to being close to the zero value at the frequency of approximately 100 Hz. One or more peaks are in general visible in the reflection coefficient. If MISW is used, the reflection coefficient shows a major resonant peak at the frequency of approximately 620 Hz, when the coefficient is equal to 1, and a second minor peak at approximately 220 Hz. If MASW is used, the reflection coefficient quickly drops to low values and remains consistent without showing relevant resonant peaks but only small humps at approximately 220 Hz and 620 Hz. The resonant frequency of the reflected wave occurring at 620 Hz is associated with the crack depth whereas the first resonant peak could be associated with the mode jump that occurs at approximately 220 Hz. This is a behaviour already observed for the numerical simulations (section 4.2.4). Bearing in mind equation (2.35), if the R-wave velocity of 360 m/s, the mode integer index d_i equal to 1 and the coefficient C equal to 2.5 are assumed, the depth of the crack h is equal to 0.23 m. The R-wave velocity was chosen from the energy maxima of the spectral image of Figure 7.4. The depth is compatible with the total thickness of the bonded layers of the road pavement.

As demonstrated in section 4.2.3, the accuracy of the wave decomposition method was affected by the distance of the sensors from the crack. With the MISW method, the amplitude of the reflected wave was significantly higher than the case of the MASW method. This helped in the identification of the peaks in the reflection coefficient. The MISW technique fulfilled the needs of the wave decomposition method better than the MASW technique since the sensors were closer to the discontinuity.

7.3 Asphalt with Crack within the Deployment of Sensors

A third experimental investigation was executed with only the MISW technique to prove its effectiveness for detection and assessment of the depth of a crack situated inside to the deployment of sensors. In this occasion, the MASW technique was not utilized for the sake of brevity, since we knew *a-priori* the existence and the location of the crack. Moreover, the wave decomposition method (see section 4.2) was applied to experimental data to assess the depth of the surface-breaking crack. The configuration is displayed in Figure 6.5(b) and Figure 7.10, with the spacing D equal to 0.10 m. The multichannel record was obtained with the MISW technique, subsequently moving the source by 0.60 m four times, resulting in a multichannel record of 24 traces and length L_s of 2.40 m. In this experimental session, a 0.01 m wide vertical cracking in the surface was visible and symmetrically located between geophone 3 and geophone 4, within the geophone array. The source consisted of a 4-oz metallic mallet striking directly onto the surface, with a flat frequency response ranging from 10 Hz to 1000 Hz (Figure 7.7).

Figure 7.10: MISW experimental set-up configuration for the asphalt test site, with the discontinuity located in the middle of the array of sensors.

The *f-k* spectrum obtained utilizing the vertical signal recorded from the geophones is shown in Figure 7.11 and it displays peaks corresponding to the direct Rayleigh modes of propagation, associated with the red bands. Once again, one can notice the presence of additional peaks of energy parallel to the direct Rayleigh wave modes of propagation in the negative wavenumber quadrant. These peaks are produced by the reflections when MISW is used in the presence of a vertical discontinuity. The offset between them is Δp and it is proportional to the length L_s of the

deployment of sensors. In this case $\Delta p = 10.50$ rad/m . The offset Δp is highlighted by double red arrows. Moreover, energy peaks in the positive wavenumber quadrant are visible: these are related to the use of the MISW technique adding a periodicity to the system and changing the uniformity of the sensors spacing if the source is not precisely moved by the wanted distance. These energy bands are highlighted in the spectrum by black arrows.

Albeit the content of energy associated with the direct Rayleigh wave is noticeable until the frequency of approximately 1 kHz, it becomes abruptly weaker from the frequency of 600 Hz revealing the existence of a cut-off frequency. The cut-off frequency is highlighted by a red arrow in the *f-k* spectrum and is due to the presence of the crack, although possible cut-off frequencies are also noticeable at approximately 100 Hz and 200 Hz. This behaviour is expected since it follows that of the numerical simulation (Chapter 6). The vertical discontinuity allows only the passage of long Rayleigh wavelengths, blocking the passage of the short ones, which are mainly reflected. Hence, it acts as a low-pass filter. The depth of the discontinuity can be inferred from the chosen value of the cut-off frequency. Remembering the frequency range of geophones, the maximum frequency detectable in these experimental sessions is approximately 1 kHz.

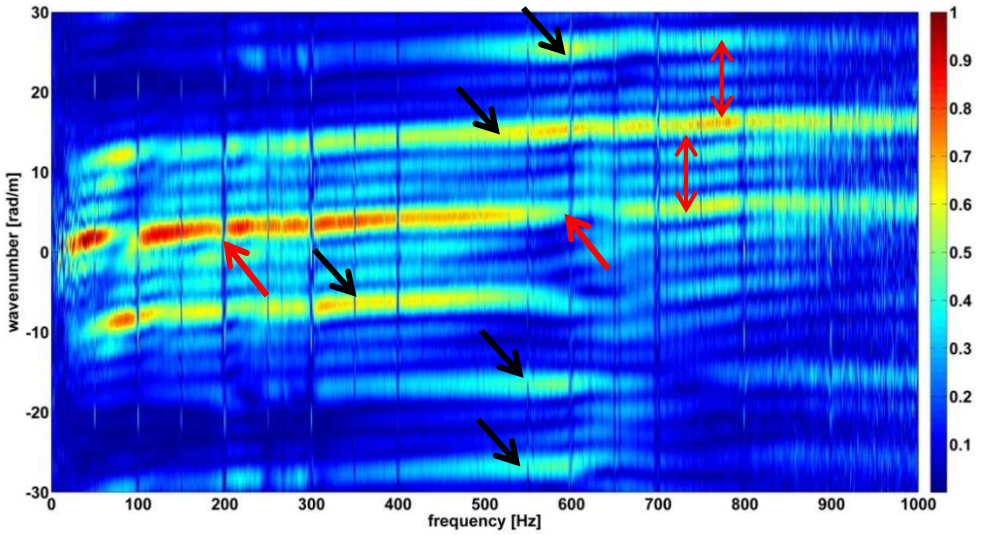

Figure 7.11. *F-k* spectrum obtained with MISW technique from the experimental investigation with a crack in the middle of the array of sensors. The direct Rayleigh modes of propagation correspond to the red peaks; black arrows highlight energy peaks produced by reflections from the faces of the vertical discontinuity when MISW is used. The red arrows highlight the cut-off frequencies due to the presence of the crack. The red double arrows highlight the offset Δp.

A vertical discontinuity located within the deployment of sensors was detected experimentally, due to the presence of a cut-off frequency in the spectral image obtained with the MISW method. Its depth could be estimated from the value of the frequency of cut-off.

The wave decomposition method was applied to the data coming from the deployment of sensors for the MISW case. The reflection coefficient was evaluated as the amplitude ratio of the negative going wave to the positive going wave at the reference node of the left end side deployment of sensors (geophone #1). The transmission coefficient was evaluated as the amplitude ratio of the direct positive going wave on the right end side of the notch to the direct positive going wave on the left end side of the notch, evaluated at their respective reference nodes (geophone #1 and geophone #4). Since the experiment was repeated moving apart the source by an equal length L_s three times, the result was the average of four tests. The wavenumber and phase velocity are extracted from the vertical *f-k* spectra obtained with the MISW technique displayed in Figure 7.12, which was conducted in a pristine area in the proximity of the location of this experiment. The black dots indicate the extracted peaks of energy, which are used as *a-priori* information in the wave decomposition method.

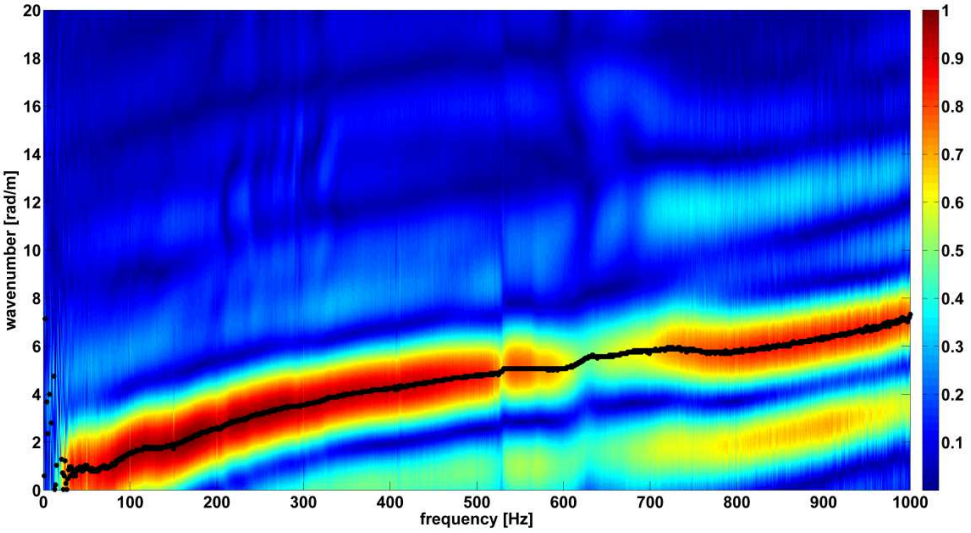

Figure 7.12: *F-k* spectrum with absence of discontinuity. The direct Rayleigh modes of propagation correspond to the red peaks. The black dots indicate the extracted energy maxima of the *f-k* spectrum used in the wave decomposition method.

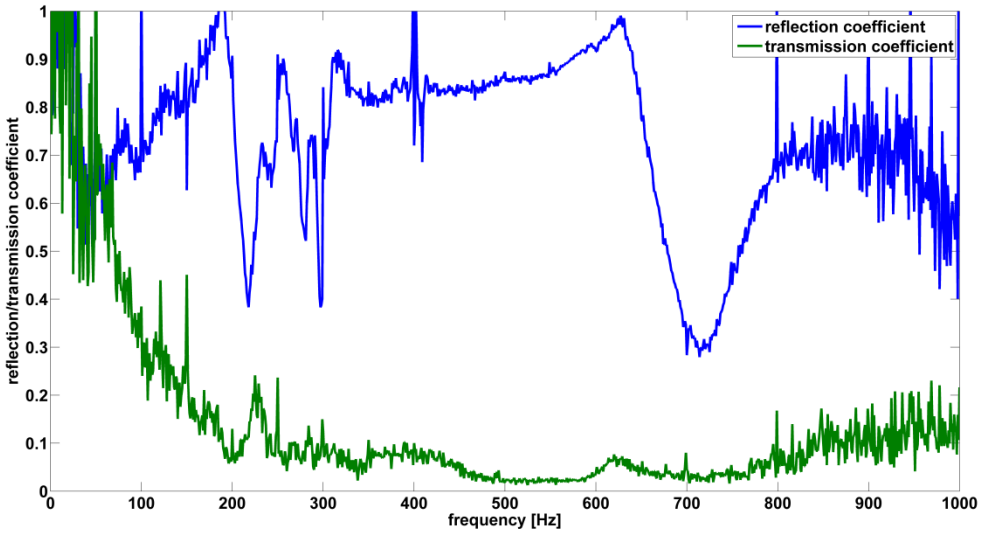

Figure 7.13: Reflection and transmission coefficients from wave decomposition method with experimental data obtained with MISW technique. The vertical discontinuity is within the deployment of sensors.

The reflection and transmission coefficient obtained with the wave decomposition method from MISW measurements are displayed in Figure 7.13. The reflection coefficient shows a trend in which it firstly decreases and then augments moving from the low to the high frequencies, with two relevant peaks at approximately 190 Hz and 620 Hz. The peaks are associated with the depth of the surface-breaking crack. The transmission coefficient has a high value at the low frequencies, dropping with a steep trend up to a cut-off frequency of approximately 200 Hz, where it approaches the zero value. A second cut-off frequency is visible at approximately 620 Hz. The resonances and the cut-offs occur at the approximately the same frequencies (as in the numerical investigations of section 4.2.2). The results obtained with the wave decomposition method are consistent with those shown in the vertical *f-k* spectrum (Figure 7.11): in fact, both methods reveal the existence of cut-off frequencies at approximately 200 Hz and 620 Hz. They are also consistent with the results coming from the numerical simulations of section 4.2.2. Bearing in mind equation (2.35), if the R-wave velocity of 500 m/s, the mode integer index d_i equal to 1 and the coefficient C equal to 2.5 are assumed for the first resonant peak, the depth of the crack h is estimated to be 1.00 m. If the R-wave velocity of 725 m/s, the mode integer index d_i equal to 2 and the coefficient C equal to 2.5 are assumed for the second resonant peak, the depth of the crack h is estimated to be 0.94 m. The R-wave velocities have chosen from the peaks of energy of the spectral image of Figure 7.12.

7.4 Comparison of Asphalt and Sensors Couplings

A big limitation for the survey and condition monitoring accomplished in asphalt within this thesis was the low frequency range of applicability of the geophones (up to 1 kHz) and their non-ideal coupling with the asphalt. This section details the investigation and the comparison among different ways to couple the accelerometers with the road surface (tarmac). The aim of this work was to find the most reliable fashion for recording the wave's amplitude and phase angle in asphalts. The comparison was made by looking at the amplitude and phase angle of the transfer function between the signal at the source and the signal picked up at the accelerometer position, placed 0.15 m from the source. The accelerometer was coupled with the asphalt surface through 7 different configurations. The source consisted of a 4-oz metallic mallet striking on a circular aluminium plate of 0.15 m diameter and 1.5cm thickness, resting on the asphalt surface. The signal at the source was acquired via an accelerometer attached onto the surface of the circular plate. For the forthcoming experimental investigations, miniature single-axis accelerometers type 352C22 and 352C04 from PCB Piezotronics were used. The different types of source-to-ground coupling tested in this section are listed hereafter and shown in Figure 7.14, where the number are in accordance with the list:

- 1. Aluminium foil (~1 mm thick) attached with instant glue (first type) with piezoelectric accelerometer attached on its top;
- 2. Aluminium foil (~1 mm thick) attached with instant glue (second type) with piezoelectric accelerometer attached on its top;
- 3. Steel cube resting on asphalt with piezoelectric accelerometer attached on its top;
- 4. Steel cube resting on asphalt with piezoelectric accelerometer screwed in on its top;
- 5. Steel cube resting on a sand bag with piezoelectric accelerometer attached on its top;
- 6. Aluminium tripod resting on asphalt with piezoelectric accelerometer attached on its top;
- 7. Aluminium tripod resting on asphalt with piezoelectric accelerometer screwed in on its top;

All the tests were repeated and recorded 5 times with a sample frequency of 20 kHz and duration of 1 sec, under the same input conditions, and then averaged in the frequency domain.

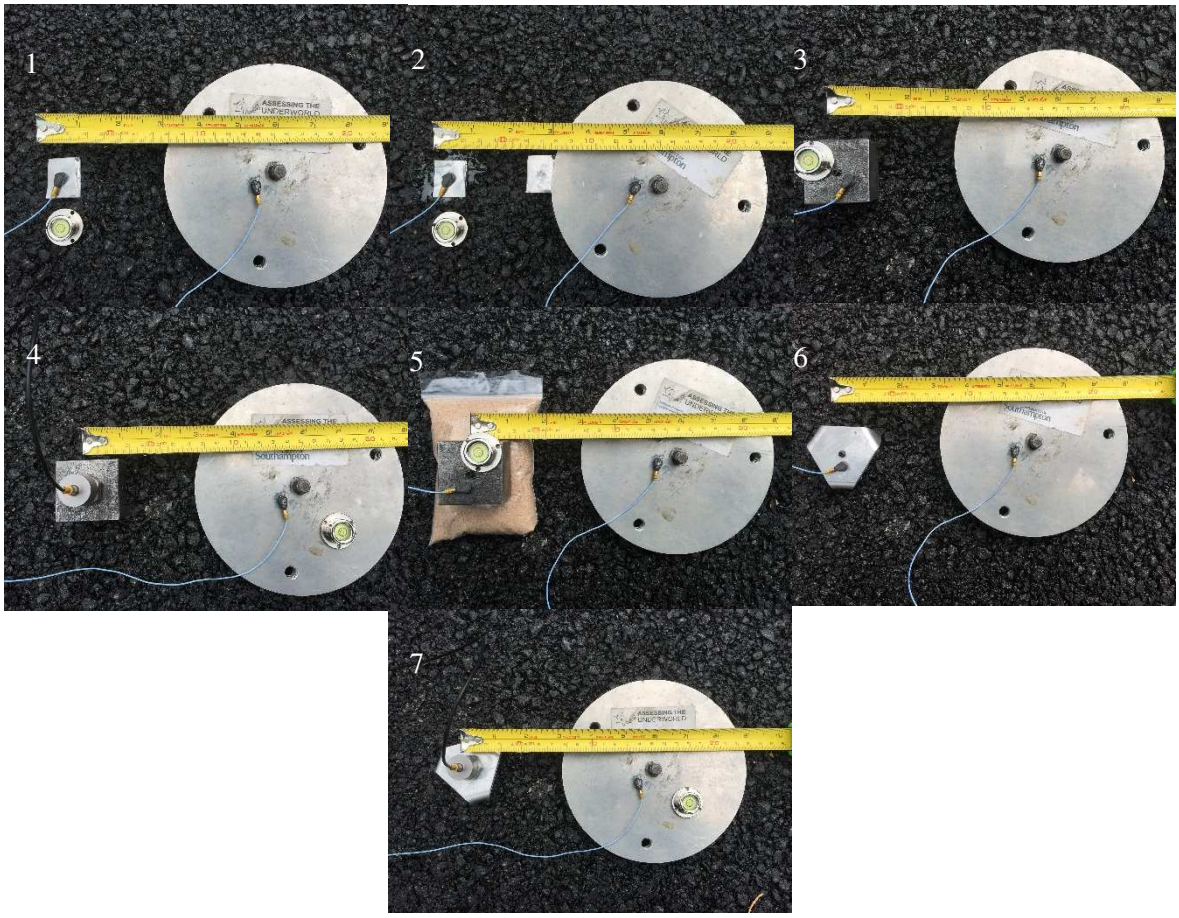

Figure 7.14. The different types of source-to-ground coupling tested in this experimental session.

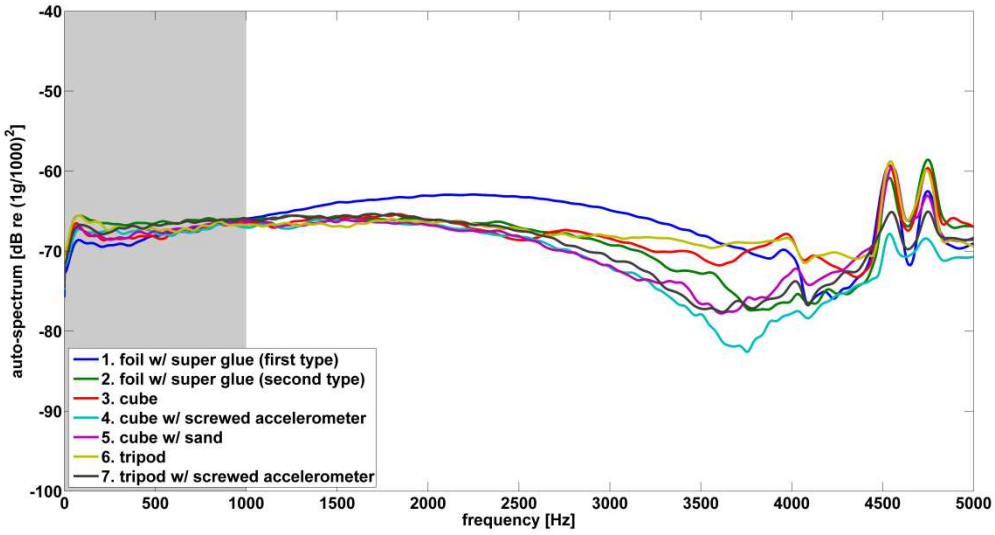

Figure 7.15: Auto-spectrum of the signal at the source for the experimental investigations. The power associated with each excitation is consistent throughout different tests.

The auto-spectrum of the signal at the source computed as per equation (3.1) shows one anti-resonance at around 4 kHz, which is probably a feature of the aluminium plate (Figure 7.15). The auto-spectrum of signal at the source shows that the power associated with each excitation is consistent throughout the different tests, with a drop of approximately 10 dB at 4 kHz. The shaded area highlights the frequencies that are affected by near-field effects. Remembering equation (2.3) and assuming a velocity of 300 m/s, the cut-off frequency to avoid near-field effect was chosen equal to 1 kHz.

The amplitude and phase of the transfer functions between the signal at the source position and that at the receiver position are displayed in Figure 7.16(a) and Figure 7.16(b). The presence of a peak in the amplitude and/or of a sudden big jump in the phase angle pattern is an indicator of some kind of resonance or anti-resonance effects.

Based on the appearance of the amplitude and phase of the transfer functions, the best way to couple sensors to the surface is the use of aluminium foil attached with super glue, since the energy is usually higher, especially that associated with the highest frequencies, and consistent through a wider range of frequencies. The use of glues assures that no resonances or anti-resonances occur up to approximately 4 kHz. The use of sand sandwiched between the sensor and the asphalt surface has the effect of dampening the frequencies higher than 500 Hz. Contrariwise, low frequencies resonate when sand is interposed between the tarmac surface and the sensors. A resonant frequency and a phase jump at approximately 500 Hz are observed when sand is used. The use of the steel cube and of the tripod resting on the road surface as a casing for the accelerometer gives the worst results in terms of energy of the transfer function, since the energy of the signal is not consistent through the frequency range, showing many resonant peaks and phase jumps in the range from 1.5 kHz to 3 kHz. The shaded area highlights the frequencies that are affected by near-field effects and by spatial aliasing. Remembering equation (2.31), the cut-off frequency to avoid near-field effect was chosen equal to 1 kHz. Remembering equation (2.34) and assuming a R-wave velocity of 1200 m/s, aliasing occurred from 4 kHz onward.

Figure 7.16(c) shows the coherence between the signal at the source position and that at the receiver position. The values of coherence when the aluminium foil is used to couple the sensors are usually high in the range 1-4 kHz, whereas the coherence is poor when the tripod and the cube were chosen.

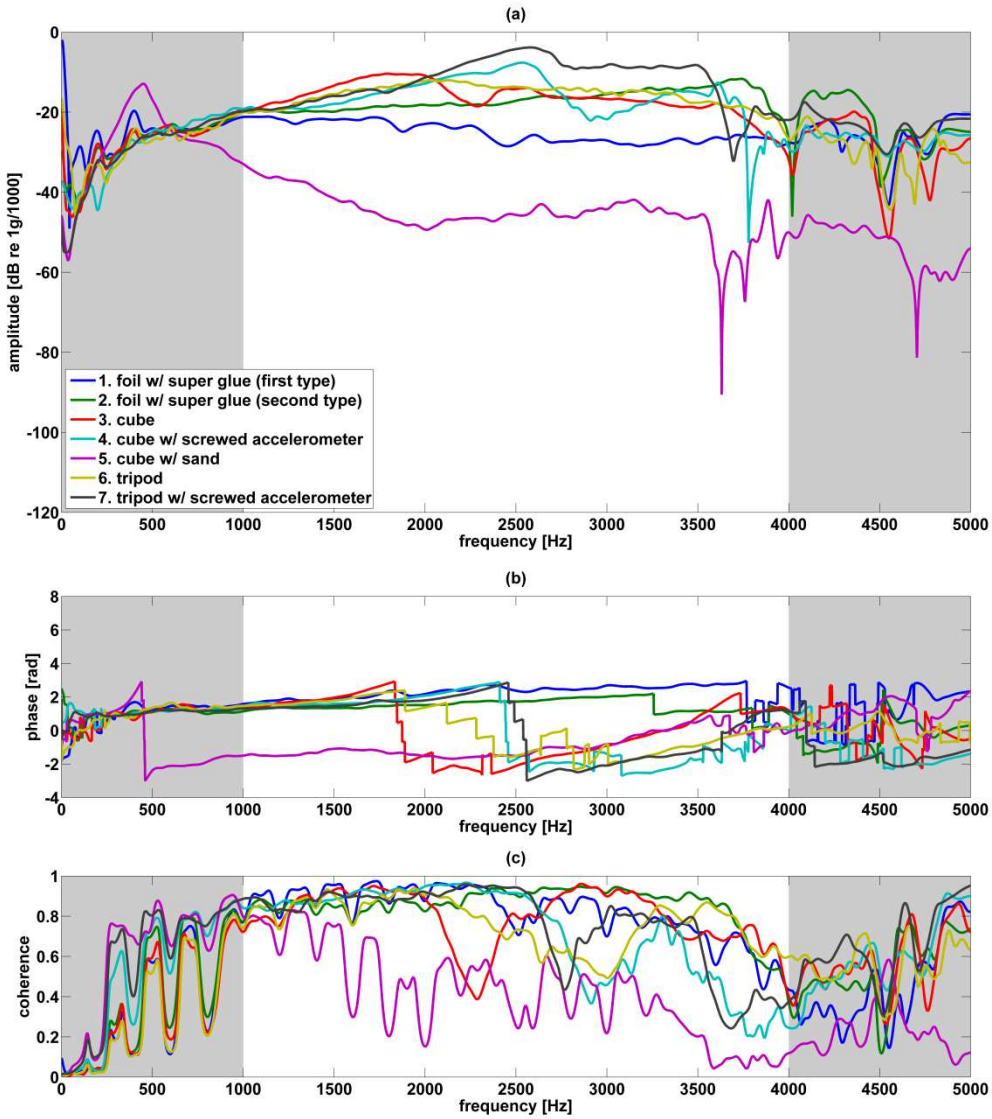

Figure 7.16: Amplitude (a) and phase angle (b) of the transfer functions between the signal at the source and the signal at the receiver position, and coherence (c), for different couplings between the sensor and the tarmac surface. The shaded area highlights the frequencies that are affected by near-field effects and by spatial aliasing.

7.5 Summary

This chapter detailed the experimental investigation performed in asphalt for the detection and the assessment of surface-breaking cracks. For each case study, the novel and innovative application of two established seismic spectral methods were employed and the results were displayed. Moreover, the wave decomposition method described in Chapter 4 was applied to the seismic data for each case.

Section 7.1 described the experimental investigation on a case without any visible surface-breaking crack, executed with the MASW and the MISW technique. The spectral images obtained with the

two methods were almost identical, confirming that no cracks were present in the volume of medium investigated. The wave decomposition method confirmed these findings by showing a very low reflection coefficient with both MASW and MISW data, which was incompatible with the presence of any discontinuity nearby the area of investigation.

Section 7.2 described the experimental investigation on a case with a crack external to the deployment of sensors, executed with the MASW and the MISW technique. In this case, the spectral images obtained with the two methods showed some relevant differences, confirming the presence of a vertical discontinuity (as proven numerically in Chapter 6). The discontinuity was located externally to the deployment of sensor. The application of the wave decomposition to the experimental data confirmed the presence of a vertical crack. Its depth was estimated based on the resonant frequency of the reflection coefficient and on the phase velocity estimated with the imaging technique.

The case of a crack within the deployment of sensors was described in section 7.3. In this case, only the MISW method was employed. The spectral image obtained with the MISW method showed peculiar features, which could be associated with the presence of the crack. Particularly, some cut-off frequencies can be inferred from the spectral image. They were related to the resonance behaviour of the vertical crack and hence to its depth. The wave decomposition method was used to compute the magnitude of the reflection and of the transmission coefficients. Their behaviour was consistent with the results obtained with the imaging techniques and they both showed multiple resonant and cut-off frequencies from which the depth of the crack was estimated.

Finally, section 7.4 presented a comparative study among different ways to couple sensors to the asphalt's surface, which indicated the use of an aluminium foil stuck on the asphalt's surface as the best way to avoid unwanted resonant effects to corrupt the quality of the seismic data.

Chapter 8: Conclusions

8.1 Review of the Thesis

The dynamic evaluation of the shear velocity profiling, condition monitoring and performance assessment of soils and roads is crucial for the determination of the level of deterioration of an infrastructure and for decisions regarding design, maintenance, strengthening and rebuilding of existing infrastructures. Traditional tests are performed with expensive, slow, disruptive and destructive tests. In recent decades, researchers' attention has been directed towards more versatile and non-invasive techniques that allow the estimation of mechanical and physical properties of materials through sensors working entirely from the surface of the medium. Among many interesting concepts, the idea of employing and monitoring the propagation of mechanical waves in structures gained interest and popularity, due to its effectiveness and accuracy.

Although a few notable authors have made substantial contributions to the field, there were still drawbacks and limitations affecting the existing seismic, non-destructive techniques. The shear wave profiling of soils and roads it is usually obtained after the inversion of an experimental dispersion curve. The latter, it is commonly obtained by imaging techniques of the vertical displacement of a seismic event, picked up at different locations with the aid of multiple geophones. Nonetheless, the use of seismic spectral methods for obtaining the shear wave profiling is hindered by resolution problems and their ability to assess the actual dispersive behavior of Rayleigh wave. Often some modes of propagation are superimposed and camouflaged under the same energy peaks due to lack of resolution. Sometimes the vertical and the horizontal components of motion show a different distribution of energy among different modes. Hence, favouring one direction with respect to the other and/or the lack of resolution of the spectral image could lead to a misinterpretation of the seismic survey and to ambiguous, if not erroneous, results.

There are currently no standard methods for the determination of the level of deterioration of a road and the interrogation of cracks. Although many attempts have been made in order to find a reliable and standard method for the assessment of cracks in roads, and many authors proposed valuable methods exploiting the properties of mechanical waves, the biggest challenge of the surface wave methods for asphalt's crack interrogation remains their application to real cases. Particularly, they all seem to lack reliability when applied to real scenarios, due to the dispersive and heterogeneous nature of the material tested.

This thesis aimed at bridging these gaps, by keeping the wave-based approach from the preliminary theoretical and numerical analysis to the experimental demonstrations. The thesis was constructed

around three main research threads. The first was the development of a new method to compute the seismic spectral images to obtain experimental dispersion curves, based on the joint use of the vertical and the horizontal direction of motion of the R-wave. The second was the development of a novel and innovative application of established methods in the field of non-destructive evaluation sensors and structural health monitoring. Particularly, two seismic spectral methods were used in synergy to detect and assess the depth of surface-breaking cracks in asphalt. The third was the development of a new wave decomposition method for the computation of the direct and reflected waves' amplitude and phase. This addressed the lack of non-destructive evaluation of vertical discontinuities in asphalt.

The study started with the investigation into the physics of elastic wave propagation in infinite and semi-infinite elastic media. Moreover, a standard analytical modelling methodology based on the stiffness matrix method for the forced and free propagation of waves in layered media was employed (Chapter 2). It was used for the inversions of experimental dispersion curves, to validate the FEM model and to display the modes of propagation in layered media.

The adopted FEM model used in the thesis and some standard signal processing techniques were introduced in Chapter 4. A two-dimensional finite element model of the ground was assembled to study the wave propagation in half-space and multi-layered systems. It used finite elements together with infinite elements, which had the aim of avoiding or at least minimizing spurious reflections from the boundaries of the model. The model proved to be consistent with the analytical solutions for wave propagation in half-space and layered media and it was extensively used for simulations within this thesis.

The rationale and the fundamentals of the spectral convolution method were discussed in Chapter 4. The spectral convolution method tackled the aforementioned limitations of the traditional signal processing methods leading to less ambiguous dispersion curves, by improving the resolution and the accuracy of the *f-k* spectrum. By adopting the wave decomposition method for the processing of seismic data, probability to fall into false interpretation of the seismic survey reduced thank to the complementary use of the vertical and horizontal components of motion of the R-wave. The spectral convolution method helped to constrain the inversion problem since it allowed obtaining a dispersion curve of the medium with reduced ambiguities. The spectral convolution method helped in separating the contribution of different modes of propagation and in locating osculation points, especially if jointly utilized with the ellipticity curve. The advantages of the new proposed method with respect to the traditional fashions to estimate the dispersion curves of soils and asphalt were shown with the aid of numerical simulations. The experimental validation for soils and asphalt investigation was presented in Chapter 5. This method proved its robustness for various types of layered media, both normally dispersive and media with big velocity contrasts or velocity inversions.

Chapter 4 also introduced the rationale and the fundamentals of the new wave decomposition method for crack interrogation. This new method tried to overcome all the limitation of the wave-based approaches for crack detection in asphalts since it managed to cope with the dispersive and heterogeneous nature of the material. It estimated the depth of normal, surface-breaking cracks by computing the reflection and transmission coefficient of the R-wave. It was based on a least square optimization algorithm, which found the best solution of a linear system. Moreover, the phase of the transmission and of the reflection coefficient could help in the location of the crack, although a wider investigation on layered media was omitted in this thesis. The numerical simulation presented in Chapter 4 helped to understand the resonant behaviour of surface-breaking cracks and to highlight the dependency of the proposed method from the number of measurements and from the distance from the crack. The method was successfully employed for the estimation of the depth of cracks in realistic layered media and the experimental validation, shown in Chapter 7, proved its robustness.

Chapter 6 described the novel and innovative application of two established seismic spectral methods for the detection and the evaluation of cracks in roads. The key concept of this study was that any relevant difference in the spectral image obtained with the two methods was an indication of the presence of a vertical discontinuity. An extensive numerical investigation highlighted the advantages of the synergistic use of the two spectral methods and it suggested a possible practical strategy for crack detection and interrogation. The chapter was concluded with a study on the space-normalised seismograms as a valuable tool for the pattern recognition of surface waves. The experimental validation described in Chapter 7 showed the advantages compared to the use of the traditional method once a time.

Chapter 7 was concluded with a comparative study among different ways to couple sensors to the asphalt's surface, which indicated the use of an aluminium foil stuck on the asphalt's surface as the best way to avoid unwanted resonant effects to corrupt the quality of the seismic data.

8.2 Summary of Novel Contributions

Proposal of the spectral convolution method to improve the accuracy and resolution of experimental dispersion measurements. The new spectral convolution method was introduced in this thesis. It was based on the simultaneous exploitation of the vertical and the horizontal components of a seismic event and it improved the resolution and the overall accuracy of the spectral image in the frequency-wavenumber (*f*-*k*) domain. Each frequency component of the vertical motion of R-wave is 90 degrees out-of-phase with the corresponding frequency components of the horizontal motion. The newly developed spectral convolution method exploited this peculiar feature of the R-wave to obtain a spectral image with better resolution and accuracy than traditional methods. It consisted of a convolution in the frequency domain between the vertical and the horizontal

components of the R-wave, which led to a wave with doubled frequency and wavenumber content. The method enabled overcoming of the common problems due to a poor resolution of the spectral image, which often lead to misinterpretation of the seismic survey. The method was proven advantageous for dispersion measurement in normally dispersive media as well as in not normally dispersive media, such as roads. It was also found to improve the accuracy of dispersion curves at the lower frequencies.

Application of traditional surface wave methods for detection of vertical discontinuities in asphalt. Assessment of the location and of the extension of cracking in road surfaces is important for determining the potential level of deterioration in the road overall and the infrastructure buried beneath it. Damage in a pavement structure is usually initiated in the tarmac layers, making the Rayleigh wave ideally suited for the detection of shallow surface defects. An investigation of two surface wave methods to detect and locate surface-breaking cracks in asphalt layers was proposed within this thesis. The aim of the study was to synergistically exploit the results from the well-established Multichannel Analysis of Surface Waves (MASW) and the more recent Multiple Impact of Surface Waves (MISW) in the presence of a discontinuity, and to suggest the best practical strategy for evaluating the presence, location and the extension of vertical cracks in roads. The study was conducted through numerical simulations alongside experimental investigations; it considered the two cases for which the cracking is internal and then external to the deployment of sensors. Any relevant differences in the spectral images obtained with MASW and with MISW were a proof of the presence of a crack. The detection strategy then consisted in repeating the MISW measurement at different locations with the aim of locating and assessing the depth of the crack, since MISW was found to enhance the visibility of the reflected waves in the frequency wavenumber (*f-k*) spectrum. The spectral methods adopted in this thesis were proven successful in the crack interrogation of asphalt, despite the heterogeneous and the dispersive nature of the material tested. The spectral image in the frequency-wavenumber domain could be used for two purposes at the same time: the shear wave profiling and the crack interrogation.

Application of the wave decomposition method for interrogation of vertical discontinuities in asphalt. The practical application of crack detection methods in asphalt is slowed down due to the dispersive behaviour of the material tested. A new signal processing technique for the measurement of the amplitude and phase of the direct and reflected Rayleigh wave was presented in this thesis. It decomposed the signal into its direct and reflected components. The method used multiple receivers and hence it found an approximate solution with a least square optimization. The resonant peak frequencies of the reflection coefficient and the cut-off frequencies of the transmission coefficient were used for assessing the depth of the crack, the phase of the reflection coefficient providing information about the location of the crack. The study was conducted through numerical simulations alongside experimental investigations and it considered the cases for which the cracking is internal

and then external to the deployment of sensors. The method was proven successful in the assessment of the depth of cracks both numerically and experimentally, despite the dispersive and the heterogeneous nature of asphalt.

Influence of the coupling between transducers and asphalt on seismic measurement. A comparison among a variety of different couplings between seismic sensors and the medium surface was accomplished with the aim of finding the optimal way for seismic measurements in asphalt. Based on the appearance of the amplitude and phase of the transfer functions, the best way to couple a piezoelectric sensor to the surface was the use of aluminium foil attached with super glue, since the energy was usually higher, especially that associated with the highest frequencies, and consistent through a wider range of frequencies. The use of glues assured that no resonances or anti-resonances occurred up to approximately 4 kHz.

Proposal of the space-normalised seismogram for crack detection. When many receivers were available and the data was analysed in the time-space domain, a normalisation of the seismogram along the space axis helped in the detection of the reflections caused by vertical discontinuities since it displayed more information than the traditional time-normalised seismogram. It could be a useful tool to support and complement the spectral methods. It added information about the presence of vertical discontinuities that were beyond the capabilities of the traditional imaging techniques and of time-normalised seismograms.

Study on the correlation between shear wave velocity and electromagnetic parameters in soils. This work was accomplished in parallel with this research project, in collaboration with the University of Birmingham. The results are shown in Appendix F in the form of a conference paper. The fundamental aim of this parallel, joint effort was to find relevant correlations between some of the electromagnetic parameters and the shear velocity of soils. In addition, one aim of this paper was to try to indirectly measure the volumetric water content of soils with the seismic methods.

8.3 Future Work

This thesis has investigated various aspects regarding the signal processing of seismic data for shear wave velocity profiling and condition monitoring of soils and roads. The following suggestions indicate the future work directions, which can be grouped into two sets:

- **Improvement of the accuracy and resolution of the experimental dispersion measurements.**
  - The convolution in time of the vertical and horizontal signals has proven to work well with analytical models (appendix E), but further investigation on its applicability on

numerical and real cases could be included in the study in order to compare this method with the spectral convolution method.

- **Interrogation of vertical discontinuities in asphalt.**
  - Although the methods proposed in this thesis proved to be successful for the interrogation of surface-breaking cracks both numerically and experimentally, their applicability could be extended to bottom-up cracks (not visible from the surface). This extension could contribute to improve the robustness of these methods for crack interrogation. The detection of bottom-up cracking could be pursued with the aid of a laboratory sample of an asphalt section. The sample should have some purpose-made cracking and could be buried in soil for *in-situ* measurement and/or buried in a sand bed in the laboratory, in both its front and flipped arrangement. Both sand and soils should limit the reflections produced by the boundaries of the sample. The geometry and the location of the slots should be decided according to the sizing of the crack and the range of frequency to be used.

  - The phase angle of the direct and the reflected waves computed with the wave decomposition method proposed in this thesis proved to give an accurate indication of the position of the discontinuities, with the numerical modelling of the half-space. The use of the phase angle of the direct and of the reflected wave as a tool to estimate the distance of a crack could be investigated in more details for layered systems, both numerically and experimentally. The study should also focus on the influence on the results of the phase changes and non-linearities occurring at the boundaries of the reflector.

  - The wave decomposition method proposed in this thesis was based on the solution of an overdetermined linear system, under the assumption that a single type of wave is present in the medium. The effect of the geometrical spreading was neglected at this stage of the investigation, but it deeply affects the quality of results, since being too far from the discontinuity does not permit to realize its presence. The addition of the geometrical spreading in the equations of the linear system could be investigated and included in the study. It would be advantageous to better spot resonances and cut-off frequencies and in general to compensate for the dependency of the results from the distance to the crack, although this may need the *a-priori* known of the location of the crack.

  - The wave decomposition method proposed in this thesis estimates the amplitudes and phases of the direct and reflected waves in asphalt in the frequency domain. The use of the coherence between the input source and the raw signals recorded at each geophone

position as a weight for the amplitudes at each frequency could be investigated. This investigation would contribute to increase the reliability of the results.

- The cross-power spectral density, the cross-correlation function or other transfer functions between the signals and the input source signal could be used instead of the raw signals recorded at each geophone location in the proposed wave decomposition method. It would be advantageous to reduce the effects of noise on the quality of the results.

Appendix A: Geotechnical Parameters of Soils

Many geotechnical properties are utilized to characterize the behaviour of a soil deposit: here only a few principal parameters are briefly recalled [102].

Mechanical properties, such as stiffness modulus and shear modulus, are highly dependent on the level of densification of soil, generally expressed by means of the void ratio e:

$$e = \frac{V_v}{V_s} \tag{A.1}$$

where V_v is the volume of voids and V_s is the volume of the solid state.

Relationship between states of matter for a soil deposit is also expressed by means of the porosity ϕ:

$$\phi = \frac{V_v}{V} \tag{A.2}$$

where $V = V_w + V_s + V_v$ is the total volume of the soil and V_w is the volume of water.

The degree of saturation S is the ratio between the volume of water V_w and the volume occupied by voids V_v. Then a soil is completely dry when $S = 0$ and completely saturated when $S = 1$.

$$S = \frac{V_w}{V_v} \tag{A.3}$$

The water content is usually expressed in terms of masses and named Gravimetric Water Content (GWC), being the ratio between the mass of water M_w and the mass of solid M_s:

$$\mathrm{GWC} = \frac{M_w}{M_s} \tag{A.4}$$

It is usually less than the unit, but in organic soils, it could reach values around 5.

The total or wet density ρ is:

$$\rho = \frac{M_s + M_w}{V} \tag{A.5}$$

The dry or bulk density ρ_d:

$$\rho_d = \frac{M_s}{V} \tag{A.6}$$

Typical values for the dry density of soils range between 1.7 and 2.2 Mg/m^3.

The Volumetric Water Content (VWC) is expressed in terms of volumes and is related to the GWV, water density ρ_w and dry density.

$$\text{VWC} = \frac{V_w}{V} = \text{GWC} \cdot \frac{\rho_d}{\rho_w} \tag{A.7}$$

Shear strength is the magnitude of the shear stress that a soil can sustain without failing. Undrained shear strength of clays S_u is determined with the unconsolidated undrained triaxial tests, as per ASTM D 4767-04.

The compression index c_c is an indicator of the compressibility of normal-consolidated soils and is determined by means of an oedometer test, as per ASTM D 2435-03.

Appendix B: Stiffness Matrix Method

The elements of the 4x4 layer stiffness matrix are given as follows for nonzero frequencies and nonzero wavenumbers [63, 67]. First, it is convenient to introduce the following notation:

ω is the angular frequency,

d is the layer's thickness,

G is the shear modulus,

$k = \dfrac{\omega}{c_m}$ is the wavenumber,

$$s = -\mathrm{i}\sqrt{1-\left(\frac{\omega}{kV_P^*}\right)^2}\ , \qquad t = -\mathrm{i}\sqrt{1-\left(\frac{\omega}{kV_S^*}\right)^2}\ . \tag{B.1}$$

The asterisk denotes a complex value that takes into account the effect of material damping ξ_P and ξ_S:

$$V_P^* = V_P\sqrt{1+2\xi_P\mathrm{i}} \qquad V_S^* = V_S\sqrt{1+2\xi_S\mathrm{i}} \tag{B.2}$$

The forced vibration problem for the j-th layer can be written in this form:

$$\begin{pmatrix} \tau_{xy}^1 \\ \sigma_y^1 \\ \tau_{xy}^2 \\ \sigma_y^2 \end{pmatrix} = K \begin{pmatrix} u_x^1 \\ u_y^1 \\ u_x^2 \\ u_y^2 \end{pmatrix} \tag{B.3}$$

where the superscript refers to the layer's interface.

The stiffness matrix for the j-th layer can be written as:

$$\mathbf{K} = \frac{(1+t^2)kG^*}{D}\begin{bmatrix}\mathbf{K}_{11} & \mathbf{K}_{12} \\ \mathbf{K}_{21} & \mathbf{K}_{22}\end{bmatrix} \tag{B.4}$$

where $D = 2(1-\cos ksd \cos ktd) + \left(st + \frac{1}{st}\right)\sin ksd \sin ktd$ and $G^* = G(1+2\xi_S \mathrm{i})$.

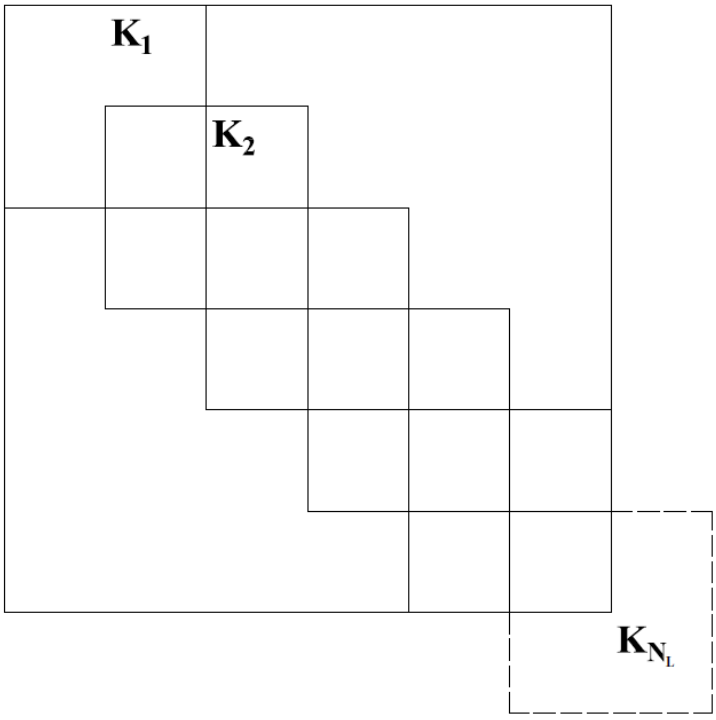

Figure B. 1: Assembly of global stiffness matrix [103].

$$\mathbf{K}_{11} = \begin{bmatrix} \frac{1}{t}\cos ksd \sin ktd + s \sin ksd \cos ktd & \frac{3-t^2}{1+t^2}(1-\cos ksd \cos ktd) + \frac{1+2s^2t^2-t^2}{st(1+t^2)}\sin ksd \sin ktd \\ \frac{3-t^2}{1+t^2}(1-\cos ksd \cos ktd) + \frac{1+2s^2t^2-t^2}{st(1+t^2)}\sin ksd \sin ktd & \frac{1}{s}\sin ksd \cos ktd + t \cos ksd \sin ktd \end{bmatrix} \tag{B.5}$$

$$\mathbf{K}_{22} = \begin{bmatrix} \frac{1}{t}\cos ksd \sin ktd + s \sin ksd \cos ktd & \frac{t^2-3}{1+t^2}(1-\cos ksd \cos ktd) + \frac{t^2-2s^2t^2-1}{st(1+t^2)}\sin ksd \sin ktd \\ \frac{t^2-3}{1+t^2}(1-\cos ksd \cos ktd) + \frac{t^2-2s^2t^2-1}{st(1+t^2)}\sin ksd \sin ktd & \frac{1}{s}\sin ksd \cos ktd + t \cos ksd \sin ktd \end{bmatrix} \tag{B.6}$$

$$\mathbf{K}_{21} = \begin{bmatrix} -s \sin ksd - \frac{1}{t}\sin ktd & -\cos ksd + \cos ktd \\ \cos ksd - \cos ktd & -\frac{1}{s}\sin ksd - t \sin ktd \end{bmatrix} \tag{B.7}$$

$$\mathbf{K}_{12} = \begin{bmatrix} -s \sin ksd - \frac{1}{t}\sin ktd & \cos ksd - \cos ktd \\ -\cos ksd + \cos ktd & -\frac{1}{s}\sin ksd - t \sin ktd \end{bmatrix} \tag{B.8}$$

The dynamic stiffness matrix of the half-space is instead:

$$\mathbf{K}_{\mathrm{H}} = kG^* \begin{bmatrix} \frac{\mathrm{i}s(1+t^2)}{1+st} & 2-\frac{1+t^2}{1+st} \\ 2-\frac{1+t^2}{1+st} & \frac{\mathrm{i}t(1+t^2)}{1+st} \end{bmatrix} \tag{B.9}$$

Appendix C: Eigenvalue Problem in a Layered System

In the case of thin layers (i.e. when the wavelength is large compared to the depth of the layer), the layer stiffness matrix can be obtained as [63, 67]:

$$\mathbf{K} = \mathbf{A}k^2 + \mathbf{B}k + \mathbf{G} - \omega^2\mathbf{M} \tag{C.1}$$

where:

$$\mathbf{A} = \frac{d}{6}\begin{bmatrix} 2(\lambda+2\mu) & & \lambda+2\mu & \\ & 2\mu & & \mu \\ \lambda+2\mu & & 2(\lambda+2\mu) & \\ & \mu & & 2\mu \end{bmatrix} \tag{C.2}$$

$$\mathbf{B} = \frac{1}{2}\begin{bmatrix} & \lambda-\mu & & -(\lambda+\mu) \\ \lambda-\mu & & \lambda+\mu & \\ & \lambda+\mu & & -(\lambda-\mu) \\ -(\lambda+\mu) & & -(\lambda-\mu) & \end{bmatrix} \tag{C.3}$$

$$\mathbf{G} = \frac{1}{d}\begin{bmatrix} \mu & & -\mu & \\ & \lambda+2\mu & & -(\lambda+2\mu) \\ -\mu & & \mu & \\ & -(\lambda+2\mu) & & \lambda+2\mu \end{bmatrix} \tag{C.4}$$

$$\mathbf{M} = \frac{\rho d}{6}\begin{bmatrix} 2 & & 1 & \\ & 2 & & 1 \\ 1 & & 2 & \\ & 1 & & 2 \end{bmatrix} \tag{C.5}$$

Appendix D: Raw Data from the Experimental Sessions

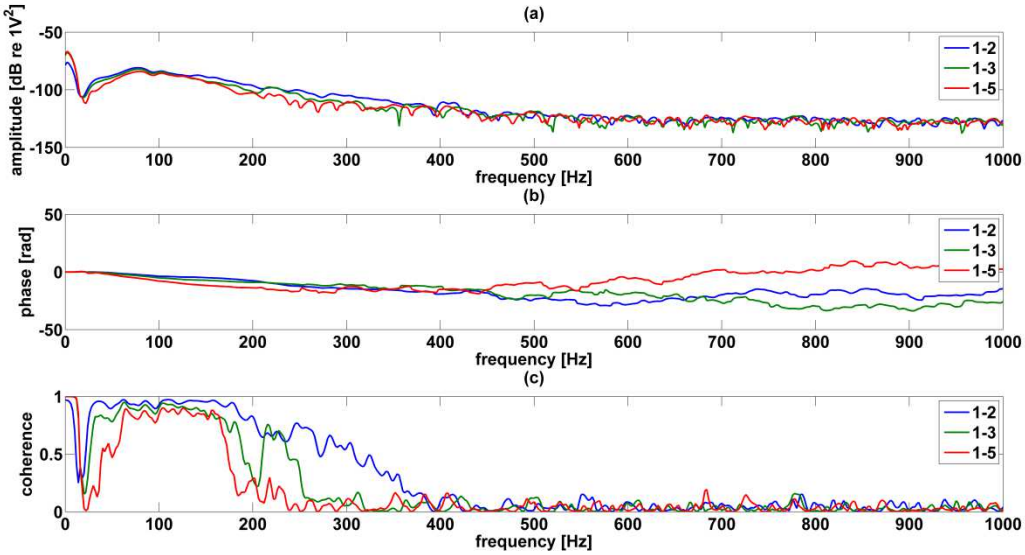

Figure D. 1: Amplitude (a) and phase angle (b) of cross-power spectrum (computed as per equation 3.1) between the signals at geophone 1-2, 1-3 and 1-5 (a), and coherence (c). Data from the experimental session of section 5.2.1, with excitation method 2 (vertical shaker parallel rakes).

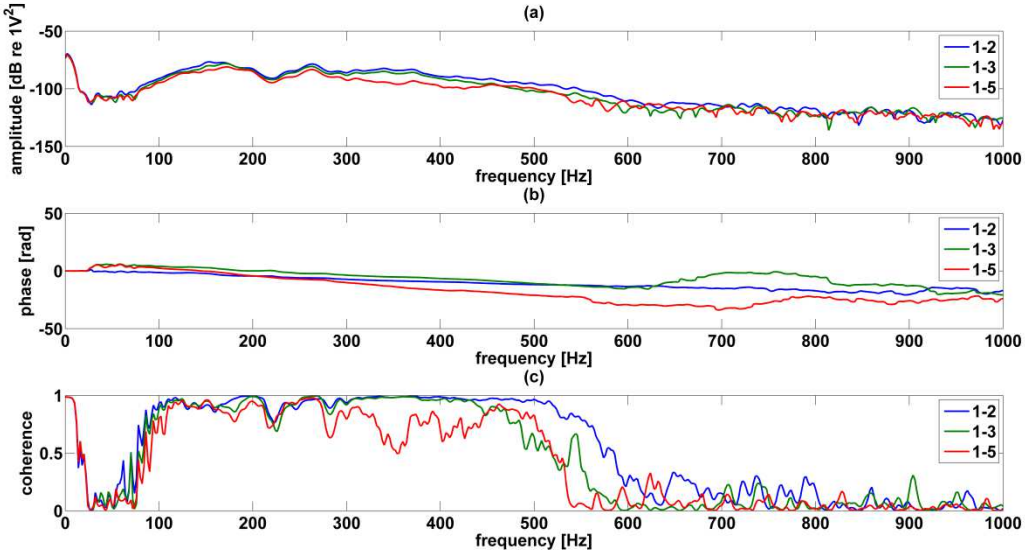

Figure D. 2: Amplitude (a) and phase angle (b) of cross-power spectrum (computed as per equation 3.1) between the signals at geophone 1-2, 1-3 and 1-5, and coherence (c). Data from the experimental session of section 5.2.2, with excitation method 5a (vertical small shaker).

Appendix E: Analytical Investigation of the Spectral Convolution Method

Equation (4.2) and equation (4.5) are used to run an analytical simulation of the R-wave with dispersive relation equal to:

$$k(\omega) = \frac{\omega}{10 \cdot \log(\omega)} \tag{E.1}$$

The length of the sensor line L_s was set equal to 10 m, whereas the length of the signal L_f was set equal to 0.5 sec. Then, the time-space representation was transformed in the frequency-wavenumber domain using the equation (3.5) and the equation (3.6).

Figure E. 1 shows the spectral image obtained from equation (4.2), i.e. only using the vertical components of the R-wave. it has a resolution dictated by the chosen length of the sensor line L_s and of the signal. The black dots represent the actual dispersive relationship, as per equation (E.1). The energy maxima in the spectra follow the black dots, which indicate the actual non-linear dispersive relationship.

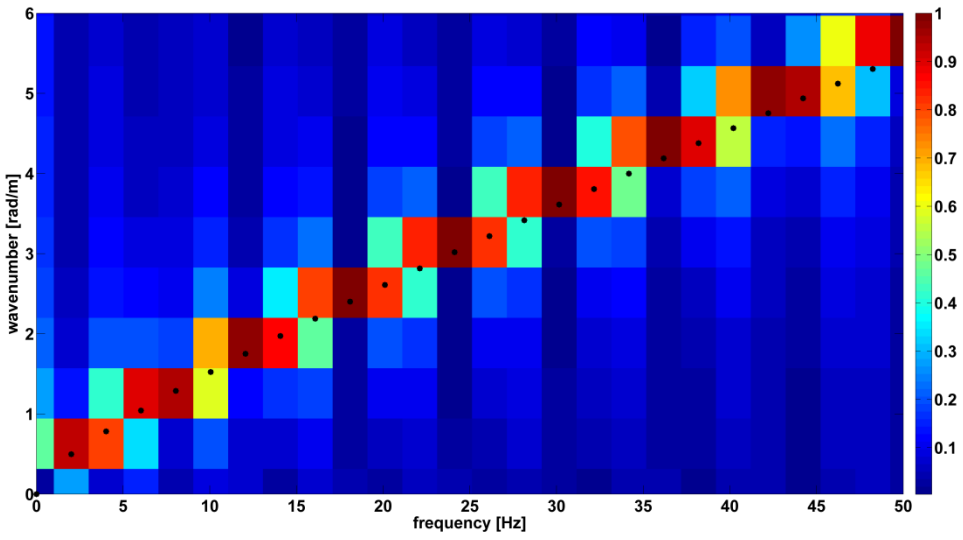

Figure E. 1: *F-k* spectrum with vertical components from analytical model of equation (4.2). L_s is equal to 10 m and L_f is equal to 0.5 sec. The black dots represent the actual dispersive relationship, as per equation (E.1). The energy maxima in the spectra follow the black dots, which indicate the actual non-linear dispersive relationship.

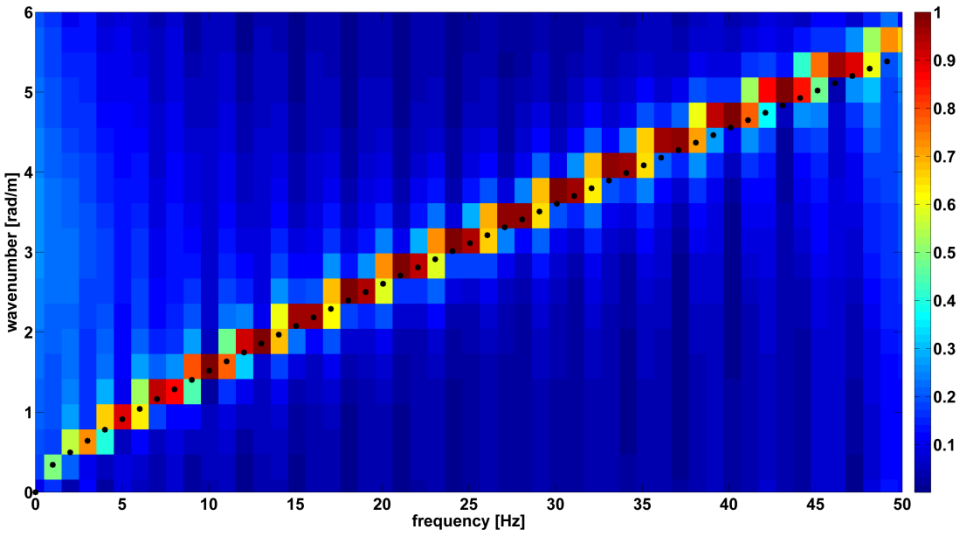

Figure E. 2: *F-k* spectrum with spectral convolution method from analytical model of equation (4.5). L_s is equal to 10 m and L_f is equal to 0.5 sec. The black dots represent the actual dispersive relationship, as per equation (E.1). The energy maxima in the spectra follow the black dots, which indicate the actual non-linear dispersive relationship.

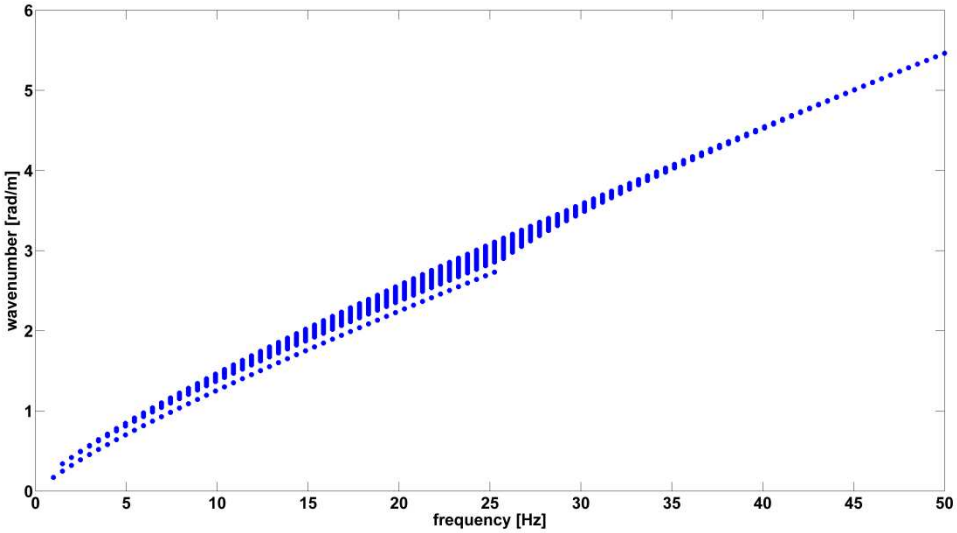

Figure E. 3: The harmonics that compose the signal when the spectral convolution method is applied to the vertical and the horizontal signal shown in the frequency-wavenumber domain.

Figure E. 2 shows the spectral image obtained from equation (4.5), i.e. using the spectral convolution method. It has a doubled resolution in both the frequency and wavenumber domains with respect to the image obtained using the vertical component. The black dots represent the actual dispersive relationship, as per equation (E.1). The energy maxima in the spectra follow the black dots, which indicate the actual non-linear dispersive relationship.

Figure E. 3 shows all the harmonics that compose the signal when the spectral convolution method is applied to the vertical and the horizontal signal, i.e. all the terms that arise from equation (4.5), shown in the frequency-wavenumber domain. The comparison with the spectral image of Figure E. 2 shows that the cross product terms, albeit present in the final spectral image, have negligible energy once the double Fourier Transform is accomplished in time and space.

Figure E. 4 shows the spectral image obtained from equation (4.2), i.e. only using the vertical components of the R-wave. The resolution is dictated by the of the sensor line L_s and of the signal, which in this case were respectively equal to 20 m and 1 sec. Hence, the spectral image has doubled resolution with respect of the image of Figure E. 1 and the same resolution of that obtained with the spectral convolution method. The black dots represent the actual dispersive relationship, as per equation (E.1). The energy maxima in the spectra follow the black dots, which indicate the actual non-linear dispersive relationship.

Figure E. 5 displays the absolute difference between the actual dispersion relationship and the peaks of energy extracted from the spectral images previously displayed. The absolute difference of the spectrum obtained with the spectral convolution method is less than that of the vertical spectrum. Hence, the spectral convolution method improves the accuracy of the spectral image. The vertical spectrum with longer sensors line and signal lengths, i.e. with doubled resolution, still gives the best results in terms of accuracy.

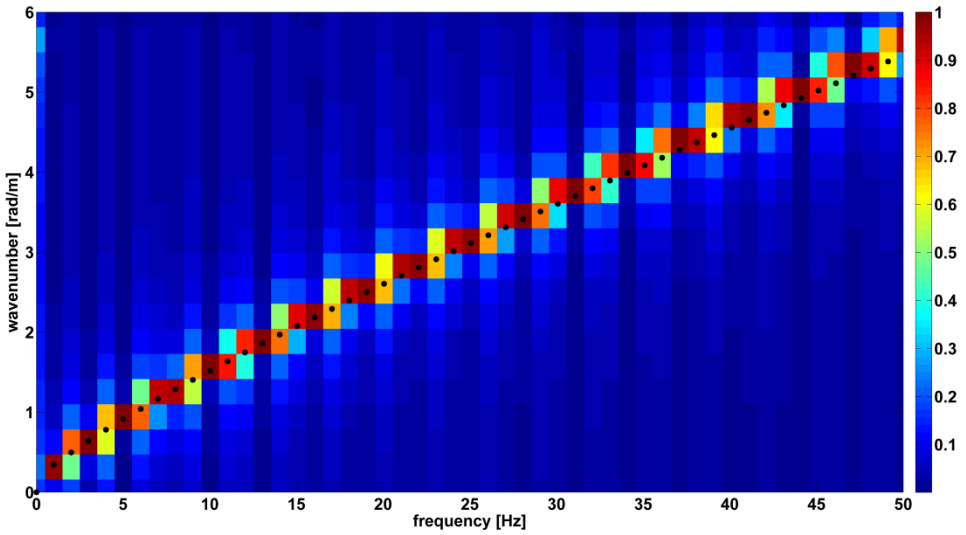

Figure E. 4: *F-k* spectrum with vertical components from analytical model of equation (4.2). L_s is equal to 20 m and L_f is equal to 1 sec. The black dots represent the actual dispersive relationship, as per equation (E.1). The energy maxima in the spectra follow the black dots, which indicate the actual non-linear dispersive relationship.

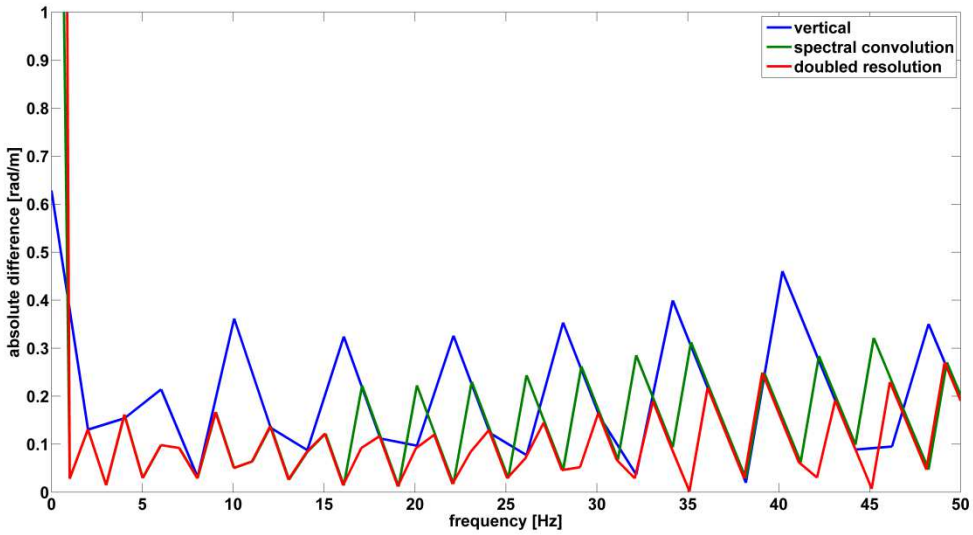

Figure E. 5: Absolute difference between the actual dispersion relationship and the peaks of energy extracted from the spectral images. Cases of vertical signal, spectral convolution between the vertical and the horizontal signals and vertical signal with doubled resolution.

Equation (4.6) describes analytically the spectral convolution method applied to the same signal (vertical or horizontal). As explained in section 4.1, it consists of two members, which destructively interact. This is observable in the spectral image obtained after applying equation (3.5) and equation (3.7). In fact, it is possible to notice that the energy maxima (the red bands) follow the actual dispersive relationship for the higher frequencies, whereas at the lower frequencies the estimation of the dispersive relationship is less accurate. A lack of accuracy at the lower frequencies is perceived by looking at the absolute difference between the actual dispersion relationship and the peaks of energy extracted from the spectral images, displayed in Figure E. 7. The absolute difference of the spectrum obtained with the self-spectral convolution method is bigger than that of the vertical spectrum. Hence, the product between the vertical and the horizontal components of motion, and not the self-product, is applied to the spectral convolution method within this thesis.

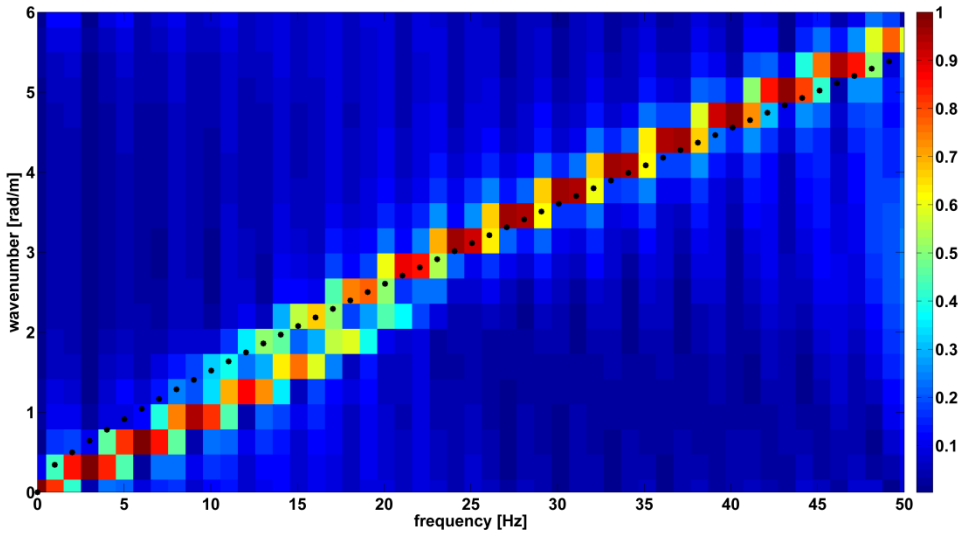

Figure E. 6: *F-k* spectrum with spectral convolution method from analytical model of equation (4.6). L_s is equal to 10 m and L_f is equal to 0.5 sec. The black dots represent the actual dispersive relationship, as per equation (E.1). The peaks of energy in the spectra follow the black dots, which indicate the actual non-linear dispersive relationship.

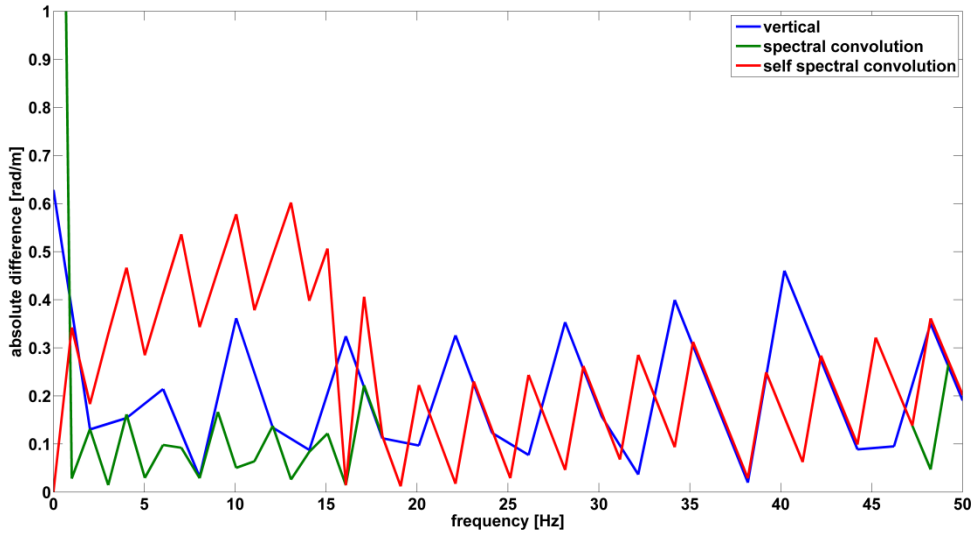

Figure E. 7: Absolute difference between the actual dispersion relationship and the peaks of energy extracted from the spectral images. Cases of vertical signal, spectral convolution between the vertical and the horizontal signals and self-spectral convolution.

Other methods to combine the vertical and the horizontal component of the R-wave other than the product in the time domain were tested within this thesis. Figure E. 8 shows the spectral image obtained with the product of the horizontal and of the vertical spectra in the frequency-wavenumber domain. The spectral image has the same resolution and accuracy of the image obtained with only the vertical or the horizontal component of motion (Figure E. 1). The difference between energy

maxima and minima increases. This method does not increase the resolution neither the accuracy of the spectral image and for this reason was abandoned.

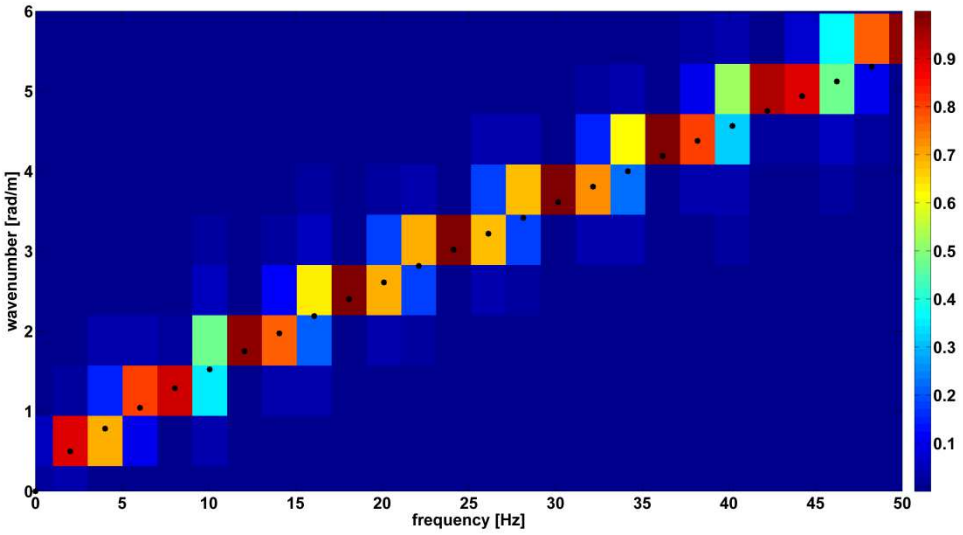

Figure E. 8: *F-k* spectrum obtained after the product of the horizontal and of the vertical spectra in the frequency-wavenumber domain. The black dots represent the actual dispersive relationship, as per equation (E.1).

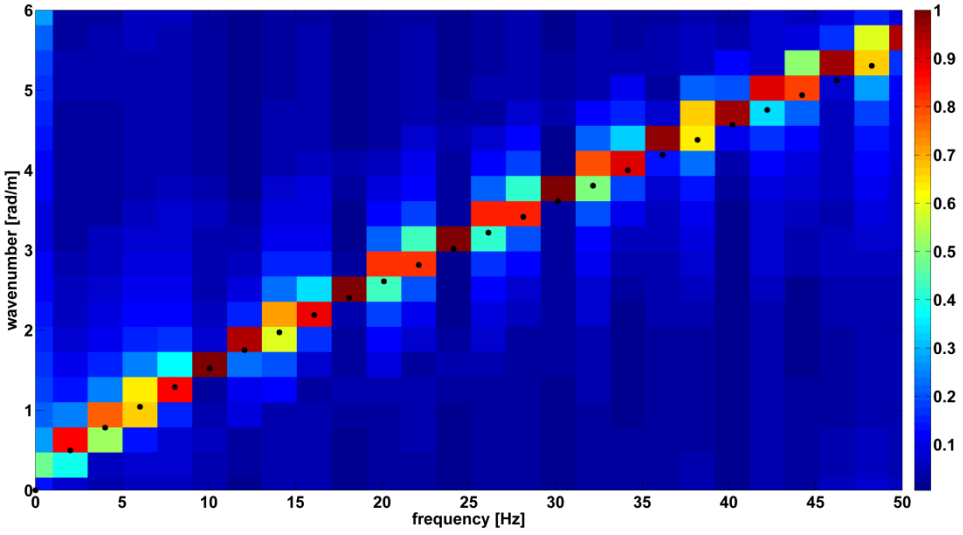

Figure E. 9: *F-k* spectrum obtained after the spectral product of the horizontal and of the vertical spectra in the frequency-space domain. Then equation (3.7) is applied. The black dots represent the actual dispersive relationship, as per equation (E.1).

Figure E. 9 shows the spectral image obtained with a product of the horizontal and of the vertical spectra in the frequency-space domain. Equation (3.7) was then applied to the frequency-space spectrum. The energy maxima in the spectra follow the black dots, which indicate the actual non-linear dispersive relationship. The spectral product in the frequency-space domain increases the resolution of the spectrum in the space domain. Since the purpose of the spectral convolution method

is to increase the resolution in both the frequency and wavenumber domain and to improve the accuracy in terms of detection of propagation modes and osculation points, this method was abandoned.

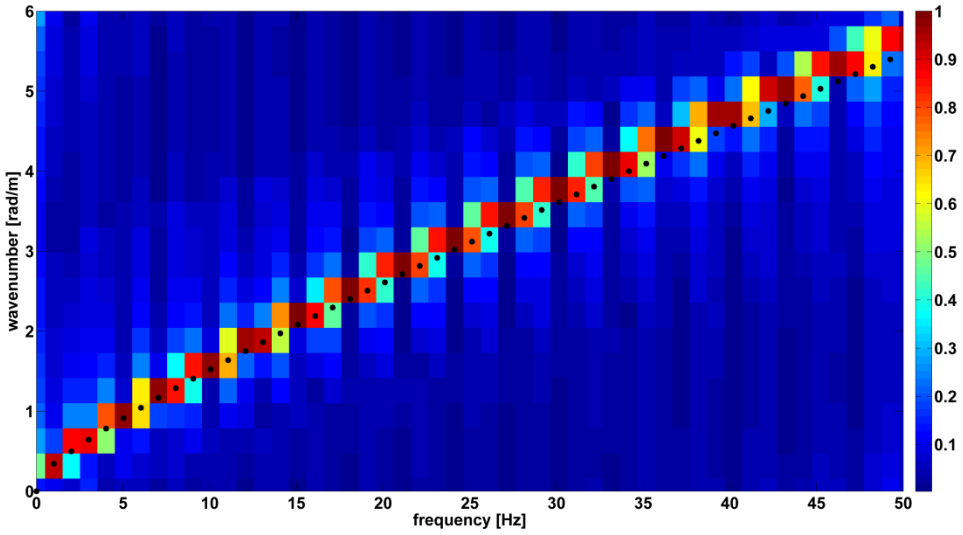

Figure E. 10: *F-k* spectrum obtained after the time convolution of the horizontal and of the vertical signals. Then equation (3.5) and (3.7) are applied. The black dots represent the actual dispersive relationship, as per equation (E.1).

Figure E. 10 shows the spectral image obtained performing a convolution of the vertical and of the horizontal signals in the time domain and then applying the equation (3.5) and the equation (3.6). The energy maxima in the spectra follow the black dots, which indicate the actual non-linear dispersive relationship. This method improves the resolution in both the wavenumber and frequency domain by a factor of two, likewise the spectral convolution method. Despite this, the application of the time convolution on numerical and experimental data failed to obtain relevant improvements on the accuracy of the dispersion curves. For this reasons the method needs future investigations and the spectral convolution method was preferred within this thesis.

Appendix F: Joint Use of Seismic and Electromagnetic Methods in Geophysical Surveys

This appendix reports the paper titled "Joint Use of Seismic and Electromagnetic Methods in Geophysical Surveys" presented at the NDT-CE 2015 International Symposium Non-Destructive Testing in Civil Engineering, held in Berlin, Germany. The fundamental aim of this paper was of finding some correlations between the properties measured with the Time Domain Reflectometry (TDR) and the phase velocity of the R-wave. In addition, one aim of this paper was of trying to indirectly measure the volumetric water content with the surface wave methods.

Shallow geophysical techniques such as seismic methods and electromagnetic methods are used in a range of applications to assess the condition of the ground. Seismic methods like MASW are typically used to determine *in-situ* soil's mechanical properties such as stiffness and density [5, 15]. Electromagnetic methods like the TDR are suited to measuring *in-situ* soil water content, clay content and to some extent, soil density [104, 105]. As with all geophysical techniques, each method has limitations and potentially suffers from non-uniqueness issues. The combined use of different shallow geophysical methods has proved useful in order to obtain more robust inversions by adding more *a-priori* information [106].

It has to be mentioned that Giulio Curioni from the University of Birmingham took all the TDR measurements displayed in the paper. His precious collaboration made possible the fulfilment of the work presented in this appendix.

Joint Use of Seismic and Electromagnetic Methods in Geophysical Surveys

Michele IODICE [1], Giulio CURIONI [2], David N. CHAPMAN [2], Jennifer MUGGLETON [1], Alexander C. ROYAL [2] and Emiliano RUSTIGHI [1]

[1] Institute of Sound and Vibration Research, University of Southampton; Southampton, United Kingdom
E_mail: erustighi@soton.ac.uk

[2] School of Civil Engineering, University of Birmingham, Edgbaston, Birmingham, United Kingdom
E_mail: g.curioni@bham.ac.uk

Abstract

Multichannel Analysis of Surface Waves (MASW) is a seismic wave propagation method which involves the measurement of Rayleigh waves propagating along the surface of a medium. The method is non-intrusive, fast and practical and it has been successfully utilized for the *in-situ* evaluation of shear modulus and layer thicknesses of soils and, more recently, pavement systems. The method is also widely utilized as a tool for monitoring stiffness during construction, for maintenance inspections and even for the detection of voids and sinkholes. Time Domain Reflectometry (TDR) is an electromagnetic method based on the measurement of the propagation velocity of a step voltage pulse along a probe inserted in the soil. Electrical properties of the soil, i.e. dielectric permittivity and bulk electrical conductivity, are determined and can be related to some geotechnical properties, e.g. the volumetric water content and potentially the soil density. Seismic wave propagation methods such as MASW are sometimes used in conjunction with electromagnetic methods, in an attempt to reduce the uncertainty associated with each individual method, and to provide an enhanced characterization of the investigated soil. It is still unknown however, whether they are mostly complementary methods or whether they share the assessment of common mechanical/geotechnical properties. In this work the potential and the limitations of the joint use of the MASW and TDR techniques were investigated through an *in-situ* near-surface programme measurement at two different soil sites, up to a depth of 1 metre. A Dynamic Cone Penetrometer test was performed and the Particle Size Distribution curve determined to extend the soil characterization, and where possible soil samples were taken at various depths in order to measure the dry density and the volumetric water content. The two techniques measured similar trends, augmenting the results obtained by each method and showing the potential for an enhanced and more complete assessment of the soil properties. In addition, bulk electrical conductivity was shown to be related to the shear modulus for the soils studied.

Keywords: Multichannel Analysis of Seismic Waves (MASW), Time Domain Reflectometry (TDR), dry density, volumetric water content (VWC), Dynamic Cone Penetrometer (DCP), phase velocity, shear wave velocity, dielectric permittivity, bulk electrical conductivity.

1. Introduction

Shallow geophysical techniques such as seismic methods and electromagnetic methods are used in a range of applications to assess the condition of the ground. Seismic methods are typically used to determine soil mechanical properties such as stiffness and density [1, 2]. Electromagnetic methods are suited to measuring soil water content, clay content and to some extent, soil density [3, 4]. As with all geophysical techniques, each method has limitations and potentially suffers from non-uniqueness issues. The combined use of different shallow geophysical methods has proved useful in order to obtain more robust inversions by adding more *a-priori* information [5]. Many efforts have been put in during the past few decades in searching for good correlations between seismic wave velocities and geotechnical parameters of soils and rocks, i.e. their mechanical properties. Many empirical correlations have been proposed between P-wave velocity and dry density of rocks, with decent correlation coefficients [6]. Kulkarni and co-workers found good relationships between geotechnical parameters and S-wave velocity of clays from coastal regions. In particular, it has been shown that the shear wave velocity in soils can be employed for estimating void ratio, bulk density, undrained shear strength and to some extent, gravimetric water content, with a certain degree of confidence. This investigation was based on the assessment of the shear velocity and geotechnical properties by means of laboratory tests on disturbed specimens [7]. Research by

other authors [8] led to similar empirical relationship between shear strength and natural water content of soils, depending on their natural physical composition. Parks [9] jointly used electromagnetic and seismic reflection method to evaluate the groundwater table in soil deposits, i.e. to identify the shallow water surface.
The present study shows the results of the combined application of a seismic and an electromagnetic method at two field test sites in the UK with the aim of comparing the two methods and identifying the potential and limitations of their joint use. This preliminary study also claims to understand the potential of surface wave methods and electromagnetic methods in assessing some geotechnical properties and in reducing the uncertainty of a geophysical survey.

2. Multichannel Analysis of Surface Waves

MASW is a seismic method that exploits the dispersive behaviour of surface waves to determine the dynamic shear modulus and thicknesses of shallow soil layers. The method consists of monitoring the propagation of Rayleigh waves over a wide range of wavelengths, at specified distances from the source. The vertical motion induced by the Rayleigh wave is recorded at different distances from the source, and each data in the time domain is then transformed into the frequency domain using a Fourier Transform. The Rayleigh velocity and shear velocity are closely linked through the Poisson's ratio of the medium; the shear velocity is linked to the shear modulus through constitutive relationships [1, 10].
The set-up configuration consists of a source of seismic energy and multiple receivers (typically 24, but also up to 48 or more) placed on the ground surface with an equal spacing along a survey line [11, 12]. The source offset x_1 and the spacing D between receivers are chosen according to the wavelength and hence the depth of investigation (Figure 1).

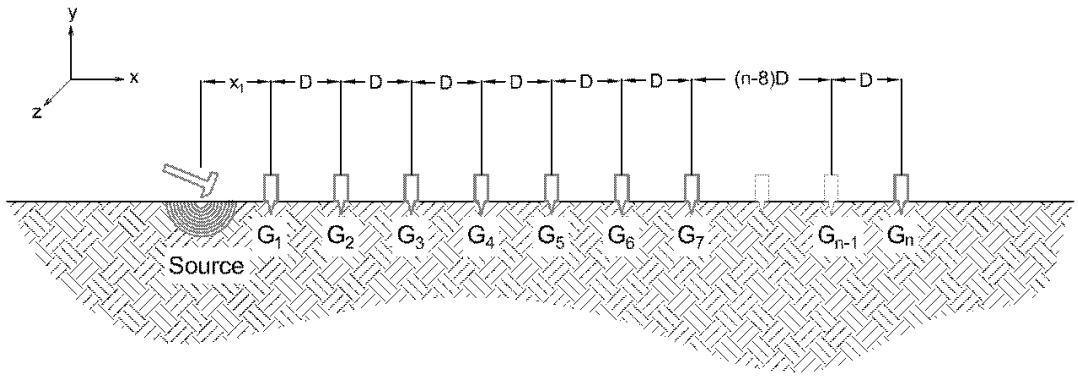

Figure 1. Typical MASW configuration, where X_1 is the source offset, G refers to a geophone, D is the receiver spacing and n is the number of receivers.

The seismic energy is recorded simultaneously by all the receivers. MASW typically uses a continuous source like a vibrator or an impulsive source like a sledgehammer [13]. When the MASW is used to determine the shear wave profile, the soil is assumed to behave as a horizontal layered model with no lateral variation in elastic properties [14]. The shear wave velocity profile is usually obtained through a numerical inversion of the experimental dispersion curve, and so is the shear modulus.

Surface Wave Spectral Method for Dispersion Calculation

With the Surface Wave Spectral Method the data collected with the surface wave method are used to construct the dispersion curve of a soil site, i.e. a depth-velocity curve. For each sensor spacing D, the phase velocity, or apparent velocity, is calculated as follows:

$$V_{ph} = \frac{D}{t(f)} = \frac{D \cdot 2\pi \cdot f}{\phi(f)} \tag{1}$$

where $\phi(f)$ is the phase difference between two signals, i.e. the phase of the cross-power spectrum between two signals. Repeating the same procedure for each possible receiver distance adds a contribution to the dispersion curve.

The definition of apparent or phase velocity is that of a velocity which does not necessarily correspond to the velocity of one mode of propagation or one wave, but is rather an average value among different types.

In this work data points with low coherence value (i.e. lower than 0.9) and with frequency value under the natural frequency of the geophones (i.e. 35Hz), are identified and discarded from the survey. To reduce the inclusion of ambient noise, 5 or more measurements are averaged (stacking).

It is clear that this technique is unable to discern different type of waves and different modes of propagation of Rayleigh waves. Rather the dispersion measurement is an average dispersion that takes into account all the phenomena occurring in the surveyed medium and hence a superposition of different modes of propagation. Therefore it is a reliable method for Rayleigh wave velocity measurement provided the first fundamental Rayleigh wave mode is dominant among all the other modes and waves in terms of energy; this is likely to be the case in homogeneous soils, when the stiffness does not vary abruptly with depth [15-17].

Seismic data are directly inverted into phase depth-velocity curves considering the effective depth of investigation equal to one third of the wavelength, from dispersion curves obtained through the spectral method. In fact for the vertical component of the wave motion the energy is more concentrated toward the surface, at a depth approximately equal to one third of the wavelength, suggesting that the measured wave velocity corresponds to the properties of material at this depth. A direct approximate inversion based on the effective depth of propagation of the Rayleigh wave is acceptable as a first approximation for the shallow subsurface, i.e. for the highest frequencies [1, 18, 19]. For the purposes of this work a more accurate inversion of the seismic data was not accomplished since the focus was on a preliminary comparison between MASW and TDR results.

3. Time Domain Reflectometry

TDR is a method for the determination of the relative apparent dielectric permittivity (k_a) and bulk electrical conductivity (EC_b) of soils [20, 21]. These electrical properties are known to be related to a number of soil properties, thus TDR is typically used in a variety of applications including agriculture, soil science and geotechnical engineering.

k_a (herein referred to as simply called permittivity) is a measure of the ability of a material to polarise when subject to an electric field. It is commonly used to measure the volumetric water content (VWC) of soil through empirical relationships, such as the widely used Topp model [21]. EC_b is a measure of the ability of a material to conduct electric current and can be used to estimate the attenuation of electromagnetic signals propagating through the soil.

TDR injects a short electromagnetic pulse into a coaxial cable and a multi-rod probe filled with or embedded in the material under test, and measures the reflected signals at the start and the end of the probe. Reflections occur in the presence of discontinuities such as a change in impedance, according to the following equation:

$$\rho = \frac{Z_s - Z_{out}}{Z_s + Z_{out}} \tag{2}$$

where Z_{out} is the impedance of the TDR unit and Z_s is the impedance of the soil sample. The TDR output is a waveform showing the reflection coefficient versus time. An example is given in Figure 2.

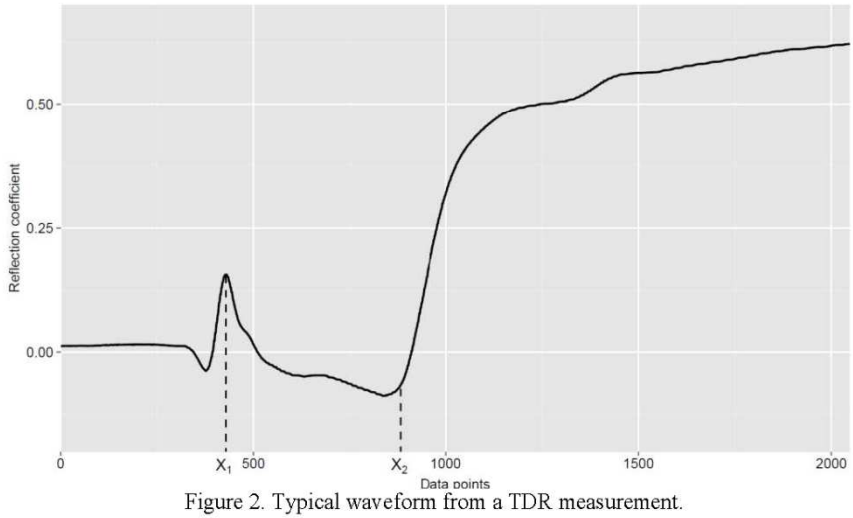

Figure 2. Typical waveform from a TDR measurement.

The propagation velocity of the electromagnetic signal propagating along the probe rods (transmitted and reflected) is proportional to the travel time for the pulse to traverse the length of the embedded waveguide (down and back) and to the length L of the waveguide (the probe rods). The travel time along the probe can be calculated from the reflections occurring at the start and at the end of the probe, x_1 and x_2 respectively. In practice, k_a is calculated by:

$$k_a = \left(\frac{x_2 - x_1}{P_P \cdot L} \right)^2 \tag{5}$$

where P_P is a relative propagation velocity, usually set equal to unity.

EC_b is measured with the method proposed by Giese and Tiemann [22] which uses the attenuation of the reflection coefficient at long apparent distances (i.e. at long reflection times). EC_b is calculated using the following expression, according to [23]:

$$EC_b = \frac{\varepsilon_0 \cdot c \cdot Z_0}{L \cdot (R_L - (L_1 \cdot R_c + R_0))} \tag{6}$$

where:

ε_0 is the absolute permittivity of free space

Z_0 is the characteristic impedance of the probe

R_L is the resistance of the sample, or load resistance

L_1 is the cable length

R_c is the cable resistance per unit length

R_0 is the extra resistance caused by the TDR device, the connectors, multiplexers and probe head

R_L is determined as follows:

$$R_L = Z_{out}\frac{1+\rho_\infty}{1-\rho_\infty} \tag{10}$$

where ρ_∞ is the reflection coefficient at long apparent distances.

4. Experimental Investigation

Experimental measurements were carried out at two different test sites up to a depth of one metre using the MASW and TDR techniques with the purpose of comparing the two methods. The test sites consisted of one predominantly clayey and of one predominantly sandy soil deposits with stiffness generally increasing with depth. A Dynamic Cone Penetrometer (DCP) test [24] was performed and Particle Size Distribution (PSD) curves determined for soil characterization purposes. When possible, dry density and VWC were measured at various depths from soil cylindrical samples of known volume taken on site, up to a depth of one metre. The PSD tests were conducted in accordance with B.S.1377.

4.1 Experimental Procedure Case Study 1

Case study 1 was located at Chilworth (UK), a few kilometres from Southampton University main campus. The experimental set-up for case study 1 consisted of a source and an array of 7 tri-axial geophones, arranged as shown in Figure 3. The data was acquired using a ProSig P8020 data acquisition unit and a laptop. The source consisted of an inertial shaker with a nominal moving mass of 1.21kg , vertically attached to one rectangular L-shaped aluminium platform, consisting of a horizontal 16.0x16.0xl.5cm plate and a vertical 10.0x16.0xl.5cm plate. The time extended signal was white noise, with a unit variance and low pass filtered at 4kHz .

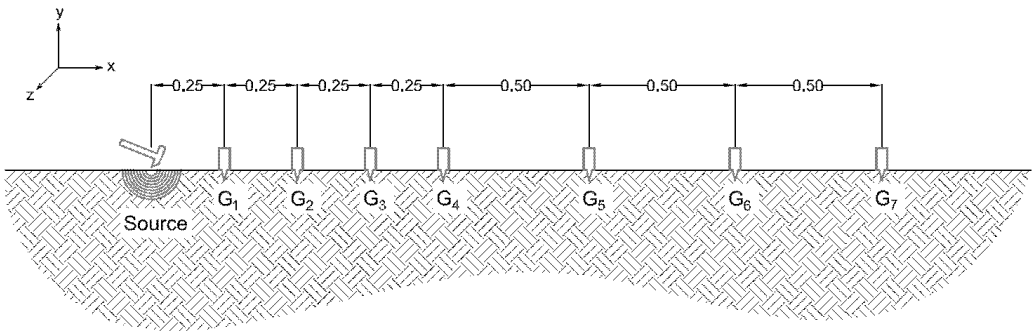

Figure 3. Experimental set-up for case study 1, G refers to a geophone and the number identifies the position. Distances are shown in metres.

TDR measurements were taken using a TDR100 device (Campbell Scientific, Logan, UT) and by inserting a TDR probe horizontally at the following depths into a shallow excavation: 0.04m, 0.28m, 0.35m, 0.45m, 0.63m. A Campbell Scientific CS635 150mm probe was used in the topsoil. However, due to the presence of large amounts of gravel and cobbles it was only possible to insert a smaller probe (model CS645, 75mm) in the subsoil. For the same reason it was not possible to collect soil samples of known volume from this site. The excavation was approximately 0.50m from the survey line in the proximity of geophone 3.
The DCP investigation was executed along the survey line, between geophone 3 and geophone 4 (see Figure 3).

4.2 Experimental results case study 1

Figure 4a depicts the phase velocity-depth curve for case study 1 obtained with a direct inversion of the dispersion curve, considering the depth of investigation of a Rayleigh wave equal to one third of its wavelength.
The phase velocity progressively increased with depth, as it is expected to behave in the presence of a regular soil profile due to increasing stiffness. It is also possible to observe two humps in the phase velocity trend, at depths of approximately 0.20m and 0.30m.
Figure 4b shows the electrical parameters measured with the TDR, i.e. k_a and EC_b, and the VWC calculated from the permittivity using the Topp model.
Both k_a and EC_b were related to the phase velocity, showing a similar trend with depth: they increased with depth and they also showed a clear hump at a depth between 0.30m and 0.40m. It should be noted that a TDR probe was not inserted at a depth of 0.20m and therefore it was not possible to confirm the presence of the hump identified by the MASW survey.

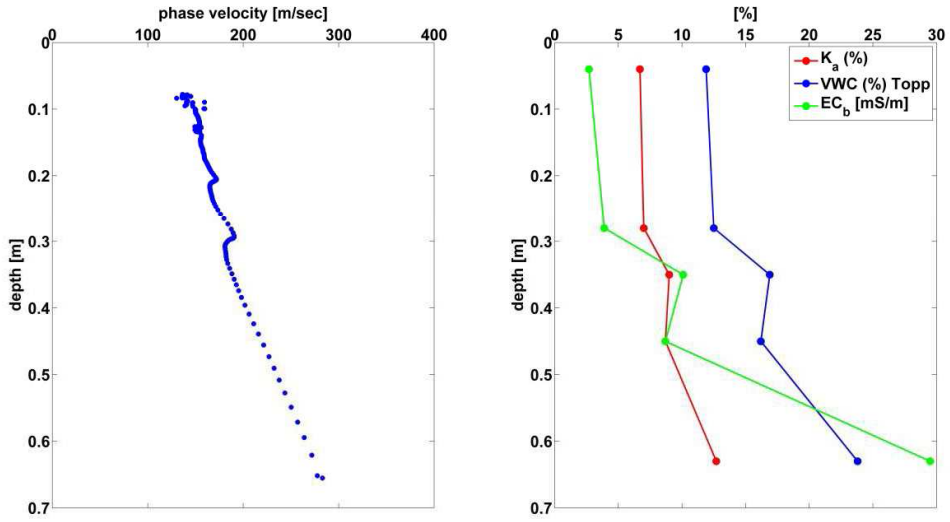

(a) (b)

Figure 4. Phase velocity-depth curve for case study 1 (a). Outputs from the TDR investigation for case study 1, with VWC calculated through the Topp model. Each marker denotes the depth at which the test is executed (b).

The DCP investigation as depicted in Figure 5a clearly showed the presence of a two-layered homogeneous soil, with a change in the slope of the DCP field test curve at a depth of

approximately 1.00m , corresponding to a change in the material stiffness. However, the DCP was not sensitive enough to slight changes in the stiffness in the first metre of depth.
The PSD curve for a soil sample taken at a depth of approximately 0.50m is shown in Figure 5b. The soil was a gravelly clay, with a percentage of fines (i.e. particles smaller than 0.063mm) of 32.

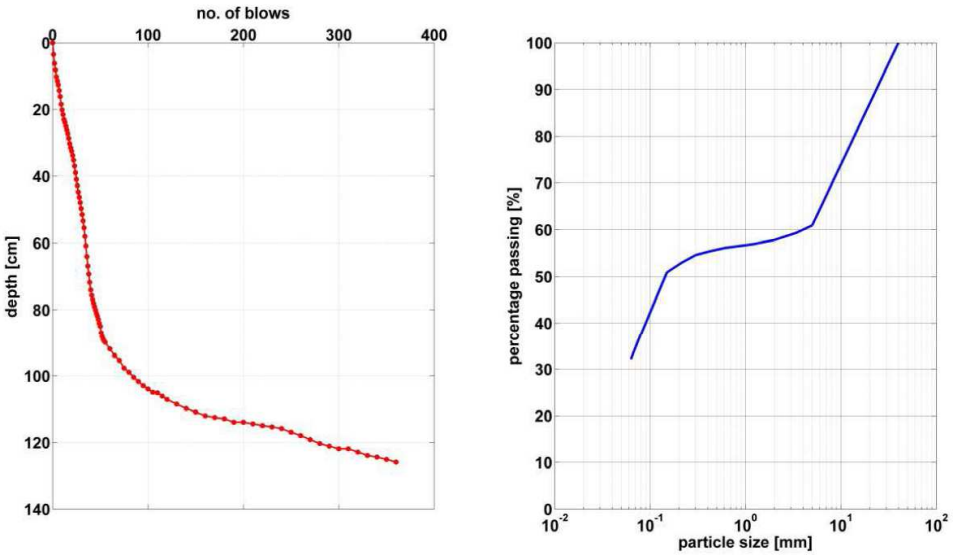

(a) (b)

Figure 5. DCP field test curve for case study 1 (a). PSD curve for case study 1 (b). The tests suggest gravelly clay and a two-layered system with a clear change in the stiffness at around one metre of depth.

4.3 Experimental procedure case study 2

Case study 2 was located at the University of Birmingham campus (UK). The experimental set-up consisted of a source and an array of 21 tri-axial geophones, as shown in Figure 6, covering a length L of 5.00m. The data was again acquired using a ProSig P8020 data acquisition unit and a laptop. The source consisted of a 4-oz metallic mallet striking a circular aluminium plate of 0.15m diameter and 1.5cm thickness. The data acquisition was triggered with respect to the hammer impact.
TDR measurements were taken by inserting a CS635 150mm probe at the following depths into a shallow excavation: 0.05m, 0.10m, 0.15m, 0.30m, 0.35m, 0.40m, 0.50m, 0.60m, 0.70m, 0.82m, 0.97m. The excavation was located approximately 1.00m far from the survey line in the proximity of geophone 8. The DCP investigation was executed along the survey line, corresponding to the position of geophone 6 (see Figure 6). In addition, soil samples of known volume were taken at different depths into the ground.

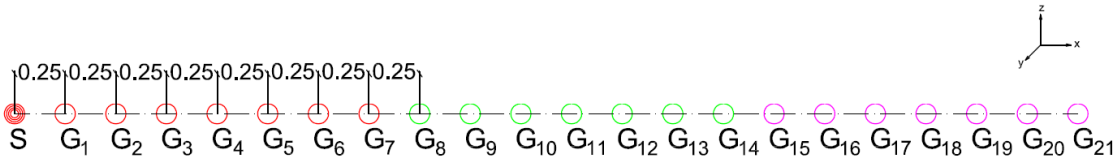

Figure 6. Experimental set-up for case study 2, G refers to a geophone, S refers to source and the number identifies the position. Distances are shown in metres (top view).

4.4 Experimental results case study 2

Figure 7a depicts the phase velocity-depth curve for case study 2 obtained with a direct inversion of the dispersion curve, considering the depth of investigation of a Rayleigh wave equal to one third of its wavelength.

The phase velocity was quite high near the surface, peaking at the depth of approximately 0.15m (probably due to a thin hard layer), followed by a sharp decrease and a slight increase at greater depths. A less noticeable peak was also present at a depth of approximately 0.40m.

Figure 7b shows the parameters measured with the TDR, i.e. k_a and EC_b, and the VWC calculated from the permittivity using the Topp model. The VWC calculated from the soil samples of known volume are also shown on Figure 7b.

The EC_b trend was consistent with the trend of the phase velocity, showing high values close to the surface, peaking at a depth of approximately 0.15m, and followed by a sharp decrease and a small increase at greater depths. A hump at a depth of 0.40m can also be seen. The k_a trend with depth was to some extent different from that of the phase velocity. In addition, the VWC computed with the Topp model did not differ significantly from the VWC measured in the laboratory.

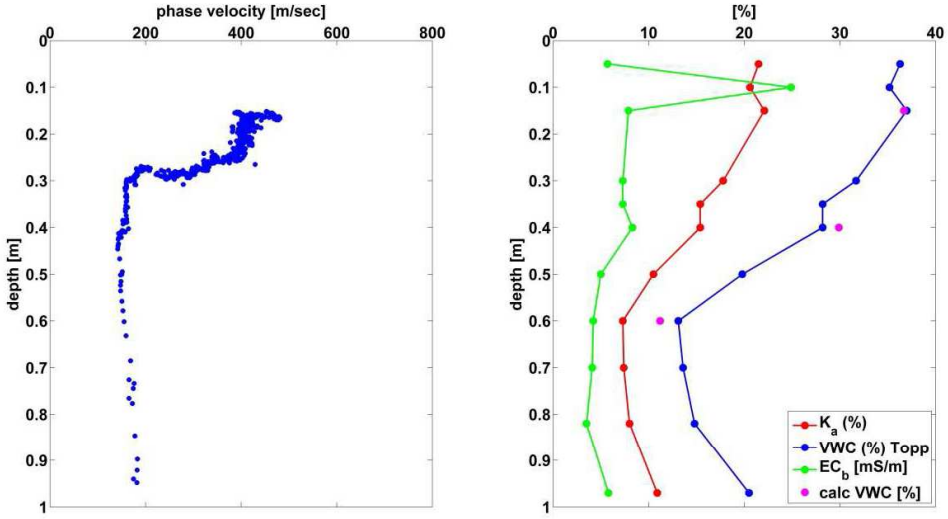

(a) (b)

Figure 7. Phase velocity-depth curve for case study 2 (a). Outputs of TDR investigation for case study 2, with VWC calculated through the Topp model and VWC measured with laboratory tests. Each marker denotes the depth at which the test is executed (b).

The DCP investigation as depicted in Figure 8a shows a soil profile with stiffness generally increasing with depth. Interestingly, a hump in the stiffness profile at a depth of approximately 0.40m was visible, which is in accordance with both the phase velocity and the EC_b profiles (Figure 7).

The PSD curve of a soil sample taken at the depth of approximately 0.60m, obtained in accordance with B.S. 1377, is shown in Figure 8b. The soil consisted of gravelly sand, with a percentage of fines below 10.

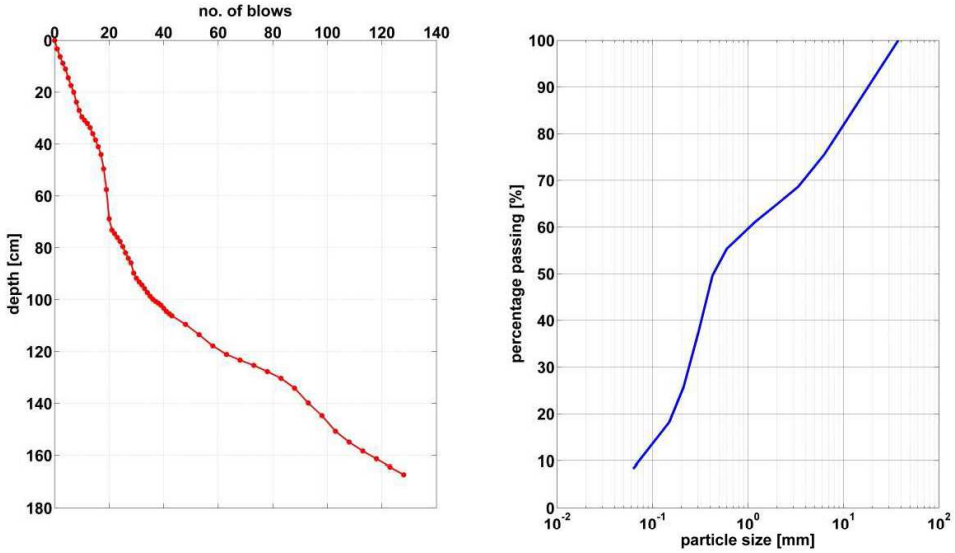

(a) (b)

Figure 8. DCP field test curve for case study 2 (a). PSD curve for case study 2 (b). The tests suggest gravelly sand and a two-layered system with a change in the stiffness at around one metre of depth.

5. Conclusions

This study has shown the joint application of a seismic (MASW) and an electromagnetic (TDR) method at two different field test sites in the UK consisting of a predominantly sandy soil and a predominantly clayey soil. The results from both investigations showed similar trends. In particular, EC_b was found to show a very similar behaviour with depth to the phase velocity, which can be assumed to equal the Rayleigh wave velocity of the fundamental mode in typical soil profiles. As the phase velocity in the soil increased, the EC_b increased, and viceversa, showing a strong positive correlation.

This agreement could be nonlinear, site and material dependent, so further investigations are needed to help better understand the relationships between shear modulus and bulk electrical conductivity of soils emerging from this preliminary study.

The positive relationship between k_a and the phase velocity, although noticeable in most cases, was slightly less evident compared to the relationship between EC_b and phase velocity.

In the case of the sandy soil (case study 2) where it was possible to collect samples of known volume, the values of VWC measured from the laboratory tests were consistent with the values calculated with TDR using the Topp model, showing only minor discrepancies. Thus, TDR was confirmed to be a reliable tool for the evaluation of *in-situ* VWC of sandy soils.

Therefore this preliminary study has shown that a joint test investigation on soil deposits using both seismic and electromagnetic techniques has the potential to improve the confidence in the data and the accuracy of shallow field surveys. In addition, this preliminary study had shown the possibility of relating the EC_b to the shear modulus of soils and, to some extent, to link the shear modulus of soils to their *in-situ* VWC. Since the comparison at this stage is qualitative, the physical meanings of these relationships, as well as their trends and limitations, are still unknown and further investigations are needed.

Acknowledgments
The authors gratefully acknowledge the financial support of the UK Engineering and Physical Sciences Research Council under grant EP/K021699 "Assessing the Underworld – an integrated performance model of city infrastructures".

References

1. Matthews, M.C., V.S. Hope, and C.R.I. Clayton. *The use of surface waves in the determination of ground stiffness profiles.* in *Proceedings of the ICE - Geotechnical Engineering*. 1996.
2. Foti, S., et al., *Application of Surface - Wave Methods for Seismic Site Characterization.* Surveys in geophysics, 32.6: 777-825, 2011.
3. Huisman, J.A., *Measuring soil water content with ground penetrating radar.* Vadose zone journal 2.4: 476-491., 2003.
4. Topp, G.C. and J.L.D.A.P. Annan, *Electromagnetic determination of soil water content: Measurements in coaxial transmission lines.* Water resources research 16.3: 574-582., 1980.
5. A. Besson, et al., *The spatial and temporal organization of soil water at the field scale as described by electrical resistivity measurements.* European Journal of Soil Science, 2010. **61**(1): p. 120-132.
6. Yagiz and Saffet, *P-wave velocity test for assessment of geotechnical properties of some rock materials.* Bulletin of Materials Science, 2011. **34**(4): p. 947-953.
7. Kulkarni, M.P., A. Patel, and D.N. Singh, *Application of shear wave velocity for characterizing clays from coastal regions.* KSCE Journal of Civil Engineering, 2010. **14**(3): p. 307-321.
8. Yun, T.S., G.A. Narsilio, and J.C. Santamarina, *Physical characterization of core samples recovered from Gulf of Mexico.* Marine and Petroleum Geology, 2006. **23**(9–10): p. 893-900.
9. Parks, E., *Analysis of Electromagnetic and Seismic Geophysical Methods for Investigating Shallow Sub-surface Hydrogeology.* 2010, Brigham Young University.
10. Houbrechts, J., et al., *Test Procedures for the Determination of the Dynamic Soil Characteristics.* 2011.
11. Nazarian, S., *Shear Wave Velocity Profiling with Surface Wave Methods.* Geotechnical Engineering State of Art and Practice: Keynote Lectures from GeoCongress 2012, pp.221-240, 2012.
12. Ryden, N., et al., *Multimodal approach to seismic pavement testing.* Journal of Geotechnical and Geoenvironmental Engineering 130.6: 636-645, 2004.
13. Park, C.B., R.D. Miller, and J. Xia, *Multichannel Analysis of Surface Waves.* Geophysics 64.3: 800-808, 1999.
14. Park, C.B., et al. *Multichannel Seismic Surface-Wave Methods for Geotechnical Applications.* in *Proceedings of the First International conference on the application of geophysical methodologies to transportation facilities and infrastructure, St. Louis.* 2000.
15. Park, C.B., R.D. Miller, and J. Xia. *Multimodal analysis of high frequency surface waves.* in *Proceedings of the symposium on the application of geophysics to engineering and environmental problems. Vol. 99.* . 1999.
16. Gucunski, N. and R.D. Woods, *Numerical simulation of the SASW test.* Soil Dynamics and Earthquake Engineering 11.4 (1992): 213-227., 1992.
17. Gucunski, N. and R.D. Woods, *Use of Rayleigh modes in interpretation of SASW test*, in *Second International Conference on Recent Advances in Geotechnical Earthquake*

Engineering and Soil Dynamics 1991: Missouri S&T (formerly the University of Missouri--Rolla), St. Louis, Missouri.

18. Nazarian, S. and K. Stokoe, *Evaluation of moduli and thicknesses of Pavement System by Spectral-Analysis-of-Surface-Waves Methods.* No. FHWA-TX-83-26+ 256-4 Intrm Rpt., The Center 1983.
19. Heisey, J.S., et al., *Determination of in Situ Shear Wave Velocities from Spectral Analysis of Surface Waves.* No. FHWA/TX-82/34+ 256-2 Intrm Rpt, 1982.
20. Curioni, G., et al., *Construction and calibration of a field TDR monitoring station.* Near Surface Geophysics 10.3: 249-261, 2012.
21. Jones, S.B., J.M. Wraith, and D. Or, *Time domain reflectometry measurement principles and applications.* Hydrological processes 16.1: 141-153, 2002.
22. Giese, K. and R. Tiemann, *Determination of the complex permittivity from thin-sample time domain reflectometry improved analysis of the step response waveform.* Advances in Molecular Relaxation Processes 7.1 : 45-59, 1975.
23. Bechtold, M., *Accurate determination of the bulk electrical conductivity with the TDR100 cable tester.* Soil Science Society of America Journal 74.2 : 495-501, 2010.
24. *Lab Quip Limited, Dynamic Cone Penetrometer Operating Instructions.*

References

[1] J. Houbrechts, M. Schevenels, G. Lombaert, G. Degrande, W. Rücker, V. Cuellar, and A. Smekal, "Test Procedures for the Determination of the Dynamic Soil Characteristics," *Railway Induced Vibration Abatement Solutions RIVAS WP 1,* 2011.

[2] R. Luna and H. Jadi, "Determination of Dynamic Soil Properties Using Geophysical Methods," in *Proceedings of the First International Conference on the Application of Geophysical and NDT Methodologies to Transportation Facilities and Infrastructure—Geophysics*, 2000.

[3] M. C. Matthews, C. R. I. Clayton, and Y. Own, "The use of field geophysical techniques to determine geotechnical stiffness parameters," in *Proceedings of the ICE-Geotechnical Engineering 143.1: 31-42*, 2000.

[4] B. Menzies, "Near-surface site characterisation by ground stiffness profiling using surface wave geophysics," *Instrumentation in Geotechnical Engineering, HC Verma Commemorative Volume: 43-71,* 2001.

[5] M. C. Matthews, V. S. Hope, and C. R. I. Clayton, "The use of surface waves in the determination of ground stiffness profiles," in *Proceedings of the ICE - Geotechnical Engineering*, 1996, pp. 84-95.

[6] C. B. Park, R. D. Miller, and J. Xia, "Multichannel Analysis of Surface Waves," *Geophysics 64.3: 800-808,* 1999.

[7] S. Nazarian, "Shear Wave Velocity Profiling with Surface Wave Methods," *Geotechnical Engineering State of Art and Practice: Keynote Lectures from GeoCongress 2012, pp.221-240,* 2012.

[8] J. Kumar and P. G. Rakaraddi, "SASW evaluation of asphaltic and cement concrete pavements using different heights of fall for a spherical mass," *International Journal of Pavement Engineering 14.4: 354-363,* 2013.

[9] J. S. Heisey, K. H. Stokoe, W. R. Hudson, and A. H. Meyer, "Determination of in Situ Shear Wave Velocities from Spectral Analysis of Surface Waves," *No. FHWA/TX-82/34+ 256-2 Intrm Rpt,* 1982.

[10] K. Stokoe and S. Nazarian, "Use of Rayleigh waves in liquefaction studies," *Measurement and use of shear wave velocity for evaluating dynamic soil properties, ASCE, 1985.*

[11] C. G. Lai, S. Foti, A. Godio, G. J. Rix, L. Sambuelli, and V. L. Socco, "Caratterizzazione Geotecnica dei Terreni Mediante l'Uso di Tecniche Geofisiche," *Numero speciale: Sviluppi nell'esecuzione e nell'impiego delle indagini geotecniche, 99-118.D.,* 2000.

[12] D. Jongmans and D. Demanet, "The importance of surface waves in vibration study and the use of Rayleigh waves for estimating the dynamic characteristics of soils," *Engineering Geology,* vol. 34, pp. 105-113, 1993.

[13] N. Ryden, C. B. Park, P. Ulriksen, and R. D. Miller, "Multimodal approach to seismic pavement testing," *Journal of Geotechnical and Geoenvironmental Engineering 130.6: 636-645,* 2004.

[14] Y. Nakamura, "A method for dynamic characteristics estimation of subsurface using microtremor on the ground surface," *Railway Technical Research Institute, Quarterly Reports 30.1,* 1989.

[15] S. Foti, S. Parolai, D. Albarello, and M. Picozzi, "Application of Surface‐Wave Methods for Seismic Site Characterization," *Surveys in geophysics, 32.6: 777-825,* 2011.

[16] T. Forbriger, "Inversion of shallow-seismic wavefields: I. Wavefield transformation," *Geophysical Journal International 153.3: 719-734,* 2003.

[17] S. Foti, R. Lancellotta, L. V. Socco, and L.Sambuelli, "Application of FK analysis of surface waves for geotechnical characterization," in *Proceedings of the fourth international conference on recent advances in geotechnical earthquake engineering and soil dynamics and symposium in honour of professor WD Liam Finn*, 2001.

[18] C. B. Park, R. D. Miller, and J. Xia, "Multimodal analysis of high frequency surface waves," in *Proceedings of the symposium on the application of geophysics to engineering and environmental problems. Vol. 99*, 1999.

[19] N. Gucunski and R. D. Woods, "Use of Rayleigh modes in interpretation of SASW test," presented at the Second International Conference on Recent Advances in Geotechnical Earthquake Engineering and Soil Dynamics Missouri S&T (formerly the University of Missouri-Rolla), St. Louis, Missouri, 1991.

[20] Tokimatsu K., Tamura S., and Kojima H., "Effects of multiple modes on Rayleigh wave dispersion characteristics," *Journal of Geotechnical Engineering,* vol. 118, pp. 1529-1543, 1992.

[21] L. Lu and B. Zhang, "Analysis of dispersion curves of Rayleigh waves in the frequency wavenumber domain," *Canadian geotechnical journal 41.4 (2004): 583-598,* 2004.

[22] G. D. Moro, *Surface Wave Analysis for Near Surface Applications*: Elsevier, 2014.

[23] J. Boaga, G. Cassiani, C.L. Strobbia, and G. Vignoli, "Mode misidentification in Rayleigh waves: Ellipticity as a cause and a cure," *Geophysics,* vol. 78, pp. EN17-EN28, 2013.

[24] J. Boaga, G. Vignoli, R. Deiana, and G. Cassiani, "The Influence of Subsoil Structure and Acquisition Parameters in MASW Mode Mis-identification," *Journal of Environmental and Engineering Geophysics,* vol. 19, pp. 87-99, 2014.

[25] C. G. Lai, "Spectral Analysis of Surface Waves Active Methods Technical Recommendations," *Rivista Italiana di Geotecnica 4/2000.*

[26] S. Yagiz, "P-wave velocity test for assessment of geotechnical properties of some rock materials," *Bulletin of Materials Science,* vol. 34, pp. 947-953, 2011.

[27] M. P. Kulkarni, A. Patel, and D. N. Singh, "Application of shear wave velocity for characterizing clays from coastal regions," *KSCE Journal of Civil Engineering,* vol. 14, pp. 307-321, 2010.

[28] T. S. Yun, G. A. Narsilio, and J. C. Santamarina, "Physical characterization of core samples recovered from Gulf of Mexico," *Marine and Petroleum Geology,* vol. 23, pp. 893-900, 2006.

[29] E. Parks, "Analysis of Electromagnetic and Seismic Geophysical Methods for Investigating Shallow Sub-surface Hydrogeology," Master of Science, Brigham Young University, 2010.

[30] G. Gazetas, "Vibrational characteristics of soil deposits with variable wave velocity," *International Journal for Numerical and Analytical Methods in Geomechanics,* vol. 6, pp. 1-20, 1982.

[31] C. B. Park, R. D. Miller, J. Xia, and J. Ivanov, "Seismic Characterization of Geotechnical Sites By Multichannel Analysis of Surface Waves (MASW) Method," presented at the Tenth International Conference on Soil Dynamics and Earthquake Engineering (SDEE), Philadelphia, 2001.

[32] N. Gucunski and R. D. Woods, "Numerical simulation of the SASW test," *Soil Dynamics and Earthquake Engineering,* vol. 11, pp. 213-227, 1992.

[33] C. B. Park, R. D. Miller, J. Xia, and J. Ivanov, "Multichannel Seismic Surface-Wave Methods for Geotechnical Applications," in *Proceedings of the First International conference on the application of geophysical methodologies to transportation facilities and infrastructure, St. Louis*, 2000.

[34] G. A. McMechan and M. J. Yedlin, "Analysis of dispersive waves by wave field transformation," *Geophysics 46.6 (1981): 869-874,* 1981.

[35] A. Goel and A. Das, "A Brief Review on Different Surface Wave Methods and Their Applicability for Non- Destructive Evaluation of Pavements," *Nondestructive Testing and Evaluation: 337-350,* 2008.

[36] L.V. Socco, S. Foti, and D. Boiero, "Surface-wave analysis for building near-surface velocity models—Established approaches and new perspectives," *Geophysics,* vol. 75, pp. 75A83-75A102, 2010.

[37] L.D. Olson and P. K. Miller, "Multiple Impact Surface Waves (MISW) - Improved Accuracy for Pavement System Thicknessess and Moduli vs. Spectral Analysis of Surface Waves (SASW)," *GeoFlorida 2010@ sAdvances in Analysis, Modeling & Design. ASCE, 2010.*

[38] Y. Nakamura, "Clear identification of fundamental idea of Nakamura's technique and its applications," in *Proceedings of the 12th world conference on earthquake engineering*, 2000.

[39] P.G. Malischewsky and F. Scherbaum, "Love's formula and H/V-ratio (ellipticity) of Rayleigh waves," *Wave motion,* vol. 40, pp. 57-67, 2004.

[40] D. Albarello, "Metodi geofisici per la caratterizzazione sismica del sottosuolo," ed, 2011.

[41] N. Ryden, C. Park, P. Ulriksen, and R. Miller, "Branching of dispersion curves in surface wave testing of pavements," in *Proceedings of the Symposium on the Application of Geophysics to Engineering and Environmental Problems (SAGEEP 2002)*, Las Vegas, NV, 2002.

[42] S. Nazarian and K. Stokoe, "Evaluation of moduli and thicknesses of Pavement System by Spectral-Analysis-of-Surface-Waves Methods," *No. FHWA-TX-83-26+ 256-4 Intrm Rpt., The Center* 1983.

[43] S. Nazarian, D. Yuan, and M. R. Baker, "Rapid Determination of Pavement Moduli with Spectral-Analysis-of-Surface-Waves Method," *Center for Geotechnical and Highway Materials Research, University of Texas at El Paso,* 1995.

[44] C. B. Park, J. Ivanov, R. D. Miller, and J. Xia, "Seismic investigation of pavements by MASW method—geophone approach," in *Proceedings of the SAGEEP*, 2001.

[45] C. B. Park, "Multichannel analysis of surface waves (MASW) for pavement-feasibility test," in *Proceedings of the 5th SEGJ International Symposium*, 2001.

[46] N. Ryden and C. B. Park, "Fast simulated annealing inversion of surface waves on pavement using phase-velocity spectra," *Geophysics 71.4 (2006): R49-R58.,* 2006.

[47] N. Gucunski and A. Maher, "Evaluation of Seismic Pavement Analyzer for Pavement Condition Monitoring," *No. FHWA-NJ-2002-012,* 2002.

[48] W. J. M. Steyn and E. Sadzik, "Application of the portable pavement seismic analyser (PSPA) for pavement analysis," presented at the 26th Annual Southern African Transport Conference and Exhibition, Pretoria, South Africa, 9-12 July, 2007, pp 11, 2007.

[49] F. Hugo and J. Lee, "Using Seismic Wave Propagation as a PMS Tool," in *Fourth International Conference on Managing Pavements*, Durban, South Africa, 1998.

[50] M. Jurado, N. Gibson, M. Celaya, and S. Nazarian, "Evaluation of Asphalt Damage and Cracking Development with Seismic Pavement Analyzer," *Transportation Research Record: Journal of the Transportation Research Board 2304.1: 47-54,* 2012.

[51] D. Yuan, S. Nazarian, D. Chen, and M. McDaniel, "Use of seismic methods in monitoring pavement deterioration during accelerated pavement testing with TxMLS," in *Proceedings of the First International Conference on Accelerated Pavement Testing, Reno, Nev.*, 1999.

[52] W. Song, J. S. Popovics, J. C. Aldrin, and P. S. Shah, "Measurement of surface wave transmission coefficient across surface-breaking cracks and notches in concrete," *The Journal of the Acoustical Society of America,* vol. 113, pp. 717-725, 2003.

[53] S. Ayter and B.A. Auld, "On the resonances of surface breaking cracks," in *Proceedings of the DARPA/AFML Review of Progress in Quantitative NDE, July 1978–September 1979*, 1980.

[54] V. Domarkas, B. T. Khuri‐Yakub, and G. S. Kino, "Length and depth resonances of surface cracks and their use for crack size estimation," *Applied Physics Letters,* vol. 33, pp. 557-559, 1978.

[55] A. Fahr and W. R. Sturrock, "Detection and characterization of surface cracks using leaky Rayleigh waves," in *Review of Progress in Quantitative Nondestructive Evaluation*, ed: Springer, 1985, pp. 559-568.

[56] M. Hirao and H. Fukuoka, "Scattering of Rayleigh surface waves by edge cracks: Numerical simulation and experiment," *The Journal of the Acoustical Society of America,* vol. 72, pp. 602-606, 1982.

[57] N. Gucunski and P. Shokouhi, "Detection and characterization of cavities under the airfield pavements by wavelet analysis of surface waves," presented at the Worldwide Airport Technology Transfer Conference, Atlantic, 2004.

[58] A. Zerwer, M. A. Polak, and J. C. Santamarina, "Effect of Surface Cracks on Rayleigh Wave Propagation: An Experimental Study," *Journal of Structural Engineering,* vol. 128, pp. 240-248, 2002.

[59] G. Hevin, O. Abraham, H.A. Pedersen, and M. Campillo, "Characterization of surface cracks with Rayleigh waves: a numerical model," *NDT & E International,* vol. 31, pp. 289-297, 1998.

[60] A. Zerwer, M. A. Polak, and J. C. Santamarina, "Rayleigh Wave Propagation for the Detection of Near Surface Discontinuities: Finite Element Modeling," *Journal of nondestructive evaluation 22.2 (2003): 39-52,* 2003.

[61] N. J. Carino, "Impact Echo: The Fundamentls," in *Internation Symposium Non-Destructive Testing in Civil Engineering (NDT-CE)*, Berlin, 2015.

[62] J. S. Heisey, "Determination of in situ shear wave velocities from spectral analysis of surface waves," MS thesis, University of Texas, Austin, 1981.

[63] E. Kausel and J. M. Roësset, "Stiffness matrices for layered soils," *Bulletin of the Seismological Society of America,* vol. 71, pp. 1743-1761, December 1, 1981.

[64] V. Roma, "Soil properties and site characterization by means of Rayleigh waves," Doctor of Philosophy thesis in Geotechnical Engineering, Department of Structural and Geotechnical Engineering, Technical University of Turin (Politecnico), 2001.

[65] "Lab Quip Limited, Dynamic Cone Penetrometer Operating Instructions."

[66] K. F. Graff, *Wave Motion in Elastic Solids*, Courier Dover Publications, 1975.

[67] J. P. Wolf, *Dynamic soil-structure interaction*: Prentice Hall int., 1985.

[68] G. F. Miller and H. Pursey, "The Field and Radiation Impedance of Mechanical Radiators on the Free Surface of a Semi-Infinite Isotropic Solid," *Proceedings of the Royal Society of London. Series A. Mathematical and Physical Sciences,* vol. 223, pp. 521-541, May 20, 1954.

[69] R. D. Woods, *Screening of Surface Waves in Soils*, Am Soc Civil Engr J Soil Mech , 1968.

[70] M. W. D. Boiero, and P. Vermeer, "Q Estimation from Surface Waves," presented at the 75th EAGE Conference & Exhibition incorporating SPE EUROPEC 2013, 2013.

[71] K. E. Bullen, *An introduction to the theory of seismology*, Cambridge University Press, 1985.

[72] S. C. Solomon, "Seismic-wave attenuation and the state of the upper mantle," Doctor of Philosophy thesis, California Institute of Technology, 1971.

[73] C. Madiai and E. Gargini, "Richiami di teoria di propagazione delle onde sismiche," *Università degli studi di Firenze*.

[74] G. Waas, *Linear two-dimensional analysis of soil dynamics problems in semi-infinite layered media*: University of California, Berkeley, 1972.

[75] S. Yoon, "Array-Based Measurements of Surface Wave Dispersion and Attenuation Using Frequency-Wavenumber Analysis," Doctor of Philosophy thesis, Georgia Institute of Technology, 2005.

[76] J. D. Zywicki and R. J. Rix, "Mitigation of near-field effects for seismic surface wave velocity estimation with cylindrical beamformers," *Journal of Geotechnical and Geoenvironmental Engineering,* vol. 131, pp. 970-977, 2005.

[77] S. B. L. Júnior, R. L. Prado, and R. M. Mendes, "Application of Multichannel Analysis of Surface Waves Method (MASW) in Area Susceptible to Landslide at Ubatuba City, Brazil," *Revista Brasileira de Geofisica 30(2): 213-224,* vol. 30, 2012.

[78] C. B. Park, R. D. Miller, and H. Miura, "Optimum field parameters of an MASW survey," *Exp. Abs.: SEG-J, Tokyo,* 2002.

[79] K. Tokimatsu, "Vs determination from steady state Rayleigh wave method," *Soils and Foundations, 31.2: 153-163,* 1991.

[80] M. Schevenels, S. A. Badsar, and G. Degrande, "The Use of the SASW method to determine the shear wave velocity and the material damping ratio of shallow soil layers," in *71st EAGE Conference & Exhibition - Workshops and Fieldtrips*.

[81] Y. Gao, M.J. Brennan, P.F. Joseph, J.M. Muggleton, and O. Hunaidi, "A model of the correlation function of leak noise in buried plastic pipes," *Journal of Sound and Vibration,* vol. 277, pp. 133-148, 2004.

[82] A. Zerwer, G. Cascante, and J. Hutchinson, "Parameter estimation in finite element simulations of Rayleigh waves," *Journal of geotechnical and geoenvironmental engineering 128.3 (2002): 250-261,* 2002.

[83] A. Zerwer, "Near Surface Fracture Detection in Structural Elements: Investigation Using Rayleigh Waves," Doctor of Philosophy thesis, University of Waterloo, 1999.

[84] "https://en.wikipedia.org/wiki/Explicit_and_implicit_methods."

[85] "Abaqus 6.12 Abaqus/CAE User's Manual."

[86] K. Edip, M.Garevski, V. Sesov, and C. Butenweg, "Numerical simulation of wave propagation in soil media," presented at the 21st European Young Geotechnical Engineers Conference, 2011.

[87] E. F. D'Azevedo, "Are bilinear quadrilaterals better than linear triangles?," *SIAM Journal on Scientific Computing,* vol. 22, pp. 198-217, 2000.

[88] R. L. Kuhlemeyer and J. Lysmer, "Finite element method accuracy for wave propagation problems," *Journal of Soil Mechanics & Foundations Div 99.Tech Rpt,* 1973.

[89] C. T. Schroder and W. R. J. Scott, "A Finite-Difference Model to Study the Elastic-Wave Interactions with Buried Land Mines," *Geoscience and Remote Sensing, IEEE Transactions on 38.4 (2000): 1505-1512,* 2000.

[90] C. T. Schroder, "On the interaction of elastic waves with buried land mines: an investigation using the finite-difference time-domain method," *Georgia Institute of Technology,* 2001.

[91] E. L. Wilson, *Static and Dynamic Analysis of Structures (4th ed.)*, 2004.

[92] J-Y Shih, D.J. Thompson, and A. Zervos, "Assessment of track-ground coupled vibration induced by high-speed trains," 2014.

[93] M. O. Al-Hunaidi, "Nondestructive evaluation of pavements using spectral analysis of surface waves in the frequency wave-number domain," *Journal of Nondestructive Evaluation,* vol. 15, pp. 71-82, 1996.

[94] J. M. Muggleton, M. J. Brennan, and P. W. Linford, "Axisymmetric wave propagation in fluid-filled pipes: wavenumber measurements in in vacuo and buried pipes," *Journal of Sound and Vibration 270.1 (2004): 171-190.*

[95] B. R. Mace and C. R. Halkyard, "Time domain estimation of response and intensity in beams using wave decomposition and reconstruction," *Journal of Sound and Vibration 230.3 (2000): 561-589.*

[96] *https://en.wikipedia.org/wiki/Overdetermined_system.*

[97] V. Ganji, N. Gucunski, and S. Nazarian, "Automated inversion procedure for spectral analysis of surface waves," *Journal of geotechnical and geoenvironmental engineering 124.8 (1998): 757-770.,* 1998.

[98] A. D. Poularikas, *Handbook of formulas and tables for signal processing* vol. 13: CRC Press, 1998.

[99] A. Preumont, *Mechatronics Dynamics of Electromechanical and Piezoelectric Systems* vol. Vol. 136, Springer, 2006.

[100] "Mott MacDonald, Southampton University Glen Eyre Pavement Survey Report," ed, 2014.

[101] W.R. Scott, J.S. Martin, and G.D. Larison, "Experimental model for a seismic landmine detection system," *IEEE Transactions on Geoscience and Remote Sensing,* vol. 39, pp. 1155-1164, 2001.

[102] R. Lancellotta and J. Calavera, *Fondazioni*, McGraw-Hill, 1999.

[103] E. Kausel and R. Peek, "Dynamic loads in the interior of a layered stratum: an explicit solution," *Bulletin of the Seismological Society of America 72.5 (1982): 1459-1481,* 1982.

[104] J. A. Huisman, "Measuring soil water content with ground penetrating radar," *Vadose zone journal 2.4: 476-491.,* 2003.

[105] G. C. Topp, J. L. Davis, and A. P. Annan, "Electromagnetic determination of soil water content: Measurements in coaxial transmission lines," *Water resources research 16.3: 574-582,* 1980.

[106] A. Besson, I. Cousin, H. Bourennane, B. Nicoullaud, C. Pasquier, G. Richard, A. Dorigny, and D. King, "The spatial and temporal organization of soil water at the field scale as described by electrical resistivity measurements," *European Journal of Soil Science,* vol. 61, pp. 120-132, 2010.